Energy Harvesting Using Screen Printed PZT on Silicon

Lei, Anders; Thomsen, Erik Vilain

Publication date:
2012

Document Version
Publisher's PDF, also known as Version of record

DTU Nanotech
Department of Micro- and Nanotechnology

Ph.D. Thesis

Energy Harvesting Using Screen Printed PZT on Silicon

Anders Lei

November 2012

DTU Nanotech - Department of Micro and Nanotechnology
Technical University of Denmark

Supervisor: Professor Erik Vilain Thomsen
Collaboration Partners: Meggitt Sensing Systems A/S & Vestas Wind Systems A/S
Funded by the Danish National Advanced Technology Foundation

Summary

The objective of the work presented in this Ph.D. thesis is to design and fabricate a miniaturised vibration energy harvester based on screen printed PZT thick film and silicon MEMS processing technology. The vision of the vibration energy harvester is to eliminate the need for batteries by harvesting energy on-site from a vibration source, thereby enabling fully autonomous wireless sensor systems.

The vibration harvester is a resonator consisting of a silicon support cantilever with screen printed PZT thick film on top and with an integrated proof mass at the cantilever tip. To achieve matching between the harvesters resonant frequency and vibration sources in the low frequency range, the thickness of the cantilever is required to be in the sub-100 µm range not to compromise the total dimension of the harvester. Fabricating this challenging and fragile design with the cantilever thickness being two orders of magnitude smaller than the cantilever length and width, is accomplished using the high control and precision of the silicon processing technology. With extensive process development the issue of fragility is minimised, and fabrication yields exceeding 90% are routinely achieved. The final fabrication process features a sequence with screen printing of the PZT thick film at an early stage and cantilever definition by etching at a later stage. Screen printing PZT on a full thickness silicon wafer enables efficient use of a high pressure treatment process with improved performance as a result. Cleanroom contamination issues in the cantilever etching due to the PZT film is solved with a KOH etch where the wafer front side is protected mechanically.

From thorough characterisation of the fabricated harvester, it is validated that the power output can be expressed as a power available term and a multiplication factor equal to or less than 1. The available power is proportional to the force acting on the cantilever squared and the inverse of the viscous damping coefficient. The latest fabricated batch of harvesters produced in average 34.5 µW of RMS power over a resistive load of 50 kΩ with an RMS acceleration of $0.5g$ at 511 Hz. The best performing devices under similar conditions produced 44.9 µW at 543 Hz. Compared to other state of the art miniaturised vibration energy harvesters, the normalised power density for the harvesters fabricated in this work is 3.5 times higher than the next best harvester.

Summary (Danish)

Målet med denne ph.d. afhandling er at designe og fabrikere en miniaturiseret vibrations energi høster baseret på silketrykt PZT tyk film og silicium processerings teknologi. Visionen for vibrations energi høsteren er at eliminere behovet for batterier ved at høste energi fra omkringliggende vibrationskilder for derved at muliggøre autonome trådløse sensor systemer.

Vibrations høsteren er en resonator som består af en silicium bjælke der er fastspændt i den ene ende og som fungerer som support for et silketrykt PZT lag. I den frie ende af bjælken er en integreret masse. For at opnå match mellem resonans frekvensen for bjælken og vibrationskilder i lave frekvensområder, skal tykkelse af bjælken være under 100 mikrometer for ikke at kompromittere den total størrelse af høsteren. Fremstillingen af dette udfordrende og skrøbelige design med en bjælketykkelse to størrelsesordner mindre en længde og bredde, er opnået ved hjælp at den høje kontrol og præcision som silicium processeringen tilbyder. Den endelige fabrikationsproces bygger på en rækkefølge hvor silketrykningen af PZT tyk filmen er foretaget i et tidligt stadie med ætsningen af bjælken senere. Ved at silketrykke på en siliciumskive a fuld tykkelse er det muligt at opnå en effektiv højtryksbehandling hvorved PZT egenskaberne bliver forbedret. Kontamineringsproblemer med PZT i ætsningen af bjælken i KOH er løst ved at benytte en mekanisk holder der beskytter siliciumskivens forside.

Ved hjælp af en dybdegående karakterisering af den fabrikerede energi høster har det være muligt at validere et udtryk for den generede effekt. Effekten kan beskrives af et udtryk som definerer den maksimale tilgængelige effekt og en multiplikationsfaktor som er under eller lig med 1. Den tilgængelige effekt er proportional med kvadratet af kraften der påvirker bjælken og omvendt proportional med den viskøse dæmpnings koefficient. De senest fabrikerede høstere generer i gennemsnit en effekt på 34.5 µW over en tilsluttet modstand på 50 kΩ ved en acceleration på $0.5g$ og en resonans frekvens på 511 Hz. Den højeste registreret effekt fra en høster under samme omstændigheder er 44.9 µW ved en resonans frekvens på 543 Hz. Sammenlignet med andre publicerede høstere i samme kategori, præsterer høsteren udviklet i dette projekt en normaliseret effektdensitet der er 3.5 gange højere end den næstbedste.

Preface

This thesis is submitted as a partial fulfilment of the requirements to obtain the Ph.D. degree at the Technical University of Denmark (DTU). The work has been carried out at the Department of Micro- and Nanotechnology (DTU Nanotech) at DTU from the 1st of December 2009 to the 30th of November 2012. The work has been supervised by Professor Erik Vilain Thomsen.

This Ph.D. project is part of the ELiminating BAtteries (ELBA) project and is funded by the The Danish National Advanced Technology Foundation (Danish: Højteknologifonden). The ELBA project is a three year collaboration between DTU Nanotech and the two companies Meggitt Sensing Systems A/S and Vestas Wind Systems A/S.

The overall vision of the ELBA project is to eliminate batteries by introducing energy harvesters enabling a new generation of distributed autonomous wireless sensing and control systems. The objective of this Ph.D. project is to develop and fabricate the integrated and miniaturized energy harvester needed to fulfil this vision of ELBA.

Acknowledgements

I would like to thank my supervisor professor Erik Vilain Thomsen for his supervision during the project. His natural enthusiasm and optimism is of tremendous value, and is passed on to everyone around him.

I would also like to thank Karsten Hansen, Louise Borregaard, Michele Guizzetti, Lise Nielsen, Konstantin Astafiev, Erling Ringgaard and Tomasz Zawada at Meggitt Sensing Systems for the outstanding collaboration and naturally for the screen printing of PZT on countless number of wafers.

A great thank should be given to the enthusiastic students who worked on the numerous student projects during the ELBA project: master student Christoffer Mølleskov Pedersen, and bachelor students Christian Dahl-Petersen, Adnan Silajdzic, Ivan Fuglø, Mikkel Wennemoes Hvitfeld Ley, Anders Thyssen, Adam Carsten Stoot and Thomas Lehrmann Christiansen whom all have contributed to the progress and work presented in this thesis.

I would also like to thank the employees at DTU Danchip for assisting in the cleanroom, the colleagues and co-workers at the DTU Nanotech and, last but not least, the other members of the MEMS-AppliedSensors group.

Finally I would like to thank two of my closest colleagues Ruichao Xu and Karen Birkelund, who both have worked on the ELBA project at DTU Nanotech.

Anders Lei
November 30th 2012, Copenhagen

Contents

Chapter 1

Introduction

The concept of energy harvesting can be slightly ambiguous. One can argue that energy harvesting covers the concept of converting any type of energy into another more desirable or usable energy, this being e.g. generation of electricity from fossil or nuclear fuel. Another more cleantech approach to the concept is that energy harvesting is the extraction of usable energy from freely available and renewable sources of energy such as wind, solar and hydropower. On a large scale the advantages of renewable sources are nowadays known to everyone, however energy harvesting is also becoming increasingly interesting on a small scale. The underlying idea of small-scale energy harvesting is to obtain an energy source that in principle is inexhaustible within a given lifespan.

1.1 Motivation for Energy Harvesting

It is clear that any small-scale device that can harvest electrical energy from renewable sources, compared to e.g. a battery with a limited lifetime, is highly interesting for several applications. One of the interesting areas is in sensor and monitoring applications in form of wireless sensor systems where batteries are used today.

1.1.1 Wireless Sensor System

The idea of the wireless sensor system is, as the name indicates, to monitor a parameter or operation using a sensor system that is free of wires. The development of such wireless sensor systems is driven by an increased need for monitoring and information of processes etc. Whenever you have important processes or operations running you want vital process information to ensure that all processes are running as efficient as possible, but also to get warnings and predictions if e.g. mechanical parts are starting to fail.

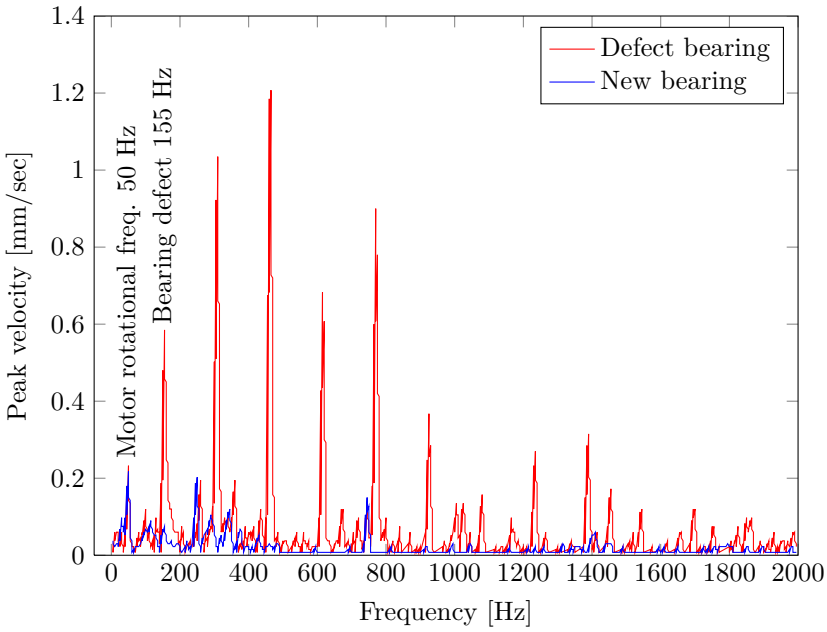

Figure 1.1: *Vibration spectrum for a defect and new outer race bearing on an electric motor. The peaks in the defect bearing vibration spectrum are the multiple harmonics of the bearing defect at* 155 Hz*. With appropriate vibration monitoring, initiatives such as maintenance can be conducted prior to a critical full failure situation. Vibration data extracted from vibanalysis.co.uk* [1].

1.1.2 Broken Bearing Example

An example of how monitoring can prevent serious and expensive mechanical breakdown is the vibration analysis of an electric motor. Figure 1.1 shows the vibration spectrum for a defect and new outer race bearing. Both spectra have a vibration peak at 50 Hz which is the motor rotational frequency. The first major difference in the spectrum is seen at 155 Hz which fits with the calculated frequency of bearing defect using motor speed, number of balls, ball diameter and pitch diameter. The following vibration peaks of the defect bearing spectrum are multiple harmonics of the bearing defect.

It is clear that with vibration spectra like in Figure 1.1, it is possible to effectively schedule and organise maintenance and thereby controllably replace the bearing before a critical full mechanical breakdown occurs. Such information will become even more important since competition and development means that the profitability of processes and general machinery lies in having as few interruptions as possible, whether they are scheduled or not. This is for instance the case within the wind turbine industry where the cost in lost electricity generation of closing down a turbine is high and can diminish the profit. Furthermore an unpredicted maintenance is especially costly on offshore turbines where access is difficult and time consuming to schedule. Mechanical failure can never be totally avoided, but if the failure can be predicted in advance, the cost of repair can be significantly decreased.

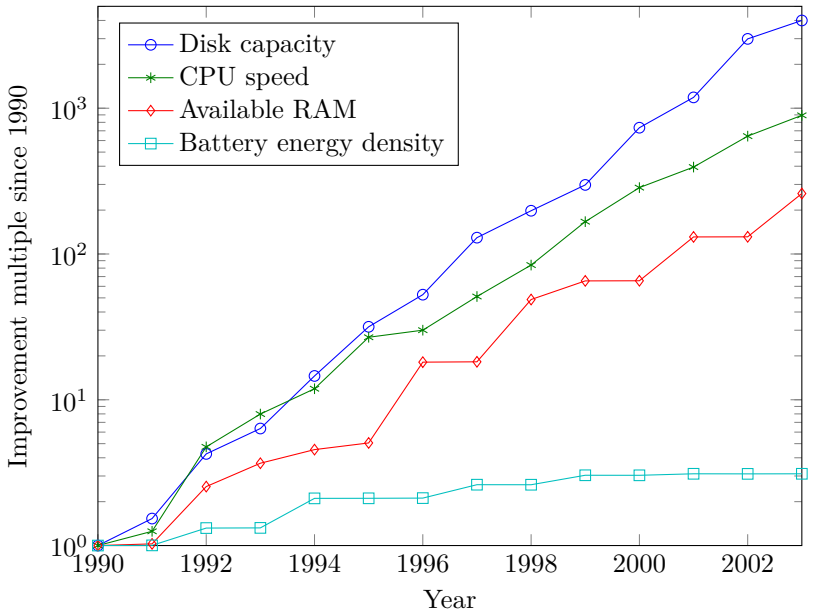

Figure 1.2: *Development in computer and battery technology since 1990. While disk capacity, CPU speed and RAM modules have experiences exponential growth in improvement, the development in batteries has stagnated since the introduction of lithium-ion batteries in the nineties. Data extracted from* [2].

1.1.3 Technological Advances

In principle the need for monitoring is not new, but as for many other technological areas, the development is driven by an increased demand in combination with one or more technological advances. A wireless sensor system roughly contains three components; an energy source, electronics including wireless link and finally the actual sensor. The technological development for each of these components is represented in Figure 1.2. Although electronics and sensor units are not plotted, it is safe to say that they follow somewhat the same trend as for available RAM, CPU speed and disk capacity. Performance-wise this means that price, power-consumption and size of electronic components have decreased substantially over the last two decades. At the same time, sensor units such as gyroscopes and accelerometers have increased in performance while decreased in size, cost and energy requirement resulting in implementation into a broad range of everyday consumer electronics. The combination of these technological advances has opened up for the realization of wireless sensor systems, but a compact lightweight energy source is still required. The choice of energy source has so far been batteries, and although their energy density improved in the nineties due to the lithium-ion technology (Figure 1.2), recent development has been marginal. Furthermore batteries suffer from a significant self-discharge over time, and the self-discharge rate increases at high temperatures, which frequently will be present in machinery, gears e.g. Overall, batteries will often constrain the total size and/or especially lifetime of the wireless sensor.

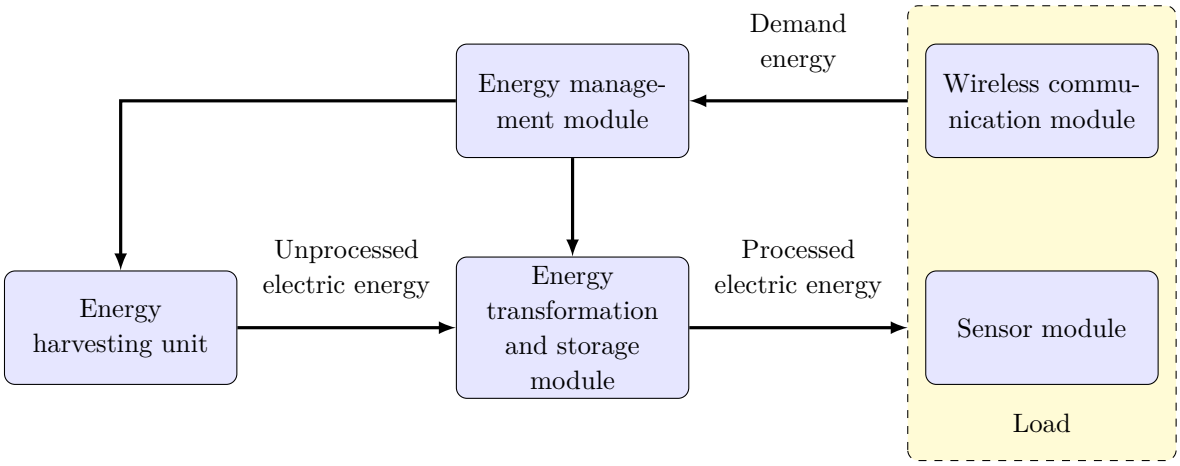

Figure 1.3: *Layout of the autonomous wireless sensor system which is the objective in the ELiminating BAtteries (ELBA) project. The harvested electrical energy is processed and accumulated in a storage module. The module powers the sensor module and wireless link. A management module controls the entire cycle with active/dwell time.*

1.2 Eliminating Batteries (ELBA)

The advantages of replacing the battery in a wireless sensor with an energy harvesting mechanism are obvious. Not only can periodically replacement of batteries by avoided, new monitoring solutions can be developed. Several interesting monitoring locations can only be accessed in the initial assembly phase, hence a fully autonomous sensor systems without need of service is required. This is the basis for the research effort named ELiminating BAtteries (ELBA), of which this work is part of. The vision of the ELBA project is to develop a wireless sensor system which encompass the components illustrated in Figure 1.3. As for any other wireless sensor, the system features a sensor module and a wireless communication link. In combination, these two parts are named *load*. Conventionally the load will be powered by a battery with a minimal amount of energy management electronics. In the case of implementing an energy harvesting unit, a module is required to process and store the harvested electrical energy. Finally, to control the system an energy management module is needed since active/dwell time of the load must be controlled according to available energy.

1.2.1 Energy Budget

For any wireless sensor system, independent of whether it is power by a battery or an energy harvester, it is an absolute necessity to reduce the energy budget to a minimum. The energy budget is mainly determined by the energy consumed by the load for one measurement including data transmission, the energy consumption in sleep mode and naturally the rate of measurements. The operation cycle of the sensor system developed in the ELBA project is

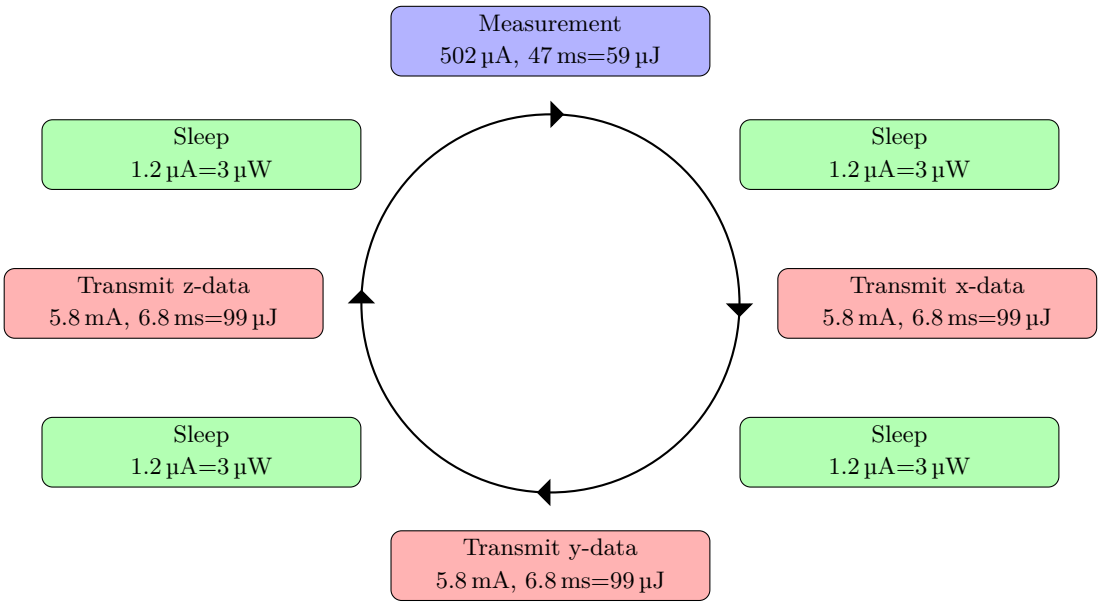

Figure 1.4: *Cycle of operation with corresponding energy budget for the wireless sensor system in the ELBA project. The cycle starts with a vibration measurement after which the system alternates between a sleep period followed by the wireless transmission of data for one axis at a time. The duration of the sleep periods are determined by the rate of accumulated energy from the harvester unit. The power and energy consumption is calculated from a voltage supply of* 2.5 V *for the system.*

sketched in Figure 1.4. The cycle starts with a three directional vibration measurement. The measured data are stored and the system is put to sleep. When sufficient energy is accumulated from the energy harvester in the storage module, the vibration data for one direction is transmitted. This sleep and transmit sequence is repeated for the remaining two directions and the cycle is ended with a final sleep period to accumulate energy for the next measurement. The current and time required for the measurement and transmissions are listed together with the resulting energy budget with a supply voltage of 2.5 V. A single cycle of measurement and transmission requires 356 µJ, and if a rate of one measurement per minute is required, the resulting average power consumption is $\approx$ 9 µW. These 9 µW is in usable DC power, the power generated by the harvester must by considerable higher to account for loss in rectifier circuit and the efficiency in capacitor charging. A rough estimate is that the harvester should provide a power three to four times the average DC power required to supply the systems operation cycle. Despite being in sleep mode, the system still consumes 3 µW equal to one third of the energy consumption at this measurement rate. Decreasing the sleep mode energy consumptions is therefore essential in the future sensor system development.

1.2.2 Sources of Ambient Energy

An energy harvesting unit is reliant on an ambient source of energy, which can be for example vibration/motion energy, thermal energy, light or RF radiation [3]. The choice of source will

affect numerous aspects of the device, but ultimately availability is the deciding factor. The focus in this work is to power a wireless sensor unit for vibration analysis inside machinery. This eliminates the use of light radiation, since the devices will be enclosed inside the machinery. This enclosure also complicates the use of RF radiation, same as for thermal gradients. As the purpose of the sensor is to measure vibrations when the machinery is active, these same vibrations can also be used as ambient source of energy. Whenever the machinery is running and monitoring is requested, the source will naturally be active as well.

1.2.3 Vibration Energy Harvesting

To harvest energy form vibrations or motion, a transducer mechanism that can convert energy from the mechanical domain into the electrical domain is required. The by far most common transducer mechanisms for this are electrostatic, electromagnetic or piezoelectric [4,5]. Which mechanism to utilise in an energy harvester, depends on several parameters but in this work, miniaturization and high energy density are essential requirements.

1.2.3.1 Electromagnetic Energy Harvesting

In electromagnetic energy harvesting, mechanical energy is converted into electrical energy by means of permanent magnets and coils moving relative to each other. The amount of electrical energy that can be generated is related to the strength of the magnet, the velocity of its motion and finally the number of coil windings. An example of a small-scale electromagnetic vibration harvester has been presented in [6]. The harvester, which is fully based on discrete components, consists of a cantilever with a coil attached at the end and magnets located on the sides. Though the performance is acceptable it serves mainly as a proof of concept. To realise a miniaturised electromagnetic harvester with integrated components, the major challenge of fabricating small-scale coils with high winding numbers and low resistance must be solved. Silicon processing of microelectromechanical systems (MEMS) devices is for instance planer, thereby the amount of windings that can be achieved are limited. This might be solved by a complicated stacking sequence, but nevertheless the deposition of wires will be equally difficult and costly. Finally the magnetic field created by the magnet might interfere with the sensor unit or electronics.

1.2.3.2 Electrostatic Energy Harvesting

An electrostatic energy harvester utilises the relative motion of the plates in a capacitor. The result is thus a varying capacitance which is caused by the change in plate separation or overlapping plate area. Planer silicon processing is well suited for fabricating a small-scale electrostatic energy harvester which requires small and precise gaps between the electrodes [7, 8]. There is however the disadvantage that the plates either needs to be charged, which

requires energy, or one must implement an electret which is a charged dielectric material. Nevertheless the achieved energy density is low [9].

1.2.3.3 Piezoelectric Energy Harvesting

Piezo is derived from Greek and means to squeeze or press, thus a piezoelectric material is a material capable of generating a displacement field when being subjected to a mechanical stress, and this displacement field gives rise to an electrical potential. This effect where stress causes a electrical potential is called the direct piezoelectric effect, the reverse situation is called the inverse piezoelectric effect. Compared to the two other vibration harvesting transducer mechanisms, the piezoelectric have gained much attention due to a high coupling efficiency and simple design enabling a high degree of miniaturisation [10]. Most piezoelectric energy harvesters utilise the stress induced in a piezoelectric layer due to the bending of a structure. In most cases this structure is a cantilever[1] with a proof mass attached at the free end, which when subjected to an external force will cause a bending moment.

1.3 Challenges

The piezoelectric energy harvester offers a high degree of miniaturization. This is essential since the total dimension of the harvester unit must not exceed the dimensions a battery would take up to power the sensor system in its lifetime. There is however a couple of challenges for the miniaturization to be successful. The most critical is the concept of frequency matching, but also choice of piezoelectric material and especially the processing of it on a small scale are crucial. Finally, one must recognise the criterion for success in the endeavour to outperform the conventional button cell battery.

1.3.1 Frequency Matching

For the cantilever based resonator which comprises the piezoelectric harvester to operate efficiently, it is essential that the resonant frequency of the cantilever matches the vibrations of the source. Table 1.1 shows a list of some common ambient sources of vibration together with acceleration amplitude and peak frequencies. In general, applicable ambient sources of vibration energy only have useful frequencies in the range of a few hundred hertz. Accordingly the harvester must be aimed towards this frequency range. The resonant frequency of the cantilever can be expressed as

$$\omega_0 = \frac{1}{2}\sqrt{\frac{H^3WE}{L^3M}} \tag{1.1}$$

were it is assumed that the cantilever consist of a single material with thickness H, width W, length L and Young's modulus of E. The mass of the cantilever is neglected and it is

[1] Beam anchored in one end while free in the other

Table 1.1: *Acceleration amplitude and peak frequencies for a range of common vibrations sources in the surroundings. Data from* [11].

Vibration source	A [$\mathrm{m\,s^{-2}}$]	f_{peak} [Hz]
Car engine compartment	12	200
Base of 3-axis machine tool	12	70
Blender casing	6.4	121
Clothes dryer	3.5	121
Door frame just after door closes	3	125
Small microwave oven	2.5	121
HVAC vents in office building	0.2-1.5	60
Windows next to a busy road	0.7	100
CD on notebook computer	0.6	75
Second story floor of busy office	0.2	100

assumed that the proof mass M is acting as a point load at the cantilever tip. The width dependency is cancelled by the proof mass, leaving cantilever length and thickness as the vital geometric parameters. Assuming that the cantilever length is constraint to 5 mm, consist solely of silicon ($E = 169\,\mathrm{GPa}$), and a realistic integrable proof mass of 30 mg per width, the cantilever thickness must be merely 4.1 µm to obtain a resonant frequency of 200 Hz. This clearly illustrates the conflict between miniaturisation while at the same time matching the resonant frequency with applicable sources. The consequences are several constrains regarding design which results in a couple of major fabrication challenges. Manufacturing structures with lateral dimensions in the millimetre range is fairly straightforward, whereas controlling the thickness in micrometre range at the same time is challenging. One fabrication technology that can operate in both these ranges is silicon and MEMS processing tools.

1.3.2 Piezoelectric Materials and Processing

There exist a variety of piezoelectric materials, some are naturally occurring crystals while others are synthetic, all with different piezoelectric properties and processing possibilities. As described previously, the harvester will be comprised by a structure with a piezoelectric layer on top. The piezoelectric material of choice must therefore be processable into this configuration. Furthermore, both the piezoelectric material and the processing technique must be compatible with silicon/MEMS cleanroom fabrication. One material that meet both requirements is lead zirconate titanate ($\mathrm{Pb[Zr}_x\mathrm{Ti}_{1-x}\mathrm{]O_3}$ $0 \leq x \leq 1$) also commonly known as PZT.

Figure 1.5 shows a roadmap of the different ranges PZT can be processed into, and the technique required to do so. In general bulk PZT provides the best piezoelectric properties, but merging bulk PZT with small-scale cantilevers and silicon processes involves positioning, gluing, and cycles of thinning and or etching [12, 13]. Overall, bulk processing is tedious and

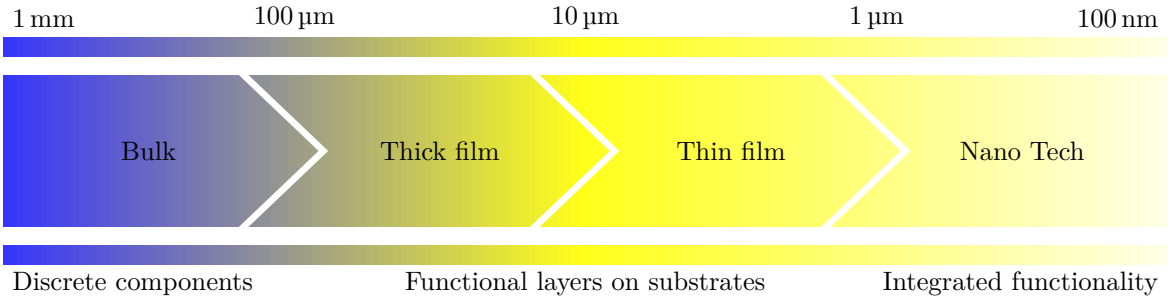

Figure 1.5: *Ranges and functionality of different processing techniques for PZT. In this work the thick film in the micrometre range is of interest. It provides better performance for energy harvesting than thin film and better integration possibilities over bulk processing.*

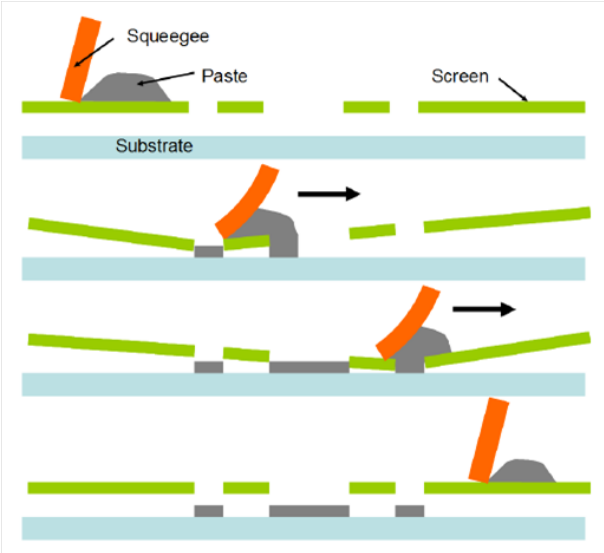

Figure 1.6: *Sketch of the screen printing process.*

not well suited for a high volume production. In the other end of the scale, nano technology and thin film provides excellent MEMS compatibility with deposition using sol-gel [14,15] and sputtering [16], and the piezoelectric properties are descent. The disadvantage, is the limited thickness. For sensing applications micro-range PZT film can be usable, but for energy harvesting thicker layers are a necessity. The most interesting region to operate within is therefore the PZT thick film range from around 10 µm and up to 100 µm. A fabrication technique that comply with this range is screen printing which is sketched in Figure 1.6. In screen printing the PZT which is in a powder state, is mixed with solvents to create a paste that is deposited through a screen using a squeegee. The technique is widely used from art to high volume electronic production, hence it is a well known accepted process. To obtain a certain film thickness the printing process is repeated with intermediate heating steps. Once the desired thickness is achieved the substrate and film is heated such that solvents used to create the paste are baked out. The PZT powder thus sinters and condenses to a

ceramic film. The concept of screen printing itself is MEMS compatible as lateral structures in the 100 µm range are possible to define with decent alignment. When screen printing PZT on silicon substrates issues though arises. Increased diffusivity in the high temperature sintering process causes the lead in the PZT and silicon to mix. As a result the piezoelectric properties of the PZT are drastically reduced and the silicon substrate is affected by a high lead contamination. The issue is solved be the company Meggitt Sensing System A/S [17] that have developed a paste which can be sintered at 850 °C reducing the diffusivity to a point where it is compatible with silicon substrates.

Although PZT by far is the most common piezoelectric material in use, not only for energy harvesting, the presence of lead is in some situations problematic. A lead-free replacement that offers nearly identical processing opportunities is sodium potassium niobate $K_xNa_{1-x}NbO_3$ (KNN). KNN is inferior to PZT in piezoelectric performance at the moment, but intense development is conducted especially since the usage of lead in the future will be increasingly restricted. Another lead-free material that in fact offers a piezoelectric performance figure of merit comparable to PZT is aluminium nitride (AlN) [18]. Aluminium nitride deposited with sputtering is highly MEMS compatible, but with low deposition rate and wafer throughput the process is not well suited for high volume production.

1.3.3 Battery Benchmark

Presently the button cell battery is the conventional choice for power supply in wireless sensors. Seeing aside from the self-discharge discussed in Section 1.1.3, which naturally poses an issue in long-term operation, an energy harvesting unit must be able to supply more energy than a conventional battery can store during the predicted lifetime of the sensor unit. Figure 1.7 shows a survey of some standard button cell batteries with different dimensions and price[2]. In Figure 1.7a the stored energy is plotted together with the diameter of the cell battery for eight different batteries. The objective in this work is to fabricate a harvester unit with a lateral dimension of 1.5 cm × 1.5 cm including packaging. The batteries with diameters below the dashed line are hence of main interest. Figure 1.7b shows the energy density and energy per euro for each of the batteries. From the survey especially the 3 V BR1225 lithium polymer battery is of interest. It is the battery with highest stored energy below the dimension limit and it performs well in energy per euro. Disregarding the self-discharge while assuming that one can use the total stored energy, the battery will be able to supply 16.5 µW of DC power in a year, more than enough to power a monitoring cycle of one measurement per minute. In practice the battery voltage will slowly decrease, and at a certain level the voltage will be insufficient for powering the unit. The optimistic number therefore only serves as a guideline for the criterion of success for the harvester.

[2]Information from RS Components

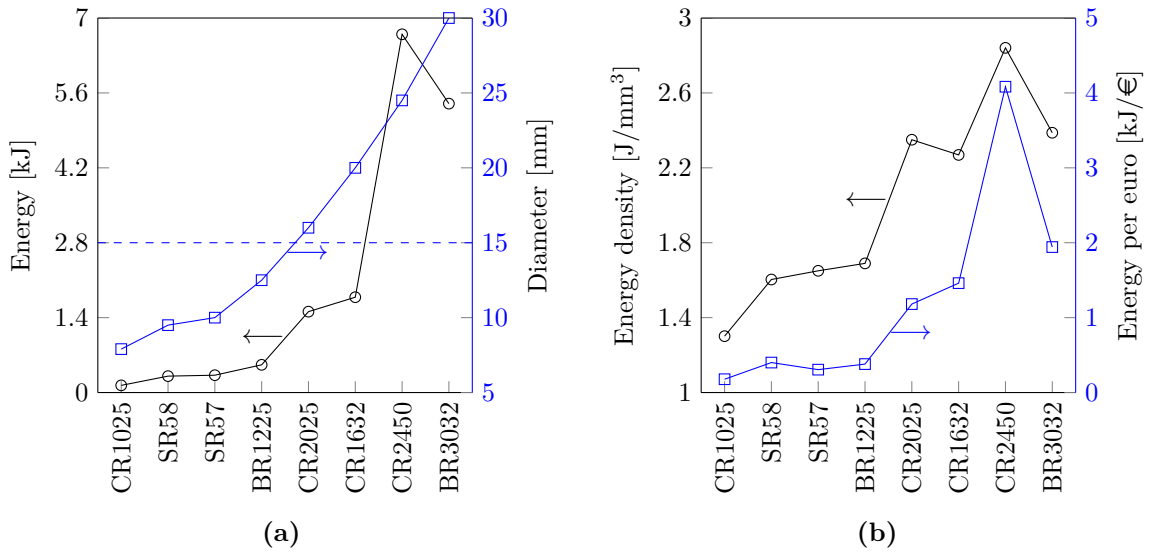

Figure 1.7: *(a) Stored energy and diameter for a range of different button cells batteries. The dashed line indicates the diameter aim for the harvester unit in this project. (b) Energy density and stored energy per euro for each of the batteries.*

1.4 Review of MEMS piezoelectric vibration harvesters

Numerous piezoelectric vibration harvesters have been presented in literature in the last decade, summarised in the reviews [19, 20]. The vast majority of these harvesters are proof of concept discrete devices in centimetre range with the sole purpose of validating theoretical models and predictions. Only a few harvesters with dimensions realistic for implementation in a wireless sensor node have been reported with review in [21]. These are all MEMS-based and fabricated using cleanroom technology, but only a few have frequencies in the interesting areas presented in Section 1.3.1. In the following three harvesters that fulfil these requirements will be presented. Two based on PZT; one fabricated with sol-gel and one with bulk processing, and then a device with sputtered AlN will be presented. Finally the harvester developed and fabricated in the ELBA project will be outlined for comparison.

1.4.1 Harvester with Sol-Gel Deposited PZT

In 2009 Shen *et al.* [15] from Auburn University reported a PZT vibration energy harvester fabricated with silicon on insulator (SOI) technology and sol-gel deposited PZT (Figure 1.8). The device, sketched in Figure 1.8a, features an integrated proof mass at the cantilever end, and the SOI wafer is used to accurately control the thickness of the silicon support beam. The piezoelectric layer is deposited with sol-gel to a thickness of 1 µm. The fabricated harvester is depicted in Figure 1.8b and is comprised of a cantilever with a total vibrating dimension of 4.8 mm in length, 1 mm in width and 0.5 mm in thickness. At an excitation acceleration of $0.75g$ ($g = 9.81\,\mathrm{m\,s^{-2}}$) the harvester generates 0.42 µW over a load of 16 kΩ with a resonant

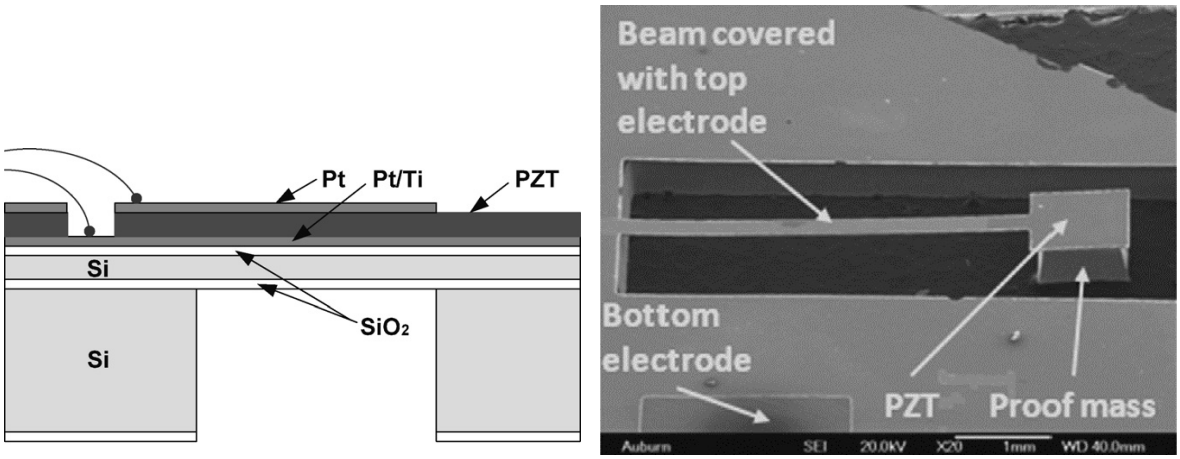

(a) (b)

Figure 1.8: *Sol-gel PZT vibration energy harvester based on a SOI wafer, Shen et al. (a) Schematic side view. (b) Scanning electron micrograph of the fabricated harvester. Both figures from* [15].

frequency of 183.8 Hz.

1.4.2 Harvester with Processed Bulk PZT

In 2011 Aktakka *et al.* [12] from the Najafi group at University of Michigan published a bulk PZT based harvester. A side view of the fabrication process is sketched in Figure 1.9a. Bulk PZT-5A is bonded to the bottom of a cavity in the device layer of a SOI wafer using a gold indium (AuIn) transient liquid phase bonding. The bulk PZT is then mechanically thinned down to the silicon surface which acts as a stop layer. Electrodes are deposited followed by a backside etch into the silicon to define the cantilever. The device is finally packaged using a silicon wafer for back cover and glass/silicon wafer as front cover (Figure 1.9b). The cantilever beam is comprised of 20 µm Si, 5 µm bond layer and 20 µm of PZT and has a total vibrating volume of 7 mm × 7 mm × 0.55 mm. At an excitation acceleration of $1.5g$ the packaged harvester generates 160.8 µW with a resonant frequency of 415 Hz.

1.4.3 Harvester with Aluminium Nitride

In 2009 Elfrink *et al.* [18] from IMEC/Holst Centre published an aluminium nitride based vibration harvester. An illustrative side-view of the harvester is sketched in Figure 1.10a. For the fabrication an ordinary silicon wafer is used and a AlN layer of 400 nm is sputtered on a platinum electrode. The cantilever is fabricated by a cavity etch from the back side in KOH, and is released with a dry etch or TMAH. The thickness of the silicon cantilever after KOH etching is 45 µm and the total cantilever length is 6.1 mm with a width of 5 mm. Packaging is performed in glass wafers with etched cavities (Figure 1.10b). Aluminium nitride has a

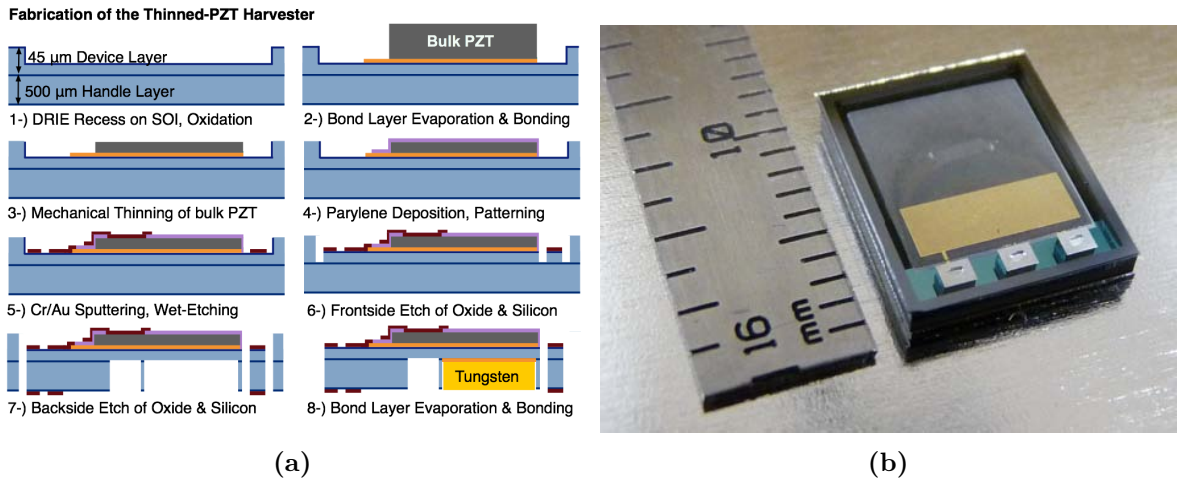

Figure 1.9: *Bulk PZT vibration energy harvester based on a SOI wafer from Aktakka et al. (a) Schematic side view of the fabrication process. (b) Photograph of the fabricated harvester in silicon/glass packaging. Both figures from* [12].

piezoelectric constant of $d_{31} = -1.1\,\mathrm{C\,m^{-2}}$ which is around ten times smaller than PZT. This is though counterbalanced by a considerable lower dielectric constant of only $\epsilon_r = 10.5$ which is two orders of magnitude smaller than PZT. The AlN thin film harvester thus generate 60 µW with $2g$ excitation acceleration at a resonant frequency of 572 Hz.

1.4.4 ELBA Harvester with PZT Thick Film

The harvester developed and fabricated in the ELBA project have many similarities with the work of Elfrink *et al.* regarding the silicon processing part. A side view sketch of the harvester is depicted in Figure 1.11a and is based on a conventional silicon wafer where the PZT thick film is screen printed on top. After the screen printing process the cantilever and proof mass are defined by a cavity etch in KOH where a wafer holder is used for mechanical front side protection of the PZT against the etch. Finally the harvester is released in a RIE process where the remaining silicon in the trench between cantilever and frame is etched. Together with a dicing process optimised for the fragile structures a yield exceed 90% is obtained from the fabrication process. The fabrication process is aimed towards high volume production with as many steps as possible being batch processes. A final fabricated unimorph harvester is seen in Figure 1.11b and consist of a 6 mm wide and 6.5 mm long cantilever with a proof mass taking up half the length. The silicon support layer is 36 µm thick with a 25 µm thick PZT layer on top. The resonant frequency is 543 Hz and a RMS power output of 44.9 µW is obtained over a resistive load of 50 kΩ at an input RMS acceleration of $0.5g$.

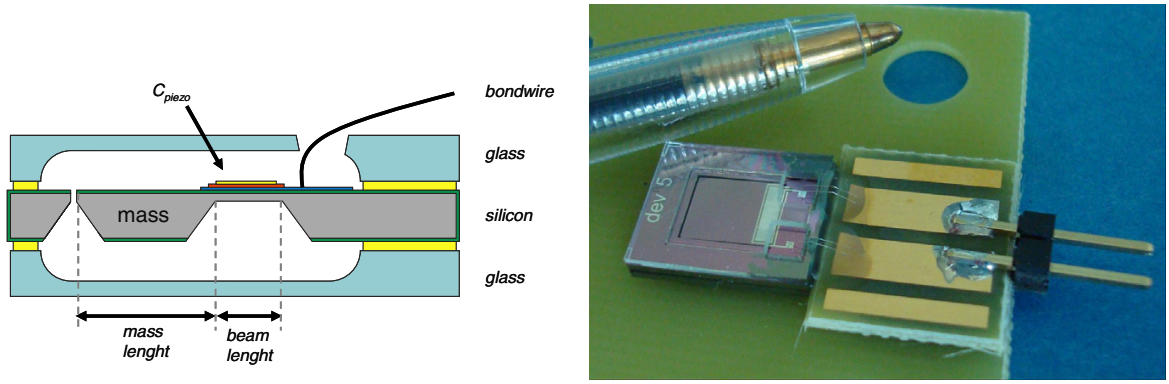

(a) (b)

Figure 1.10: *Aluminium nitride vibration energy harvester from Elfrink et al. (a) Schematic side view of the packaged harvester. (b) Photograph of the fabricated harvester in glass packaging mounted on a printed circuit board. Both figures from* [18].

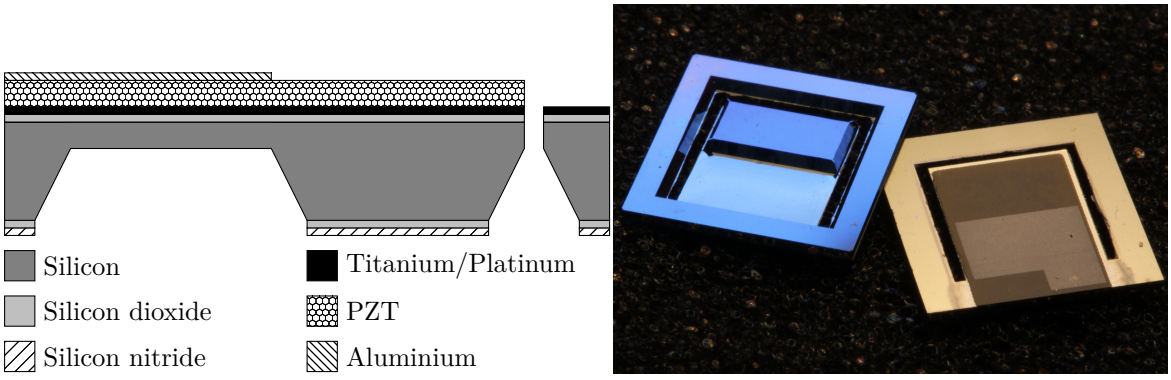

(a) (b)

Figure 1.11: *Thick film PZT vibration energy harvester developed in the ELBA project. (a) Schematic side view of the harvester. (b) Photograph of front and back side of the fabricated harvester.*

Table 1.2: *Comparison of harvesting performance of the devices reviewed in Section 1.4. The sol-gel device has the lowest performance due to the limited thickness of the active piezoelectric layer. The AlN harvester is performing better than the sol-gel device but is surpassed by both the ELBA and bulk PZT harvester. The highest normalised power density is obtained for the ELBA harvester, by nearly a factor of 3.5 over the bulk PZT harvester. The FOM including bandwidth is highest for the bulk PZT harvester as the bandwidth is 5 times wider than the ELBA harvester.*

Reference	Type	Acc. [g]	F_{res} [Hz]	P [µW]	F_{BW} [Hz]	P norm. [mW/cm^3/g^2]	FOM [Hz·mW/cm^3/g^2]
Shen [15]	Sol-gel PZT	0.75	183	0.42	0.8	0.31	0.25
Aktakka [12]	Bulk PZT	1.5	415	160.8	33.3	2.65	88.2
Elfink [18]	AlN	2	572	60	2	1.00	2.0
ELBA	Thick film PZT	0.5	543	44.9	6.8	9.21	63.0

1.4.5 Harvester Comparison

A direct comparison between small-scale vibration harvesters is difficult due to the use of different piezoelectric materials and deposition techniques in combination with a diverse device dimensions, power outputs and resonant frequency. The most common approach is to normalise the power output (P) with respect to input acceleration squared and unpacked active device volume (beam width × total beam length × die thickness). A slight alternation to the normalised power density is presented in [12] where it is suggested to multiply the normalised power density with the power spectrum bandwidth (F_{BW}). This should allow for a fair comparison between devices with different resonant frequencies (F_{res}) since the vibration energy is inversely proportional to the vibration frequency for a constant input acceleration. The resulting comparison of both normalised power density an FOM between the three reviewed harvesters and the ELBA harvester developed in this work is listed in Table 1.2.

The sol-gel based harvester is performing low in comparison simply due to the limited PZT thickness and consequently high capacitance. The advantage is a cleanroom compatible fabrication process well suited for high volume fabrication with a low cost. The AlN based harvester performs better than the sol-gel harvester, but both the normalised power density and FOM is lower compared to the ELBA and bulk PZT based harvester. The advantage of AlN is that it is lead-free and highly cleanroom compatible. The disadvantage is the sputtering deposition which is time-consuming and requires good process control in order to achieve a crack-free film at a descent thickness. This limits the possibility of fabricating AlN based harvesters in a higher volume. The normalised power density for the ELBA harvester developed in this work is 3.5 times higher than the bulk PZT based harvester. When comparing the FOM where the bandwidth is included, the bulk PZT harvester is performing 40% better than the ELBA harvester due to a 5 times wider bandwidth. Implementing bulk PZT with MEMS fabrication processing is however tedious as it involves positioning, gluing and cycles of thinning and or etching. Accordingly bulk PZT is of limited interest from a fabrication point of view. There are advantages and disadvantages for all the four harvester and al-

though a wide bandwidth in many application perspectives is desirable, the combination of high power density and relatively low fabrication cost, the ELBA harvester has the highest commercialisation potential.

1.5 Overview of the Thesis

The thesis is divided into the following chapters

- **Chapter 2 - Piezoelectric Harvesting Theory:** With a single degree of freedom system and a lumped element model, the performance of the harvester is analytically modelled. With a derived expression for the output power, the optimal harvester design is analysed.
- **Chapter 3 - Process Development:** The extensive process development leading to the fabrication process for the vibration harvester is presented. The chapter outlines the important improvements in this iterative progress.
- **Chapter 4 - Harvester Design and Fabrication:** The final harvester design and fabrication process is reviewed in details. The chapter ends with a few unsolved issues and recommendations for future work.
- **Chapter 5 - Harvester Characterisation:** With a thorough characterisation of a single device, the performance of the ELBA harvester is reviewed in details. From the measurements the derived analytic expression for the power is validated.
- **Chapter 6 - Uniformity Characterisation:** The harvester uniformity on a wafer level and between wafers are presented. A total of 165 harvesters from 4 different wafers are characterised in the uniformity analysis.
- **Chapter 7 - Bistable Energy Harvester:** Preliminary experimental results on a bistable energy harvesting system is presented. With a bistable system high power can be generated at low frequencies far from the harvesters resonant frequency.
- **Chapter 8 - Conclusion and Outlook:** This chapter summarises the most important results obtained in the thesis and conclusions are presented. An outlook is given with suggestions for future work in the aim of fulfilling the vision of the ELBA project.

Chapter 2

Piezoelectric Harvesting Theory

With the increasing interest within the field of vibration energy harvesting, the modelling and analysis of these devices have attracted many researchers with numerous publications as a result, and with following reviews in [20, 22]. The piezoelectric harvester is a distributed system and full distributed parameter models have be derived [23–25] which agrees excellent with experimental data. These models are quite complex and though closed-form expressions can be deducted they are not well suited for geometric optimization. The advantage of the distributed model is that it can capture the operation at higher modes, but for this work the harvester will only operate at the fundamental resonant frequency. With this condition it is possible to use a simple single degree-of-freedom (SDOF) model with lumped parameters considering the cantilever as a mass-spring-damper system. The SDOF approach is the most common in literature [26, 27] and has proven to give accurate predictions at the fundamental resonant frequency [2, 28] and reasonable predictions for higher resonant modes if adequate modes are included in the equivalent circuit [29]. Unfortunately none of the models referred to, can adequately predict the harvester in this work since the models only treat cantilevers with small proof masses correctly.

The model derived in this work will be based on a SDOF lumped parameters model derived from the piezoelectric constitutive equations together with the solution to the static Euler Bernoulli beam equation. The chapter will start by presenting the piezoelectric constitutive equations followed by a few initial considerations concerning uni- and bimorph harvesters. Then the boundary conditions for the model will be defined and an analysis of bending versus stretching is presented. The different parts of the model will be derived. This involves linking the generated charge and current to the cantilever deflection and defining the moment created in the cantilever from the induced voltage. The deflection of the cantilever is derived from the static beam equations, and the solution will be compared to numerical simulations. To accurately predict the resonant frequency for harvesters with long proof masses relative to total cantilever length, the Rayleigh-Ritz energy optimization method is used and verified by numerical simulations. Finally all the different components will be implemented in the equivalent circuit model that connects the electrical and mechanical domains. Conclusively

Table 2.1: *Tensor notation of piezoelectric material parameters.*

Material parameter	Notation	Unit
Permittivity	$\varepsilon_{ik} = \frac{\partial D_i}{\partial E_k}$	$[\mathrm{F\,m^{-1}}]$
Piezoelectric coefficient	$d_{ikl} = \frac{\partial D_i}{\partial T_{kl}} = \frac{\partial S_{ij}}{\partial E_k}$	$[\mathrm{m\,V^{-1}}]$
Elastic compliance	$s_{ijkl} = \frac{\partial S_{ij}}{\partial T_{kl}}$	$\mathrm{m^2\,N^{-1}}$

the final expression for the harvester performance will be elaborated. The chapter will end with design recommendations based on the derive expression.

2.1 Linear Piezoelectric Constitutive Equations

Piezoelectric materials exhibit per definition elastic, dielectric and coupled elastic-dielectric properties. In order to model the behaviour of the piezoelectric energy harvester it is thus necessary to have a set of constitutive equations for the relations between the electrical and mechanical properties. From the thermodynamics of deformation and energy density of elastic deformation the following linear constitutive equations can be derived in tensor index notation as

$$dD_i = \left(\frac{\partial D_i}{\partial E_k}\right)_T dE_k + \left(\frac{\partial D_i}{\partial T_{kl}}\right)_E dT_{kl} \tag{2.1a}$$

$$dS_{ij} = \left(\frac{\partial S_{ij}}{\partial E_k}\right)_T dE_k + \left(\frac{\partial S_{ij}}{\partial T_{kl}}\right)_E dT_{kl} \tag{2.1b}$$

where E is the electric field, D is the electric displacement field, T is the stress and S is the strain. The subscript T means that the derivative is at zero or constant stress, similar with subscript E which means derivative at zero or constant electric field. As will be used later Equation (2.1a) represents the direct piezoelectric effect, and Equation (2.1b) the indirect piezoelectric effect. The constitutive equations can also be written in closed form with Einstein summation as

$$D_i = \varepsilon_{ik}^T E_k + d_{ikl} T_{kl} \tag{2.2a}$$

$$S_{ij} = d_{ijk} E_k + s_{ijkl}^E T_{kl} \tag{2.2b}$$

the subscripts are now changed to superscript and the parameters in tensor notation listed in Table 2.1 are used. By introducing the matrix indices p and q as replacements for the tensor double indices (ij) and (kl) the dielectric, elastic and piezoelectric constants can be expressed in compressed matrix notation as ε_{ik}^T, s_{pq}^E and d_{iq}. For anisotropic materials (triclinic) without symmetry center, the matrices of the individual constants are fully filled, but since the PZT ceramic in the polarised state exhibits a hexagonal crystal symmetry, the permittivity can be written in matrix form as

$$\varepsilon_{ik}^T = \begin{pmatrix} \varepsilon_{11} & 0 & 0 \\ 0 & \varepsilon_{22} & 0 \\ 0 & 0 & \varepsilon_{33} \end{pmatrix} \tag{2.3}$$

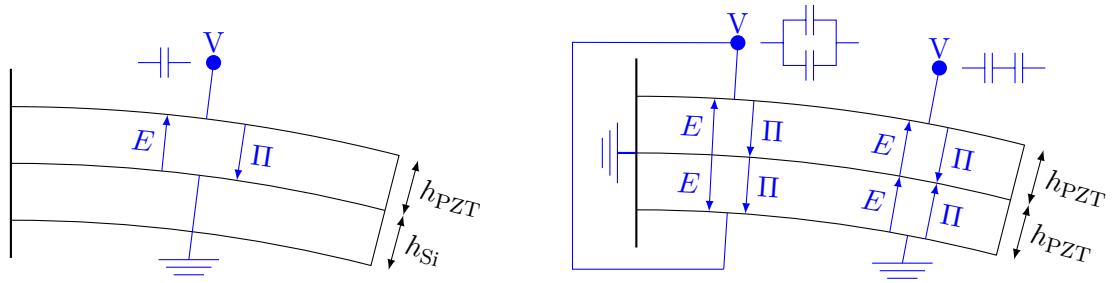

(a) *Unimorph configuration.* **(b)** *Bimorph configuration.*

Figure 2.1: *Sketch of the two configurations used in piezoelectric vibration energy harvesting. (a) The unimorph harvester consists of one active piezoelectric layer supported by an elastic support. (b) The bimorph harvester cantilever consists solely of two PZT layers. The piezoelectric layers in the bimorph harvester are operated in either series of parallel mode depending on the poling directions of the layers. Blue parts of the sketch indicate electrical notations.*

and similar for the elastic compliance

$$s_{pq}^{E} = \begin{pmatrix} s_{11} & s_{12} & s_{13} & 0 & 0 & 0 \\ s_{12} & s_{11} & s_{13} & 0 & 0 & 0 \\ s_{13} & s_{13} & s_{33} & 0 & 0 & 0 \\ 0 & 0 & 0 & s_{44} & 0 & 0 \\ 0 & 0 & 0 & 0 & s_{44} & 0 \\ 0 & 0 & 0 & 0 & 0 & 2\left(s_{11} - s_{12}\right) \end{pmatrix} \tag{2.4}$$

and finally for the piezoelectric coefficient

$$d_{iq} = \begin{pmatrix} 0 & 0 & 0 & 0 & d_{15} & 0 \\ 0 & 0 & 0 & d_{15} & 0 & 0 \\ d_{31} & d_{31} & d_{33} & 0 & 0 & 0 \end{pmatrix} \tag{2.5}$$

2.2 Uni- Bimorph Piezoelectric Harvester

Piezoelectric vibration harvesters are generally divided into two types depending on the cantilever configuration. The most common configuration, which also is used by all the harvesters presented in the Section 1.4 on page 11, is with one active piezoelectric layer placed on an elastic support. This configuration, known as the *unimorph* harvester, is sketched in Figure 2.1a. When the unimorph cantilever undergoes bending, an electric field arise in the opposite direction as the poling Π. The second configuration is the *bimorph* where the cantilever contains two (or more) active piezoelectric layers, either by them self (Figure 2.1b) or as a sandwich around an elastic support. The advantage of this configuration is that all the strain caused by a bending is used to generate electric fields. The bimorph harvester can be operated in a series and parallel mode depending on the directions of the poling. If the layers are poled opposite, the electric field in bottom and top layer will align due to tension and compression

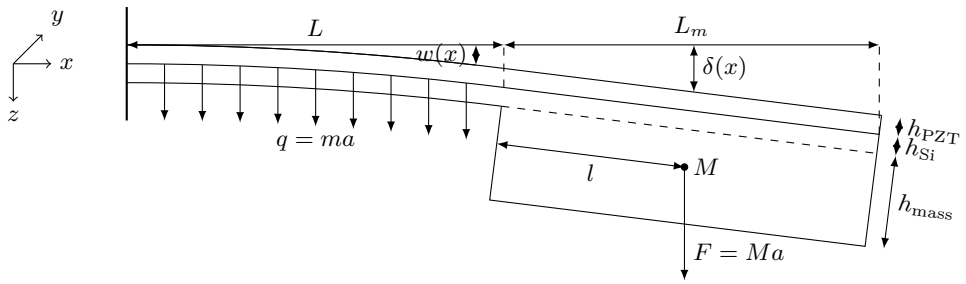

Figure 2.2: *Cross sectional sketch of the harvester which is modelled in the analysis. Notice that the z-direction is pointing downwards, with its origin at the neutral axis.*

on each side of the neutral axis. This is the series operation and only contacts on bottom and top electrodes are needed. If the layers are poled in same direction, the fields will be opposite and a contact to the middle electrode is needed and the layers will be contacted in parallel. The generated power is independent of the type of connection, but the current is two times higher for the parallel connection, while voltage is two times higher for the series connection. The choice could ultimately be dictated by the optimal load which is four times lower for the parallel case.

Both uni- and bimorph configurations have been fabricated and tested in the ELBA project. From a fabrication point of view the unimorph is simplest since the PZT will be supported by a substrate, in this case silicon which provides good stability and control. From an analytical point of view the unimorph is both simpler since only one active layer must be taken into account, but also more complicated since one must find the optimal material interface compared to the neutral stress axis and the combined mechanical stiffness from the two materials. The fabrication and characterisation in this work will mainly focus on the unimorph hence this configuration will be analysed in this theory section. Analysis of a bimorph harvester can be seen in [30].

2.3 Unimorph Harvester Model

The piezoelectric vibration harvester that will be analysed in this work is depicted with a cross sectional sketch in Figure 2.2. Notice that the z-direction is pointing downwards, with its origin at the neutral axis. The harvester consist of a unimorph cantilever with length L attached to a rigid frame in one end and a proof mass M with length L_m in the other. The thickness of the silicon support and piezoelectric layers are h_{Si} and h_{PZT} respectively, while the thickness of the proof mass is h_{mass}. The force due to an input acceleration a on the thin cantilever part of the beam is defined as a force per length $q = ma$ [$\mathrm{N\,m^{-1}}$] where $m = W(h_{\mathrm{Si}}\rho_{\mathrm{Si}} + h_{\mathrm{PZT}}\rho_{\mathrm{PZT}})$ [$\mathrm{kg\,m^{-1}}$] is the mass per unit length of the cantilever with ρ_{Si} and ρ_{PZT} being the respective material densities for silicon and PZT while W is

the width of the cantilever. It is assumed that the attack point of the force F on the proof mass is at the geometric centre of the proof mass which in longitudinal direction is located at a distance $l = L_m/2$ from the cantilever end point. The vertical displacement of the attack point relative to the neutral axis is ignored in the analysis. The force on the proof mass is therefore implemented in the analytic model as a bending moment of Fl and a shear force F acting on the cantilever end L in the static beam equation. The mass of the proof mass is found from $WL_m((h_{\mathrm{Si}} + h_{\mathrm{mass}})\rho_{\mathrm{Si}} + h_{\mathrm{PZT}}\rho_{\mathrm{PZT}})$. The deflection of the cantilever in longitudinal direction is denoted $w(x)$ and follows a curvature defined by the Euler Bernoulli beam equation. The proof mass is much thicker than the cantilever and therefore assumed to be completely rigid. As a consequence the deflection of the proof mass $\delta(x)$ follows a straight tangent line from the cantilever end point deflection. The electrodes on each side of the piezoelectric layers are for the model considered infinitely thin and therefore not contributing to the mechanical behaviour of the cantilever. With the cantilever rigidly fixed at the clamped end, the boundary conditions for the cantilever deflection w, deflection slope w'_x and elongation u at $x = 0$ becomes

$$w(x = 0) = 0 \tag{2.6a}$$
$$w'_x(x = 0) = 0 \tag{2.6b}$$
$$u(x = 0) = 0 \tag{2.6c}$$

2.3.1 Plane Stress

Even though the matrices for the individual materials constants in the constitutive equations are reduced due the symmetry of PZT, further assumptions are needed to simplify the analytic model. The aim of the ELBA project is to fabricate harvesters with low resonant frequencies, hence the length of the cantilever will be significantly larger than the thickness of the PZT and silicon layers combined. In situations where the cantilever length is significantly larger than the transverse dimensions, it is often assumed that no transverse stress will develop in the cantilever. This unidirectional assumption means that all other stresses than T_1 is zero. Since the objective in the ELBA project also is to generate power, the width of the cantilever must be as wide as possibly allowed by the overall device size constrain. As will be evident later, the cantilever will thus take a shape where the width is comparable with the length. For such a plate-shape cantilever it is more appropriate to assume that the cantilever edges are not free to move, meaning that the lateral strain S_2 is zero while the lateral stress T_2 becomes *non-zero*. The shear stresses are also neglected since they, as the constitutive equations indicate, are small and therefore do not contribute to the electric field. With the much smaller thickness compared to lateral dimensions, only the electric field in the piezoelectric layer normal to the electrodes $E_z = E_3$ is considered. Since there are no free space charges in the PZT film, the electric displacement is divergence free ($\nabla \cdot \mathbf{D} = 0$) and it can be assumed that $\partial_z D_z = 0$.

The piezoelectric constitutive equations in Equation (2.2) can accordingly be expressed as

$$D_3 = \varepsilon_{33}^T E_3 + d_{31}\left(T_1 + T_2\right) \tag{2.7a}$$
$$S_1 = d_{31}E_3 + s_{11}^E T_1 - s_{12}^E T_2 \tag{2.7b}$$
$$S_2 = 0 = d_{31}E_3 - s_{12}^E T_1 + s_{11}^E T_2 \tag{2.7c}$$

Using Equations (2.7b) to (2.7c) the S_1 strain can be rewritten to

$$S_1 = E_3\left(d_{31} + d_{31}\frac{s_{12}^E}{s_{11}^E}\right) + T_1\left(s_{11}^E - \frac{{s_{12}^E}^2}{s_{11}^E}\right) \tag{2.8a}$$
$$= E_3\left(d_{31} + d_{31}\nu\right) + T_1\left(s_{11}^E - s_{11}^E\nu^2\right) \tag{2.8b}$$

where the proportionality ratio ν between the compliance coefficients s_{12}^E and s_{11}^E also known as Possion's ratio is implemented. Performing similar operation on Equations (2.7a) to (2.7c) while using the following effective terms for the material parameters

$$s^E = s_{11}^E - s_{11}^E\nu^2 \tag{2.9a}$$
$$d = d_{31} + d_{31}\nu \tag{2.9b}$$
$$\varepsilon^T = \varepsilon_{33}^T - \frac{d_{31}^2}{s_{11}^E}\nu \tag{2.9c}$$
$$\tag{2.9d}$$

the constitutive equations can be written as

$$D_3 = \varepsilon^T E_3 + dT_1 \tag{2.10a}$$
$$S_1 = dE_3 + s^E T_1 \tag{2.10b}$$

In alternate forms, which will be useful later in the analysis, the constitutive equations can be expressed in the following way

$$T_1 = \frac{1}{s^E}S_1 - \frac{d}{s^E}E_3 \tag{2.11a}$$
$$D_3 = \frac{d}{s^E}S_1 + \varepsilon^T\left(1 - \frac{d^2}{s^E\varepsilon^T}\right)E_3 = \frac{d}{s^E}S_1 + \varepsilon^T\left(1 - k_{\text{eff}}^2\right)E_3 \tag{2.11b}$$

where

$$k_{\text{eff}} = \sqrt{\frac{d^2}{s^E\varepsilon^T}} \tag{2.12}$$

is the effective piezoelectric coupling coefficient. If the harvester was considered completely unidirectional the piezoelectric coupling coefficient would reduce to $k_{31} = \sqrt{d_{31}^2/\left(s_{11}^E\varepsilon_{33}^T\right)}$.

2.3.2 Bending vs. Stretching

The induced strain from which electrical energy are to be extracted, can be generated by both bending and stretching of the beam according to the expression

$$S_1 = u_x' - zw_{xx}'' \tag{2.13}$$

In the following it will be evident that the induced strain is primarily generated by bending, hence the effect of stretching can be neglected in the further analysis.

For simplicity it is for the bending vs. stretching comparison assumed that the cantilever is bimorph hence consisting only of PZT. The stress T induced by a force on a cross sectional area Wh is defined as

$$T = \frac{ma}{Wh} \tag{2.14}$$

and in terms of strain

$$S = \frac{ma}{Wh}s \tag{2.15}$$

where m is the system mass, a the input acceleration, W the width and h the height of the cross-section.

In bending, the maximum stress is at the cantilever surfaces at the anchoring point. Here the moment M is at it greatest namely $M_0 = FL$ where F is the force acting on the cantilever at a distance L which is the cantilever length. The following equation based on the static Euler Bernoulli beam theory

$$M_0 = FL = 2W \int_0^{h/2} zTdz \tag{2.16}$$

can therefore be used to find the mean stress by integrating the stress in one half part of the cantilever $h/2$ and multiplying by two since an equal but opposite signed stress will be induced in the other part of the unimorph cantilever. Solving the equation for the stress and converting to strain the following arises

$$\overline{S} = 4\frac{L}{h}\frac{ma}{Wh}s \tag{2.17}$$

Comparing the strain induced by bending in Equation (2.17) and stretching in Equation (2.15), bending yields a geometric stress amplification of $4L/h$. Consequently bending is the main contribution as long as the length of the cantilever is larger than the thickness. For the harvesters in this work the L/h ratio is around 150 thus bending produces 600 times more strain than stretching. Stretching is therefore neglected in the following analysis. The strain in Equation (2.13) can therefore be reduced to

$$S_1 = -zw''_{xx} \tag{2.18}$$

and the stress in Equation (2.11a) can accordingly be expressed as

$$T_{\mathrm{PZT}} = -\frac{zw''_{xx}}{s^E_{\mathrm{PZT}}} - \frac{d}{s^E_{\mathrm{PZT}}}E_3 \tag{2.19a}$$

$$T_{\mathrm{Si}} = -\frac{zw''_{xx}}{s_{\mathrm{Si}}} \tag{2.19b}$$

for the silicon (T_{Si}) and piezoelectric (T_{PZT}) parts of the cantilever respectively. The effective compliance $s^{(E)}$ for each of the materials are designated with subscripts.

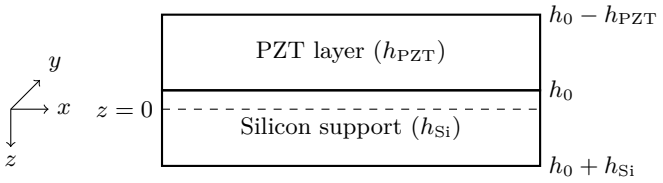

Figure 2.3: *Sketch of the neutral plane position in a unimorph cantilever consisting of a joined silicon support and a PZT layer with equal thickness. The distance from neutral axis at $z = 0$ where no strain is present to the material interface is denoted h_0, from which correct integration limits can be defined.*

2.3.3 Neutral Axis

In the expression for induced strain from bending in Equation (2.18) it is defined that no strain can arise at $z = 0$ which is known as the neutral axis. In situations where the interface between the materials in the cantilever line up at this exact position, the further analysis is uncomplicated since the integration limits over the cantilever layers are straightforward. This would for instance be the case for a unimorph cantilever consisting of two identical piezoelectric layers. For the unimorph configuration it is required to find position of the material intersection relative to the neutral axis. The problem is sketched in Figure 2.3, where a silicon support layer and a PZT layer with equal thickness are joined. Since the stiffness of silicon is higher than for PZT, the neutral axis of no strain will be position somewhere in the silicon support. The distance from this neutral axis to the interface is h_0, from which the correct integration limits over the different material layers in the cantilever can be defined.

The material interface, h_0, is found from analysing the longitudinal forces. Since pure bending is assumed, the sum of all normal forces in x-direction on the cantilever cross section is zero when subjecting the cantilever to an external bending moment

$$\sum F_{x,\perp} = 0 \tag{2.20}$$

which gives rise to the following relation

$$W \int_{h_0}^{h_{\mathrm{Si}}+h_0} T_{\mathrm{Si}} dz + W \int_{h_0-h_{\mathrm{PZT}}}^{h_0} T_{\mathrm{PZT}} dz = 0 \tag{2.21}$$

where the limits from Figure 2.3 is used to integrate over each of the materials. Integrating over the stresses in Equation (2.19) for each of the materials and seeing aside from the electric field in the PZT layer due to short-circuit condition, the following expression for h_0 is deduced

$$h_0 = \frac{-h_{\mathrm{Si}}^2 s_{\mathrm{PZT}}^E + h_{\mathrm{PZT}}^2 s_{\mathrm{Si}}}{2\left(h_{\mathrm{Si}} s_{\mathrm{PZT}}^E + h_{\mathrm{PZT}} s_{\mathrm{Si}}\right)} \tag{2.22}$$

2.4 Current vs. Deflection Slope Rate

The first step of the model derivation is to find the induced charge and hence current from a certain cantilever deflection. The charge Q on the electrodes caused by this deflection can be found using Gauss' Law hence integrating the displacement field in Equation (2.11b) over the volume of the active PZT layer and dividing with the thickness of the PZT layer

$$Q = \frac{1}{h_{\mathrm{PZT}}} \int_{\mathrm{V}} D_3 d\mathrm{V} = \frac{W}{h_{\mathrm{PZT}}} \int_0^L \int_{h_0 - h_{\mathrm{PZT}}}^{h_0} D_3 dz dx \tag{2.23a}$$

$$= W \int_0^L \frac{(h_{\mathrm{PZT}} - 2h_0)}{2} \frac{d}{s^E_{\mathrm{PZT}}} w''_{xx} + \varepsilon^T \left(1 - k^2_{\mathrm{eff}}\right) E_3 dx \tag{2.23b}$$

$$= \frac{(h_{\mathrm{PZT}} - 2h_0)\, W}{2} \frac{d}{s^E_{\mathrm{PZT}}} w'_x(L) + \frac{\varepsilon^T \left(1 - k^2_{\mathrm{eff}}\right) WL}{h_{\mathrm{PZT}}} V \tag{2.23c}$$

$$= \Gamma w'_x(L) + CV \tag{2.23d}$$

The electric field in the PZT layer is along the way converted to a voltage V over the capacitor $C = \varepsilon^T \left(1 - k^2_{\mathrm{eff}}\right) WL/h_{\mathrm{PZT}}$ which is the capacitance of the PZT layer at constant strain. The factor $\Gamma = \left(d/s^E_{\mathrm{PZT}}\right)(h_{\mathrm{PZT}} - 2h_0)\, W/2$ is introduced as the coupling coefficient from cantilever end slope to charge. The current can now defined as

$$I = \frac{\partial Q}{\partial t} = \dot{Q} = \Gamma \dot{w}'_x(L) + C\dot{V} \tag{2.24}$$

2.5 Moment vs. Voltage

With the current defined, it is required to derive the back-coupling in form of a moment from the resulting voltage. With an applied voltage to the PZT layer of the cantilever, the cantilever will bend due to the tensile or compressive stress induced in the piezoelectric layer. The internal bending moment M created in the cantilever by the field is

$$M = W \int_{h_0}^{h_0 + h_{\mathrm{Si}}} z T_{\mathrm{Si}} dz + W \int_{h_0 - h_{\mathrm{PZT}}}^{h_0} z T_{\mathrm{PZT}} dz \tag{2.25a}$$

$$= -\frac{W}{s_{\mathrm{Si}}} w''_{xx} \int_{h_0}^{h_0 + h_{\mathrm{Si}}} z^2 dz - \frac{W}{s^E_{\mathrm{PZT}}} w''_{xx} \int_{h_0 - h_{\mathrm{PZT}}}^{h_0} z^2 dz - W \left(\frac{d}{s^E_{\mathrm{PZT}}}\right) \int_{h_0 - h_{\mathrm{PZT}}}^{h_0} z E_3 dz \tag{2.25b}$$

$$= -YI_{\mathrm{eff}} w''_{xx} + \frac{(h_{\mathrm{PZT}} - 2h_0)\, W}{2} \frac{d}{s^E_{\mathrm{PZT}}} h_{\mathrm{PZT}} E_3 \tag{2.25c}$$

$$= -YI_{\mathrm{eff}} w''_{xx} + \Gamma V \tag{2.25d}$$

where the expression YI_{eff}

$$YI_{\mathrm{eff}} = \frac{1}{3} W \left(\left((h_0 + h_{\mathrm{Si}})^3 - h_0^3 \right) / s_{\mathrm{Si}} + \left(h_0^3 - (h_0 - h_{\mathrm{PZT}})^3 \right) / s^E_{\mathrm{PZT}} \right) \tag{2.26}$$

is introduced as an effective product of the combined compliance and area moment inertia of the unimorph cantilever. In the derivation it is assumed that the change in electric field is linear between the two electrodes of the PZT layer. It is noted that the coupling coefficient Γ for moment and voltage correctly is identical to the coupling for current and deflection slope rate.

2.6 Deflection vs. Deflection Slope

The generated current and voltage are now both linked to the deflection of the cantilever. The next step in the analysis is to find the deflection of the cantilever due to an external force, and in this process finding the relation between the cantilever deflection and the cantilever deflection slope. For this the Euler Bernoulli static beam equation for small deflections and constant stiffness and inertia is used

$$\frac{d^4w}{dx^4} = \frac{q}{YI_{\text{eff}}} \tag{2.27}$$

where q is the distributed load (force per unit length) of the cantilever. To solve the equation the following boundary conditions are used

$$\left.\frac{d^3w}{dx^3}\right|_{x=L} = -\frac{F}{YI_{\text{eff}}} \tag{2.28a}$$

$$\left.\frac{d^2w}{dx^2}\right|_{x=L} = \left.\frac{M}{YI_{\text{eff}}}\right|_{x=L} = \frac{Fl+\Gamma V}{YI_{\text{eff}}} \tag{2.28b}$$

$$\left.\frac{d^2w}{dx^2}\right|_{x=L} = 0 \tag{2.28c}$$

$$w(0) = 0 \tag{2.28d}$$

The solutions for deflection and deflection thereby becomes

$$w(x) = \frac{\Gamma V}{2YI_{\text{eff}}}x^2 + \frac{4F(3l+3L-x)+q(6L^2-4Lx+x^2)}{24YI_{\text{eff}}}x^2 \tag{2.29}$$

$$w'_x(x) = \frac{\Gamma V}{YI_{\text{eff}}}x + \frac{3F(2l+2L-x)+q(3L^2-3Lx+x^2)}{6YI_{\text{eff}}}x \tag{2.30}$$

It is preferable to evaluate the relation between deflection and cantilever tip slope at a point as close to the centre of mass as possible. The proof mass implemented in the fabrication process is around 20 times thicker than the cantilever. It is therefore reasonable to assumed that the overall beam centre of mass will be close to the longitudinal proof mass midpoint $(L+l)$ according to the sketched cantilever in Figure 2.2 on page 20. With the straight tangent line assumption of the proof mass, the deflection at the proof mass midpoint (w_c) becomes

$$w_c = w(L) + lw'_x(L) = \Lambda w'_x(L) \tag{2.31}$$

Table 2.2: *Parameters, values and FEM configurations used to compare numerical simulations with the analytic model which is evaluated with different assumptions. The ratio α indicated the ratio between cantilever and mass of the full beam length.*

Model	Description
FEM ani.	Si anisotropic PZT isotropic
FEM iso.	Si isotropic PZT isotropic
$q \neq 0$	Full model
$q \neq 0$ $s = s_{11}$	Unidirectional compliance
$q = 0$	q neglected

Geometric parameters	
L_{total}	$= 6.5\,\text{mm}$
L	$= L_{\text{total}}\alpha$
L_m	$= L_{\text{total}}(1-\alpha)$
l	$= L_m/2$
W	$= 6\,\text{mm}$
h_{Si}	$= 36\,\mu\text{m}$
h_{PZT}	$= 25\,\mu\text{m}$
h_{mass}	$= 464\,\mu\text{m}$

Material constants	
$s_{[110]}$	$= 1/(169\times10^9)\,\text{m}^2\,\text{N}^{-1}$
ν_{Si}	$= 0.0606$
s_{Si}	$= s_{[110]}(1-\nu_{\text{Si}})$
$s_{11,\text{PZT}}$	$= 1/(71\times10^9)\,\text{m}^2\,\text{N}^{-1}$
ν_{PZT}	$= 0.33$
s_{PZT}	$= s_{11,\text{PZT}}(1-\nu_{\text{PZT}})$
ρ_{Si}	$= 2330\,\text{kg}\,\text{m}^{-3}$
ρ_{PZT}	$= 7200\,\text{kg}\,\text{m}^{-3}$

where Λ is introduced as a geometric length factor describing the relation between centre of mass deflection and cantilever tip slope. The evaluation is conducted in short-circuit condition $V = 0$ since this corresponds to the purely mechanical situation. Using that $F = Ma$ and $q = ma$ in Equations (2.29) to (2.30), Λ can accordingly be expressed as

$$\Lambda = \frac{w(L) + l w'_x(L)}{w'_x(L)} = \frac{L^2(4l+3L)m + 8\left(3l^2+3lL+L^2\right)M}{4\left(L^2m+6lM+3LM\right)} \tag{2.32}$$

where the applied input acceleration a correctly vanish in the geometric length factor. The spring constant, which is also evaluated at $L + l$, is therefore

$$k_c = \frac{F_{\text{ext}}}{w_c} = \frac{a\,(M+mL)}{w_c} = \frac{24(Lm+M)\text{YI}_{\text{eff}}}{L^3(4l+3L)m + 8L\left(3l^2+3lL+L^2\right)M} \tag{2.33}$$

With the relation between deflection and deflection slope, the short-circuit current can be found from Equation (2.24) as

$$I_{sc} = \Gamma \dot{w}'_x(L) = \frac{\Gamma}{\Lambda}\dot{w}_c \tag{2.34}$$

2.7 Finite Element Modelling

The geometric length factor, Λ, will be part of the equivalent circuit model later in the analysis in form of a transformer. To verify this important factor, the analytic expression is compared to the results of numerical simulations from a finite element model (FEM). The software used is the commercially available software Comsol Multiphysics with version number 4.3. Table 2.2 shows an overview of the parameters, values and FEM configurations used in the comparison. The geometric parameters are identical to the design which is extensively characterised in Chapter 5, and the material constants are the theoretically expected values. Two different FEM configurations have been considered for the cantilever oriented in the [110]-direction; one where the silicon support is simulated as anisotropic and one where the silicon is considered isotropic. Silicon is anisotropic, but as will be evident, considering the silicon support as isotropic with the effective compliance defined in Equation (2.9a) on

page 22 is a reasonable simplification. The analytic expression for the closed circuit deflection in Equation (2.29) is evaluated in its full form ($q \neq 0$) and with two assumptions, one with unidirectional compliance ($q \neq 0,\ s = s_{11}$) and the second with the mass of the thin cantilever neglected ($q = 0$).

Figure 2.4a shows the deflection at proof mass midpoint as function of cantilever to proof mass ratio α. The results are all normalised to the peak deflection for the anisotropic FEM model. When $\alpha = 1$ the cantilever equals the full beam length, hence no proof mass is present, while if $\alpha \to 0$ the cantilever vanish and the beam becomes a bulky structure with a uniform thickness equal to the thickness of proof mass. The isotropic FEM simulation and the full analytic expression follows the anisotropic FEM closely, while the unidirectional compliance expression deviates at ratios between 0.4 and 0.8. As expected the simplified expression with q neglected fails increasingly for higher ratios where the proof mass decreased. In Figure 2.4b the deflection slope at L is plotted, again normalised to the peak deflection slope of the anisotropic FEM simulation. The discrepancy between the simulations and expressions are as expected similar to those observed under the deflection analysis, though the maximum value is shifted from a cantilever ratio of 0.59 for the deflection to 0.53 for the deflection slope. Figure 2.4c shows the deflection and deflection slope errors for the isotropic FEM model and full analytic expression relative to the anisotropic FEM simulation. With an error of less than 0.5% for the FEM isotropic model, the assumption of considering the silicon isotropic instead of anisotropic is reasonable. The relative error of the analytic expression is around 1% which originated from the difference in proof mass symmetry around the neutral axis and the neglect of proof mass rotation effects. The relative errors on analytic expressions with unidirectional compliance and no cantilever mass as neglected since these are a factor of 5-10 higher than for the full expression.

Having found both proof mass midpoint deflection and deflection slope at L the geometric length factor Λ can easily be derived. In Figure 2.4d the error of Λ relative to the anisotropic FEM model is plotted. It is clear that with low errors in deflection and deflection slope the error of the isotropic FEM is small. The analytic expressions with effective and unidirectional compliance are equal, which is correct since Λ is a geometry factor independent of material parameters. The simplified expression ($q = 0$) fails significantly at ratio of 0.7 an upwards, while the error is comparable or even smaller for ratios small than 0.6. With an error of less than 2% it is concluded that the analytic expression is sufficient precise for further analysis.

2.8 Mechanical Resonant Frequency

The accuracy of the analytic model depends on the fact that the model predicts the correct mechanical resonant frequency which corresponds to short-circuit operation. When a correct resonant frequency is deduced, an effective mass can be estimated from the spring constant in Equation (2.33). To find the natural frequency of the harvester the Rayleigh-Ritz method is used. In this method the resonant frequency is identified from the maximum potential and

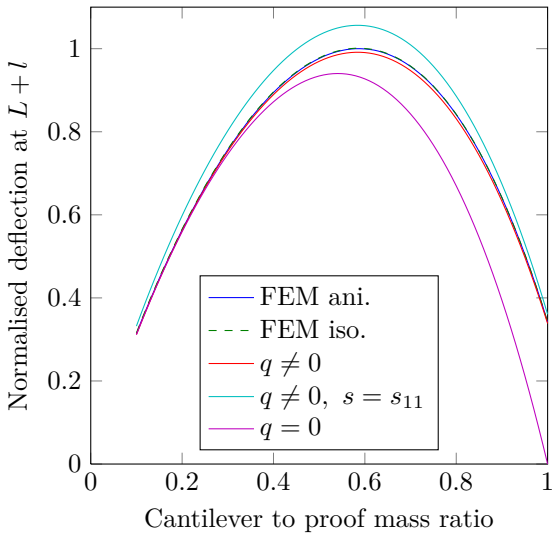

(a) *Deflection at $L+l$ as a function of cantilever ratio. Deflection normalised to peak deflection from FEM anisotropic model*

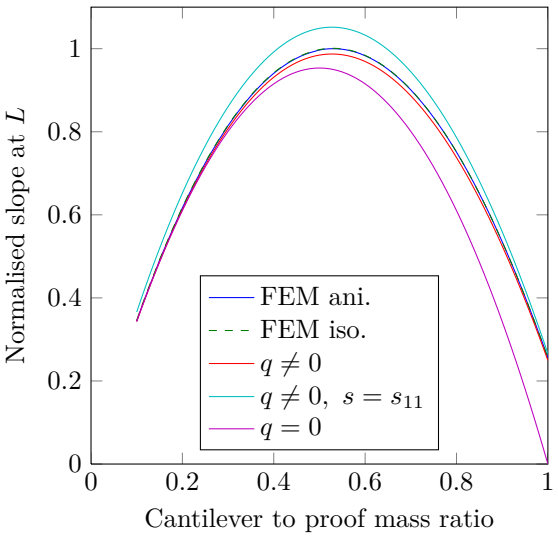

(b) *Deflection slope at $L+l$ as function of cantilever ratio. Slope normalised to peak deflection slope from FEM anisotropic model*

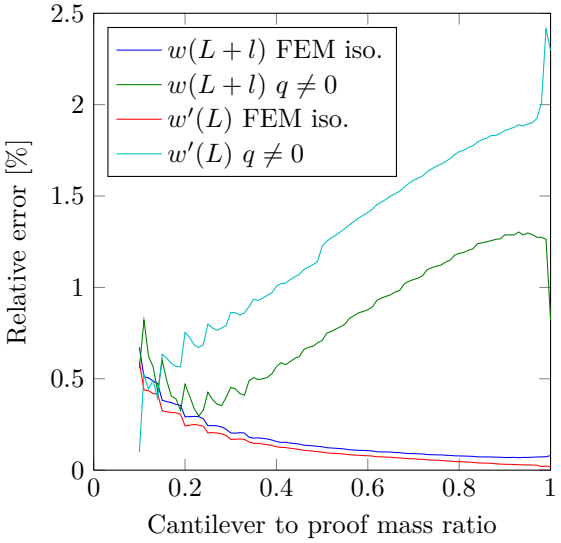

(c) *Error of analytic and FEM isotropic model relative to FEM anisotropic model for deflection and deflection slope vs. cantilever ratio.*

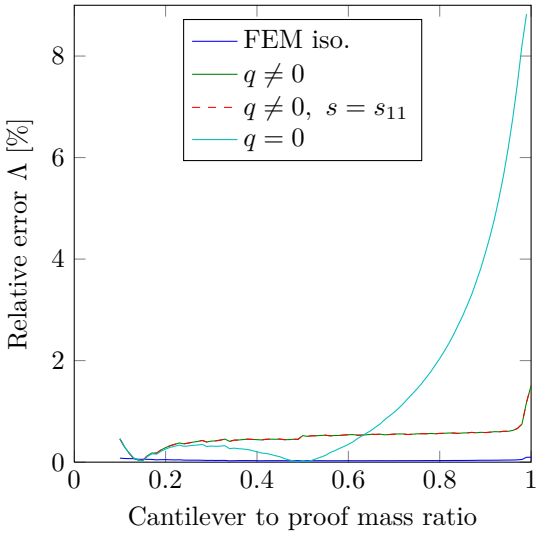

(d) *Error on the geometric length factor $\Lambda = w_c/w'_x(L)$ relative to the FEM anisotropic model.*

Figure 2.4: *Comparison between FEM and analytic expressions for the deflection at $L+l$ and deflection slope at L and consequently the geometric length factor Λ. For the FEM the silicon is simulated as both anisotropic and isotropic, errors are relative to the FEM anisotropic model. For the analytic part, the full expression is plotted for both effective ($s = s_{11}(1-\nu^2)$) and unidirectional (s_{11}) compliances together with a simplified, $q = 0$, expression with cantilever mass neglected.*

kinetic energies since these quantities equals each others at resonance. In the Rayleigh-Ritz method it is assumed that under a sinusoidal excitation, the cantilever motion is equal to a quasi static spatially dependent trial function multiplied by a sinusoidal time dependence. A time dependent deflection function is therefore defined as

$$\xi(x,t) = w(x)\cos(\Omega t) \tag{2.35}$$

where Ω is the angular frequency of the motion. The maximum potential energy is obtained when the cantilever deflection is the highest which occurs at $|\cos(\Omega t)| = 1$. The maximum potential energy is thus equal to the total stored energy in the cantilever at the deflection $w(x)$ in Equation (2.29). The total stored energy in a deformed body is given by the total strain energy

$$E_s = \frac{1}{2}\int_{\mathrm{V}} \mathbf{TS} dV \tag{2.36}$$

where T is the stress and S the strain vectors. Using the same boundary conditions as previously with only S_1 being non-zero, the potential energy of the cantilever in short-circuit conditions becomes

$$E_{\mathrm{pot}} = \frac{1}{2}\int_{\mathrm{V}} T_1 S_1 dV = \frac{1}{2}\int_0^L \int_0^W \left(\int_{h_0}^{h_0+h_{\mathrm{Si}}} T_{\mathrm{Si}} S_{\mathrm{Si}} dz + \int_{h_0-h_{\mathrm{PZT}}}^{h_0} T_{\mathrm{PZT}} S_{\mathrm{PZT}} dz \right) dy dx \tag{2.37}$$

$$= \frac{1}{2}\int_0^L \left(\frac{W(w''_{xx})^2}{s_{\mathrm{Si}}} \int_{h_0}^{h_0+h_{\mathrm{Si}}} z^2 dz + \frac{W(w''_{xx})^2}{s_{\mathrm{PZT}}} \int_{h_0-h_{\mathrm{PZT}}}^{h_0} z^2 dz \right) dx \tag{2.38}$$

$$= \frac{1}{2}\int_0^L Y I_{\mathrm{eff}} (w''_{xx})^2 dx = \frac{Y I_{\mathrm{eff}}}{2}\int_0^L (w''_{xx})^2 dx \tag{2.39}$$

The velocity profile of the cantilever is the derivative of the time dependent function

$$\frac{\partial \xi(x,t)}{\partial t} = -\Omega w(x)\sin(\Omega t) \tag{2.40}$$

It is easy to identify that the maximum velocity is present when $|\sin(\Omega t)| = 1$, which is exactly when the deflection of the cantilever is zero. The velocity profile of the cantilever at maximum velocity is therefore

$$v_{\max}(x) = -\Omega w(x) \tag{2.41}$$

The maximum kinetic energy for the cantilever can be found by integrating the squared deflection profiles for cantilever and proof mass multiplied by mass per unit length and divided by two

$$E_{\mathrm{kin}} = \Omega^2 \frac{1}{2}\left(m\int_0^L w(x)^2 dx + \frac{M}{L_m}\int_L^{L_m} \delta(x)^2 dx \right) \tag{2.42}$$

where

$$\delta(x) = w(L) + (x-L)\left.\frac{dw(x)}{dx}\right|_{x=L} \tag{2.43}$$

is the deflection profile of the proof mass. From the Rayleigh-Ritz maximum energy method it therefore follows that

$$E_{\text{kin}} = E_{\text{pot}} \Rightarrow \Omega_0^2 = \frac{YI_{\text{eff}} \int_0^L (w''_{xx})^2 dx}{m \int_0^L w(x)^2 dx + \frac{M}{L_m} \int_L^{L_m} \delta(x)^2 dx} \tag{2.44}$$

where Ω_0 is the first mechanical resonant frequency.

2.8.1 FEM Verification

The evaluated expression for the resonant frequency is extensive and will not be given here, instead it will be validated by a FEM simulation as done previously for the deflection and deflection slope in Section 2.7. The parameters, values and FEM configurations are identical to those listed in Table 2.2. Figure 2.5a shows the two FEM simulated and two analytic resonant frequency results as function of cantilever ratio. The results are normalised to the resonant frequency obtained from the analytic FEM simulation with no proof mass ($\alpha = 1$). The isotropic FEM and analytic model with effective compliance follows the anisotropic FEM closely, while the analytic expression with unidirectional compliance result in a frequency slightly smaller. This is expected since the unidirectional compliance will be higher than the effective compliance and vice versa for the resulting stiffness. The difference is illustrated in Figure 2.5b where the error of the models relative to the anisotropic FEM simulation is plotted. The analytic expression with effective compliance gives less than 1% error in the ratio range of interest. The minimum resonant frequency is obtained at a cantilever to mass ratio of 0.52 for both the anisotropic FEM model and the analytic expression with effective compliance.

2.8.2 Effective Mass

Having defined expressions for both the spring constant and the resonant frequency, the effective mass for the mass-spring-damper system in the equivalent circuit model can be estimated from

$$m_{\text{eff}} = k_c/\Omega_0^2 \tag{2.45}$$

where k_c is the spring constant evaluated at the proof mass midpoint from Equation (2.33) on page 27.

Figure 2.6 shows the calculated effective mass relative to the actual mass ($M + Lm$) for the analytic model with and without cantilever load q as a function of cantilever ratio. At low cantilever ratios the two models line up, which is expected since the mass of the cantilever becomes increasingly neglectable. At higher cantilever ratios the model without cantilever load fails increasingly, and approaches ∞ as the proof mass vanishes. On the other hand the model including cantilever load allows for predictions for the full range of cantilever ratios.

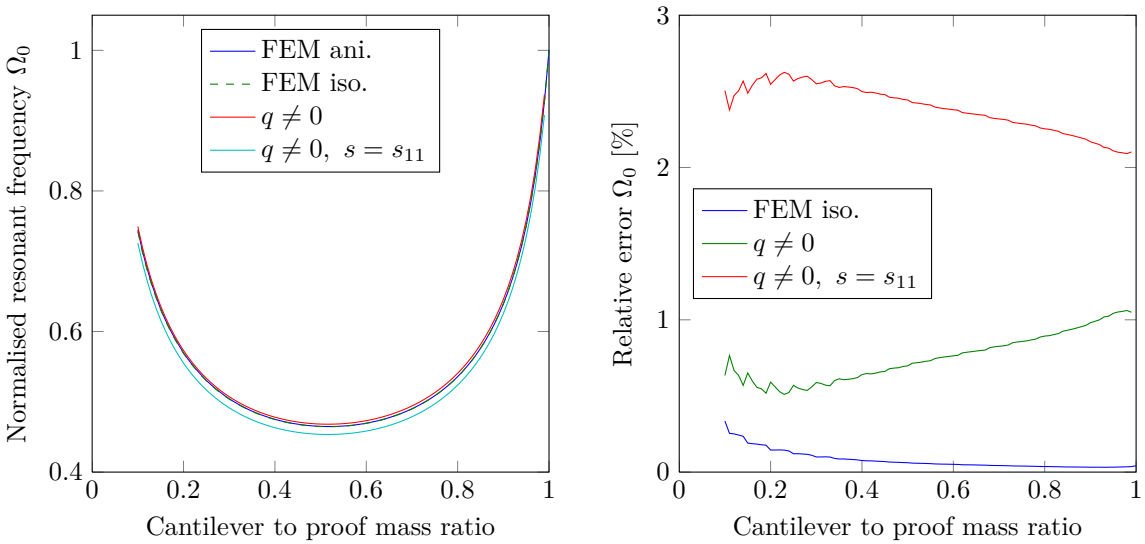

(a) *Resonant frequency normalised to the resonant for FEM anisotropic model at a ratio of 1 as function of the cantilever mass ratio.*

(b) *Resonant frequency error relative to the FEM anisotropic model.*

Figure 2.5: *Comparison between FEM simulations and analytic predictions for the resonant frequency. The silicon part of the cantilever is numerically simulated as both anisotropic and isotropic, while the analytic expressions are evaluated with both effective and unidirectional compliance. The minimum resonant frequency is obtained at a ratio of 0.52.*

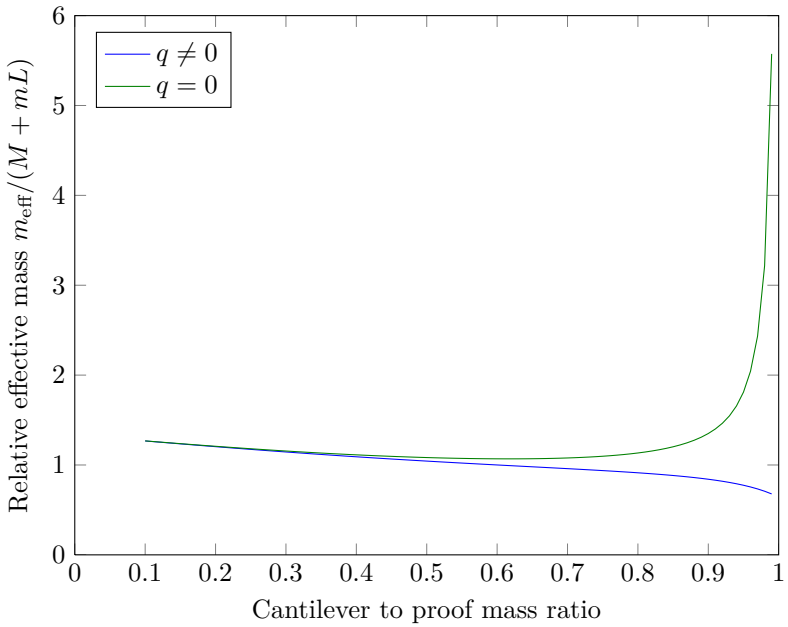

Figure 2.6: *Effective mass for the mass-spring-damper system relative to the actual mass of the cantilever and proof mass. The analytic expression is evaluated with both cantilever load, q, included and excluded.*

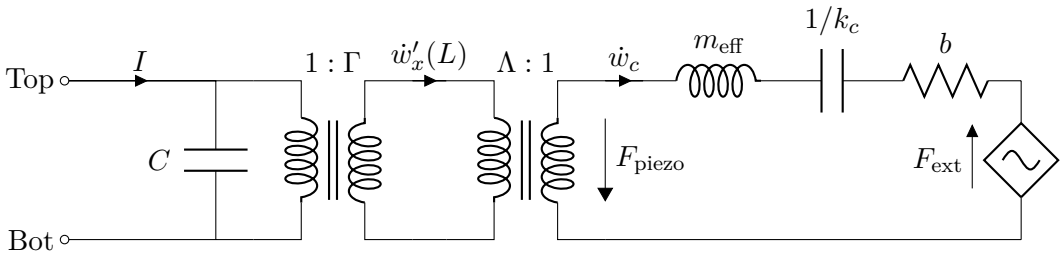

Figure 2.7: *Full equivalent circuit of the piezoelectric unimorph vibration energy harvester. The electrical domain holds a capacitor C for the dielectric piezoelectric layer and a transformer* $1 : \Gamma$ *which relates bending moment with voltage and deflection slope rate with current. The mechanical side contains the proof mass m, the equivalent spring constant* k_c*, a mechanical loss resistor b, the external input force* F_{ext} *and the back-coupled force from the piezoelectric layer* F_{piezo} *to the mechanical domain. The model furthermore contains the transformer* $\Lambda : 1$ *that relates the displacement velocity and slope rate of the cantilever.*

Regardless of what analytic assumptions is chosen, Figure 2.6 shows that it some cantilever ratios it is necessary to evaluate an effective mass for the mass-spring-damper system. This will be used in the equivalent circuit in the next section.

2.9 Equivalent Circuit

The full equivalent circuit of the harvester is graphically presented in Figure 2.7. The model is built up around two transformers. The first one $(1 : \Gamma)$ relates bending moment with voltage and deflection slope rate with current, and the second transformer $(\Lambda : 1)$ relates the deflection velocity and slope rate of the cantilever. The mechanical right side contains the lumped elements from the spring-mass-damper system, with m_{eff} as the effective proof mass, k_c as the equivalent spring constant and b as a mechanical loss resistor representing the viscous losses in the system. F_{ext} is the external driving force acting on the cantilever and proof mass, and F_{piezo} is the back-coupled force from the piezoelectric layer to the mechanical domain. The electrical left side consist of a capacitor for the capacitance between the electrodes around the dielectric piezoelectric layer. A summary of the device equations that this circuit represents is

$$I = \dot{Q} = \Gamma \dot{w}'_x(L) + C\dot{V} \tag{2.46a}$$

$$w_c = \Lambda w'_x(L) \tag{2.46b}$$

$$F_{\text{ext}} + F_{\text{piezo}} = m_{\text{eff}}\ddot{w}_c + b\dot{w}_c + k_c w_c \tag{2.46c}$$

The force from the piezoelectric layer to the mechanical domain can be found from the moment in Equation (2.25d) on page 25 where $M = \Gamma V$ when only a voltage is present. This moment can be translated to a mechanical force from the relation $w_L = \Lambda w'_x(L) \Rightarrow M = \Lambda F$. The moment from the voltage over the piezoelectric layer thus equals a force of $F_{\text{piezo}} = V\Gamma/\Lambda$.

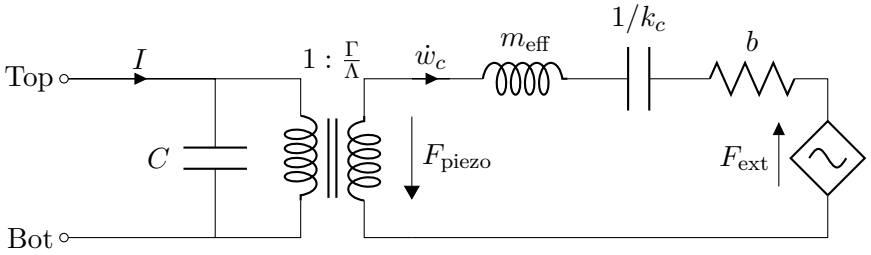

Figure 2.8: *Simplified equivalent circuit of Figure 2.7.*

The circuit model in Figure 2.7 can therefore for simplicity be reduced by merging the two ideal transformers as seen in Figure 2.8. The lumped model equations then reduces to

$$I = \frac{\Gamma}{\Lambda}\dot{w}_c + C\dot{V} \tag{2.47a}$$

$$F_{\text{ext}} + \frac{\Gamma}{\Lambda}V = m_{\text{eff}}\ddot{w}_c + b\dot{w}_c + k_c w_c \tag{2.47b}$$

In the further analysis of the system, it is useful to implement Laplace transformed quantities such that the final lumped model equations becomes

$$I = \frac{\Gamma}{\Lambda}\dot{w}_c + sCV \tag{2.48a}$$

$$F_{\text{ext}} + \frac{\Gamma}{\Lambda}V = Z_{\text{m}}\dot{w}_c \tag{2.48b}$$

with

$$Z_{\text{m}} = sm_{\text{eff}} + b + k_c/s \tag{2.49}$$

where Z_{m} is the mechanical impedance of the mass-spring-damper system, and $s = j\Omega$ is the complex frequency. At the mechanical resonant frequency $w_0 = \sqrt{k/m_{\text{eff}}}$ the mechanical impedance is at is minimum with a value equal to the viscous damping coefficient b of the system. Assuming that the PZT harvester is connected to a resistive load R_l which dissipates the generated electrical power, the electrical impedance Z_{e} can be expressed as

$$Z_{\text{e}} = \frac{R_l}{1 + sCR_l} \tag{2.50}$$

With the load R_l connected to the harvester, the current in Equation (2.48a) can be expressed as $I = -V/R_l$. The voltage is then found from the lumped model equations as

$$V = -F_{\text{ext}}\frac{(\Gamma/\Lambda)\,R_l}{(\Gamma/\Lambda)^2\,R_l + (sCR_l + 1)\,Z_{\text{m}}} = -F_{\text{ext}}\frac{(\Gamma/\Lambda)}{(\Gamma/\Lambda)^2 + Z_{\text{m}}/Z_{\text{e}}} \tag{2.51}$$

and the power dissipated in the resistor can accordingly be calculated as

$$P = \frac{|V|^2}{R_l} = \frac{|F_{\text{ext}}|^2}{R_l}\frac{(\Gamma/\Lambda)^2}{\left|(\Gamma/\Lambda)^2 + Z_{\text{m}}/Z_{\text{e}}\right|^2} \tag{2.52}$$

2.9.1 Peak Power

Besides the mechanical parameters included in the expression for the power output, the resistance of the external connected load highly influences the power. Maximum power is transferred when the impedance of the connected resistor Z_l equals the complex conjugate of the piezoelectric impedance ($Z_l = Z^*$). The internal piezoelectric impedance Z can from the Thevenin-Norton source transformation theorem by found by

$$Z = \frac{V_{\text{oc}}}{I_{\text{sc}}} \tag{2.53}$$

where V_{oc} is the open circuit voltage, and I_{sc} the short-circuit current. Expressions for both can be deducted from the voltage in Equation (2.51) as

$$V_{\text{oc}} = \lim_{R_l \to \infty} V = -F_{\text{ext}} \frac{(\Gamma/\Lambda)}{(\Gamma/\Lambda)^2 + CsZ_m} \tag{2.54a}$$

$$I_{\text{sc}} = \lim_{R_l \to 0} \frac{V}{R} = -F_{\text{ext}} \frac{(\Gamma/\Lambda)}{Z_m} \tag{2.54b}$$

The piezoelectric internal impedance can thereby be expressed as

$$Z = \frac{Z_m}{(\Gamma/\Lambda)^2 + CsZ_m} \tag{2.55}$$

When the harvester is operated at its mechanical resonant frequency, the mechanical impedance Z_m reduces to the viscous damping term, and the piezoelectric impedance becomes

$$Z(\Omega_0) = \frac{b}{(\Gamma/\Lambda)^2 + Cj\Omega_0 b} \tag{2.56}$$

As the connected resistor is purely real $Z_l = R_l \Rightarrow R_l = |Z|$, the peak power at the mechanical resonant frequency can be expressed as

$$P_{\text{peak}}(\Omega_0) = \frac{F_{\text{ext}}^2}{4b} \frac{2}{1 + \sqrt{1 + (\Gamma/\Lambda)^{-4} b^2 C^2 \Omega_0^2}} = \frac{F_{\text{ext}}^2}{4b} \frac{2}{1 + \sqrt{1 + \dfrac{1}{Q_{\text{mec}}^2 K_{\text{sys}}^4}}} \tag{2.57}$$

where K_{sys} is the system coupling coefficient

$$K_{\text{sys}}^2 = (\Gamma/\Lambda)^2 / (k_c C) \tag{2.58}$$

and Q_{mec} the mechanical quality factor

$$Q_{\text{mec}} = k_c/(b\Omega_0) = m_{\text{eff}}\Omega_0/b = \sqrt{m_{\text{eff}} k_c}/b \tag{2.59}$$

Using the following definitions

$$P_{\text{av}} = F_{\text{ext}}^2/(4b) \tag{2.60a}$$

$$\chi = \frac{2}{1 + \sqrt{1 + \dfrac{1}{Q_{\text{mec}}^2 K_{\text{sys}}^4}}} \tag{2.60b}$$

the peak power output $P_{\text{peak}}(\Omega_0) = P_{\text{av}}\chi$ can therefore by expressed by a maximum available power (P_{av}) multiplied by a factor (χ) which is less than of equal to 1 depending on the system coupling coefficient and mechanical quality factor. The viscous damping coefficient in P_{av} can be replaced by the mechanical quality for the system through Equation (2.59) hence the maximum available power for the system can be expressed as

$$P_{\text{av}} = \frac{F_{\text{ext}}^2 Q_{\text{mec}}}{4 m_{\text{eff}} \Omega_0} \tag{2.61}$$

2.10 Design Recommendation

Having derived the power expression for the system, it is possible to examine the influence of the geometric parameters of the harvester design, with mind on optimizing the power output. The mechanical quality factor for the total cantilever is difficult to estimate. While Q_{mec} for the PZT material used in this work is estimated to around 100, Q_{mec} is higher for the silicon. In total, Q_{mec} is a combination of the individual quality factors and also geometric effects. Assuming the mechanical quality factor to be a fixed number, the parameters of interest are hence cantilever width, thickness and length together with the ratio between cantilever and proof mass of the cantilever. From the expression for the resonant frequency in Equation (2.44) on page 31, it can be identified that Ω_0 is independent of the cantilever width as the increases stiffness for wider cantilevers is cancelled out be the equally increased mass. The available power is therefore proportional to the cantilever width according to $F_{\text{ext}}^2/m_{\text{eff}} \approx (M + mL)$ in Equation (2.61). Concerning the cantilever length, the external force increases with length as the mass increases, at the same time the resonant frequency will decrease as approximately $\propto \sqrt{(L+l)^{-3}}$. The length and width of the cantilever should accordingly be as long a wide as the total harvester dimensions facilitate. The optimal cantilever ratio at which maximum power is obtained can also be deduced from the available power by inserting the expressions for F_{ext}, m_{eff} and Ω_0 which all will be functions of the cantilever ratio term α. In Figure 2.9a the normalised available power for the analytic expressions with and without load from the cantilever, are plotted as function of cantilever ratio. The parameters listed in Table 2.2 are used in the evaluation. The peak available power for the expression with $q \neq 0$ is obtained at a ratio of 0.34, and for $q = 0$ at 0.28. The cantilever part should therefore only take up around 1/3 of the total cantilever length while the proof mass should cover the remaining part. The last geometric parameter that can be adjusted is the cantilever thickness and the ratio between the silicon and PZT layers in the cantilever. From the available power figure, the effect of thickness can by directly extracted. If the thickness decreases, the stiffness and resonant frequency decreases. The effect on the input force by decreasing thickness is however limited as the proof mass accounts for the majority of the system mass. The cantilever should therefore in principle be as thin as possible, while still mechanical stable for handling and use.

With the effect of total cantilever thickness set, the thickness ratio between silicon and PZT layer is examined by evaluating the power multiplication factor χ and the system coupling

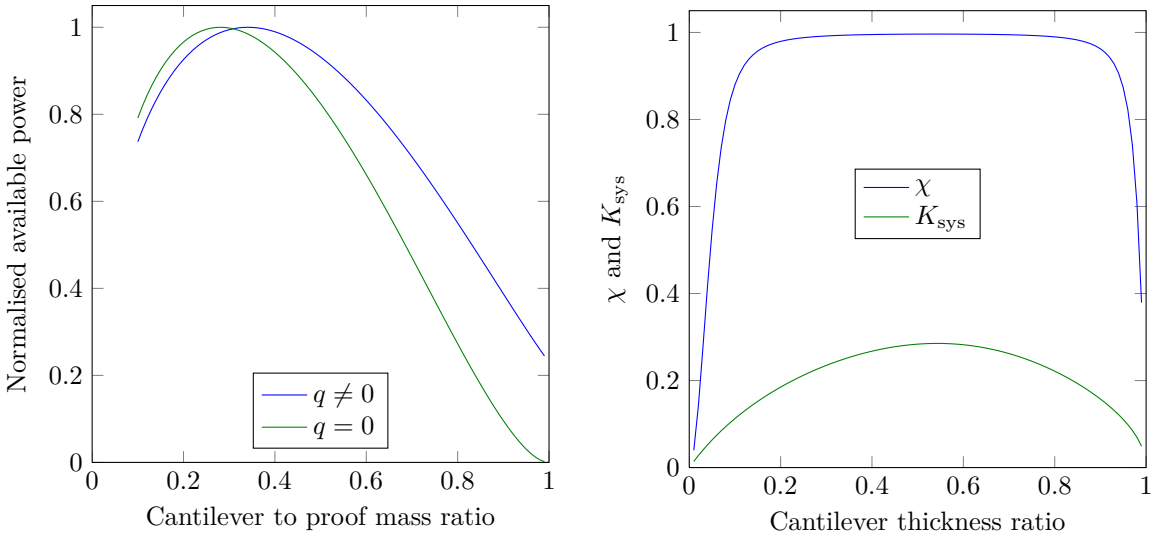

(a) *Available power.*

(b) *Optimal silicon to PZT ratio.*

Figure 2.9: *(a) Normalised available power for the analytic expression with and without cantilever load plotted as function of cantilever ratio. The maximum available power is obtained at a ratio of 0.34 for $q \neq 0$ and 0.28 for $q = 0$. (b) The power multiplication factor χ and system coupling coefficient as function of cantilever thickness ratio. If the ratio is 0 the cantilever is purely PZT, while at 1 the cantilever is all silicon. K_{sys} is maximum at a ratio of 0.54, but the mechanical quality factor is sufficiently high so that the power factor χ is at maximum in a wide range of thickness ratios.*

Table 2.3: *Piezoelectric and dielectric constants for the PZT thick film used in the ELBA project. The effective parameters defined in Equations* (2.9b) *to* (2.9c) *are also evaluated with the parameters from Table 2.2.*

	d_{31} [pC N^{-1}]	$d = d_{31}(1+\nu)$ [pC N^{-1}]	ε_{33}	$\varepsilon = \varepsilon_{33} - d_{31}^2/s_{11}\nu$
PZT thick film	-89	-118.4	$825\varepsilon_0$	$804\varepsilon_0$

coefficient K_{sys} for changing layer ratios. The change in P_{av} is neglected as no significant change in mass occurs, while the effect on resonant frequency is disregarded as only a slight change is occurring at the ratios of interest. For the evaluation of χ and K_{sys} the dielectric and piezoelectric constants in Table 2.3 are used for the PZT thick film together with the geometric and material parameters listed in Table 2.2. In Figure 2.9b χ and K_{sys} are plotted as function of thickness ratio, where a ratio of 0 is a full PZT cantilever and vice versa for a ratio of 1. The maximum K_{sys} is at a thickness ratio of 0.54. At this ratio the neutral plane is positioned around 1/4 into the silicon support layer. The optimal material joint relative to the neutral plane is a compromise between building up as much strain as possible per volume in the piezoelectric layer, while at the same time keeping the piezoelectric layer capacitance low. For the harvester under consideration in this work, the expected mechanical quality factor is sufficiently high to make the power factor term χ reach its maximum value of 1 in a broad range of thickness ratios from 0.2 to 0.8. Though the thickness ratio apparently seem of minor importance regarding χ, later characterisation will demonstrate that the influence of thickness ratio to Q_{mec} is of great importance.

2.10.1 Tapered Cantilever Design

The expected mechanical quality factor of the system is of a value where the power factor χ will be at its maximum for near all design parameters as seen in the thickness ratio evaluation. It is therefore of interest to increase the available power without exceeding the allowed total harvester dimensions. From the P_{av} expression in Equation (2.61) it is clear that a situation where the mechanical resonant frequency can be decreased without decreasing the mass would be of interest. For this exact purpose, several works on tapered cantilever structures have been published [31–33]. In the tapered design the cantilever width at the proof mass connection is smaller than the cantilever width at the clamped end. As a result the stress distribution becomes more uniform over the cantilever length, and in fact the stress per volume becomes higher for the tapered design. More importantly for the harvester in this work, the stiffness of the cantilever decreases, causing a decrease in the resonant frequency. This decrease in resonant frequency occurs without changing the dimensions of the proof mass, hence the majority of the system mass is kept constant, and a higher available power figure is obtained. Figure 2.10 shows the normalised resonant frequency as function of cantilever width of the proof mass connection. When the width ratio at mass is equal to 1 the harvester becomes rectangular. The data is obtained from FEM simulations, and plotted for cantilever length

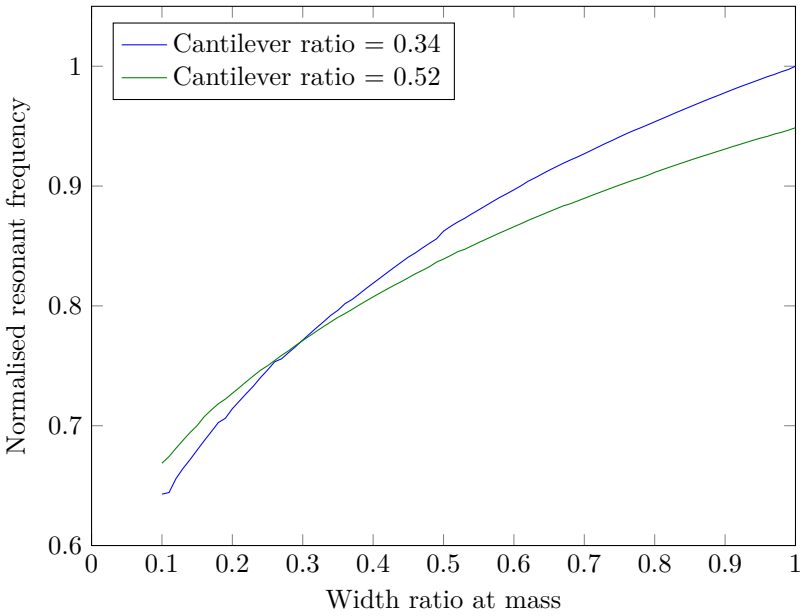

Figure 2.10: *Normalised resonant frequency as function of cantilever width ratio at mass. Results are obtained from FEM simulations and plotted for cantilever ratios of 0.34 and 0.52 where optimal power and lowest resonant frequency are achieved respectively.*

ratios of 0.34 and 0.52. By decreasing the width ratio at mass from 1 to 0.75, 0,5 and 0.25 a respective decrease in resonant frequency of 5.9%, 13.8% and 25.4% is obtained for the power optimised cantilever ratio of 0.34. For the low frequency cantilever ratio of 0.52 the numbers are 5%, 11.6% and 20.9%. Implementing a tapered cantilever should therefore provide an increase in available power as the resonant frequency is lowered without significantly reducing the total cantilever mass.

2.11 Summary

An analytic model predicting the harvester performance has been derived from a single degree-of-freedom model with lumped parameters considering the energy harvester as a mass-spring-damper system. The different configurations with either one or more active piezoelectric layers was presented, and the unimorph case with only one piezoelectric layer positioned on a elastic support was chosen for the analysis. The electric field in the piezoelectric layer can be generated by both bending and stretching, it was thus proven that bending will give rise to around 600 times more stress than stretching. Accordingly stretching is neglected in the analytic model. In the preliminary phase of the analysis, the effective material parameters were defined for the case of a plate structure with a thickness mush smaller than width and length, and from this the concept of neutral axis and material interface and their position with respect to each other was covered. The relations between generated charge and cantilever deflection slope and bending moment and voltage were defined, resulting in an identical

coupling coefficient for both relations. From the Euler Bernoulli static beam equation a characteristic geometric length factor was derived for the relation between cantilever slope and deflection. This factor together with the solution to the beam equation was compared to numerical simulations from a finite element model, and the error was found to less than 1%. The resonant frequency of the harvester was derived from the Rayleigh-Ritz energy maximization method. The derived expression was compared to finite element simulations with an error of less than 1%. With the relations for induced charge and moment defined, an equivalent circuit with the mechanical and electrical domains was set up. From this the generated voltage and consequently power in an external connected load was derived. The power output at mechanical resonant frequency and under optimal load conditions were the load matched the complex conjugate of the internal piezoelectric impedance was defined. From this, the power output can be expressed as an available power for the harvester together with a multiplication factor that is equal to one or less depending on the system coupling factor and mechanical quality factor. It is demonstrated that the expected mechanical quality factor for the harvester in this work is sufficient high for the multiplication factor being nearly 1. It is therefore mainly the available power term that determines the power output.

Having defined both resonant frequency and power, the effect of geometrical design parameters was examined. To maximise the available power the harvester should in general be as wide and long as the total system dimension allows. With fixed total cantilever length, maximum power is obtained at a cantilever to mass ratio of 0.34, meaning that the proof mass should take up around 2/3 of the total beam. Contrary, if a low resonant frequency is the aim, the cantilever to mass ratio should be around 0.52. Besides increasing the cantilever width and length, both of which are constraint by outer dimensions, the available power can be enhanced by designing the cantilever as a taper. The cantilever width at the mass will be smaller than at the clamped end for a tapered cantilever, as a result the stiffness and resonant frequency is lowered without a decrease of the total harvester mass.

Chapter 3

Process Development

The overall objective of this work is to develop and fabricate energy harvesters for the ELBA project. From a research point of view it means, that while it is of interest to design, develop and fabricate the best performing energy harvester possible, the final objective is to end up with a reliable and realistic fabrication process that allows for high volume fabrication and potentially commercialization. Achieving the best possible combinations of these two aims, requires extensive process development. The nature of process development means that it is a result of obtained knowledge from a continuous experimental iteration progress. The purpose of this chapter is to give an overview of this iteration progress leading to the final fabrication process. Concurrently, the chapter will outline the numerous different designs and configurations used, and the development of these as they are closely linked to the fabrication process. The overview will be build up around the bachelor and master projects conducted prior and during the ELBA work as these all are based on a new set of lithography masks, harvester designs and fabrication techniques including sequence. Only critical conclusions and important considerations will be presented, while smaller design and fabrication improvements will be included in the presentation of the final recommended fabrication process in the following chapter.

3.1 Objectives and Challenges

To understand the governing factors in the considerations regarding design and fabrication, it is necessary to identify the objectives. Next, it is essential to organise these objectives by importance since their impact under several circumstances contradicts each other. From an application point of view, the sole purpose of the vibration harvester is to deliver power to the wireless sensor unit. For this the frequency matching described in section Section 1.3.1 on page 7 is decisive, but it must be accomplished within an acceptable total volume. For the latter, a maximum lateral footprint of $10\,\text{mm} \times 10\,\text{mm}$ and total height of $< 5\,\text{mm}$ is defined for the bare silicon processed harvester during the entire development phase. Regarding frequency matching, no source of vibrations was specified for the ELBA project, hence no

exact target resonant frequency is defined. From a technological and fabrication point of view, it is challenging to achieve low frequencies when the beam length is restricted. The solutions is to use thin cantilevers with large proof masses as sketched in Figure 2.2 on page 20. Achieving resonant frequencies of 200 Hz to 500 Hz has therefore been set as aim. From this range, higher frequencies will naturally be easier to obtain. The criterion for success from the application side is consequently as high power as possible, from a harvester with limited volume at a low frequency. The engineering challenge is therefore to achieve these aims with a design, in combination with a fabrication process, that fulfils the last objective of high yield and high volume fabrication.

3.1.1 Basic Design and Fabrication

The basic design of a unimorph harvester can be broken down to three parts, the cantilever stack of silicon and PZT, the proof mass and finally a frame surrounding the beam. The frame is vital as it functions both as clamping for the cantilever and for handling and protection of the fragile beam structure. The outer frame dimensions are equal to the limited footprint of 10 mm × 10 mm, while the inner opening available for the beam is 7 mm × 7 mm. With a separation or trench between beam and frame of 500 µm the maximum beam width and length can be 6 mm and 6.5 mm respectively. From a processing point of view, the fabrication is governed by the two most essential steps, the definition of the thin cantilever with proof mass and the screen printing of PZT. Defining the cantilever and proof is accomplished by etching nearly all the way through a wafer. The thickness of the silicon support in the unimorph cantilever is hence defined from the remaining silicon when the etch is stopped. The choice of technique for the cantilever definition process and the sequence with respect to the PZT screen printing, are based on numerous considerations which will be reviewed with their impact in the following.

3.2 Work Prior to ELBA

The ELBA project was initiated at the end of 2009, prior to this two projects were carried out on silicon processed unimorph energy harvester as forerunners for ELBA project. These two projects were mainly based on experiences with screen printed PZT and silicon processes obtained from the development of a piezoelectric ultrasonic transducer [34] and a piezoelectric accelerometer [35].

3.2.1 Borregaard and Kvaal 2009

In the beginning of 2009 Borregaard and Kvaal made the first attempt during their bachelor project [36]. The governing steps in the fabrication process were conducted such that the cantilever was defined early in the process using a deep reactive ion each (DRIE), and the

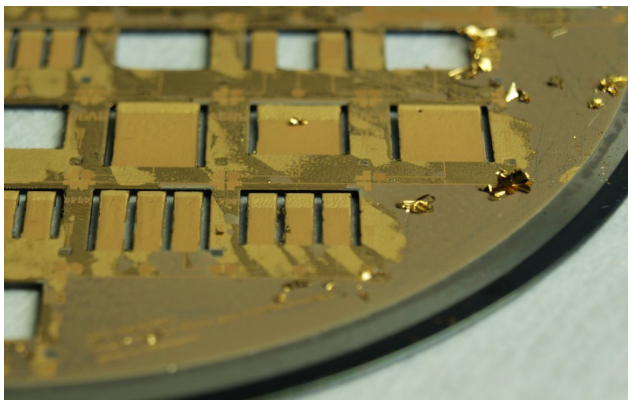

(a) *Borregaard and Kvaal 2009* [36].

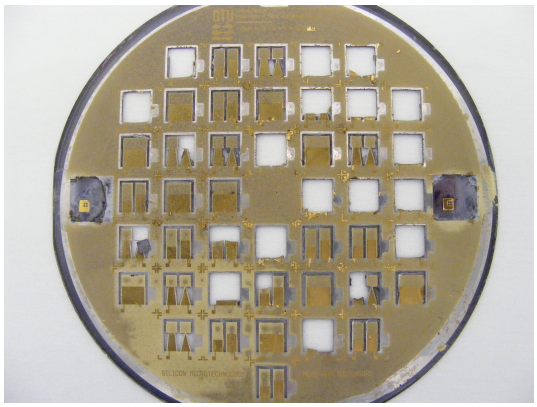

(b) *Nagstrup 2009* [37].

Figure 3.1: *(a) Photograph of a wafer after lift-off. Large areas of metal remains due to bad resist coverage before the metallization process. To ease the lift-off process ultrasound was used resulting in the loss of several devices. (b) Photograph of the final wafer after lift-off and trench etch. It is clear that despite process improvement, a substantial amount of devices was lost during the fabrication sequence.*

screen printing of PZT would then follow after. Cross-sectional sketch of the process flow is available in Appendix B.1 on page 184. As the first fabrication attempt, the project relied on using well known tools for fast prototyping. The DRIE process is costly and not well suited for high volume fabrication, but with a high etch rate and vertical slopes it is developed for the purpose of etching deep holes or even through entire wafers. To accurately control the final thickness of the silicon support, silicon-on-insulator (SOI) wafers were used for the fabrication with the buried oxide functioning as an etch stop layer. In the DRIE process the wafer is cooled by gasses on the side not exposed to etching, a good clamping between wafer and chuck is therefore required. This is not possible if the wafer is covered with PZT which is porous and in addition has a high surface roughness. Besides this, equipment contamination issues from the lead in the PZT are not even considered. Using DRIE therefore only leaves the option of screen printing the PZT later in the process sequence. The drawback of having this sequence is that during the screen printing process a force is applied to press the PZT paste onto the substrate. This force acts vertically on the fragile thin cantilevers and can easily damage or break the structure. The cantilever fragility was further enhanced in the work of Borregaard and Kvaal as the cantilevers were released prior to screen printing with decreasing mechanical stability as a result. The final critical step in the fabrication is the top electrode. Depositing and patterning of metal is a trivial step in any cleanroom, where e-beam evaporation and lift-off techniques among the most used techniques. This combination however leads to some unfortunate consequences and effects for the ELBA harvester. As a result of the screen printing process, the edges of printed areas contains narrow and relative high peaks. These peaks arise when the paste is pressed up at the edges of the screen during the printing process. With a height of tens of µm combined with the holes from the trench openings, it was difficult to achieve a conformal resist coating of the PZT and in particular the edge peaks using the available spinning technique. As a consequence the lift-off process were

highly problematic as metal evaporated on areas with little or no resist coverage is difficult or impossible to remove. To assist the lift-off process ultrasound was used, which caused significant loss of cantilevers due to critical vibrations. The final fabrication result is depicted in Figure 3.1a. Several devices are lost, and large flakes and areas of metal remains despite lift-off with ultrasound. As a consequence of the incomplete lift-off, a considerable amount of devices was short-circuited which naturally causes problems in the polarization step. The overall result was that only one working harvester was obtained out of a total of 240. The majority of harvesters were lost due to fragility problems as the cantilevers were defined at an early stage of the process.

3.2.2 Nagstrup 2009

Simultaneously with the last phase of the project by Borregaard and Kvaal, a new project on energy harvesters was carried out by Nagstrup in his master thesis [37]. This work from the last part of 2009, used a SOI wafer based fabrication process identical to its predecessor, except from the trench etch which was moved in sequence to after the screen printing process. Cross-sectional sketch of the process flow is available in Appendix B.2 on page 185. The motivation was to decrease the beam fragility for the screen printing process and to ease the conformal resist coating for the lift-off process. In the work of Borregaard and Kvaal the cantilevers were released in a KOH etch of the trench prior to screen printing. With limited possibility of protecting the PZT against the KOH etch, the cantilever release was carried out by a reactive ion etch (RIE) of the trench. The result of the changed sequence is depicted in Figure 3.1b with an obtained yield of 42% before the polarisation of the devices. The precise effect of the improved lift-off process regarding short-circuit problems in the polarisation process was not concluded. Three different rectangular and two different tapered designs were fabricated in the work, but with poor polarisation and too few chips, no conclusions were drawn concerning optimal design.

3.3 Process Development in ELBA

The process development during the ELBA project, will start by reviewing the iterative progress in two bachelor projects. After this, the introduction of a KOH etch for cantilever definition post screen printing will be reviewed, and finally the results of a bachelor project with bimorph harvesters will be outlined. All the projects were supervisor by the author.

3.3.1 Thyssen and Stoot 2010

The work by Thyssen and Stoot [38] in their bachelor project in the first part of 2010, was based on the fabrication sequence from Nagstrup with DRIE etching of SOI wafers followed by screen printing of PZT and cantilever release in RIE. Cross-sectional sketch of the process

flow is available in Appendix B.3 on page 186. Instead of using the lift-off method for the top electrode definition with numerous complications as consequence, the top electrode was defined used a shadow mask technique. The top electrode pattern was transferred to a 350 µm wafer as holes using a DRIE process. This wafer was then placed, aligned and fastened on top of the device wafer, and metal was evaporated through the holes in the wafer with direct patterning as consequence. The advantage of using a shadow mask is obvious as no leftover metal remains and no ultrasound is required. The compromise is however a smaller alignment precision as the shadow mask in this non-standard technique requires manual positioning and alignment under a microscope.

3.3.1.1 High Pressure Treatment

Besides the improvement of implementing shadow masks, the PZT deposition process was developed with an additional step. Between the screen printing and sintering a step was added to increase the density and hence piezoelectric performance of the PZT thick film. The step involves high pressure treatment (HPT) in a cold isostatic pressing (CIP) process of the porous PZT film before sintering [17, 39].

The PZT printed wafer is packed and vacuum sealed in a flexible plastic or rubber mould. The mould is placed in a high pressure chamber, where water transfers a high pressure evenly on the wafer and PZT thick film. The pressure decreases the PZT layer porosity and a higher density film as achieved after the following sintering. The cantilever cavities on the wafer backside were filled with silicone for the thin fragile cantilevers to withstand this CIP process. Figure 3.2a shows the silicone when removed from the wafer. Besides providing support, a better vacuum sealing was obtained for the mould. The drawback of this solution was problems with the silicone sticking to the cantilever, hence the cantilever could break when removing the silicone, or as seen in Figure 3.2b the silicone would leave a considerable amount of residuals that was difficult to remove. The effect of the CIP process is depicted in the scanning electron micrographs in Figures 3.2c to 3.2d where a PZT thick film is examined with and without the CIP process. The PZT grain size is increased while the porosity is decreased when the film is high pressure treated. The result is higher mechanical stiffness, density and piezoelectric performance if the PZT.

Despite the issues with silicone during the CIP process, the introduction of shadow mask for top electrode definition increased the fabrication yield to 75% for the high pressure treated unimorph harvester wafer seen in Figure 3.3a. This yield was unfortunately almost reduced to the half during the dicing process. For the dicing, the wafer is attached to a slightly adhesive film, and a stream of water is used in the cut line to remove material and cooling of the diamond blade. As the wafer was diced from the frontside the pressure from the water on the thin cantilever causes several devices to break, and the subsequent release from the adhesive film causes further losses. The amount of harvesters was therefore too few for reaching a clear conclusion regarding design, especially since the yield of tapered harvesters was significant lower than rectangular designs.

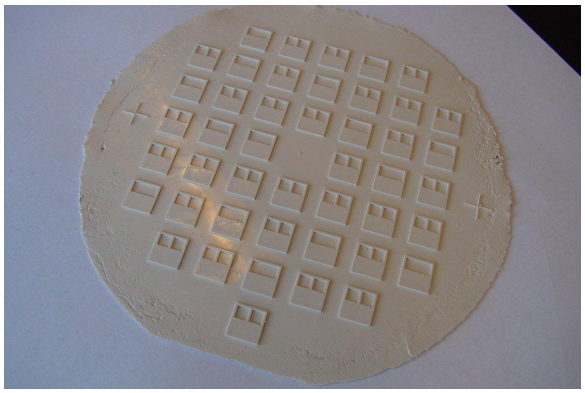

(a) *Silicone when removed from wafer.*

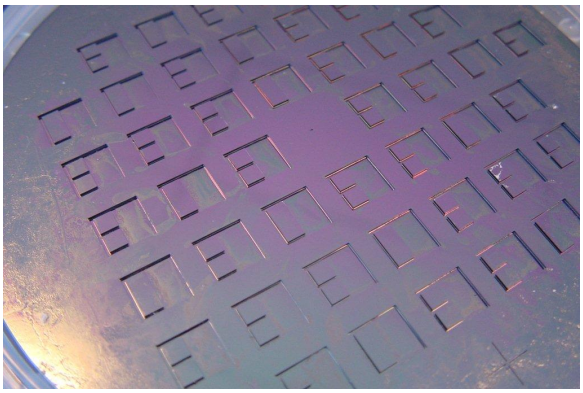

(b) *Silicone residuals on silicon wafer.*

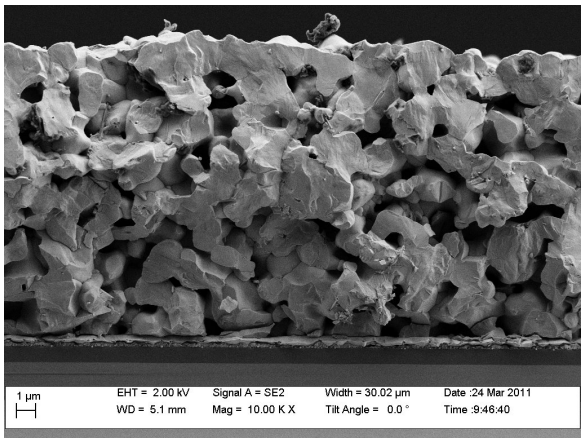

(c) *PZT without high pressure treatment.*

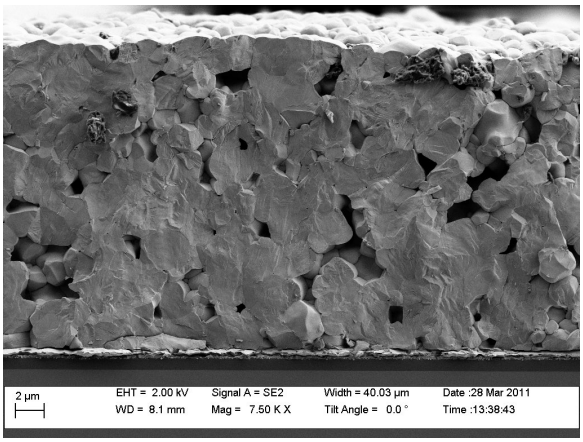

(d) *PZT with high pressure treatment.*

Figure 3.2: *High pressure treatment of the PZT thick film. (a) Silicone used to fill the cantilever cavities in the cold isostatic pressing process. (b) Besides breaking cantilevers in the removing process, the adhesion of the silicone to wafer caused a considerable amount of residuals on the wafer. (c) Scanning electron micrograph of the PZT thick film without high pressure treatment. (d) PZT layer with high pressure treatment. The PZT grain size is increased while the porosity is decreased. The result is better mechanical and piezoelectric performance.*

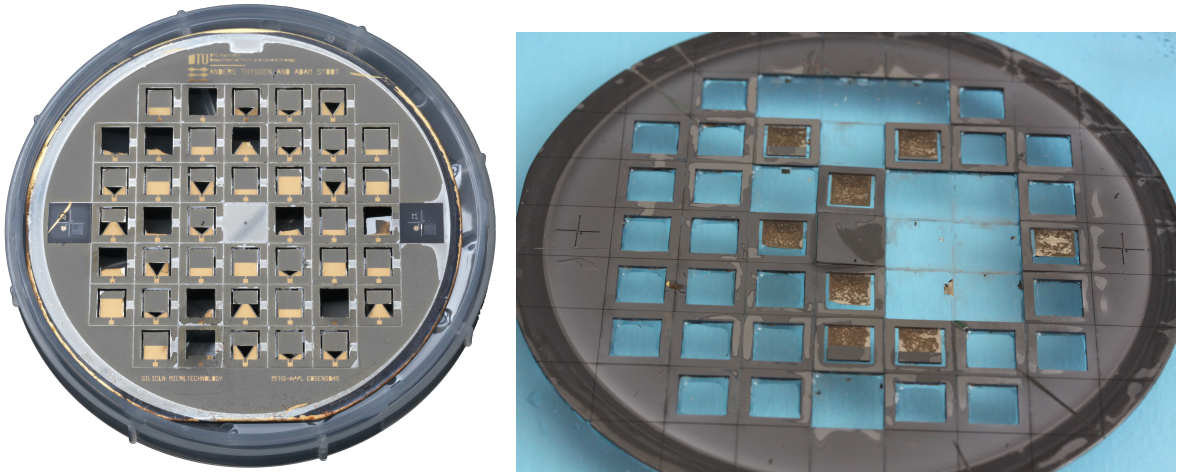

(a) *Thyssen and Stoot 2010* [38]. **(b)** *Christiansen 2010* [40].

Figure 3.3: *(a) Outcome of the unimorph fabrication process by Thyssen and Stoot with top electrode by shadow mask and high pressure treated PZT. The wafer features a wide number of design, and is yet to be diced. (b) Final result after dicing of the bimorph fabrication process by Christiansen. The first attempt to manufacture a pure PZT/PZT harvester.*

3.3.2 Christiansen 2010

Simultaneously with the work by Thyssen and Stoot, another bachelor project was carried out by Christiansen [40]. The purpose of this work was to utilise an identical fabrication process as Thyssen and Stoot for a first attempt to fabricate a bimorph harvester consisting solely of two PZT layers. Instead of frontside RIE etching of the trench, a backside RIE etch removes the silicon support needed in the screen printing, and at the same time the harvesters are released. Cross-sectional sketch of the process flow is available in Appendix B.4 on page 187. Since accurate thickness control is not needed for the sacrificial silicon support layer, the SOI wafer could potentially be replaced by a conventional silicon wafer. This would however require a timed etch in the DRIE, and hence SOI wafers were used for the fabrication. With two PZT layers, the screen printing process was performed twice with a shadow mask metallization step in between for the middle electrode. The bimorph process exposes the fragile cantilevers to two rounds of screen printing, and in combination with the dicing process, only a few chips survived as seen in Figure 3.3b. Unfortunately it was not possible to use the more dense and mechanical stable high pressure treated PZT for the bimorph harvester in the project by Christiansen.

3.3.3 Implementation of KOH Etching

To address the issue of screen printing on the fragile cantilevers with resulting low yield, the sequence of cantilever definition and screen printing was altered at this point in the process

development. Screen printing the PZT on a full wafer without cavities on the backside would eliminate several problems. The wafer would be easier to handle and the printing process would not risk breaking any devices. Secondly the silicone filling used in the CIP process would be obsolete. Defining the cantilevers dry etching after PZT deposition is difficult due to critical clamping in DRIE processes, and in a normal RIE process it would a highly time-consuming process. The natural alternative is a wet etch such as e.g. KOH. Despite the extensive time required to etch nearly through a wafer, it is a low cost process without need for advanced equipment, and it offers batch possibilities ideal for high volume production. The PZT thick film cannot withstand exposure to KOH but special types of resist exist that can be used as protection layer in KOH etch. The disadvantage of these resistant types of resist is that they are equally hard to remove afterwards. A mechanical protection of the PZT for the KOH etching process was therefore employed. This step will be further elaborated in the final fabrication process description. The result of the changed sequence with KOH etching is seen in Figure 3.4a where a wafer with full yield is pictured before the dicing process. After the dicing process a final yield of >90% was achieved. These results are published in [41] with copies in Appendix A.1 on page 131. The design featured several different tapered and rectangular designs for optimal design characterization. The lowest resonant frequencies were in accordance with theory found for the tapered cantilevers compared to the rectangular beams, while for the rectangular beams a cantilever ratio of 50% resulted in the lowest frequency. The power performance was highest for the rectangular beams over the tapered cantilevers, and the highest power was as expected achieved for a cantilever ratio of 30%, meaning that the proof mass equals 70% of the beam length. The results are published in [42] with copies in Appendix A.3 on page 141. During the characterization process, the tapered design exhibited issues with mechanical stability as transverse rotation of the mass during excitation caused fracturing at the mass anchoring. This in combination with low power performance caused tapered designs to be discarded in the remaining part of the project despite low resonant frequencies.

3.3.4 Pedersen 2011

With the improved results obtained using the KOH etching, a second attempt on fabricating bimorph harvesters was carried out in the bachelor project by Pedersen [43] in the first part of 2011. Cross-sectional sketch of the process flow is available in Appendix B.5 on page 188. With a full wafer and no fragility issues, both layers of screen printing PZT could undergo a CIP process to be high pressure treated for improved mechanical performance and stability. The design featured only rectangular cantilevers, and implemented rotation of every second row of harvesters. This design change was initiated as adhesion problems on convex corners of the PZT were periodically observed in the previous process iterations. Rotating every second row resulted in fewer convex corners, especially around the critical cantilever clamping region and electrode contact areas. Figure 3.4b shows a wafer with bimorph harvester after KOH and cantilever release but before dicing. A full yield is obtained at this point while a yield of 98% is achieved after the dicing process. Notice how the rotation causes some rows of

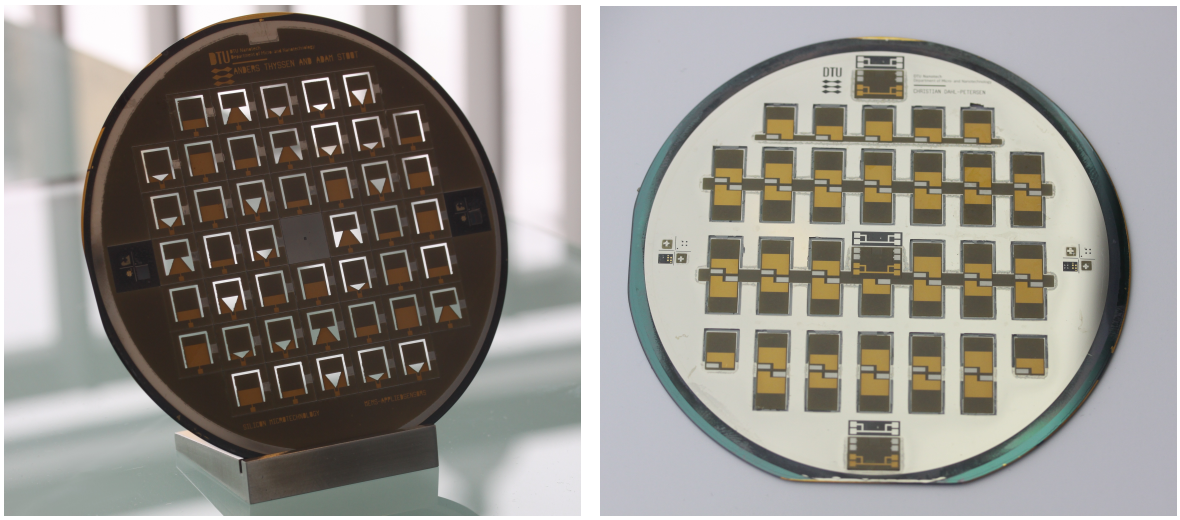

(a) *Lei et al.* [41]. **(b)** *Pedersen 2011* [43].

Figure 3.4: *(a) By replacing DRIE with KOH etching the cantilever definition could be moved in sequence to after PZT screen printing. As a result a wafer with full yield prior to dicing was achieved. (b) Successful fabrication of bimorph harvesters prior to dicing, achieved with the implementation of KOH etching.*

cantilevers to point opposite compared to the row next by.

3.4 Summary

The process development during the ELBA project has primarily focused on the technique used for cantilever and proof mass definition, and the sequence relative to the screen printing process. The first attempt used DRIE etching for the cantilever definition and subsequent screen printing. Having the etch step this early in the fabrication caused numerous fragility problems during handling, screen printing and general processing. Compared to works prior to ELBA, a shadow mask technique was implemented in replacement of lift-off for the top electrode step. This significantly improved the yield as no critical ultrasound was required, and short-circuit problems were eliminated. To address the problem of fragile cantilevers from an early stage etch, the DRIE process was replaced by and KOH etch of the cantilever cavities following after the PZT deposition. To protect the PZT in the KOH etch, a mechanical frontside protection was employed, and yields exceeding 90% was made achievable. Screen printing on a full wafer also significantly eased the process of high pressure treating the PZT film for improved density. With these progresses, bimorph harvesters consisting solely of two PZT layers were fabricated with high yield results. Testing of tapered cantilevers showed lower frequencies compared to rectangular designs, but the power was in general lower. For the rectangular design the cantilever ratio of 50% resulted in the lowest resonant frequency while a ratio of 30% achieved the highest power output, both in accordance with theoretical predictions. The following chapter will in details present the final fabrication

process developed in the ELBA project.

Chapter 4

Harvester Design and Fabrication

With the review of the process development during the ELBA project in the previous chapter, the recommended design and fabrication will be presented in the following. Initially the proposed design from the iterative experimental process will be reviewed. The focus will be on the different parameters and margins with underlying motivation. Following this, the fabrication process focusing on yield and high volume production will be outlined together with results on both unimorph and bimorph harvesters. The last part of the chapter will deal with a few issues and complications from the fabrication process, and finally a few results on lead free harvesters are presented.

4.1 Chip Design

From the theory chapter it was clear that the cantilever should be as wide and long as allowed by the volume constraints of the harvester. Theoretically a tapered design should result in lower resonant frequency and higher power compared to a rectangular cantilever. This was though not backed up experimentally during process development, and since high yield is equally essential as low frequency the tapered design is discarded. The resulting basic design for a rectangular cantilever with a cantilever to proof mass ratio of 0.5 is depicted in Figure 4.1. The figure shows a 10:1 representation of the full chip design together with a 100:1 zoom of the PZT and electrode margins and a 30:1 zoom of the geometric parameters around the electrical contact area. The design features both the unimorph and the bimorph harvester configuration and is coded in a generic T-Cell in the CAD layout editor L-Edit. The code is available in Appendix C and features variables for all the geometric parameters in the design, including cantilever to proof mass ratio and cantilever width at mass ratio for potential test of tapered designs. With frame and trench included in the allowed footprint of 10 mm × 10 mm, the maximum beam length and width is 6.5 mm and 6 mm respectively.

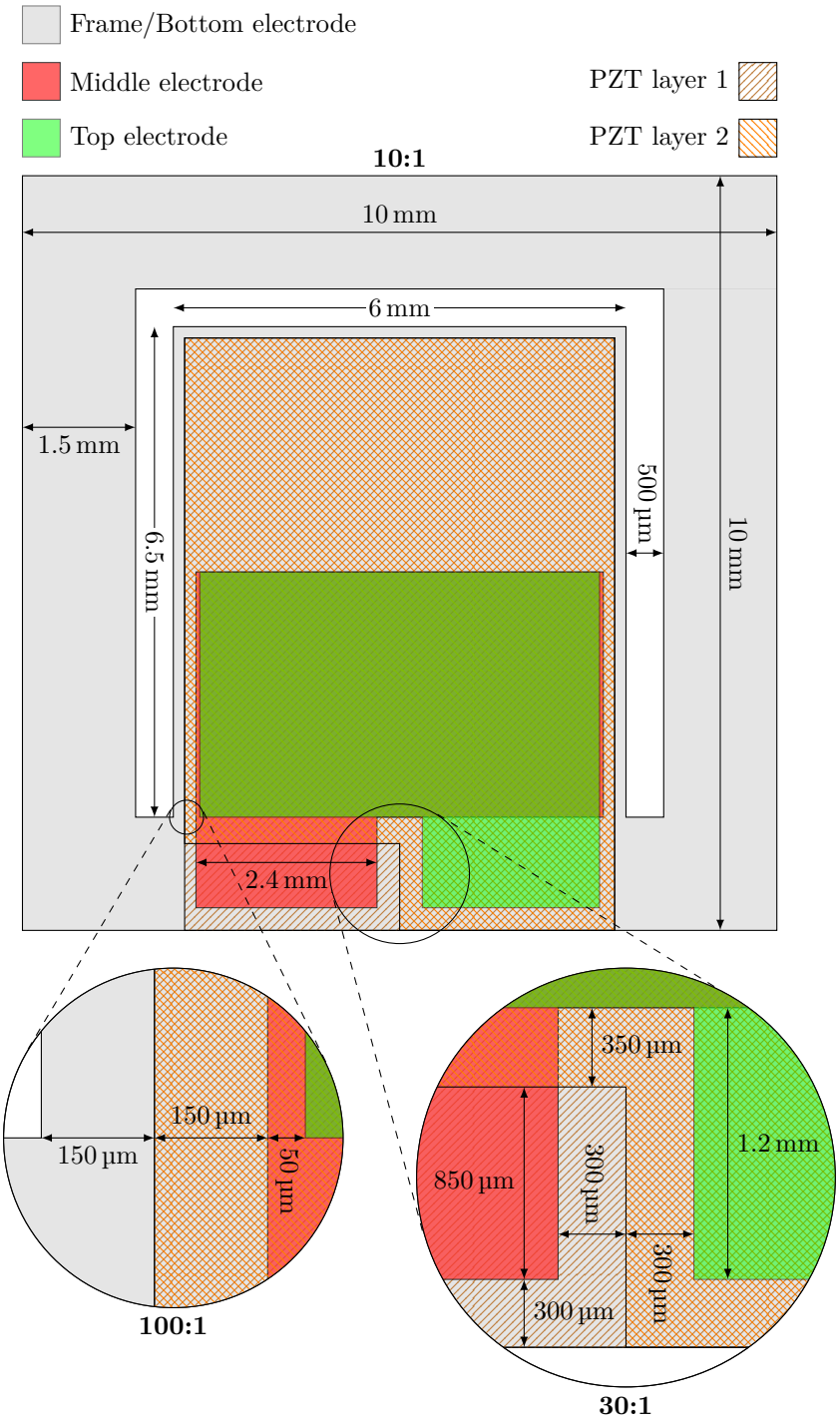

Figure 4.1: *Basic design of the ELBA harvester in 10:1 representation. The design features both the unimorph and bimorph harvester. Lower left is a 100:1 zoom of the PZT and electrode margins, and lower right is a 30:1 zoom of the geometric parameters for the electrical contact area.*

4.1.1 Margins

The equipment used for the PZT screen printing process provides an alignment precision of around 100 µm, but depending on the exact viscosity of the PZT paste, the paste can experience a minor amount of float. To prevent any PZT in the trench of the bottom electrode the margin between PZT layer and bottom electrode is set to 150 µm. The margin from PZT to middle electrode must include the alignment accuracy of both PZT and the shadow mask. Assuming that the shadow mask accuracy is better than 50 µm, the PZT to middle electrode margin is 150 µm to prevent short circuiting the middle and bottom electrode. The final margin between middle and top electrode is set to 50 µm which should prevent short circuiting in worst case alignment scenarios.

The contact pads to middle and top electrodes are comprised by rectangles of $2.4\,\text{mm} \times 1.2\,\text{mm}$ which are extended over the frame. The power output of the harvester is inversely proportional to the PZT layer capacitance, accordingly the electrode area outside the active area on the thin cantilever should be minimised. Meanwhile, must the contact pads be easy accessible for the back-end processes of poling, characterization and eventual packaging. The contact pads are designed so that electrical contacts can be obtained with both spring connectors and conducting glue. In the printing of the second PZT layer for the bimorph harvester a region of 1.15 mm from bottom chip is left open for contact to middle electrode. The transverse distance between middle and top electrode contact pad area is $2 \times 300\,\mu\text{m}$. Photographs of the final fabricated unimorph and bimorph harvesters are seen in Figure 4.10.

4.1.2 KOH Etch Compensation

The anisotropic nature of the KOH etch with etch rate depending on crystal planes must be accounted for in the mask. If the backside cavity etch was a mirror of the frame and proof mass, the convex corners of the proof mass would be rounded, but furthermore the trench width of 500 µm would not be sufficient for etching to a depth of 500 µm. The problem is sketched in Figure 4.2a where the left etch opening has stopped in a {111}-plane ditch. Defining the width of the trench to W_T the opening in the mask must be this width and in addition twice the width (W_b) of the sloped {111}-planes after the etch have reached the desired depth H. The etched width W_b can be found from the plane angle ($\tan 54.7^\circ = \sqrt{2}$) as $W_b = H/\sqrt{2}$ which is $\approx 350\,\mu\text{m}$ for a 500 µm thick wafer. Figure 4.2b illustrates the resulting KOH compensated distance between proof mass and frame in a top view. The last part of the KOH etch design is the convex corner compensation of the proof mass. Numerous different corner compensation structures have been presented in literature [44, 45], one of the simplest is the pointy corner structure seen in Figure 4.2b. The width of the corner compensation must be twice the desired etch depth H and the length should as minimum by 1.6 times the width of the structure. With a desired etch depth of 500 µm the length of the corner compensation hence becomes 1.6 mm.

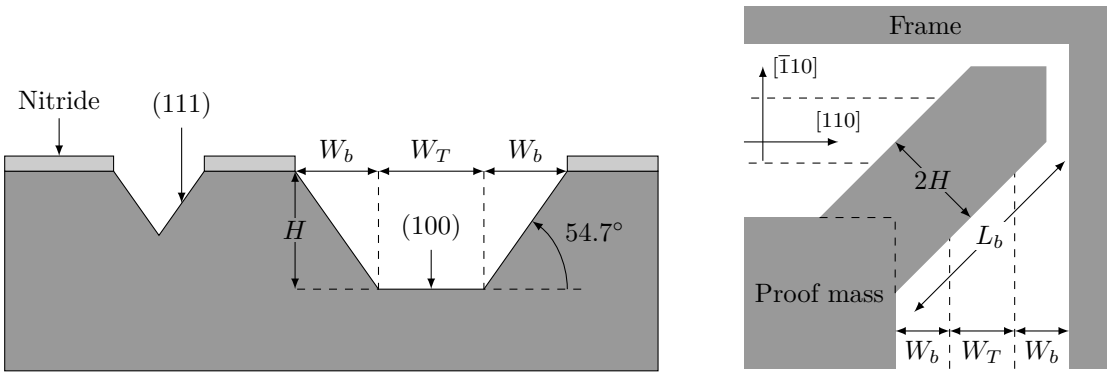

(a) *KOH etch on (100) Si wafer.* **(b)** *Convex corner compensation.*

Figure 4.2: *(a) Side view sketch of the anisotropic KOH etch. The left part shows how a too small opening causes the etch to stop in a* $\{111\}$*-plane ditch. The etch width* W_b *can be expressed as* $H/\sqrt{2}$ *and must be account for when designing the KOH etch mask. (b) Top view illustration of the compensated proof mass to frame distance and the convex corner compensation. The length of the compensation structure should as minimum be 1.6 times the width of the structure.*

4.1.3 Final Set of Lithography and Screen Printing Masks

The final set of lithography and screen printing masks are seen in Figure 4.3. For the unimorph harvester (Figure 4.3h) the fabrication process consist of three conventional mask steps Figure 4.3(a),(b) and (g), one screen printing mask Figure 4.3(c) and one shadow mask step Figure 4.3(f). The fabrication of the bimorph harvester features two conventional mask steps Figure 4.3(a) and (b), two screen printing masks Figure 4.3(c) and (e) and two shadow mask steps Figure 4.3(d) and (f).

4.2 Harvester Fabrication

The review of fabrication process will be based on the steps sketched in the cross-sectional process flow in Figure 4.4. The process flow illustrates the fabrication of the unimorph harvester, but its bimorph counterpart will be included in the review as well. Finally, recommendations for minimising losses in the dicing process will be given.

4.2.1 (a) Substrate

All of the fabrication iterations presented in the process development chapter were based on SOI wafers. The advantage of the SOI wafer, whether dry or wet etching is used, is the buried oxide which functions as a build-in etch stop layer. For the unimorph harvester the thickness of the silicon support can be precisely controlled, and for both configurations the etch process itself is eased as no exact timing is required. The SOI wafer is however

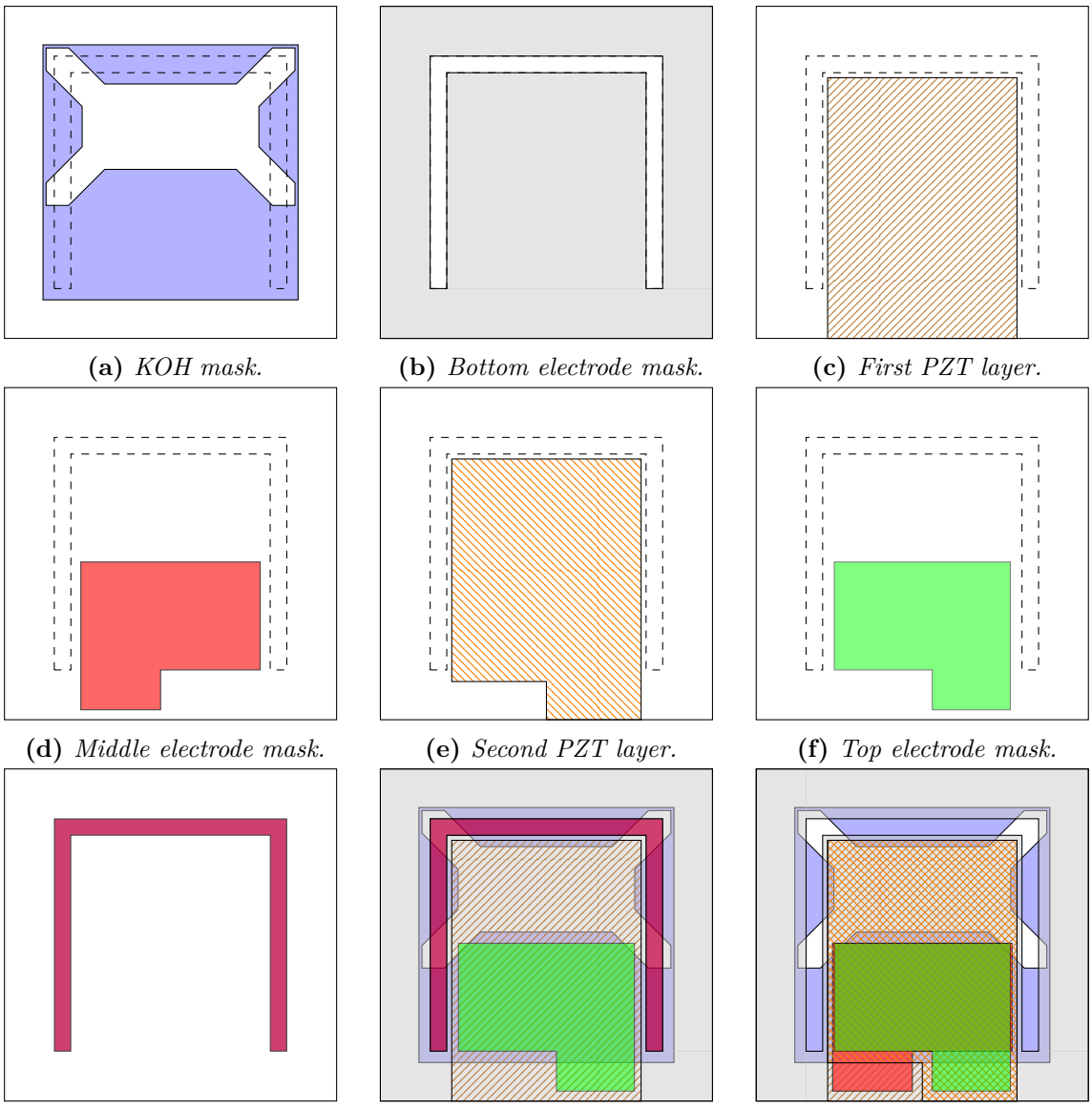

(a) *KOH mask.* **(b)** *Bottom electrode mask.* **(c)** *First PZT layer.*

(d) *Middle electrode mask.* **(e)** *Second PZT layer.* **(f)** *Top electrode mask.*

(g) *Trench etch mask.* **(h)** *Full unimorph process.* **(i)** *Full bimorph process.*

Figure 4.3: *Final set of lithography and screen printing masks used in the ELBA harvester fabrication process. The dashed line indicate the opening in bottom electrode equal to the expected cantilever size after KOH etch. The unimorph process (h) consist of three conventional mask steps (a),(b) and (g), one screen printing mask (c) and one shadow mask step (f). The bimorph process (i) consist of two conventional mask steps (a) and (b), two screen printing steps (c) and (e) and two shadow mask steps (d) and (f).*

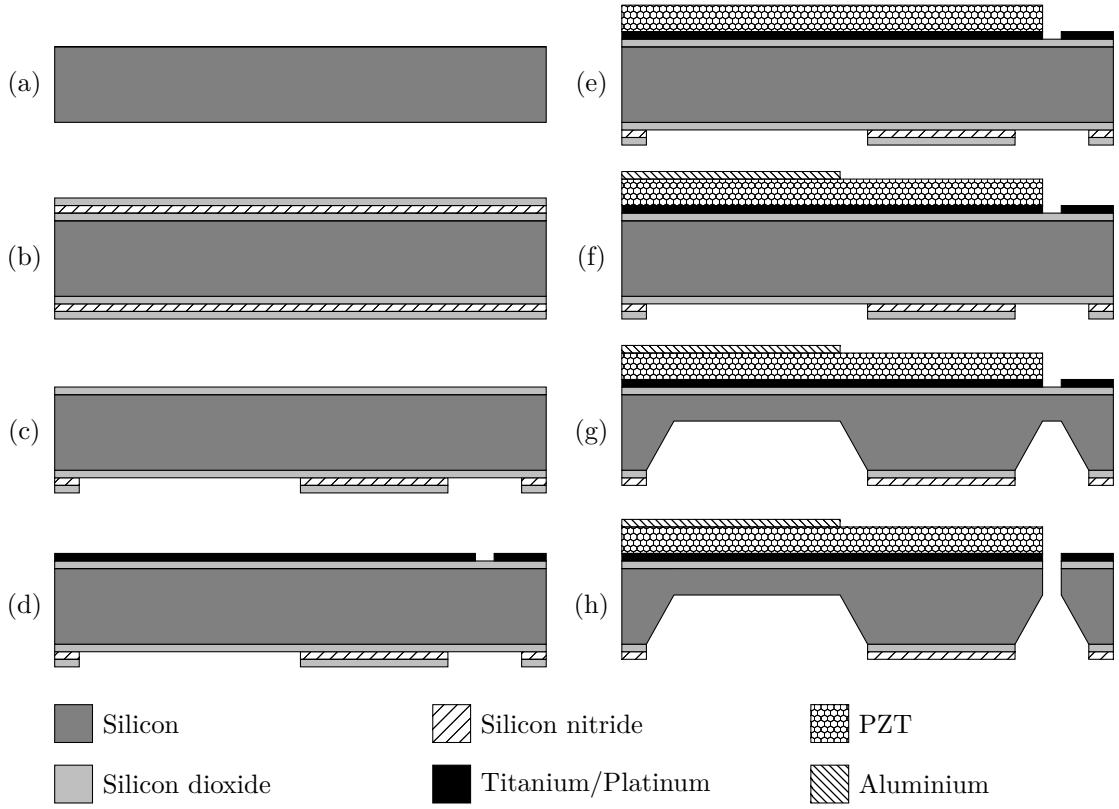

Figure 4.4: *Cross-sectional sketch of the process flow for the unimorph harvester. (a) Double side polished* 4″ 500 µm *thick silicon wafer. (b)* 1000 nm *thick thermal oxide,* 170 nm *LPCVD stoichiometric nitride and* 300 nm *LPCVD TEOS based oxide. (b) KOH etch openings in nitride defined with UV lithography, BHF and phosphoric acid. (d) Bottom electrode of* 50 nm *titanium and* 500 nm *platinum deposited with e-beam evaporation and patterned with etch in nitric acid hydrochloride. (e) Screen printing of PZT thick film. (f) E-beam evaporation of* 600 nm *aluminium top electrode with shadow mask technique. (g) Cantilever and proof mass definition in KOH etch with mechanical frontside protection. (h) Cantilever release with RIE etching of the trench.*

considerable more costly compared to a conventional silicon wafer. With cost reduction as the governing factor the presented fabrication process is based on a conventional wafer. The loss of accurate thickness control for the unimorph harvester is at the moment less important as subsequent frequency adjustment is required. The starting point for the process is therefore a conventional double side polished 4″ wafer of 500 µm thickness. The doping type and level is irrelevant for the application, and should hence only be taken into account for specific equipment limitations.

4.2.2 (b) Thin Film Growth and Deposition

The silicon surface is covered with a 1000 nm silicon dioxide (SiO_2) from a wet thermal oxidation process. This is followed by a low-pressure chemical vapour deposition (LPCVD) of 170 nm stoichiometric silicon nitride and a LPCVD deposition of 300 nm SiO_2 based on tetraethyl orthosilicate (TEOS). The relatively thick thermal oxide functions as part of a diffusion barrier between the silicon substrate and the lead containing PZT for the high temperature sintering process. The nitride layer is used as masking layer for the KOH etching process after the PZT screen printing, while the TOES is used for masking material in the nitride patterning step.

4.2.3 (c) Nitride Patterning

With UV lithography on the wafer backside, the pattern (Figure 4.3a) for the later cantilever and proof mass definition in KOH is defined in photoresist. With the photoresist as masking material, the pattern is transferred to the TEOS based SiO_2 in a buffered hydrofluoric (BHF) etch. The frontside TEOS based SiO_2 is in this step also removed. The photoresist is stripped and the KOH pattern is transferred to the nitride in a hot phosphoric acid etch. With no protection on the frontside the nitride is fully removed and only the thermal oxide remains. Figure 4.5a shows the wafer backside with openings in the nitride for later KOH etching.

4.2.4 (d) Bottom Electrode

The bottom electrode serves two purposes, it provides one of the two electrodes comprising the active PZT region and it functions as a diffusion barrier. During the PZT sintering process, the wafer and PZT is heated to above 800 °C. At this temperature the diffusivity of both silicon and the lead in the PZT is increased and mixing is prone to occur. With lead diffusion into the silicon and vice versa, the adhesions between the silicon, electrode and PZT are affected negatively and the piezoelectric properties of the PZT are reduced. To limit this mixing by diffusion a layer of titanium and platinum is used. The titanium is used as adhesion layer while the thermally stable and little reactive platinum is used for the barrier [46]. The effectiveness of the diffusion barrier depends on the thickness of the platinum layer as diffusion cannot by avoided but only reduced. From a study of this effect

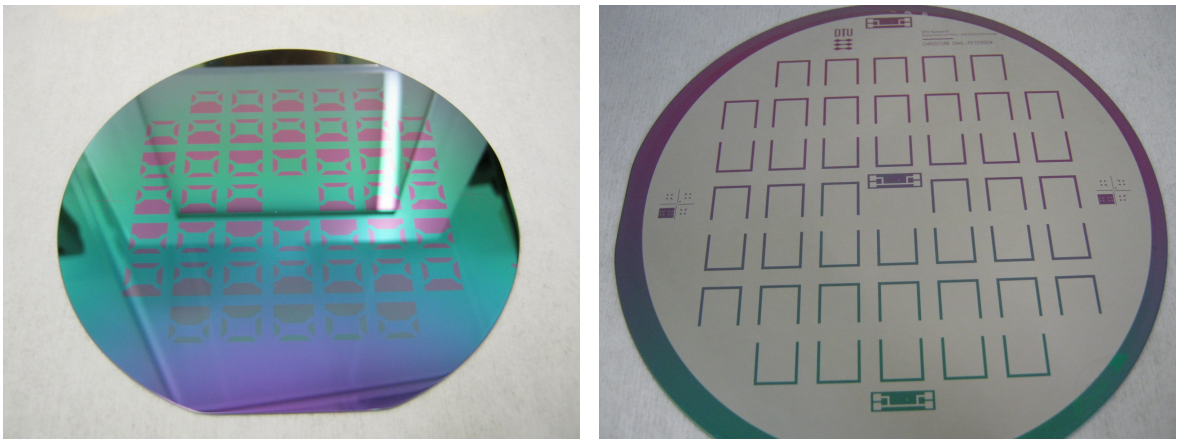

(a) *Backside openings in nitride.* **(b)** *Patterned bottom electrode.*

Figure 4.5: *(a) Patterned nitride on the wafer backside with openings for the KOH etch process for cantilever definition. Wafer frontside with bottom electrode consisting of* 50 nm *Ti and* 500 nm *Pt. The electrode pattern is resolved with a metal etch, and functions as both diffusion barrier and one of the two electrodes comprising the active PZT region.*

in [35] it was concluded that a platinum layer of 500 nm is required for adequate prevention of the diffusion and mixing. The most common approach of metallization is to use a lift-off method for patterning. Evaporation of 500 nm platinum however involves a substantial heating of the substrate. With this extensive heating the photoresist becomes burned with risk of cracks to evolve. The burned photoresist is challenging to dissolve in the lift-off process and hence a solution with a metal etch after evaporation is used. With the metal deposited, UV lithography followed by a wet etch in nitric acid hydrochloride is used to pattern the bottom electrode layer (Figure 4.3b). The patterned bottom electrode is depicted in Figure 4.5b.

4.2.5 (e) PZT Screen Printing

The next step in the fabrication process is the PZT screen printing with the pattern in Figure 4.3c. The principle of screen printing is sketched in Figure 1.6 on page 9. The process is carried out by the project partner Meggitt Sensing Systems with the equipment shown in Figures 4.6a to 4.6b. The PZT thick film of type TF2100 (Datasheet available in Appendix D.1) is printed in layers with intermediate heating steps until the desired thickness is achieved. The wafer and PZT thick film is then high pressure treated and finally sintered at a temperature around 850 °C. A wafer with high pressure treated screen printed PZT is depicted in Figure 4.6c. Despite the 500 nm thick platinum layer, the effect of the combination between lead and high temperature in the sintering process is visible in Figure 4.6d. Electrode areas near PZT are altered compared to areas further away from the PZT. This effect can in severe situations result in decreased adhesion later in the process.

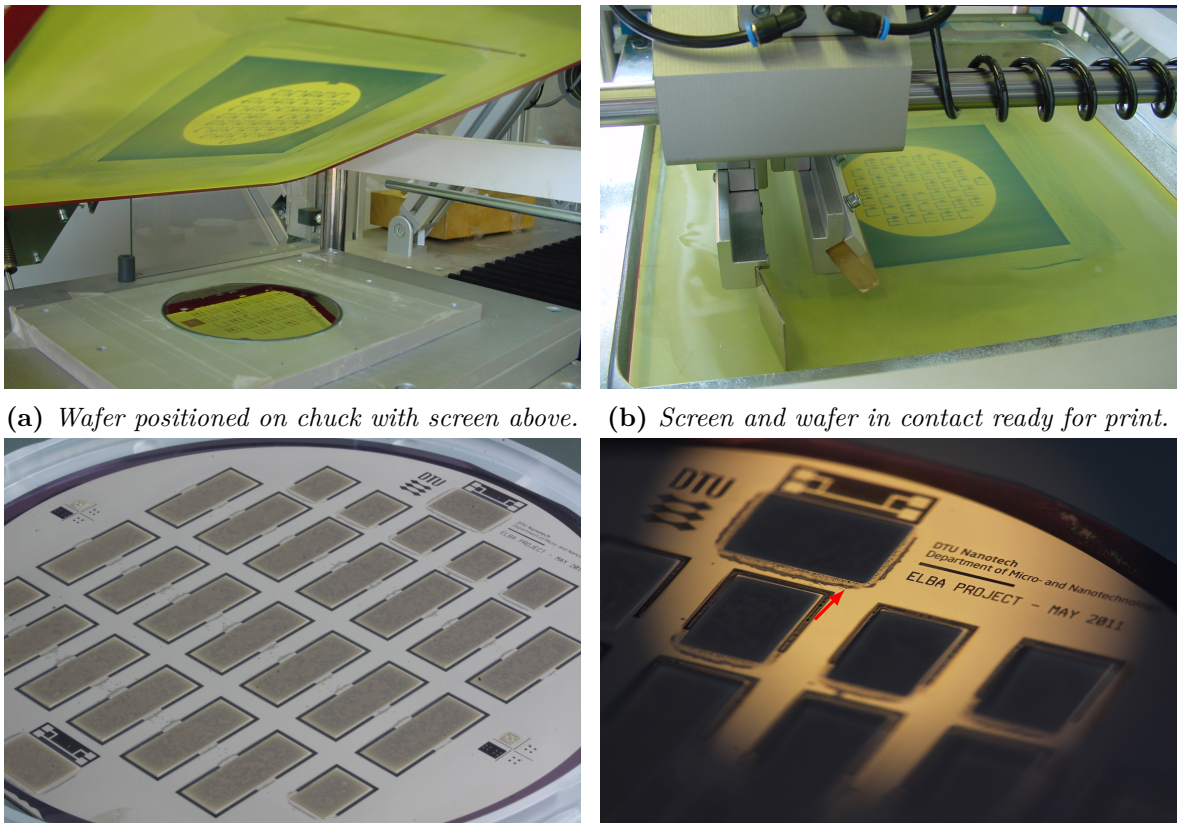

(a) *Wafer positioned on chuck with screen above.*

(b) *Screen and wafer in contact ready for print.*

(c) *PZT screen printed wafer.*

(d) *Zoom of affected bottom electrode.*

Figure 4.6: *(a) and (b) Screen printing equipment used at Meggitt Sensing Systems. The wafer is positioned, pre-aligned and fastened to a chuck with vacuum. The screen is brought in contact with the wafer and the squeegee presses the paste through the screen. (c) and (d) Screen printed PZT on wafer with rotated design configuration. (d) Arrow indicate the areas of the bottom electrode next to the PZT which are affected by the combination of lead and high temperature sintering.*

4.2.6 (f) Top Electrode

The shadow mask for the top electrode is fabricated separately by transferring the electrode pattern (Figure 4.3f) into a wafer with a DRIE process. The shadow mask is fabricated on a 4″ silicon wafer with a thickness of 350 µm. The thickness, which is less than standard silicon wafers, is selected as the shadow mask inevitable will cause shading effects in the metal evaporation. Assuming that the area where the e-beam strikes the crucible can by treated as a point source the shading effect can be estimated from

$$\frac{\text{wafer radius}}{\text{wafer to crucible distance}} = \frac{\text{shading distance}}{\text{shadow mask thickness}} \tag{4.1}$$

The e-beam evaporation is performed in a Wordentec QCL 800 which has an approximate source distance of 0.5 m. With this, the shading distance is 3.5 µm for the 350 µm thick shadow mask. The fabricated shadow mask is depicted in Figure 4.7a, with the holes for evaporation clearly visible. The disadvantage of a shadow mask compared to the conventional lift-off is the alignment precision. Using the etched holes, the shadow mask is positioned and aligned manually under a microscope as seen in Figure 4.7b. The precision of this manual positioning is seen in Figure 4.7c where the alignment errors for left and right marks are plotted for 33 wafers. In general the error is less than 40 µm and hence the shading distance of the shadow mask is significantly less than the alignment precision. The margin required to encompass this lack of precision is though still orders of magnitude smaller than the electrode area (Figure 4.7d), hence the advantages of shadow masks outnumbers the significant lack of precision compared to conventional mask alignment.

The PZT layer, on top of which the top electrode is deposited, has in silicon processing terms a high surface roughness of 1 µm to 3 µm [30]. To obtain a uniform conducting electrode the metal thickness must be sufficient enough to cover the surface roughness. The surface roughness and required metal thickness was studied in [46] with the conclusion that the top electrode thickness must exceed 500 nm. No heating processes exist in the remaining part of the fabrication process, hence aluminium is used with a thickness of 600 nm. For the bimorph harvester configuration the steps of screen printing and electrode deposition are conducted twice. After the first PZT layer a middle electrode (Figure 4.3d) is deposited with shadow mask technique. As this electrode will undergo a high temperature process in the sintering of the second PZT layer (Figure 4.3e), this layer is comprised of 500 nm platinum. The top electrode deposition is identical to that for the unimorph harvester. Figure 4.7d shows a unimorph harvester wafer with a top electrode consisting of 500 nm aluminium with 100 nm gold deposited through a shadow mask.

4.2.7 (g) KOH Etching

The next step in the fabrication process is the critical KOH etching for the cantilever and proof mass definition. To protect the frontside in the etch a tandem wafer holder from Advanced Micromachining Tools is used (Appendix D.2). The wafer holder which is manufactured in

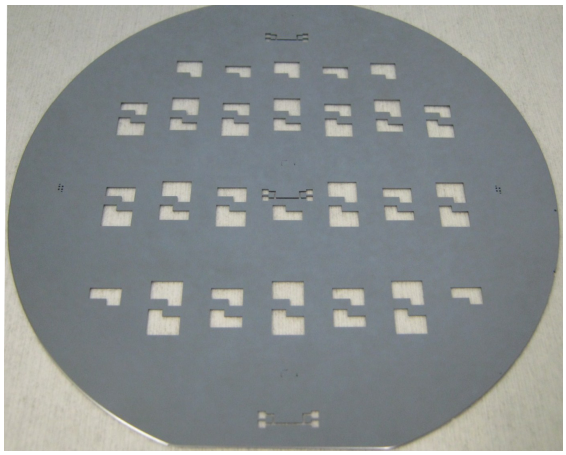

(a) *Shadow mask for top electrode.*

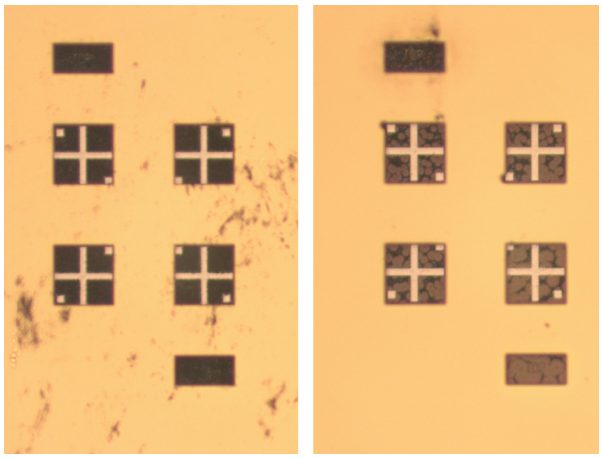

(b) *Left and right shadow mask alignment.*

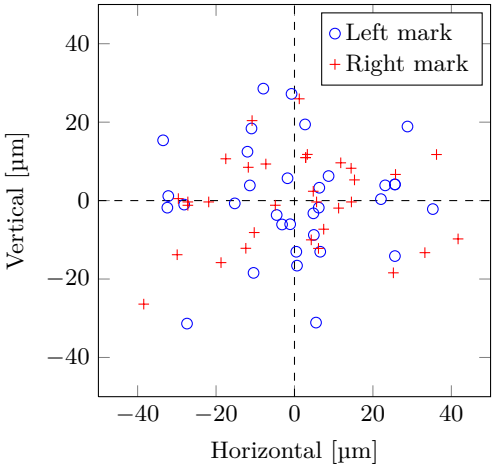

(c) *Alignment precision.*

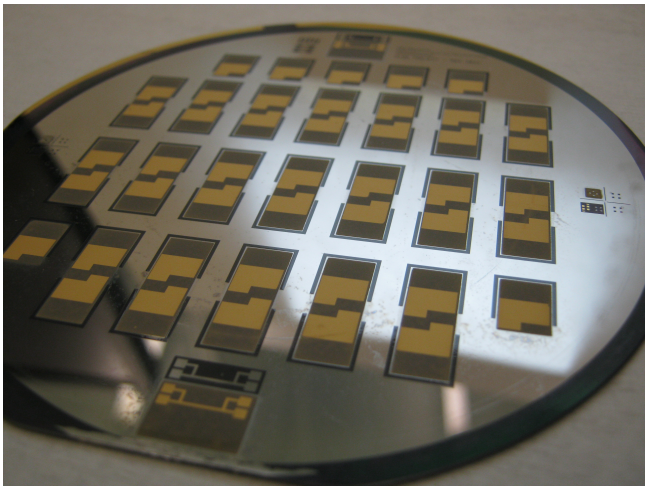

(d) *PZT with top electrode.*

Figure 4.7: *Top electrode deposition. (a) Shadow mask used for patterning of top electrode instead of commonly used lift-off. The mask is fabricated with DRIE in a* 350 µm *thin silicon wafer to reduce shading effects in the metal evaporation. (b) Using the etched holes in the wafer, the shadow mask is aligned to alignment marks on the substrate. The square openings in the shadow mask are* 350 µm × 350 µm*. (c) Obtained alignment precision of the shadow mask patterning method. (d) Wafer with thick film PZT and shadow mask patterned top electrode.*

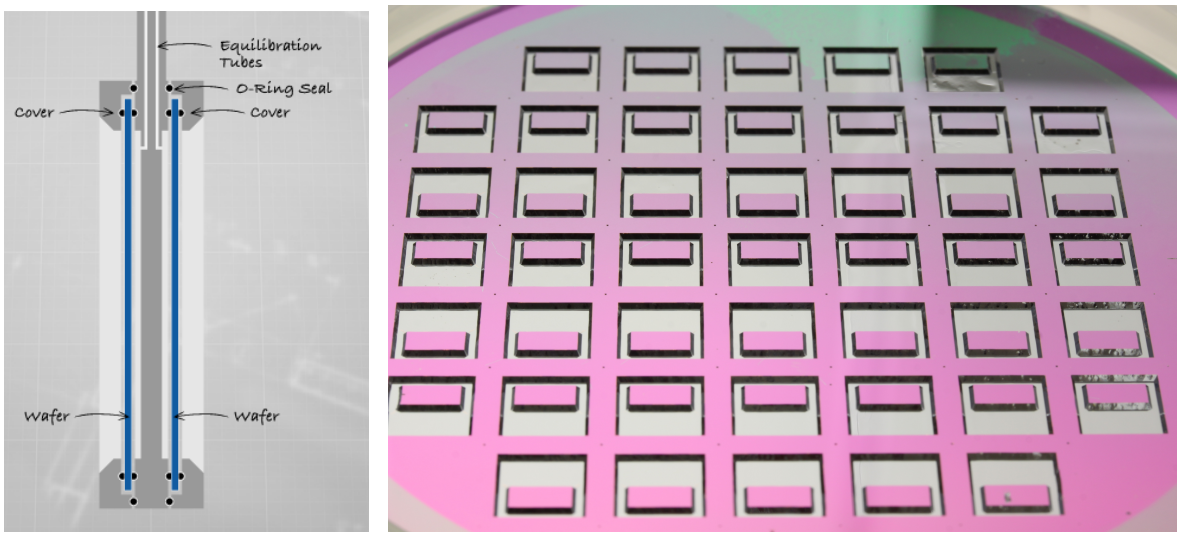

(a) *Mechanical protection.* **(b)** *Wafer backside after KOH etch.*

Figure 4.8: *(a) Wafer holder for mechanical protection of the wafer frontside in the KOH etching for cantilever and proof mass definition. The holder from Advanced Micromachining Tools can hold two wafers simultaneously, and uses three o-rings to seal of the protected wafer side. Equilibrium tubes through the holder handle is used to equalise the pressure difference with water, which is especially important at the end of the etch. Picture is from Appendix D.2. (b) Photography of the resulting wafer backside after KOH etching.*

polyether ether ketone (PEEK) is sketched in Figure 4.8a. Using a cover that is fastened by six screws the wafer frontside is sealed of using three o-rings. The cavity on the protected side of the wafer is filled with water through tubes in the handle. This pressure equalisation is especially important at the end of the etch process where the cantilevers are thin and increasingly fragile. Once the wafer is situated in the holder the 1 µm thick thermal oxide in the nitride openings is removed in BHF and the silicon is etched in the anisotropic KOH etch process. The KOH is a 28 wt% mixture heated to 86 °C for high etch rate. If using a SOI wafer the buried oxide layers acts as an etch stop layer, and with a significant decrease in bubble formation it is clearly visible when the etching is complete. For conventional wafers it is necessary to follow the etch with both timing and intermediate thickness measurements. The etched wafer backside is depicted in Figure 4.8b. At the perimeter of the wafer a rim of a few millimetre is clearly visible. The rim indicated the position of one of the two outer o-rings in the holder. The small structures at each harvester corner are marks for the dicing process later.

4.2.8 (h) Cantilever Release

With the cantilever and proof masses defined in the KOH etch, the final silicon processing step is the cantilever release. The wafer frontside is covered with 10 µm thick photoresist

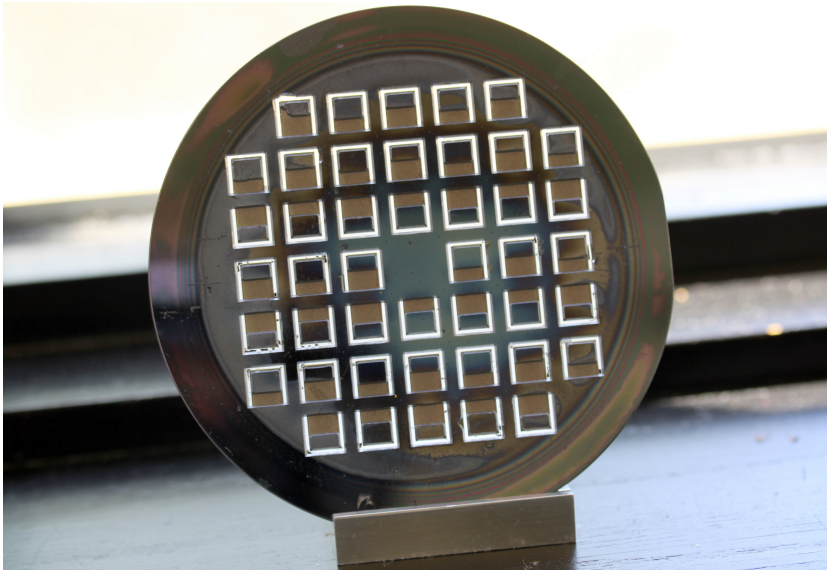

Figure 4.9: *Photograph of the backside of a wafer with bimorph harvesters after RIE etching. Compared to the wafer backside after KOH etching in Figure 4.8b it is clear that the silicon support is etched in the RIE process, leaving only two layers of PZT as cantilever. The etch of the silicon support also releases the cantilevers from the device frame.*

repeated twice to ensure a reasonable conformal coating of the thick PZT areas. For the unimorph cantilever, the photoresist in the trench is removed with UV lithography (pattern in Figure 4.3g), and the thick thermal oxide in the trench is etched in BHF. In a RIE process the cantilevers are finally released by etching through the silicon in the trench from the wafer frontside. For a wafer with bimorph harvesters, the frontside is covered with photoresist in an identical step as the unimorph harvester. This prevents potential equipment contamination in the following RIE process where the silicon support and also trench is etched from the wafer backside. The frontside photoresist is removed in a plasma ashing, and the wafer is ready for the final dicing process. A successful release etch of a wafer with unimorph harvester is depicted in Figure 3.4a on page 49, while Figure 4.9 depicts a successful RIE etch of a wafer with bimorph harvesters. Besides releasing the cantilevers from the device frame, the silicon support is etched in the process as well leaving only the two PZT layers as cantilever. That the silicon support is removed for the bimorph wafer in Figure 4.9 is visible from the clear color and surface change when comparing with the wafer backside after KOH etching in Figure 4.8b.

4.2.9 Dicing

The last step in the fabrication, and the first step in the back-end processing, is the dicing of the wafer into individual chips. With the cantilevers released the harvesters are in their most fragile state, and thus the dicing process is not straightforward. The equipment available

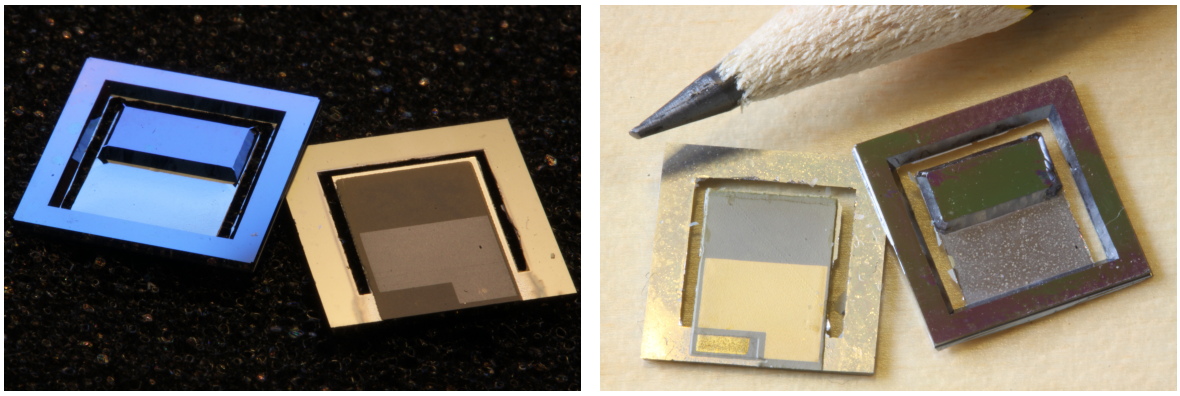

(a) *Final unimorph harvester.* **(b)** *Final bimorph harvester.*

Figure 4.10: *Final fabricated and diced harvester devices. (a) Front- and backside of the unimorph harvester. The cantilever is fully covered with PZT, while the top electrode only covers the thin cantilever part of the beam. The bottom electrode is extended to the entire frame. (b) Front- and backside of an bimorph harvester consisting solely of two PZT layers with a middle electrode in between. Notice how the cantilever on the backside is rough and dim on the unimorph harvester while the silicon on the unimorph in (a) is shiny.*

is a DISCO DAD 321 Automatic Dicing Saw and in a usual dicing process the substrate is placed on a stretched slightly adhesive film which again is clamped to the dicing chuck with vacuum. After dicing, typically from the frontside, to a depth leaving 130 µm of substrate remaining, the adhesive film is peeled off and the individual devices are released by breaking the remaining substrate. This approach was used in the first couple of fabrication iterations, but the loss of devices was quite significant during the dicing as the wafer was cut from the frontside, but also the later separation from the adhesive film was problematic. In the recommended process the wafer is placed with the frontside towards the adhesive film, the cutting is thereby performed from the backside eliminating the risk for the cut line water stream to break the thin cantilever. The dicing depth should be aimed so that around 100 µm silicon is remaining as this reduces the force needed to break the individual devices apart. For the separation from the adhesive film, the wafer is placed in a Petri dish with the film facing up and immersed in acetone. The acetone cause the film to loose the adhesion and roll up after which the film can be removed manually without risk of breaking cantilevers. The final fabricated and diced harvester is seen in Figure 4.10 with front- and backside of both a unimorph and bimorph harvester.

4.3 Complications and Future Work

The fabrication process just reviewed is developed from numerous iterations and fabrication attempts. While it in most cases result in successful fabricated wafers with yields of more than 90%, there are a few issues and complications that can affect the fabrication negatively. The

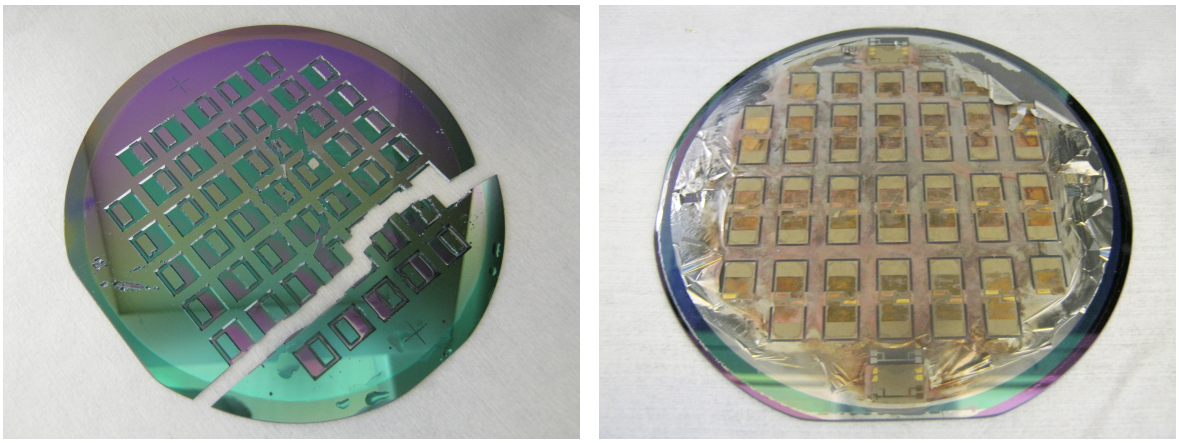

(a) *Wafer fracture and nitride defects.* **(b)** *Frontside exposed to KOH.*

Figure 4.11: *Defects that can occur in the KOH etching process. (a) Once the cantilevers are defined the wafer becomes frail and fractures can arise when the wafer is removed from the tight sealing with the o-ring. This risk is increased by the occurrence of nitride defects also visible in (a). Small defects in the nitride can result in unwanted etching of harvester frames, proof masses and wafer rim. If the defects occurs in alignment with the etched cavities, the risk of wafer fracture is increased. (b) If the wafer frontside is not sealed properly to the etch bath, the KOH will damage the electrodes and PZT.*

two main reasons for an unsuccessful fabrication is a failed KOH etch and adhesion problems between bottom electrode and silicon. This section will present a few ideas on future work concerning the fabrication.

4.3.1 Failed KOH Etching

The wafer backside seen in Figure 4.8b is the result of a successful KOH etch process. There are however several different factors that can lead to an unsuccessful etch with complete loss of the wafer as consequence. To obtain a good sealing of the wafer frontside, the screws forcing the cover onto the wafer and o-rings are strongly tightened. This in combination with the lengthy heating during the etch causes the inner o-ring and wafer to stick quite tightly. The removal of the wafer is therefore not trivial as the wafer at this time is frail due to the large cavities on the backside.

An unsuccessful wafer release from the o-ring is seen in Figure 4.11a where the wafer is broken into two parts due to a large fracture in the wafer. The removal process can be eased by applying a slight overpressure on the wafer frontside through the equilibrium tubes. This prevents the development of vacuum pockets in the cavity between wafer and holder. The unsuccessful release in Figure 4.11a also illustrates how defects in the protective nitride layer can cause unwanted etching of harvester frames, proof masses and wafer rim. Besides ruining a few devices by etching the frame and anchoring, the defects can if aligned with fragile directions on the wafer increase the risk of critical fractures to arise.

Figure 4.11b depicts another unsuccessful KOH etch process. On this wafer the frontside was not sealed properly, and hence electrodes and PZT layers have been exposed to KOH. The bottom and top electrodes are severely damaged, while the PZT is not yet visibly damaged as the etch was stopped when the sealing was broken. If KOH enters the frontside bubbles are formed which will be visible at the outside entrance of the equilibrium tubes.

4.3.2 Adhesion Issues

The second severe issue that can heavily affect the fabrication outcome is adhesion problems between the bottom electrode and the substrate. The issue arises mainly for the unimorph harvester in the cantilever release step. Before releasing the cantilever in the RIE process it is necessary to remove the oxide in the trench with a BHF etch. Under normal circumstances etching of a 1 µm thermal oxide is straightforward but in this case it is complicated by lead contamination. During the high temperature sintering process, lead can diffuse into the exposed silicon and oxide in the 500 µm wide trench opening of the bottom electrode/diffusion barrier.

Figure 4.12a shows how the contamination is clearly visible under an optical microscope where it shows up as domains with radial patterns on the oxide surface. This effect is also reported in [47]. Prior to the ELBA project, this oxide contamination has been studied with topography analysis in [34] showing a height variation of 2.6 µm and with energy dispersive x-ray spectroscopy (EDX) in [37] showing a high amount of lead on the oxide surface after the sintering process. The same trench location as seen in Figure 4.12a is depicted in Figure 4.12b after a 15 minutes BHF etch which should be sufficient for etching the 1 µm thermal oxide. The trench is then etched in RIE for 120 minutes and depicted in Figure 4.12c. Even though 60 minutes of RIE should be sufficient for etching the remaining 20 µm of silicon, the trench in Figure 4.12c is not etched through. The lead contamination complicates the BHF etch as 15 minutes is not sufficient to remove the oxide. Figure 4.12d shows a wafer after a 45 minutes BHF etch. The color of the trench have turned from the dark color seen in Figures 4.6c to 4.6d on page 59 to white indicating that the majority of the oxide is removed. As a consequence of the prolonged BHF etch, the bottom electrode is peeled off on a large part of the wafer. The problem is believed to arise from under-etching of the bottom electrode in BHF. If the BHF solution during the prolonged etching gets in contact with the bottom electrode, the titanium adhesion layer will be etched with increased rate due to creeping between the layers. If in addition parts of the titanium is oxidised to titania in the high temperature sintering process, the etch rate is further increased. Throughout the project a margin of 5 µm between the bottom electrode and the opening in the photoresist for the trench etch has been used. This should be sufficient with regard to alignment precision from a conventional mask process, but with the prolonged BHF etch time it is likely that the margin is insufficient for keeping BHF and bottom electrode apart. The margin has been increased to 100 µm in the latest design iteration, but it has not yet been possible to evaluate the effect.

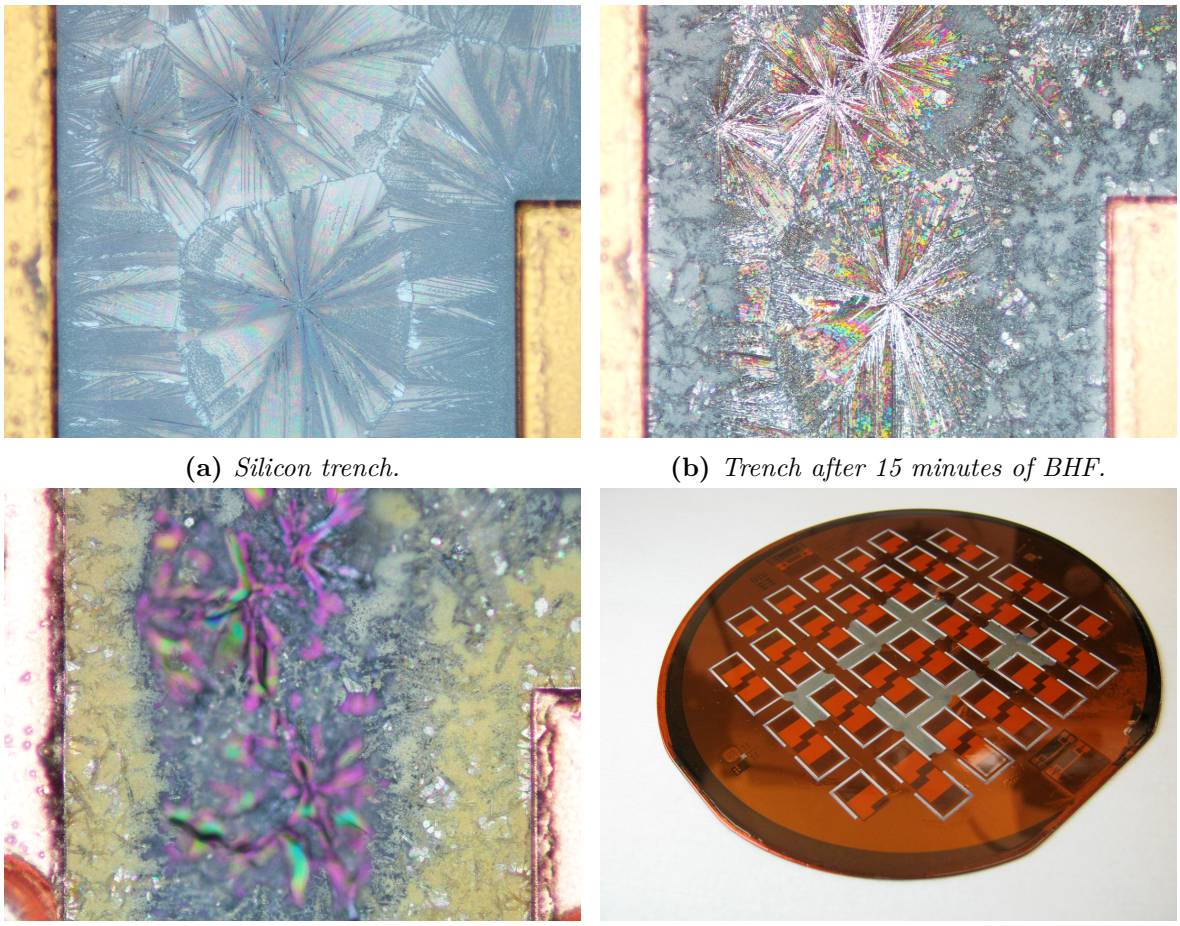

(a) *Silicon trench.*

(b) *Trench after 15 minutes of BHF.*

(c) *Trench after 120 minutes of RIE.*

(d) *Adhesion issues after 45 minutes of BHF.*

Figure 4.12: *Trench contamination and resulting adhesion problems. (a) The high temperature sintering process of the PZT thick film causes lead to diffuse into the exposed* 500 µm *wide trench openings of the bottom electrode/diffusion barrier. The contamination is visible as domains with radial patterns on the oxide surface. (b) Despite of 15 minutes of BHF etch which should be sufficient to etch the* 1 µm *thick oxide, the contamination is still clearly visible. (c) Even though a RIE time of 60 minutes should be sufficient to etch the remaining* 20 µm *of silicon, the trench is clearly not successfully etched. The oxide layer is not sufficiently removed in the BHF etch. (d) To completely remove the oxide, the BHF etch time is increased, resulting in adhesion problems to arise between the bottom electrode and the substrate.*

4.3.3 Diffusion Barrier

From the previous section it is clear that even with a platinum layer of 500 nm issues with diffusion and adhesion can arise. Besides being not fully adequate as diffusion barrier, the thick platinum layer also account for a considerable share of the total fabrication cost. It is therefore highly desirable to implement a diffusion barrier that can either stand alone, or assist the platinum layer and thereby decrease the required platinum thickness. During the ELBA project the following different diffusion barriers have been tested titania (TiO_2), alumina (Al_2O_3), titanium tungsten (TiW) and zirconia (ZrO_2). The titania was produced by oxidation, alumina was both deposited with sputtering and sol-gel, titanium tungsten with sputtering as well and zirconia with sol-gel. None of the alternative diffusion barriers were however successful [48]. Especially sol-gel based zirconia is interesting as it has been tested with success in [49, 50] although with a PZT sintering temperature lower than for the PZT thick film used in this work. The sol-gel method is however complex, and it has not been possible to obtain a zirconia layer of adequate thickness of quality in the ELBA project. Sol-gel based zirconia is a very low cost alternative or improvement for the diffusion barrier, and it should therefore be further investigated.

4.3.4 Electroplating of Platinum

The relatively thick platinum layer used as diffusion barrier and bottom electrode is deposited using e-beam evaporation. This is a highly standardised metallisation process for silicon and MEMS processing with precise thickness control. The disadvantage of the evaporation process is that a considerable amount of evaporated metal is lost in the chamber. The evaporation is concentrated to a small area where the e-beam strikes the crucible, and to obtain a uniform coating with low shading effect from surface topography of e.g. photoresist, the wafer is positioned at a relatively large distance in order to obtain a collimated path of evaporated metal. Consequently the processing cost is significantly higher than the actual cost of the platinum deposited on the wafer. Depositing the platinum in an electroplating process instead should therefore reduce the cost as platinum mainly is used for coating the wafer. Wafers with a seed electrode of 50 nm/50 nm Ti/Au deposited with e-beam evaporation, were electroplated with platinum at an external supplier. A platinum layer of 500 nm identical to the conventional e-beam process was electroplated on a full wafer after which the platinum was patterned. The patterning was performed in a identical wet etch as for the e-beam process with the result seen in Figure 4.13a. Despite an etch time less than 1/4 of the normal etch, the electrode openings are significantly over-etched with severe roughness problems at the edge. Figure 4.13b shows the wafer after the PZT screen printing and sintering process. The electroplated bottom electrode is visible affected with major color differences of the electrode around the PZT areas. Conclusively the diffusion barrier capabilities of the electroplated platinum are significantly lower than for the e-beam evaporated platinum. Further electroplating test are under preparation, with the aim of electroplating thicker layers of platinum followed by high temperature treatment to increase the layer density.

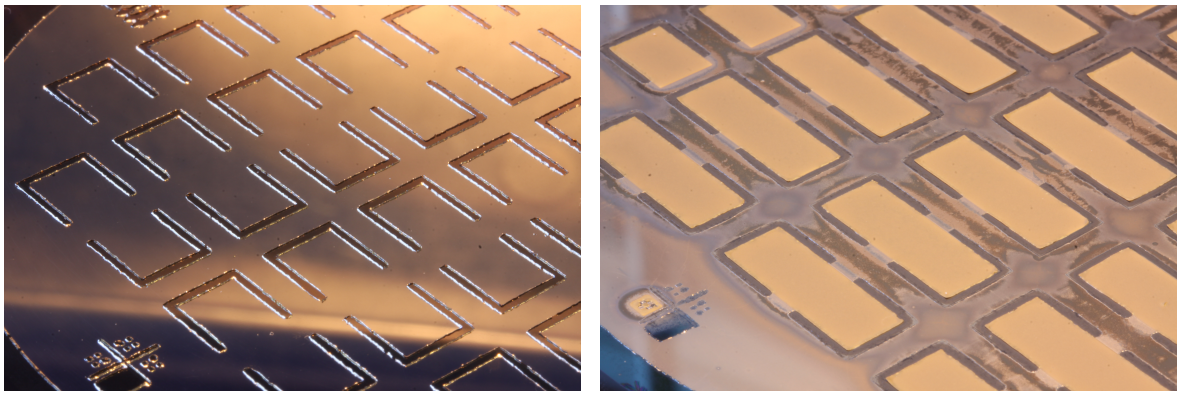

(a) *Electroplated Pt after wet etch.* **(b)** *Electroplated wafer with PZT.*

Figure 4.13: *Preliminary results on electroplating of platinum. (a) Wafer with* 500 nm *electroplated platinum, plated on a electrode of* 50 nm/50 nm *Ti/Au. Electrode is patterned in a wet etch and significant problems with over-etch and edge roughness is observed. (b) Electroplated wafer after screen printing of PZT and sintering. The electroplated platinum electrode is visible affected with clear color variation around the PZT areas.*

4.3.5 Anchoring Stress and Electrode Edge Position

The area of highest stress in the cantilever is at the anchoring between the cantilever and frame. This is illustrated in Figure 4.14a where the stress distribution along the length of the cantilever is plotted around the anchoring. The stress distribution is obtained from a numerical 2D FEM simulation with the harvester design and parameters from Section 4.1 on page 51 and Table 2.2 on page 27. The silicon and PZT layers are separated by a horizontal black line, and the neutral axis of zero stress can be visible identified, with an exact position of 28.5% into the silicon layer from the material interface. This is close to the position of 1/4 into the silicon layer which was the result of the optimal silicon to PZT thickness ratio found in Section 2.10 on page 36. While the stress as expected is highest at the cantilever surfaces close to the anchoring point, it is clear that the stress in the PZT layer expands over the anchoring point. As the middle and top electrode pattern edge in Figure 4.1 on page 52 is designed to be located exactly at the anchoring point of $x = 0$ in Figure 4.14a, this frame stress is not designed to be included in the active part of the PZT layer. The error in the shadow mask alignment plotted in Figure 4.7c on page 61 however showed that the vertical alignment (x-direction in Figure 4.14a) can be off by $\pm 40\,\mu m$ meaning that the electrode edge can expand over the anchoring, or it can be to short. The effect of the electrode edge position is plotted in Figure 4.14b. The stress in the PZT layer is from the FEM simulation integrated over a volume which is a function of the electrode edge position relative to the anchoring point. The resulting stress is normalised to the situation with the electrode edge being exactly at $x = 0$. It is clear that volume stress is lost if the electrode edge is positioned out on the cantilever, while stress is gained if the edge expands over the frame. The position of the middle and top electrodes has in the latest design iteration been expanded over the frame by $100\,\mu m$ to include some of the frame stress, and to account for error in shadow mask

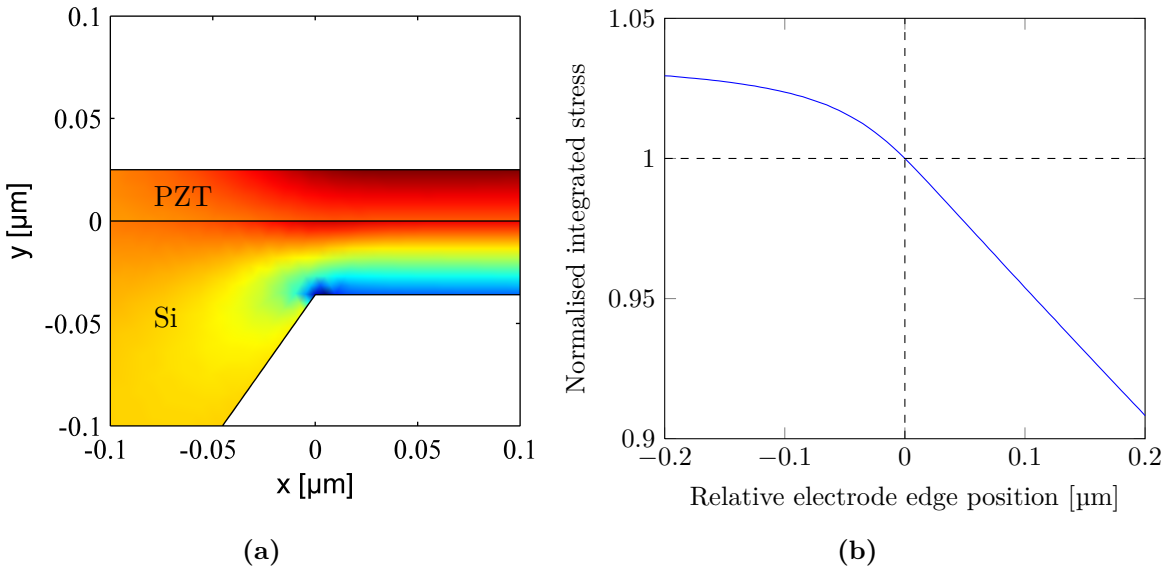

Figure 4.14: *(a) Stress distribution along the length of the cantilever at the anchoring point. Data obtained from a 2D FEM simulation. The PZT top layer and silicon is separated by the horizontal black line. The neutral axis of zero stress is visible around 1/4 into the silicon, and the stress in the PZT layer clearly expands over the anchoring point. (b) Effect of top or middle electrode position. The stress in the PZT layer is integrated for different electrode positions relative to the anchoring point at $x = 0$ in (a).*

alignment. It has not yet been possible to evaluate the effect.

4.4 Lead-Free Harvester

PZT contains more than 60% lead which is becomingly increasingly undesirable due to its toxicity and problematic waste treatment. As described in the introduction, aluminium nitride is one of the alternatives but also sodium potassium niobate (KNN) is of interest as it can be processed with similar techniques as PZT. As part of the development phase in the ELBA project, KNN harvesters have therefore been fabricated using an identical fabrication process as for the PZT harvesters. A KNN prototype is seen in Figure 4.15 where the frontside is photographed after the backside KOH etching. The color of the KNN layer is white compared to the grey/brown color of the PZT. The preliminary result of the KNN development indicates that a platinum layer of lesser thickness is sufficient in the high temperature sintering process to avoid mixing issues. Secondly the problems with trench etching described in Section 4.3.2 are nearly eliminated. Potentially wafers with KNN harvester could be manufactured with less cost than for PZT harvesters.

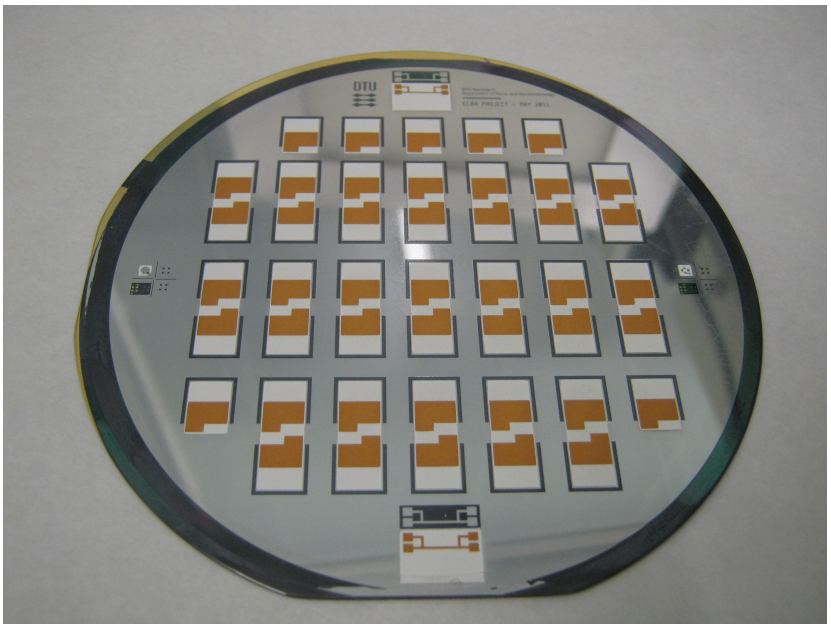

Figure 4.15: *Prototype of sodium potassium niobate (KNN) based energy harvester. Wafer frontside after KOH etching of backside cavities.*

4.5 Summary

The final harvester design features a 10 mm × 10 mm silicon chip with a rectangular cantilever of 6.5 mm in length and 6 mm in width. The cantilever is surrounded by a frame of 1.5 mm for anchoring and handling the harvester. The separation between cantilever and frame is 0.5 mm, and the ratio between the thin part of the cantilever and the integrated proof mass is 50%.

The unimorph fabrication process consist of three conventional mask lithography steps, one screen printing mask and one shadow mask electrode deposition. The bimorph harvester fabrication consist of two lithography masks, two screen printing masks and two shadow mask steps. The fabrication process can be carried out using both SOI and conventional silicon wafers. Openings in the nitride on the wafer backside is created for later KOH etching. A bottom electrode is deposited and patterned on the frontside followed by the screen printing of PZT. A top electrode is deposited through a shadow mask for direct patterning. For bimorph harvesters the screen printing and shadow mask process is repeated twice. The wafer frontside is protected with a mechanical holder and the cantilever and proof masses are defined by a deep cavity etching in KOH. The cantilevers are released in a RIE etch and the devices are separated in dicing process. Finally the PZT layers are polarised. The majority of the fabrication steps are batch processes aimed for minimizing the fabrication cost. Suggestions for further development includes an assisting diffusion barrier and new methods for minimizing or reducing the cost of the thick platinum layers which comprises a substantial amount of the fabrication cost.

The described fabrication process routinely achieves a yield exceeding 90%, and the fabricated harvesters will in the following two chapters be characterised thoroughly and on a uniformity basis.

Chapter 5

Harvester Characterisation

The characterisation of the fabricated ELBA harvesters will be divided into two chapters. In this chapter a single harvester device is thoroughly characterised. Having established all the different parameters and quantities and how they are measured in this analysis, the next chapter will present a uniformity characterisation of the general harvester performance on a wafer level.

This chapter will start with a review of the experimental methods used. Next the thorough characterisation of the unimorph harvester with ID *2D* from wafer *SiW1* will be presented. The *SiW1* wafer is part of the uniformity characterisation in the next chapter (Table 6.1 on page 94), and the *2D* harvester is selected to represent the average harvester performance as close as possible from the respective wafer. The harvester has a cantilever to mass ratio of 0.5, while the remaining geometric parameters are identical to those listed in Table 2.2 on page 27.

5.1 Experimental Methods

From a wireless sensor application perspective, the most important characteristics of a vibration energy harvester are resonant frequency, bandwidth and of course power output. There are however a number of underlying parameters of interest which requires both static and dynamic characterisation of the harvester. In this work the static characterisation only involves the measurement of the PZT layer capacitance, but with a contact force sensor one can identify the spring constant from applied static force and resulting deflection or vice versa under short circuit conditions for the harvester. Similarly the resulting force from an applied voltage or vice versa can be used to estimate the Γ/Λ [$\mathrm{N\,V^{-1}}$] factor. As will be evident later, these parameters can also be indirectly estimated from dynamic measurements. The dynamic characterisation can in general be divided into two methods depending on whether the cantilever is excited by the indirect piezoelectric effect, or if an external force is applied and the direct piezoelectric effect accordingly is measured.

5.1.1 Indirect Piezoelectric Effect

When using the indirect piezoelectric effect for dynamic characterisation, the PZT layer is connected to a voltage source with a time-varying output. In this characterisation the voltage source used is an Agilent 4294A Precision Impedance Analyzer which can measure the electrical properties capacitance, impedance and phase angle of the piezoelectric layer as a function of frequency for applied voltages up to 1 V. It will later in the data presentation be demonstrated how the resonant frequency and effective system coupling factor can be deduced from the impedance measurements.

5.1.2 Direct Piezoelectric Effect and Shaker Setup

In the characterisation of the direct piezoelectric effect the harvester is subjected to a dynamic external mechanical force and the resulting generated charge and voltage is measured. To apply this dynamic actuation a shaker is used in a setup sketched in Figure 5.1. The B&K Mini Shaker 4810 (Appendix D.3) is driven by an amplified sinusoidal signal from a function generator. The acceleration of the shaker actuation is measured by a reference accelerometer mounted between the shaker and the harvester. The reference accelerometer and charge amplifier used is elaborated in the following section. The output of the harvester is connected to a resistance box which simulates load conditions. To measure the deflection of the harvester under the dynamic excitation, a displacement sensor is positioned above the shaker and harvester. The displacement sensor used is a ILD2300-10 laser triangulation sensor with a resolution of 150 nm at 20 Hz sampling rate (Appendix D.4). The entire setup is connected and controlled by a computer using LabView. The computer is connected to a National Instruments data acquisition box for direct measurement of the voltage outputs of the charge amplifier and energy harvester. The alternating voltage output of the harvester is processed in LabView and stated in root mean square (RMS) values (V_{RMS}), and the generated RMS power (P_{RMS}) by the harvester over the resistance box accordingly becomes

$$P_{\mathrm{RMS}} = \frac{V_{\mathrm{RMS}}^2}{R_l} \tag{5.1}$$

where R_l is the load resistance.

5.1.2.1 Reference Accelerometer

To determine the excitation acceleration of the harvester, a Brüel & Kjær standard piezoelectric reference accelerometer type 8305 is used (Appendix D.5). The accelerometer functions in principle as a charge source, and accordingly the sensitivity $S_a = 0.92\,\mathrm{pC}/g$ is expressed in terms of charge per unit acceleration. The reference accelerometer is connected to a charge amplifier which converts the charge output to an amplified voltage output which then can be measured by the data acquisition box. A diagram of part of the charge amplifier is seen in Figure 5.2. The full diagram is available in Appendix D.6 and holds additional electronics

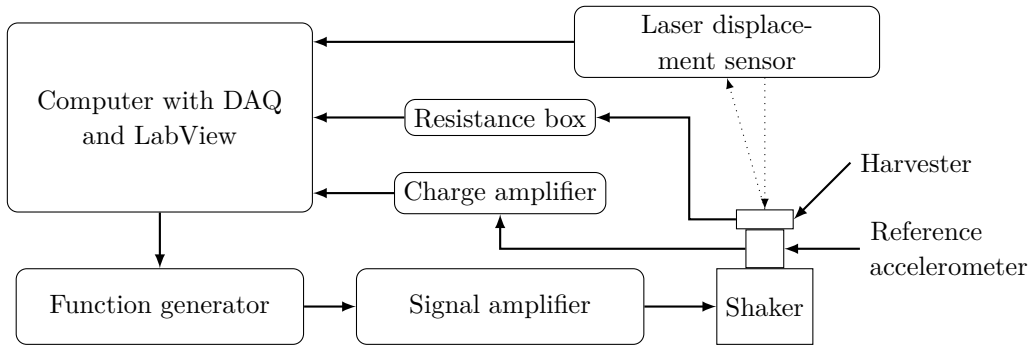

Figure 5.1: *Shaker setup for measuring the power generated by the harvester. The input signal for the B&K Mini Shaker 4810 is generated by an Agilent 3320A function generator and is amplified in a Pioneer VSC-405RDS MKII audio amplifier. To measure the shaker excitation acceleration a B&K Piezoelectric Accelerometer Type 8305 connected to a charge amplifier is used. The deflection of the harvester under excitation is measured with an ILD2300-10 laser displacement system from Micro-Epsilon. Load conditions for the harvester are simulated with a 1040 resistance box from Time Electronics. The voltage from the harvester and charge amplifier are measured using a SCB-68 connector block and a PCI-6052E DAQ both from National Instruments. The setup is controlled by a computer using LabView.*

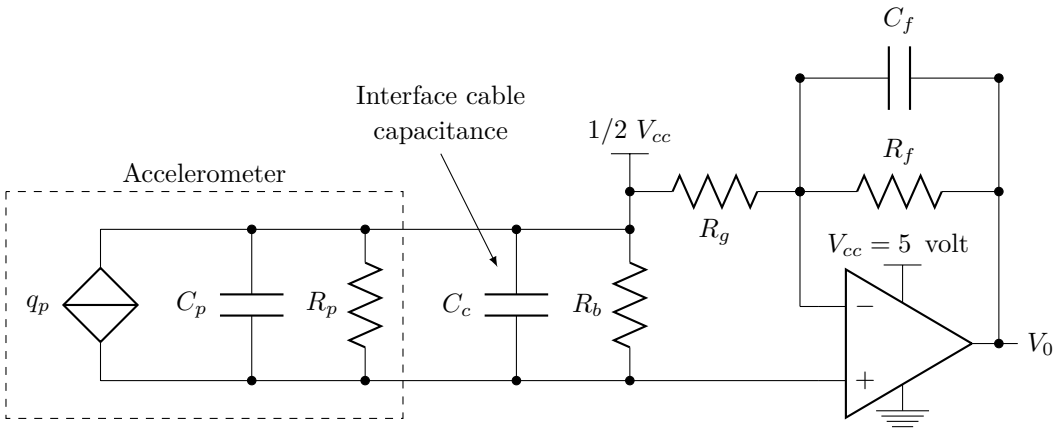

Figure 5.2: *Circuit diagram of the reference accelerometer in connection with the charge amplifier. The full diagram is available in Appendix D.5. The generated charge in the accelerometer is converted to a multiplied voltage such that the acceleration can be extracted from voltage measurements in a data acquisition box. The voltage output is multiplied by the ratio of the resistors $R_g = 20\,\mathrm{k}\Omega$ and $R_f = 200\,\mathrm{k}\Omega$. The low-pass frequency is determined by the resistor R_f and the capacitor $C_f = 220\,\mathrm{pF}$ while the high-pass frequency is determined by the capacitors C_p and C_c and the resistors R_p and R_b.*

to achieve a steady 5 V input on the charge amplifier from a 9 V battery which is used to eliminate noise from a power supply. Besides the charge source, the accelerometer holds a capacitor C_p with a value of 180 pF and a resistor R_p with a resistance of 1000 GΩ. In parallel with the accelerometer there is the capacitance of the interface cable $C_c = 20\,\text{pF}$ and a high pass resistor $R_b = 100\,\text{MΩ}$. The voltage amplification is determined by the ratio between the resistor $R_g = 20\,\text{kΩ}$ and the resistor $R_f = 200\,\text{kΩ}$ which is connected in parallel with a capacitor $C_f = 220\,\text{pF}$ comprising the circuit low pass filter. The low-pass frequency of the charge amplifier is accordingly determined by

$$F_{\text{low-pass}} = \frac{1}{2\pi R_f C_f} = 3617\,\text{Hz} \tag{5.2}$$

end the high-pass frequency

$$F_{\text{high-pass}} = \frac{1}{2\pi\left(R_p \parallel R_b\right)\left(C_p \parallel C_c\right)} = 8\,\text{Hz} \tag{5.3}$$

The voltage output of the charge amplifier is expressed as

$$V_0 = \frac{q_p}{(C_p + C_f)}\left(1 + \frac{R_f}{R_g}\right) + \frac{V_{cc}}{2} = \frac{aS_a}{200\,\text{pF}}11 + \frac{V_{cc}}{2} \tag{5.4}$$

where q_p in the last equation is replaced by the accelerometer sensitivity and acceleration, which can be easily extracted from the measured voltage. In the same way as for the harvester, the voltage output of the charge amplifier is processed in LabView and the RMS value is deduced. Accordingly the shaker excitation acceleration is stated in RMS values as fractions of the gravitational acceleration g ($9.81\,\text{m}\,\text{s}^{-2}$).

5.2 Impedance Measurements

Figure 5.3 shows the measured piezoelectric impedance around the resonant frequency for the fabricated ELBA harvester. From the theory in Section 2.9.1 on page 35 the impedance, Z, of the harvester can be expressed by

$$Z = \frac{Z_m}{(\Gamma/\Lambda)^2 + j\Omega C Z_m} \tag{5.5}$$

where $Z_\text{m} = j\Omega m_\text{eff} + b - jk_c\Omega^{-1}$ is the mechanical impedance. At the mechanical resonant frequency $f_r = \Omega_0/(2\pi) = \sqrt{k/m}/(2\pi)$ the mechanical impedance is reduced to the mechanical damping (b) as the equivalent inductance of the proof mass cancels out the equivalent capacitance for the spring constant. Accordingly the lowest impedance, $|Z|_\text{min}$, is obtained at f_r. In the other end, the highest impedance, $|Z|_\text{max}$, is obtained at what is know as the anti-resonant frequency $f_a = f_r\sqrt{1 + K_\text{sys}^2}$ where $K_\text{sys} = (\Gamma/\Lambda)^2/(k_c C)$ is the system coupling coefficient defined in Equation (2.58) on page 35. At the anti-resonant the equivalent capacitor acts as an additional mechanical spring due to the piezoelectric coupling and the denominator in

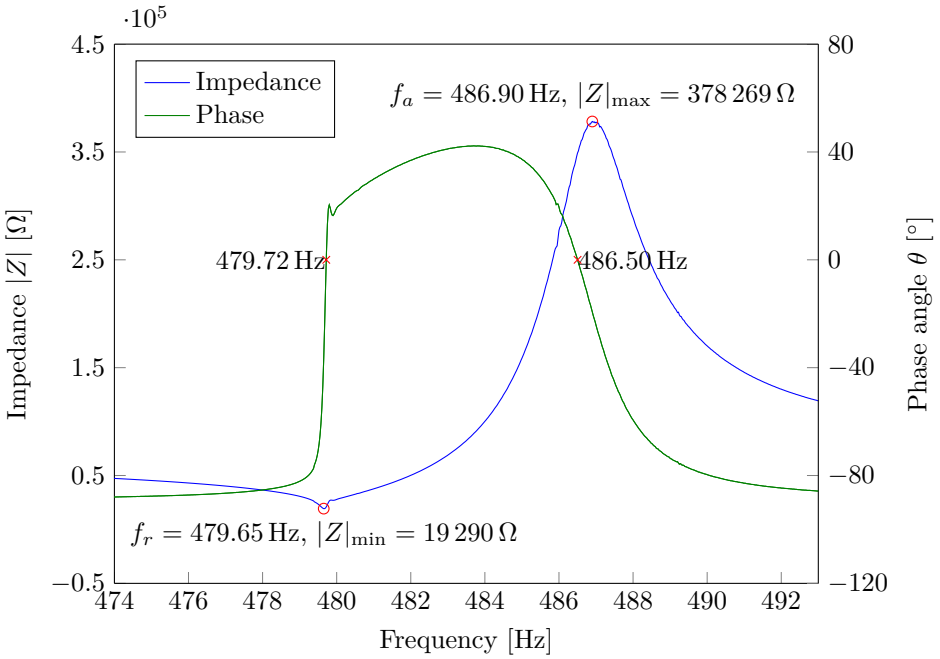

Figure 5.3: *Measured impedance of the piezoelectric harvester as function of frequency under a voltage supply of* 1 V. *The minimum impedance is obtained at the resonant frequency f_r where the mechanical impedance accordingly is reduced to only mechanical damping. The maximum impedance is obtained at the anti-resonant frequency f_a where the equivalent capacitance act as an additional mechanical spring due to the piezoelectric coupling.*

Equation (5.5) is minimised. From the expression for the anti-resonant frequency, the system coupling coefficient can be easily deduced, and an effective system coupling coefficient, K_{sys}, can be calculated from the impedance measurement as

$$K_{\text{eff}} = \sqrt{\frac{f_a^2}{f_r^2} - 1} \tag{5.6}$$

which for the frequencies obtained in Figure 5.3 equals a value of 0.175. The effective coupling coefficient can be compared to the effective piezoelectric coupling coefficient ($k_{\text{eff}} = \sqrt{d^2/\left(s^E \varepsilon^T\right)}$) defined in Equation (2.12) on page 22 which expresses the theoretic maximum coupling coefficient for a piezoelectric structure. With the stated PZT thick film material properties in Table 2.3 on page 38, a maximum coupling coefficient of 0.396 is obtained. This is for a structure of purely PZT, the value must accordingly be divided by two ($0.396/2 \approx 0.2$) for the unimorph harvester as the silicon support is not piezoelectric active. The effective coupling coefficient will always be less than the theoretical maximum of 0.2 due to geometric factors, bending deformation etc.

Besides the piezoelectric impedance, $|Z|$, the corresponding phase angle (θ) is also plotted in Figure 5.3. As reviewed in the theory chapter, the impedance of the connected load Z_l must equal the complex conjugate of the piezoelectric impedance ($Z_l = Z^* = |Z|e^{-j\theta}$) for

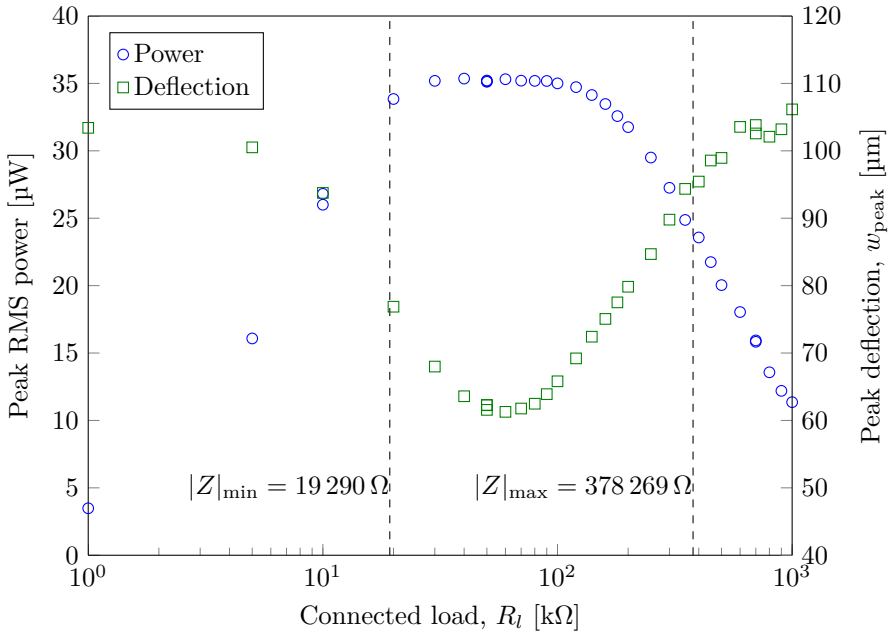

Figure 5.4: *Peak RMS power output and peak deflection as function of the resistance of the connected load. Vertical lines indicates the load values at which maximum power was predicted from the impedance measurements in Figure 5.3. The discrepancy is believed to originate from non-linear effects. RMS excitation acceleration used is 0.5g.*

maximum power transfer between the two. Since the connected load is purely real ($Z_l = R_l$), maximum power is only transferred when the phase angle θ is zero and the phase factor $e^{-j\theta}$ becomes 1. As evident from Figure 5.3 the phase angle passes the zero phase line twice, hence there should be two frequencies with two different loads where maximum power is obtained; one close to resonant with a low resistance and one close to anti-resonant with high load. The two points are marked on the plot with corresponding frequency listed next by. If it was possible to connect a load with a complex impedance, maximum power transfer could also occur in the range between the two points of zero phase angle.

5.3 Optimal Load

The sole purpose of a vibration energy harvester is to deliver electrical power to a system in form of an electrical circuit. As evident from the impedance measurements in the previous section, the size of the connected load is important to obtain as high power transfer as possible, hence the concept *impedance matching*.

From the impedance measurements it was predicted that maximum power should be transferred at two load values close to $|Z|_{\min} \approx 20\,\text{k}\Omega$ and $|Z|_{\max} \approx 380\,\text{k}\Omega$. If this indeed is the case is empirically tested in Figure 5.4 where the RMS power is plotted as function of the resistance of the connected load. The peak RMS power is extracted as the maximum power

obtained from a frequency sweep for each resistive load value. The plot also contains the simultaneously measured peak deflection at the proof mass anchoring point obtained with similar procedure as for the power. The characterisation is performed with a RMS excitation acceleration of $0.5g$. Vertical lines at the resistance values equal to $|Z|_{\min}$ and $|Z|_{\max}$ from the impedance measurements are plotted for comparison. The power output at $|Z|_{\min}$ is close to the maximum power which is obtained from a relatively broad range of load values. The power at $|Z|_{\max}$ is on the contrary significantly lower than the maximum power obtained. The reason for this discrepancy compared to the predictions from the impedance measurements, is due to non-linear effects which changes the behaviour of the cantilever around resonance. The non-linearity significantly complicates the interpretation of the optimal power results, as resonant frequency becomes depended on a range of parameters. This will be further illustrated in the next section.

If the harvester was linear, it would be expected that the minimum deflection for the power vs. load in Figure 5.4 would correspond to the impedance of the anti-resonant $|Z|_{\max}$. This can be understood by considering the expected power. If power output ($P = I^2 R_l$) is to be equal for both $|Z|_{\min}$ and $|Z|_{\max}$ a high value of R_l must equal a low current which again is proportional to the deflection slope and hence deflection. Although several other effects from the non-linearity influences the result, the minimum deflection load of $60\,\mathrm{k}\Omega$ observed in Figure 5.4 contra $|Z|_{\max}$ of $380\,\mathrm{k}\Omega$ in Figure 5.3 serves as an illustration of the significant influence of the non-linearity.

The importance of impedance matching is indisputable, and any presented data on power output for vibration energy harvesting will be performed under optimal load conditions. As evident from the optimal load mapping in Figure 5.4, the range of maximum power output is broad for the ELBA harvester. This characteristic has several advantages. Operating with a broader range of optimal loads, provides more freedom in the design and engineering of the connected electronic circuit which will comprise the load in the actual wireless sensor. Secondly and more important, with a broad range of loads the choice of load can be used to obtain a certain output voltage. With a constant power output, a low load value will result in a low voltage output, and vice versa for higher loads. For the AC output from the harvester to be useful for the electronics it is must be converted to DC using a rectifier circuit. Additionally the DC power must be stored on e.g. a capacitor in the charging time of the sensor. Having a high voltage for both the rectification and charging are beneficial as the efficiency of the energy processing thereby can be increased.

5.4 Power Output vs. Acceleration

Having determined the optimal resistance and range for maximum power transfer from harvester to load, the next step in the characterisation is to examine the harvester performance as function of excitation amplitude. According to Equation (2.57) on page 35 is the power

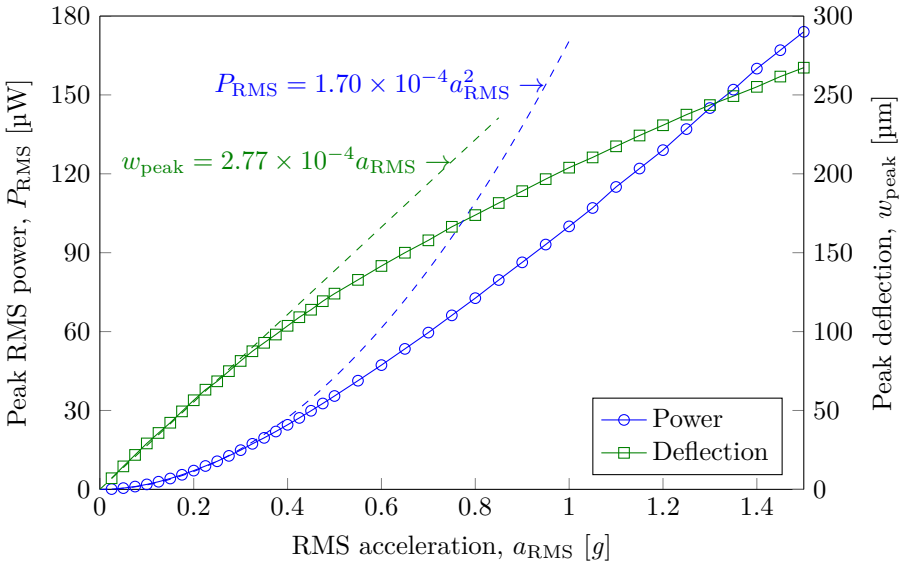

Figure 5.5: *Peak RMS power output and peak deflection as function of the excitation acceleration. The results are obtained from frequency sweeps around resonance with a connected load of* 75 kΩ*. Dashed lines are squared and linear fits for measurements up to 0.2g and indicates the expected behaviour for the power output and deflection respectively. The deviation from the expected trend is caused by non-linearity.*

output of the harvester determined by

$$P = P_{\mathrm{av}}\chi = \frac{F_{\mathrm{ext}}^2}{4b}\chi = \frac{F_{\mathrm{ext}}^2 Q_{\mathrm{mec}}}{4m_{\mathrm{eff}}\Omega_0}\chi \tag{5.7a}$$

$$\chi = \frac{2}{1 + \sqrt{1 + \dfrac{1}{Q_{\mathrm{mec}}^2 K_{\mathrm{eff}}^4}}} \tag{5.7b}$$

where P_{av} is the maximum available power and χ is a multiplication factor with a maximum value of 1. According to Equation (5.7a) is the power output predicted to be proportional to the excitation acceleration squared. It then naturally follows that the deflection of the harvester is expected to be proportional to the excitation acceleration. These dependencies are examined in Figure 5.5 where the peak RMS power and peak deflection are plotted as function of excitation acceleration. The power and deflection values are extracted from frequency sweeps for each acceleration as peak values from the resulting frequency response spectra for power and deflection respectively. The measurements are conducted with a connected load of 75 kΩ, and the deflection is measured at the proof mass midpoint. The two dashed lines are squared and linear fits for the measurements up to $0.3g$ and represents the theoretic expected tendency for power and deflection respectively.

For low accelerations up to $0.3g$ both power and deflection follows the expected tendencies, while they both levels off at higher accelerations. By analysing the low acceleration regime where the observations follow the expected tendencies, a couple of parameters in

Equation (5.7a) can be extracted from the fitted functions. It will later be proven that it is reasonable to assume that the multiplication factor χ is 1, hence the fitted function for the power should correspond to the power available term P_{av}. With a total mass of the cantilever of $m = 26.8\,\text{mg}$ the viscous damping coefficient b can be extracted from

$$P_{\text{RMS}} \backsimeq \frac{m^2 g^2}{4b} a_{\text{RMS}}^2 = 1.70 \times 10^{-4}\,\text{a}_{\text{RMS}}^2 \Rightarrow \tag{5.8a}$$

$$b = 1.02 \times 10^{-4}\,\text{N s m}^{-1} \tag{5.8b}$$

where it must be taken into account that the acceleration is stated in fractions of $g = 9.81\,\text{m s}^{-2}$. With an estimate for the viscous damping, the mechanical quality factor Q_{mec} of the resonator can be determined from Equation (2.59) on page 35 as

$$Q_{\text{mec}} = m_{\text{eff}} \Omega_0 / b \tag{5.9}$$

From the effective mass study in Figure 2.6 on page 32 it was found that m_{eff} roughly equals the mass m when the cantilever to mass ratio is 0.5. Ideally the resonant frequency Ω_0 used in the derivation should be the natural frequency of the resonator, meaning the purely mechanical situation without connected load. In the following the resonant frequency of the loaded situation F_{res} is however used since the induced error is less than 1%. With $F_{\text{res}} = 486.5\,\text{Hz}$ and $m_{\text{eff}} = m$ the mechanical quality factor is calculated to 807. Inserting this Q_{mec} value in the expression for χ in Equation (5.7b) together with the value of 0.175 for K_{eff} obtained in the impedance analysis in Section 5.2 a multiplication factor of 0.9996 can be derived. Accordingly the assumption of $P \backsimeq P_{\text{av}}$ used in the analysis is valid.

The acceleration study in Figure 5.5 also features the peak deflection measured at the proof mass midpoint. The peak deflection w_{peak} can be expressed by

$$w_{\text{peak}} = Q_{\text{load}} z \tag{5.10}$$

where z is the input displacement of the shaker and Q_{load} is the loaded quality factor. The expression in Equation (5.10) can also be written with the mechanical quality factor, but then the peak deflection w_{peak} expresses the deflection in a purely mechanical situation where only viscous damping affects the system. The loaded quality factor is the equivalent for a situation where the harvester is damped by both the viscous damping an the damping induced from the connected load in the electrical domain. The input displacement from the shaker is determined by $z = a/\Omega^2$ and hence the load quality factor can be extracted from the linear fit for the deflection measurements at low accelerations as

$$w_{\text{peak}} = \frac{Q_{\text{load}}}{\Omega^2} a_{\text{peak}} = \frac{g\sqrt{2} Q_{\text{load}}}{\Omega^2} a_{\text{RMS}} = 2.77 \times 10^{-4}\,\text{a}_{\text{RMS}} \Rightarrow \tag{5.11a}$$

$$Q_{\text{load}} = 186 \tag{5.11b}$$

where the relation between peak and RMS values must be accounted for. It should be stressed that the loaded quality factor calculated from the deflection measurements contains a potential high error. When using the deflection ratio to calculate a quality factor, it is essential that

the deflection analysis is obtained at the centre of mass for the resonator. The exact position of the centre of mass is not straightforward to determine for the harvester, but as used in the theory chapter a good assumption is around the centre of the proof mass which accounts for the majority of the total mass. In addition to this uncertainty, the laser deflection sensor is positioned manually over the harvester by eyesight, hence the alignment and precision is limited, and ultimately the potential error in Q_{load} can be significant. The obtained Q_{load} is naturally smaller than Q_{mec} due to the induced damping from the electrical domain. This is also evident from the optimal load analysis in Figure 5.4 on page 78 where it was observed that the peak deflection was lowest at maximum power transfer which corresponds to the where the damping from the connected load is greatest.

From the acceleration analysis in Figure 5.5 it is clear the while both deflection and acceleration follows the expected tendency at accelerations up to $0.3g$ they both deviates from the predictions at higher accelerations where the proportionality levels off. The responsible phenomenon behind the decreasing proportionality is non-linearity, which was also observed in the optimal power analysis.

5.5 Non-linearity

The motion of the harvester is in Equation (2.47b) on page 34 described as a driven harmonic oscillator according to Newton's second law. Non-linearity arises if one or more of the parameters m_{eff}, b or k_c in the driven oscillator changes from being constant, to dependant on deflection and hence velocity and acceleration to some degree. The direct inverse proportionality between power and viscous damping coefficient in Equation (5.7a) strongly indicates that the deviation from the predicted power vs. acceleration tendency in Figure 5.5 is caused by an increased viscous damping a high accelerations. This would naturally translate to a decreasing proportionality for the deflection since a decrease in Q_{mec} is expected to result in a decrease in Q_{load}. The investigation of the non-linear effect is however complicated by the fact that all three parameters governing the harvester motion are interconnected. The viscous damping coefficient is defined as

$$b = k_c/(\Omega_0 Q_{\text{mec}}) = m_{\text{eff}}\Omega_0/Q_{\text{mec}} = \sqrt{k_c m_{\text{eff}}}/Q_{\text{mec}} \tag{5.12}$$

and the effective mass m_{eff} and the spring constant k_c are linked by the resonant frequency $\Omega_0 = \sqrt{k_c/m_{\text{eff}}}$. Accordingly the individual parameters must be examined.

5.5.1 Non-linear Spring Constant

Of the parameters influencing the motion of the harvester, the one that is easiest and most direct to investigate is the spring constant through the measured resonant frequency. This is examined in Figure 5.6 where the peak frequency (F_{res}) from the frequency sweeps performed in the acceleration analysis in Figure 5.5 is plotted. Only the observations at low accelerations

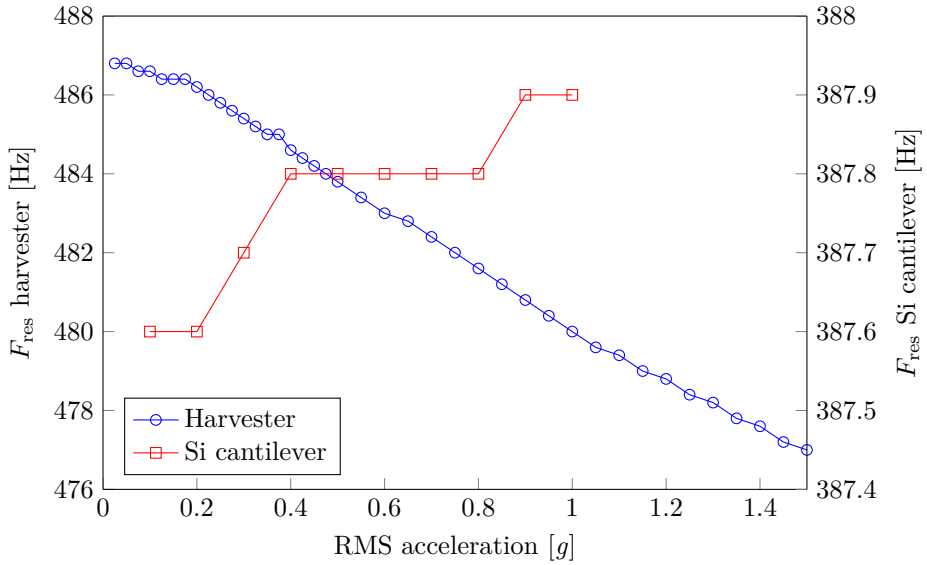

Figure 5.6: *Resonant frequency as function of input acceleration. F_{res} is the peak frequency from the frequency sweeps in Figure 5.5. F_{res} decreases nearly linearly with acceleration, and indicates a softening effect where the spring constant is decreasing with increasing acceleration. The phenomenon is not observed for the bare silicon cantilever, implying that the softening effect is caused by the PZT.*

up to $0.2g$ indicate a constant resonant frequency, while a linearly decreasing relation is obtained from higher accelerations. A total decrease of 10 Hz (2%) is observed for the range up to $1.5g$. Since the resonant frequency is dependent on acceleration and hence deflection, either/or both the spring constant and effective mass must accordingly be dependent on deflection. The effective mass is mainly determined by the geometry of the cantilever, and thus a deflection dependency will accordingly be caused by geometric non-linearities. If this is the case, is also investigated in the frequency analysis in Figure 5.6 where the resonant frequency extracted from deflection measurements for a bare silicon cantilever is examined. The design of the silicon cantilever is identical to the harvester, and the thickness of the silicon is equal to the silicon support thickness of the unimorph harvester. The frequency of the silicon cantilever is with variations in 0.1 Hz range constant within the uncertainty of measurements. Except from the unlikely situation of a non-linearity in effective mass and spring constant equalising each other, it can be concluded that the cantilever design should not give rise to non-linearities in either of the two parameters. The tendency of decreasing F_{res} for the harvester can for this reason only be caused by a non-linearity in the spring constant originating from the PZT layer. The phenomenon responsible is known as *material softening*, and is a commonly observed effect for small scale PZT resonators with high deflections [51–53]. As the name indicates, material softening covers the concept of decreasing material stiffness which occurs due to increasing stress. The stiffness of the PZT layer decreases with increasing acceleration and consequently F_{res} will shifts downwards.

A decrease in resonant frequency could potentially arise from a change in the damping ratio

ζ defined by

$$\frac{F_{\text{res}}}{\Omega_0} = \sqrt{1 - 2\zeta^2} = \sqrt{1 - \frac{1}{2Q_{\text{mec}}^2}} \tag{5.13}$$

where F_{res} is the measured peak amplitude frequency and Ω_0 is the purely mechanical resonant frequency. The effect of damping on the frequency is primarily a concern for resonators with mechanical quality factors below 40. Since Q_{mec} was found to be more than 800 from the fitted power measurements, changes in resonant frequency due to damping is neglected.

5.5.2 Non-linear Viscous Damping

The analysis of the spring constant and effective mass is unambiguous, and while the non-linear spring constant affects the behaviour of the motion, the effect is to small to account for the observed decrease in proportionality for the power in Figure 5.5. The discrepancy can as predicted only originate from an increased viscous damping, but investigating b is less straightforward than the previous analysis of resonant frequency. To eliminate the effect of damping from the load the analysis must be performed with the PZT layer short-circuited (SC). From these SC measurements the viscous damping coefficient can be indirectly estimated be calculating the mechanical quality factor as in accordance with Equation (5.12).

Figure 5.7a shows the deflection spectra around the resonant frequency for three different accelerations with the harvester in SC mode. Conventionally the mechanical quality factor is calculated be dividing the resonant frequency with the full width at half maximum (FWHM) bandwidth of the squared deflection spectrum. An advantage of this approach is that the aforementioned problem of induced error from the manual alignment of the deflection sensor by eyesight to the best guess centre of mass can be avoided. The method is however only valid if the shape of the frequency response is Gaussian. As evident from Figure 5.7a it is not the case since the shape is obvious asymmetric. This asymmetric shape is elaborated further in a following section. Without the conventional approach, the mechanical quality factor must be estimated with the same method as for the loaded situation in Equation (5.10) with peak deflection of the cantilever to input displacement of the shaker. Consequently the error can potentially be significant, but since the point of deflection measurement is constant for all the different excitation accelerations, the tendency should not be affected.

The calculated Q_{mec} from the SC measurements in Figure 5.7a is plotted in Figure 5.7b, again with the bare silicon cantilever for comparison. The mechanical quality factor for the silicon cantilever is calculated with similar method of peak deflection to input displacement ratio. The range of accelerations used is lower compared to the load measurements in Figure 5.5 on page 80 because without damping the harvester reaches the critical stress point of fracture at a lower acceleration. The mechanical quality factor is higher for the bare silicon chip. This is expected since Q_{mec} for silicon is higher than for PZT, resulting in a combined Q_{mec} that is reduced. If the tendency in Q_{mec} for the harvester is extrapolated to zero acceleration where non-linearity is diminished, a mechanical quality factor for the harvester is found to

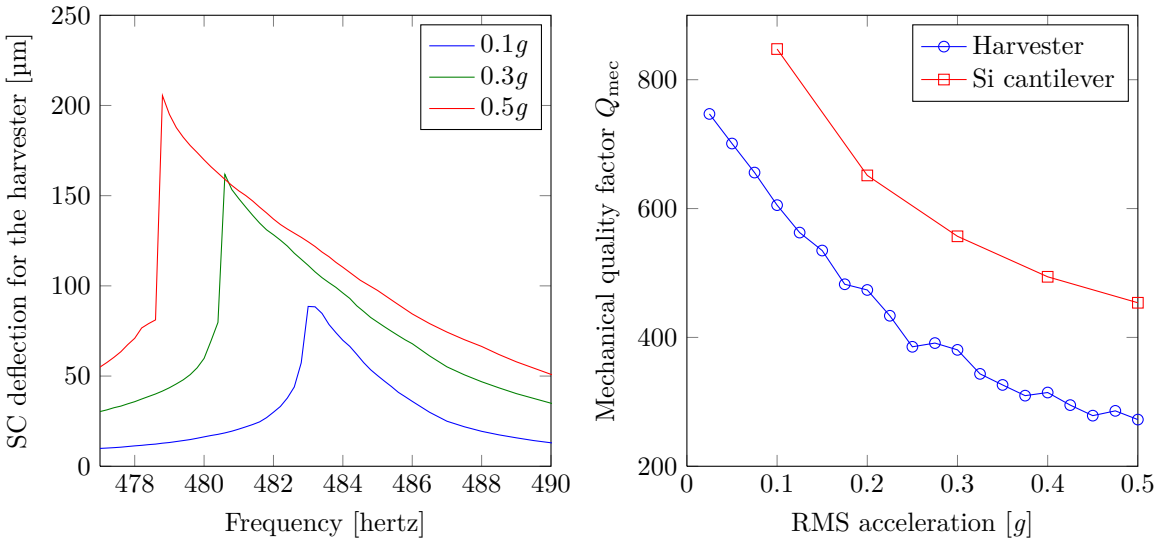

Figure 5.7: *Analysis of the mechanical quality factor. (a) Deflection spectra of the harvester with short-circuited PZT layer. The asymmetric shape of the response peak preclude the conventional method of frequency over bandwidth for the calculation of Q_{mec} which instead is obtained as the ratio of harvester deflection to input displacement. (b) Calculated Q_{mec} for both the harvester and a bare silicon cantilever. The tendency of decreasing Q_{mec} is clear for both cantilevers and indicates that the viscous damping coefficient b increases with acceleration.*

approximately 800. This is in accordance with the value of 807 obtained from the calculations using the fitted tendency of power as function of acceleration in Figure 5.5 on page 80. Figure 5.7b also clearly indicates that Q_{mec} decreases for increasing acceleration. For the harvester Q_{mec} is more than reduced by half from $0.1g$ to $0.5g$, and the tendency shows high similarity to the obtained Q_{mec} of the bare silicon cantilever. It should be stressed that as a consequence of the observed high non-linearity, a direct comparison between both load and SC conditions for the harvester and the silicon cantilever is difficult since the deflection ranges for each of them are different.

From the frequency analysis in Figure 5.6 it was indicated that the pure spring constant for the silicon cantilever was unaffected by the increase in acceleration. From the definition of viscous damping coefficient in Equation (5.12) it can hence be implied that the decreasing tendency of Q_{mec} observed for the silicon cantilever must originate nearly directly from b which must increase with deflection. Since the harvester is based on the exact same silicon cantilever with the PZT thick film screen printed on top, the tendency in increased viscous damping coefficient must be expected to be present for the harvester. The full mechanical behaviour for the ELBA harvester is ultimately a complicated combination of a non-linear viscous damping coefficient and non-linear effects from the material stiffness of the PZT layer. As a result, a direct comparison between the theoretic predictions in Equation (5.7a) and the power output obtained in one deflection range and Q_{mec} determined from another deflection range is extraordinary difficult.

5.5.3 Air Damping

The decreasing tendency in Q_{mec} strongly implies that the viscous damping coefficient is not constant but dependant on deflection and hence also velocity. Often the influence from air damping is ignored when considering small scale devices, simply because of the small surface areas. With the ELBA harvester consisting of a relatively large plate structure air damping might be of importance. This is examined in Figure 5.8 where the harvester is characterised in a vacuum chamber. The vacuum chamber does not facilitate the deflection sensor, hence only load measurements are conducted with information on power output, power spectrum quality factor (Q_{pow}) and resonant frequency plotted as function of pressure in mbar. The power is plotted in absolute values on the left y-axis, while all three parameters normalised to ambient conditions are plotted on the right y-axis. From the normalised resonant frequency it can be concluded that air damping is not influencing the spring constant of the harvester noticeably. This is in accordance with the theoretic predictions. The power output is observed to increase considerable as the pressure is decreased. At 3 mbar the power is increased by near 12%, and in general the power follows the exact tendency of the calculated Q_{pow}. The calculated Q_{pow} is approximately equal to Q_{load} but it contains a slight error from the asymmetric shape of the power spectrum. The exact relationship between Q_{pow} and Q_{mec} is not directly obtainable, but with Q_{pow} increasing less than the power it can be implied that the proportionality between Q_{mec} and Q_{pow} and hence Q_{load} must be higher than lin-

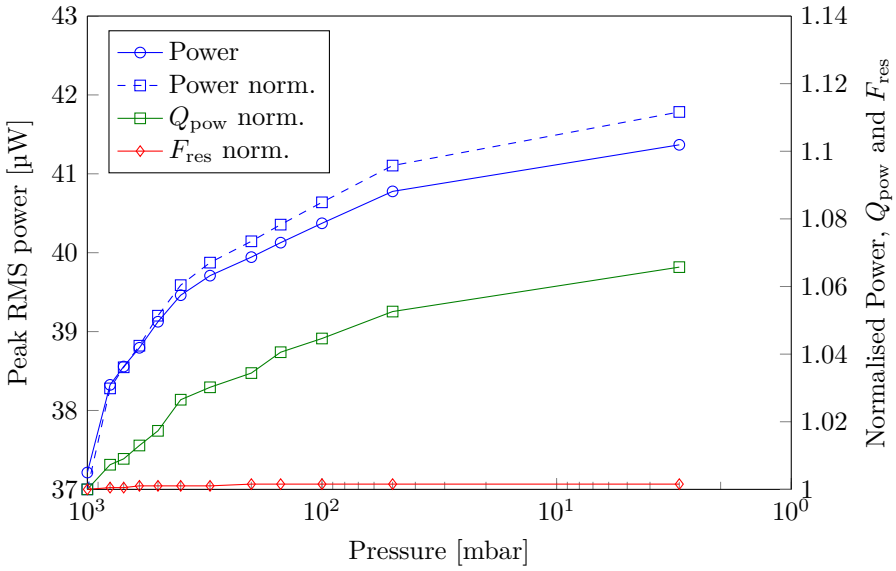

Figure 5.8: *Vacuum chamber characterisation of the harvester with parameters plotted as function of pressure. The resonant frequency is nearly constant indicating a spring constant independent of air damping. Power and power spectrum quality factor both increases with similar tendency. The power increases more than Q_{pow} indicating a higher order relation between Q_{pow} and Q_{mec}. Air damping do influence the quality factor, but can only account for part of the observed tendency in Figure 5.7b.*

ear. Again a direct comparison is difficult as the deflection ranges varies. Assuming that the mechanical quality factor increases proportional with the power as function of pressure, it can be concluded that air damping influences the harvester, but it can only account for part of the Q_{mec} tendency and accordingly decrease in viscous damping observed in Figure 5.7b. From the bare silicon cantilever and vacuum analysis, it is implied that a significant increase in structural/material damping occurs for increasing acceleration. This could be etc. heat generation, but further analysis is required to draw detailed conclusions.

5.5.4 Electric Non-linearity

The analysis of non-linearity has so far only treated parameters in the mechanical domain. Since the stiffness of the PZT is affected at the induced deflections, the electrical properties of the PZT and accordingly power output might be altered as it is known that the piezoelectric constant decreases with increasing stress [54]. If this effect contributes to the decrease in proportionality between power and acceleration in Figure 5.5 is examined in the following. By replacing the excitation acceleration a of the shaker with the shaker displacement $a = z\Omega^2$ in the power expression in Equation (5.7a) on page 80, the following relation emerged

$$P_{\text{RMS}} \backsimeq \frac{F_{\text{ext}}^2}{2 \times 4b} = \frac{m^2\Omega^4 z^2}{8b} = \frac{m^2\Omega^4}{8bQ_{\text{load}}^2} w_{\text{peak}}^2 \tag{5.14}$$

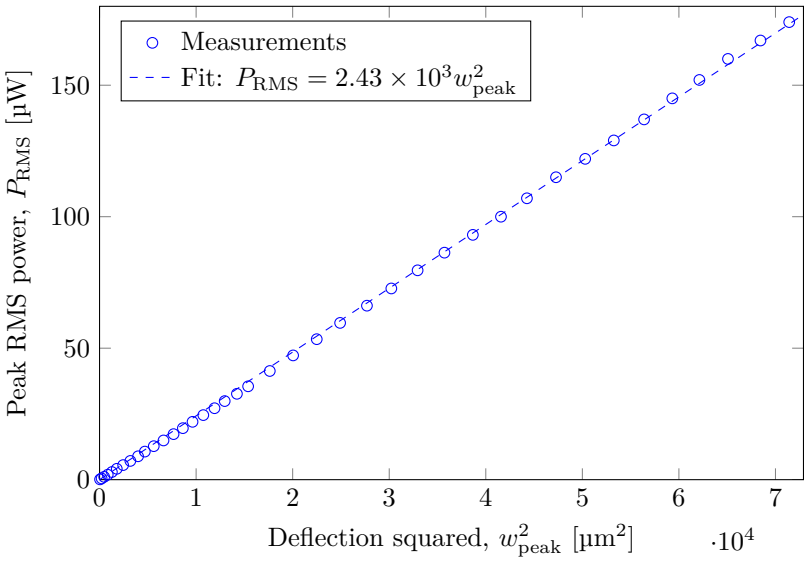

Figure 5.9: *Peak RMS power output as function of squared deflection for the measurements in Figure 5.5. The result show a highly linear relation, indicating that the decreasing proportionality between power output and acceleration in Figure 5.5 is purely caused by effects from mechanical non-linearities.*

indicating a linear proportionality between power and deflection squared. This expectancy is indeed observed in Figure 5.9 where the power measurements in Figure 5.5 is plotted as function of deflection squared instead of acceleration. The dielectric and piezoelectric properties of the PZT are included in the loaded quality factor, and with the proportionality observed in Figure 5.5 it can be concluded that if non-linearity occurs in the piezoelectric properties, it is not significant enough to affect the system. The non-linearities observed in the previous section can accordingly be assumed to be purely mechanical.

From the fitted regression in Figure 5.9 and the loaded quality factor of 191 found in Equation (5.11b) on page 81, the viscous damping coefficient can from Equation (5.14) be calculated to

$$\frac{m^2\Omega^4}{8bQ_{\mathrm{load}}^2} w_{\mathrm{peak}}^2 = 2.43 \times 10^3 w_{\mathrm{peak}}^2 \Rightarrow b = 9.30 \times 10^{-5}\,\mathrm{N\,s\,m^{-1}} \tag{5.15}$$

where $m = 26.8\,\mathrm{mg}$ and $\Omega = F_{\mathrm{res}} = 486.5\,\mathrm{Hz}$. Contrary the viscous damping coefficient of $1.02 \times 10^{-4}\,\mathrm{N\,s\,m^{-1}}$ found from the power measurements in Equation (5.8b) on page 81, the one in Equation (5.15) is found through the measured deflection and loaded quality factor. The little difference ($< 10\%$) between the two damping coefficients, indicates that the power expression derived in the theory chapter has the correct proportionality with regards to acceleration and cantilever deflection. It furthermore indicates that the manual alignment of the laser and the assumption of centre of mass is reasonable adequate.

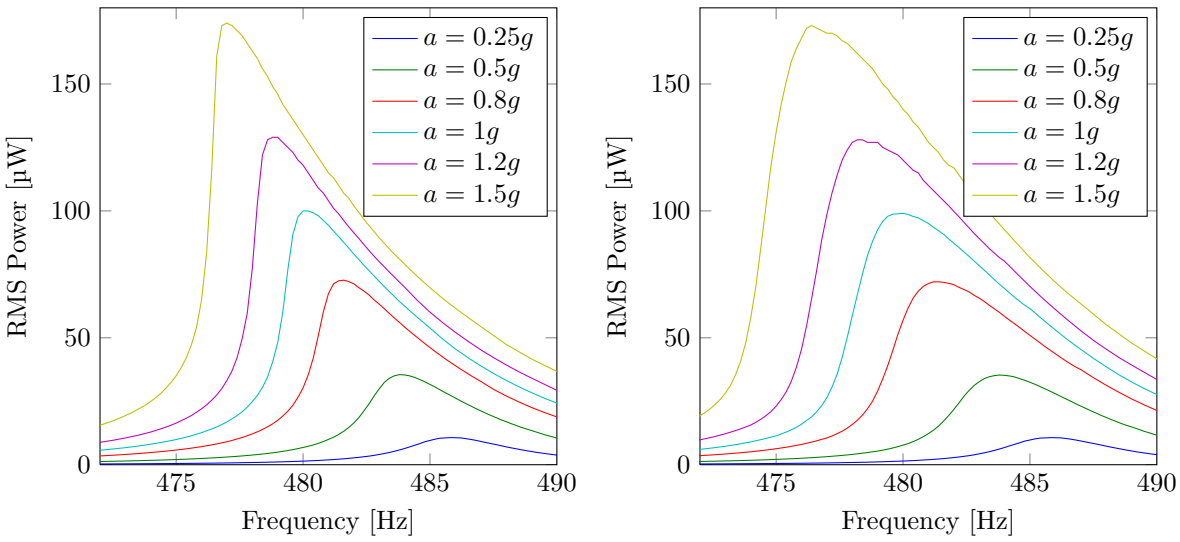

(a) *Frequency response from up sweep*

(b) *Frequency response from down sweep*

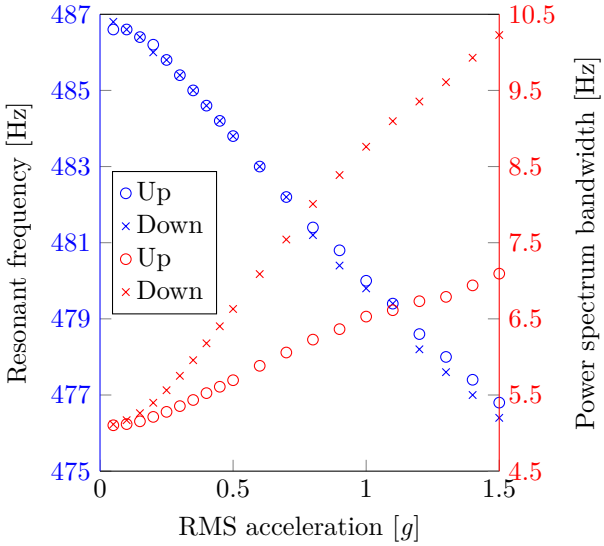

(c) *Frequency response from down sweep*

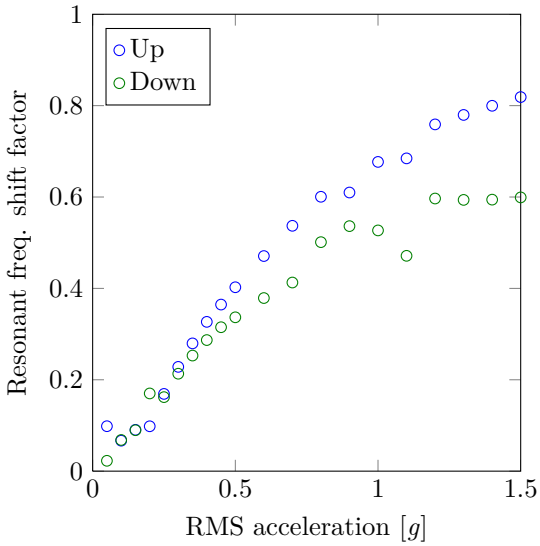

(d) *Frequency response from down sweep*

Figure 5.10: *Non-linear power spectra caused by the material softening. (a),(b) The shape of the power spectrum in the frequency response is highly influenced by the direction of the frequency sweep. (c) Contrary to the resonant frequency which is not noticeable influences by the sweep direction, the FWHM bandwidth of the spectrum is significantly larger for the down sweep. (d) Change of symmetry between resonant frequency and bandwidth. Shift factor of 0 means symmetry while 1 means a fully asymmetric peak.*

5.5.5 Non-linearity and Frequency Response

All the shaker results presented so far are extracted from measurements where the frequency is swept from low to high in a range around the resonant frequency. For a perfect linear resonator the frequency response from such a sweep should be independent on the sweep direction, but with the non-linearity and in particular material softening observed for the ELBA harvester the sweep direction becomes a factor. The effect is illustrated in Figures 5.10a to 5.10b where the frequency response from the power vs. acceleration study is plotted for a selection of acceleration.

In Figure 5.10a the frequency sweep direction is from low to high (up sweep) while a high to low (down sweep) direction is used in Figure 5.10b. It is apparent that the shape of the power spectrum changes with increasing acceleration where the softening effect becomes important. The position of the resonant frequency where peak power is obtained, is not significantly affected by the sweep direction according to Figure 5.10c. The main effect occurs for the FWHM bandwidth of the power spectrum where the down sweep direction results in significantly larger bandwidths compared to the up sweep. Consequently the approach of calculating the loaded quality factor by dividing the resonant frequency with the bandwidth is highly influenced by the sweep direction. Simultaneously with affecting the bandwidth, the sweep direction also influences the symmetry between the resonant peak and FWHM bandwidth. To describe the change in symmetry, a shift factor is introduced. The shift factor expresses the position of the resonant frequency with regard to the midrange position of the FWHM bandwidth (symmetry point). This difference is normalised to the FWHM bandwidth halved meaning a value of 0 is equal to a fully symmetrical peak while a value of 1 corresponds to the least symmetric situation with the resonant frequency and left FWHM bandwidth frequency aligning. At this point, also known as the bifurcation point, the slope of the power spectrum curve becomes infinite. Figure 5.10d shows this shift factor for the up and down sweep directions. The symmetry clearly decreased for higher accelerations with the up sweep direction being the most significant. From a harvester motion point of view the non-linear power spectrum can be described as the harvester realising the resonant frequency too late for the up sweep, and accordingly must counterbalance by a rapid increase in deflection (Figure 5.10a). For the down sweep the situation is the opposite. The harvester predicts the resonant point being closer hence the high frequency tail of the spectrum is much broader (Figure 5.10b) and with higher amplitude compared to the low frequency tail. This tail characteristic is present for both up and down sweeps, but most distinct for down sweeps.

5.6 Summary

This chapter presented a thorough characterisation of a representative unimorph harvester from the uniformity analysis in the following chapter. From impedance measurements an effective system coupling coefficient of 0.175 was found. This is close to the theoretic maximum value of 0.2 for a unimorph harvester. From the phase of the impedance two load values was

predicted for optimal power transfer. This was not in accordance with the empirical results from power vs. load analysis which showed a maximum power output over a broad load range of 20 kΩ to 150 kΩ. The discrepancy is believed to be caused by non-linear effects. The broad range of optimal loads provides a high degree of freedom in the design process for the electronic circuit connected to the harvester.

Measurements of the power output as function of excitation acceleration showed the expected squared relation between power and acceleration up to $0.3g$, while the measurements showed a decreasing proportionality a higher accelerations. Similar behaviour was observed for the peak deflection of the proof mass midpoint. By further analysis of the deflection in comparison with a bare silicon cantilever with similar geometry and design, it was concluded that the decreasing proportionality is caused be an increasing viscous damping coefficient for increasing accelerations. The effect of air damping in the increased viscous damping was analysed by characterising the harvester in vacuum. It was found that air damping contributes to the viscous damping, but it can only account for part of the observed tendency. The effect of material softening in the PZT film was examined by comparing the resonant frequency as function of acceleration for both the harvester and the bare silicon cantilever. With the resonant frequency being constant for the silicon cantilever, the analysis unambiguously proved the softening effect of PZT. The mechanical behaviour of the harvester is ultimately a complicated combination of a non-linear viscous damping and the non-linear softening effect. An analysis of the generated power as function of deflection squared showed linear relationship, hence concluding that the piezoelectric properties are considered constant and not affected by the non-linearities in the mechanical domain.

From the combination of analysis and regression of the power and deflection measurements at low accelerations, the mechanical quality factor measured with the harvester in short-circuit mode and the power vs. deflection, it was possible to verify the power output expression obtained in the theory chapter. The power expression will be used to elaborate tendencies in the next chapter where the uniformity characterisation is presented.

Chapter 6

Uniformity Characterisation

In the previous chapter a thorough analysis of a single harvester device was presented. This chapter will present a uniformity characterisation of the general harvester performance on a wafer level. A uniformity analysis is highly essential as it gives indications on the maturity of the fabrication process with regard to standardisations and application possibilities. The chapter will start with an overview of the wafers used in the characterisation followed by the uniformity analysis. Then, an overview of the development in device performance during the ELBA project is presented and lastly the achieved normalised power density are compared to other state of the art vibration harvesters with dimensions in similar range.

6.1 Wafers Characterised

The wafers used for the characterisation are listed in Table 6.1 and are based on two different batches of fabricated harvesters, each with two wafers. The first batch is fabricated using SOI wafers which gives precise control of the thickness of the silicon part (h_{Si}) in the unimorph harvester. The thickness of 20 µm is therefore predetermined from the SOI wafer, while the PZT layer thicknesses are in the range of 22 µm to 24 µm. The second batch is fabricated using conventional silicon wafers, which gives a reduction in fabrication cost but does not feature a build-in etch stop layer as the SOI wafer. The thickness of the silicon part of the cantilever can consequently vary from wafer to wafer, and additional the thickness can vary across the wafer due to differences in etch rate.

6.2 Wafer Level Analysis

The main purpose of the uniformity characterisation is to evaluate the average harvester characteristics from a fabricated wafer batch, and in this process examine the following variation. As evident from the theory chapter and the thorough analysis of a single device in the previous chapter, the harvester characteristics are determined by a number of geometric,

Table 6.1: *Wafers used in the characterisation process. The four wafers are all fabricated with the lateral harvester design presented in Section 4.1 on page 51 and Table 2.2 on page 27, the differences are on the silicon and PZT thick film thicknesses. The conventional silicon wafers are double side polished (DSP).*

Wafer ID	Type	Yield [%]	PZT (h_{PZT}) [µm]	Si (h_{Si}) [µm]
SOIW1	SOI	91.1	23	20
SOIW2	SOI	84.5	22	20
SiW1	DSP Si	93.3	25	36
SiW2	DSP Si	97.8	25	38

mechanical and electrical parameters. Accordingly, a thorough characterisation of all involved parameters is a comprehensive task. In view of that, an approach focusing on the application perspective is utilised with the analysis being reduced to the mapping of capacitance, impedance and shaker measurements including deflections. From this, a number of direct empirical quantities can be measured leading to the direct estimate of some parameters, and indirect estimates of the remaining. This will be elaborated during the data presentation. The uniformity analysis is performed at different stages during the development work, and as a result not all of the characterisations have been conducted on the four wafers investigated. Table 6.2 gives an overview of the individual wafers and measurements conducted, together with the quantities that can be directly measured and estimated.

From the characterisation of the individual harvesters on each wafer, the arithmetic mean ($\bar{x}$) and standard deviation (σ) are calculated together with the relative standard deviation (RSD)

$$\mathrm{RSD} = \frac{\sigma}{\bar{x}} \times 100 \tag{6.1}$$

which allows for comparing the variation and uniformity between the different wafers and parameters. Besides the mean based values, the uniformity analysis will be presented in form of histograms where the count is normalised to the device yield. Mappings of the different directly measured and calculated quantities listed according to the wafer layout is available in Appendix E on page 213.

6.2.1 Capacitance and Resonant Frequency

The majority of the geometric parameters, in particular the lateral ones, are determined by the lithography and screen printing process. Variation in these processes naturally occurs, but they are considered to be minor compared to the lateral dimensions of the harvester. For that reason the governing geometric parameters are considered to be the thickness of the silicon and PZT layers in the thin part of the cantilever. For the silicon part the thickness variation should be minimal for the SOI wafer, whereas a variation must be expected from the conventional silicon wafer due to KOH etch rate variations. A thorough analysis of etch

Table 6.2: *Overview of the wafers and experimental methods used for the uniformity analysis. From each experimental method one or more direct quantities can be measured or estimated directly. From these, the remaining parameters determining the characteristics of the harvester can be indirectly estimated. The experimental work is conducted at different stages in the development, hence some combinations are missing.* (*) *Only a representative selections of devices are characterised.*

Wafer ID	Cap. C	Impedance $Z_{\min}$, K_{eff}	Shaker: OC V_{oc}, F_{res}	Shaker: load P_{RMS}, F_{res}	Defl. w, Q_{load}
SOIW1	✓		✓	✓*	
SOIW2	✓		✓		
SiW1	✓	✓	✓	✓	✓
SiW2	✓	✓		✓	✓

uniformity by direct thickness mapping have not been conducted, only a limited number of random samples have been tested together with deviating devices, and likewise for the thickness of screen printed PZT layer. The variation in thickness of the PZT layer can also be indirectly estimated by measuring the PZT layer capacitance. Figure 6.1 shows a histogram of the measured capacitance for the four wafers characterised with results summarised in Table 6.3. The wafer characterisations plotted as wafer layout are available in Figures E.1a to E.1b on page 215 and Figures E.2a to E.2b on page 217. Besides some outliers in the low end, the histogram exhibits a normal distribution as expected from a reliable fabrication process. Identical design is used for all four wafers hence it is reasonable to assume the electrode area to be constant. The capacitance of the SOI wafers are as expected higher since the PZT layer thickness is lower than for the conventional silicon wafers (*SiW*). The variation is in general lowest for the *SiW* wafers, which is also evident from the histogram where e.g. 45% of the devices on wafer *SiW1* are within a capacitance interval of 0.1 nF. As it is assumed that the variations in electrode area defined by the shadow mask is relatively low, the observed variations in capacitance primarily arises from varying PZT layer thickness and dielectric constant. Decoupling the two requires extensive thickness analysis of the high roughness PZT layer. Assuming that the variation in capacitance originates solely from the thickness, the observed RSD corresponds to a thickness variation of 0.6 µm to 1.2 µm for the four wafers. With the nature of screen printing process, the layer thickness (20 µm to 25 µm) and high pressure treatment in mind, these absolute variations must be considered as being in the low end. Using the PZT layer thickness measured from a few random samples of each wafer, a dielectric constant of approximately 700 is estimated. This is lower than the value of 825 obtained in [39] for a similar high pressured treated PZT thick film. This indicates a higher porosity of the PZT thick film investigated in this work.

While indirect estimates of the PZT layer thickness can be extracted from the capacitance measurements, a mapping of the harvester resonant frequency can provide similar information on the thickness of both the silicon and PZT layer. Figures 6.2a to 6.2b shows the histograms of the frequency analysis divided into plots for the two types of wafers used. The measured

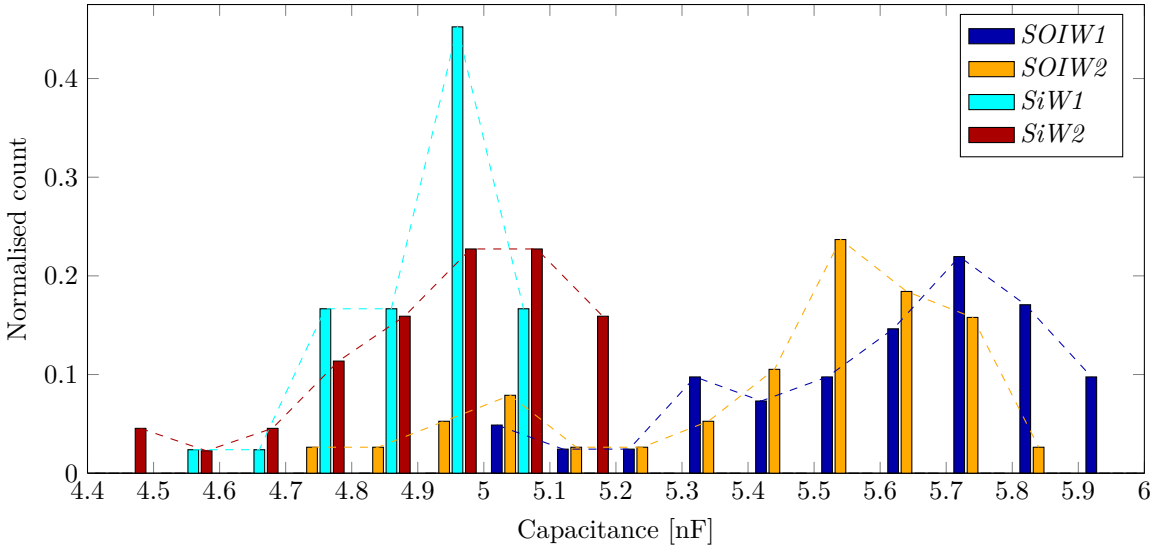

Figure 6.1: *Histogram of the measured capacitance for all four wafers. The spread is lower for the conventional silicon wafers compared to the SOI wafers. Assuming the variation is not caused by varying dielectric constants, the variation in capacitance gives a direct estimate of the variation in PZT layer thickness. The histogram count is normalised to the device yield of the individual wafers.*

Table 6.3: *Results of the uniformity analysis of capacitance and resonant frequency for the four wafers listed in Table 6.1 on page 94. Thickness values are obtained from profilometer measurements of a few random samples.*

	h_{PZT}, h_{Si}	Capacitance			Resonant frequency	
Wafer ID	[µm]	$\overline{C} \pm \sigma$ [nF]	RSD [%]	$\varepsilon_{33}/\varepsilon_0$	$\overline{F_{\mathrm{res}}} \pm \sigma$ [Hz]	RSD [%]
SOIW1	23, 20	5.64 ± 0.24	4.3	730	333.9 ± 9.4	2.8
SOIW2	22, 20	5.45 ± 0.29	5.3	675	312.9 ± 13.9	4.4
SiW1	25, 36	4.89 ± 0.12	2.4	688	482.8 ± 8.1	1.7
SiW2	25, 38	4.92 ± 0.18	3.6	691	511.6 ± 11.8	2.3

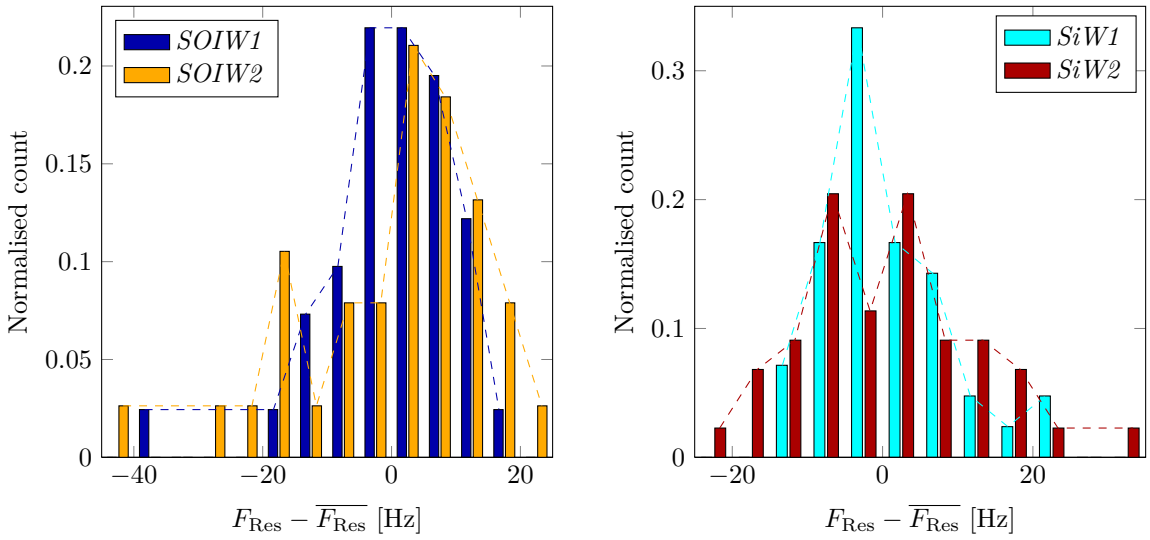

(a) *SOI wafers.* **(b)** *Conventional silicon wafers.*

Figure 6.2: *Histograms of the uniformity analysis of resonant frequency. For the purpose of overview the histograms are centred around the mean frequency which allows for direct estimation of frequency variations in absolute values. (a) Resonant frequencies obtained from peak observations in open circuit voltage measurements. (b) Resonant frequencies obtained from peak observations in power measurements.*

frequencies plotted as wafer layout are available in Figures E.1c to E.1d on page 215 and Figures E.2c to E.2d on page 217. The summarised uniformity results are listed in Table 6.3. The histograms are centred around the mean frequency values for each wafer dataset to allow for comparison as the mean frequencies differs from wafer to wafer. Accordingly the interesting overview of absolute spread in frequency is maintained compared to a normalisation. Besides a few outliers for the SOI wafer, the observations follows roughly a normal distribution with an absolute variation for both types of wafers of $\approx 20\,\mathrm{Hz}$ resulting in nearly similar standard deviation. From a fabrication perspective it is desirable to have a low variation in frequency as this indicates high uniformity control of the fabrication process. A slight spread in frequency can however also be used as an advantage. If the resonant frequency of the vibration source varies from e.g. changes in temperature, having several harvesters with slightly varying frequencies can cover this shift [55–57].

When comparing the obtained RSD numbers for frequency and capacitance, the variation is in general lower for the frequency while the numbers indicate a correlation between high variation in capacitance leading to high variation in frequency. While it can assumed that the variation in capacitance originates from variations in thickness and dielectric constant, the frequency is less straightforward to interpret since it is also governed by the silicon layer thickness, the material stiffness and density through the mass. Nonetheless, if the variation in capacitance is in fact caused by the PZT layer thickness, this variation must to some degree be present in the observations of the frequency. To verify this, the normalised resonant frequency is in Figure 6.3 plotted as function of the normalised capacitance for all four characterised wafers.

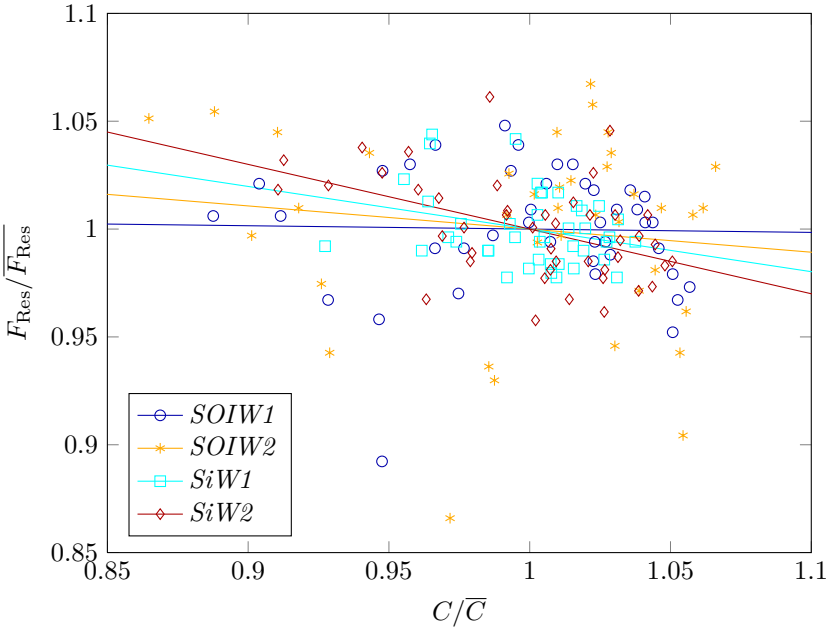

Figure 6.3: *Normalised resonant frequency as function of normalised capacitance for all four characterised wafers. Observations are plotted as points together with a linear fit including all observations for each wafer individually. With the capacitance being inversely proportional to the PZT layer thickness the frequency must accordingly follow a tendency inversely proportional to the capacitance. This trend is observed for all four wafers.*

Besides points for the individual observations a linear fit is added for each wafer. While the capacitance is inversely proportional to the PZT layer thickness, the exact frequency dependency of PZT thickness is a complicated function of effective stiffness with the silicon layer and neutral plane position. The tendency will however be that increasing PZT thickness will cause increasing frequency. This inverse proportional tendency between frequency and capacitance is seemingly present for the linear fits in Figure 6.3. A correlation is found between slope and variation within each of the wafer types, whereas the overall correlation is less evident. This is expected with the numerous parameters that influences both frequency and capacitance. While it e.g. is reasonable to assume a low variation of stiffness and density for the silicon, the stiffness and density for PZT is expected to differ from the printing process and in particular the high pressure treatment process. Despite the complicated relation between frequency and the thickness of the PZT part of the cantilever, the simplified relation of frequency being proportional to $\sqrt{H^3}$ indicates an amplification of a variation in thickness. With precautions, it may accordingly be implied that the higher variation in capacitance is partly due to variations in dielectric constant and therefore porosity.

6.2.2 Voltage and Power Output

Impedance, load and deflection measurements have not yet been conducted on the harvesters from the SOI wafers, as a result it is difficult to evaluate any parameters others than the measured open circuit voltage. In view of that, the first part of the harvester performance analysis will only deal with the study and comparison of the variation in performance between the wafers. The uniformity analysis of the open circuit voltage (V_{oc}) for the SOI wafers and power output (P_{RMS}) for the *SiW* wafers are plotted in separate histograms in Figures 6.4a to 6.4b with results summarised in Table 6.4. The measurements are plotted as wafer layout in Figures E.1e to E.1f on page 215 and Figures E.3a to E.3b on page 219. The values for V_{oc} and P_{RMS} are the peak measurements from frequency sweeps in upwards direction. Same frequency sweeps from which also the peak frequency values in Figure 6.2 are extracted.

The analysis reveals a variation in V_{oc} that for the SOI wafers is more than 10 times higher compared to the V_{oc} of *SiW1*, and 6-8 times higher than the observed variations in the capacitance and frequency for the same wafers in Table 6.3 on page 96. Also evident from Table 6.4 is that the performance is considerable lower for both V_{oc} and for the power of the 10 representative harvesters from *SOIW1* compared to the *SiW* wafers. Compared to the observed variation in capacitance and resonant frequency for the SOI wafers, the variation in V_{oc} is unexpectedly high. This is most likely due to the quality factor and accordingly the power multiplication factor χ. Later deflection analysis of a single harvester from *SOIW1* under load conditions with a RMS acceleration of $0.5g$ measured a loaded quality factor of 48. This must be compared to a Q_{load} of 191 for the *2D* harvester from *SiW1*. Due to the asymmetric response function Q_{load} is calculated from proof mass midpoint deflection and hence potentially holds a considerable error. Since the quality factor is proportional to the resonant frequency, it is expected to be only 2/3 (330 Hz/500 Hz) of that for the *SiW1*

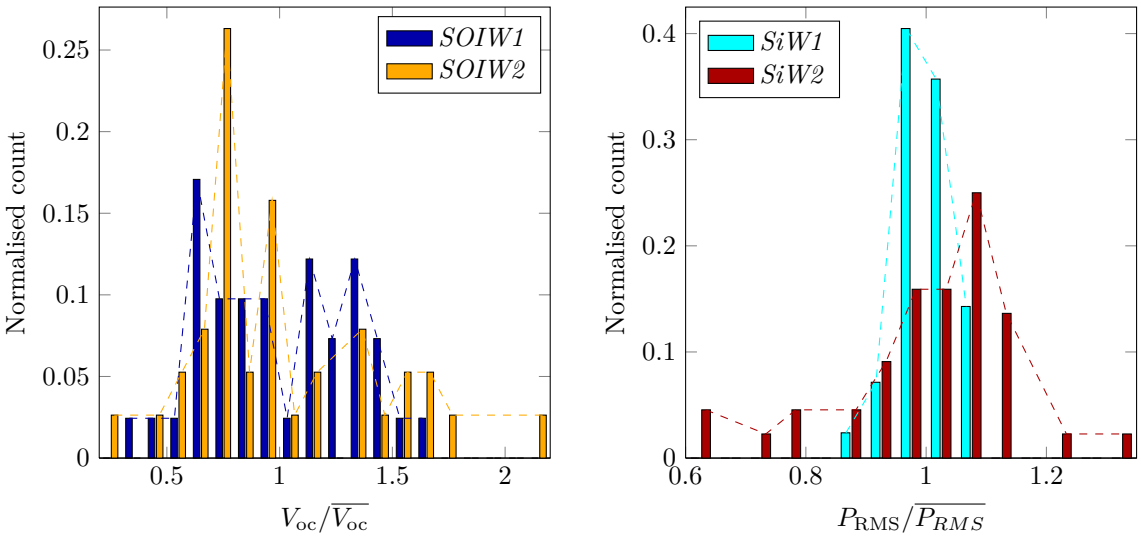

(a) *Normalised open circuit voltage.* **(b)** *Normalised power output.*

Figure 6.4: *(a) Histogram of the normalised peak RMS open circuit voltage for the two SOI wafers. (b) Histogram of the normalised peak RMS power output for the two conventional silicon wafers. The measurements are performed with an excitation acceleration of 0.5g*

Table 6.4: *Results of the uniformity analysis of open circuit voltage for the SOI wafers and SiW1 and power output for the two conventional silicon wafers. The variation is significantly higher for the SOI wafers compared to the SiW wafers. This is believed to partly originate from higher deflections and therefore effect of softening at identical excitation accelerations of 0.5g.* (*) *Only 10 representative harvester have been characterised.*

	Open circuit voltage		Power output		
Wafer ID	$\overline{V_{oc}} \pm \sigma$ [V]	RSD [%]	Load [kΩ]	$\overline{P_{RMS}} \pm \sigma$ [µW]	RSD [%]
SOIW1	1.60 ± 0.52	32.2	$50 - 150^*$	$7.3 \pm 3.0^*$	41.5^*
SOIW2	1.38 ± 0.55	40.0	-	-	-
SiW1	2.85 ± 0.06	2.4	75	31.0 ± 1.4	4.6
SiW2	-	-	50	34.5 ± 4.6	13.4

harvester. The remaining decrease is caused by a changed thickness ratio of PZT to silicon. From Figure 5.7b on page 85 it was evident that the quality factor of silicon is higher than for PZT, and with a higher PZT/silicon thickness ratio the low quality factor of PZT becomes increasingly dominant. This naturally leads to a considerable decrease in power output since the power is directly proportional to the mechanical quality factor which naturally is related to Q_{load}. A second effect of decreasing quality factor is that the multiplication factor χ will decrease and in addition the variation in system coupling coefficient will become more significant. This is treated further in the next section. In total, the power output of the 10 representative harvester from *SOIW1* seen in Table 6.4 is less than 1/4 of the power of the *SiW* wafers and with a significantly larger variation. For the *SiW* wafers the variation in power performance is considerable higher for *SiW2* compared to *SiW1* and originates from a few outlying harvesters with both higher and lower power performance as seen in Figure 6.4b. Disregarding the highest and the three lowest outliers, the variation is decreased from 13.4% to 9.2%. The increase in variation from open circuit voltage to power for *SiW1* is naturally expected as power is proportional to voltage under load conditions squared.

6.2.3 Loaded Quality Factor and K_{eff}

The remaining part of the uniformity analysis will focus on the two conventional silicon wafers and the results obtained from the impedance and deflection measurements, and it will be attempted to use the result in a comparison with the theoretically predicted power. From the thorough characterisation in the previous chapter, the following expressions

$$P = P_{\text{av}}\chi = \frac{F_{\text{ext}}^2}{4b}\chi = \frac{F_{\text{ext}}^2 Q_{\text{mec}}}{4m_{\text{eff}}\Omega_0}\chi \tag{6.2a}$$

$$\chi = \frac{2}{1+\sqrt{1+\dfrac{1}{Q_{\text{mec}}^2 K_{\text{eff}}^4}}} \tag{6.2b}$$

were verified. Accordingly the generated power can be determined by a power available term P_{av} and a multiplication factor χ equal to or less than 1. Both the total mass and effective mass are determined mainly by geometries defined with lithography, hence they are expected to differ only slightly. With the assumption that the natural frequency is equal to the frequency where peak power is obtained (F_{res}), the missing parameters in the power expression is the χ factor and the viscous damping coefficient b hence also the mechanical quality factor Q_{mec} as these are closely related. The effective system coupling coefficient K_{eff} which is required for evaluating χ, is calculated directly from the impedance measurements. Determining either b or Q_{mec} is on the contrary less straightforward than the other parameters in the uniformity analysis. As evident from the thorough analysis in the previous chapter, the viscous damping coefficient can be extracted using the following three approaches:

1. Extraction from power vs. acceleration at low accelerations using the power expression.
2. Extraction from power vs. deflection using the power expression.

3. Estimation from mechanical quality factor calculated from short-circuit mode.

The first two methods are related since they both rely on the power expression in Equation (6.2a), and they require numerous acceleration measurements. Especially the first approach requires several measurements at low accelerations where the non-linearity is less pronounced. In addition the second one requires a reasonable estimate of the loaded quality factor. Ideally the third approach should be used, but as clearly illustrated in Figures 5.7a to 5.7b on page 85 the non-linearity is severely affecting the short-circuit measurements due to the increased deflections compared to the loaded situation.

While the first approach listed is too time-consuming and the third approach is too uncertain due to non-linearity the second approach is potentially useful. At the time of characterisation, the loaded quality factor was calculated from the deflection measurements in the same frequency sweeps as the power output in Figure 6.4b was extracted. Using this loaded quality factor and Equation (5.15) on page 88 the viscous damping coefficient can be calculated. The approach is however vulnerable to a high error since only a single measurement at $0.5g$ acceleration is available and the uncertainty in the determination of Q_{load} due to the manual laser alignment for each harvester is significant. In the following analysis the obtained loaded quality factor is therefore used in a more comparative manner. In the theory chapter the mechanical quality factor was found to be roughly four times higher than the loaded quality factor. Assuming that this ratio is comparable from harvester to harvester a tendency should exist between a high loaded quality factor and power. If this is the case is examined in the following.

The results from the uniformity characterisation of the calculated K_{eff} is plotted in Figure 6.5a with summarised results listed in Table 6.5. The characterisation plotted as wafer layout is available in Figures E.3c to E.3d on page 219. The coupling K_{eff} for *SiW1* is slightly (7.8%) higher than for *SiW2* which also has a higher variation due to the outliers in both low and high end as seen in Figure 6.5a. In Section 5.2 on page 76 a theoretic maximum coupling coefficient of 0.2 was found for a unimorph harvester. The calculated K_{eff} is 10-25% lower than this, which is expected since the 0.2 represents an ideal unimorph piezoelectric structure. From the theoretic expression for the system coupling coefficient in Equation (2.58) on page 35 it can be identified that K_{eff} is proportional to the piezoelectric coefficient d amongst others. Again separation of the parameters is difficult, but a low variation in K_{eff} may imply a low variation in d. It will however be illustrated later that compared to Q_{mec} the variations in K_{eff} and d are insignificant, especially for high values of Q_{mec}.

The uniformity analysis of the calculated Q_{load} is seen in Figure 6.5b, with raw wafer layout data in Figures E.3e to E.3f on page 219. The calculated values are except from some outliers on wafer *SiW2* normally distributed. The average Q_{load} for *SiW2* is 16% higher than *SiW1*. This follows the results from the power characterisation in Table 6.4 where the average power output for *SiW2* was 10% higher than for *SiW1*. The dissimilarity in difference percentage is expected, because while the power is assumed proportional to Q_{load} through Q_{mec}, it is inversely proportional to the resonant frequency which according to Table 6.3 on page 96 in

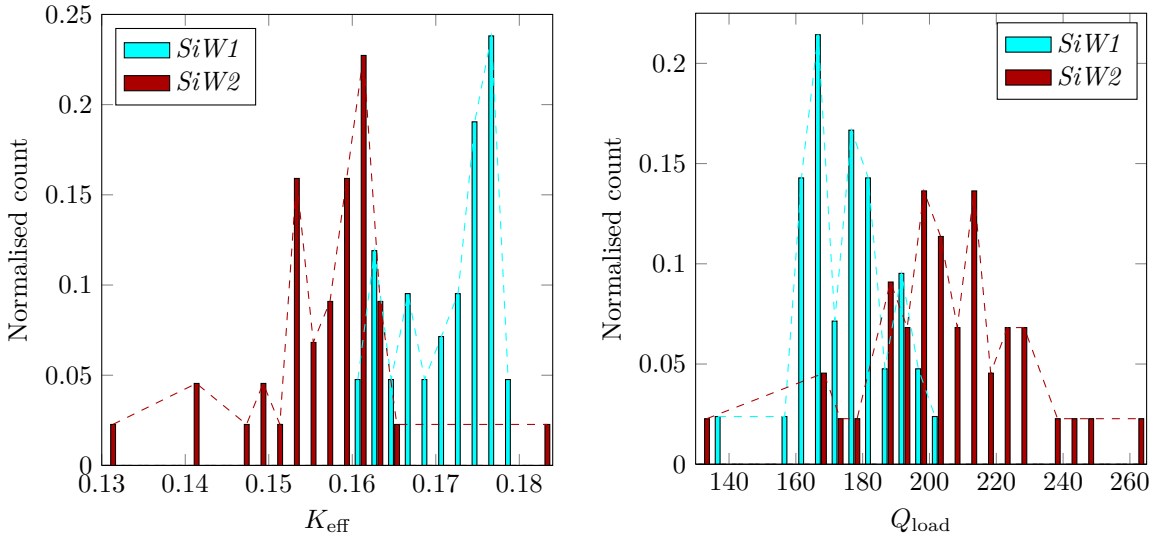

(a) **(b)**

Figure 6.5: *(a) Histogram of the effective system coupling coefficient estimated from the impedance measurements. The theoretic maximum coupling coefficient is in Section 5.2 on page 76 determined to 0.2. (b) Histogram of the estimated loaded quality factor. The histogram for Q_{load} has a high similarity with the power histogram in Figure 6.4b on page 100 emphasising the significant relation between the two through Q_{mec} in P_{av}.*

Table 6.5: *Summarised results of the uniformity analysis of the effective system coupling coefficient and loaded quality factor. K_{eff} is in average slightly higher for SiW1 while the calculated average Q_{load} is higher for SiW2. The higher quality factor is in accordance with the higher power for SiW2 listed in Table 6.4. Similarly the Q_{load} variation for SiW2 is higher.*

	K_{eff}		Q_{load}	
Wafer ID	$\overline{K_{\text{eff}}} \pm \sigma$	RSD [%]	$\overline{Q_{\text{load}}} \pm \sigma$	RSD [%]
SiW1	0.1708 ± 0.0055	3.2	175.8 ± 13.0	7.4
SiW2	0.1563 ± 0.0076	4.8	204.7 ± 22.3	10.9

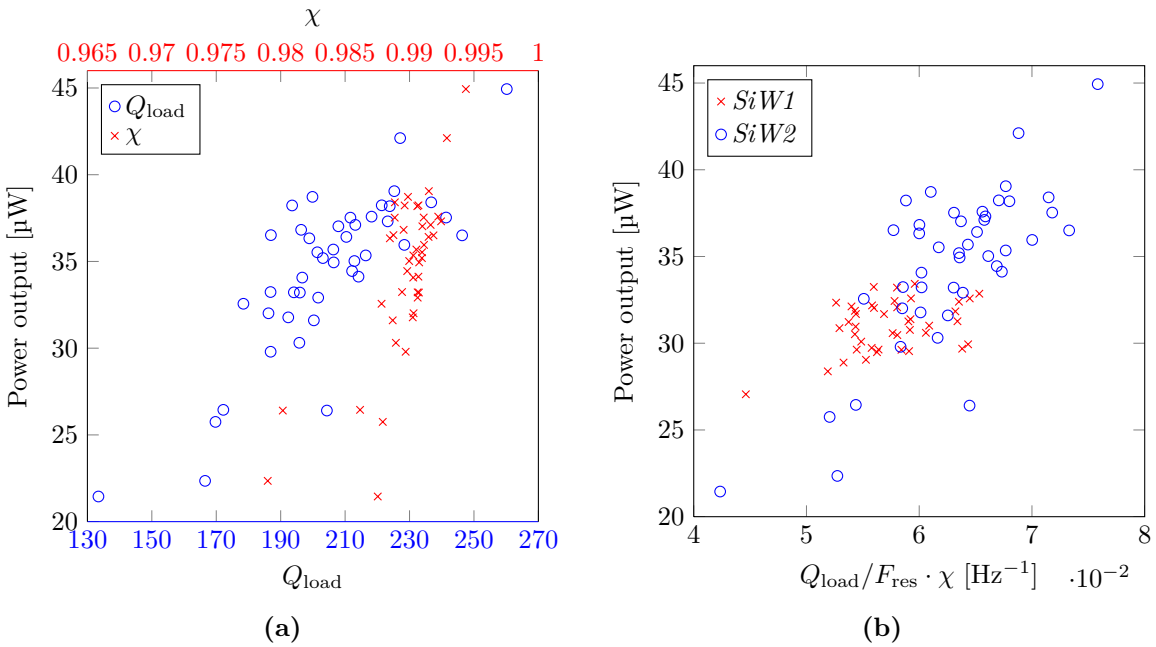

Figure 6.6: *(a) Power output for SiW2 plotted as function of both Q_{load} and χ. The linear relationship predicted by theory is most evident for Q_{load} and for the outlying observations. (b) Power output for both wafers plotted as function of the part of the power output expression estimated from the impedance measurements. Again linear relationship is predicted from theory.*

average is 5% higher for *SiW2*. The RSD variation for *SiW2* is significantly influenced by the lowest and highest outlier. Discarding these two outliers the variation decreases to 8.8%. It is expected that the variation in Q_{load} is higher than for the power due to the manual alignment of the laser deflection measurement system.

To test the general experimental coherence of the power prediction in Equation (6.2a), the generated power is in Figure 6.6a plotted as function of both Q_{load} and the multiplication factor χ. For the evaluation of χ from Equation (6.2b) the loaded quality factor is used instead of Q_{mec}. This naturally introduces an error since Q_{load} is smaller than Q_{mec}, nonetheless it should be sufficient to observe the expected tendency. Similarly, it is again assumed that the power is proportional to Q_{load} through Q_{mec} and that the difference is a factor which is complicated by the non-linearity of the system. Though a relatively large spread is observed Figure 6.6a visibly confirms the linear relation between P_{RMS} and Q_{load} while the linear relation with χ is less noticeable. Even with the smaller Q_{load}, the χ factor is close to the maximum value of 1 which is in coherence with the predictions from the design optimisation in Section 2.10 on page 36 of the theory chapter. The loaded quality factor and χ factor can be multiplied and divided by the resonant frequency F_{res} which then comprises the part of the power in Equation (5.7a) that is obtained from the different parts of the uniformity characterisation. The result is plotted for both *SiW* wafers in Figure 6.6b and again the linear tendency for especially *SiW2* is visible due to the outliers. Ideally the power measurements in

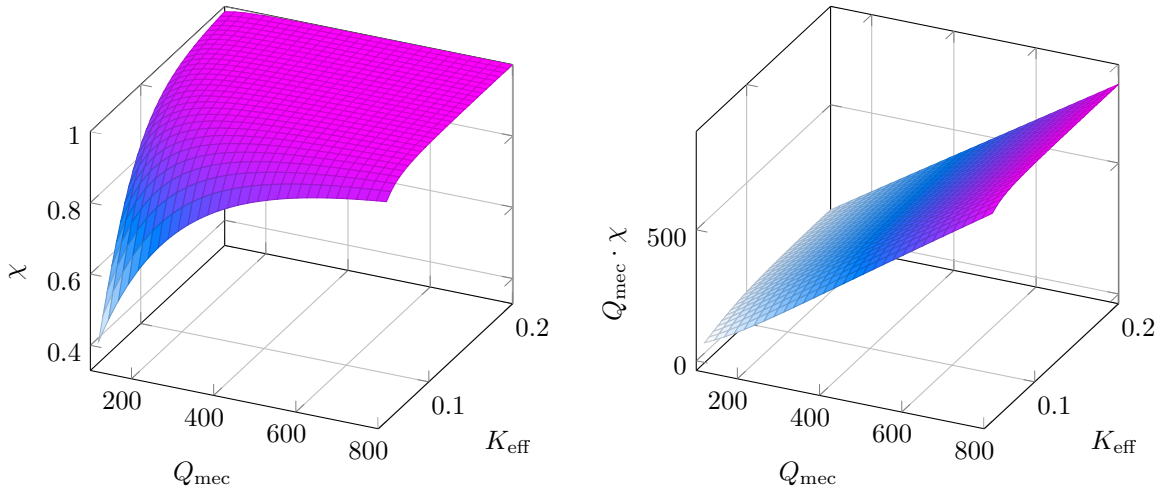

Figure 6.7: *Effect of the mechanical quality factor and effective system coupling coefficient on the power performance of a vibration harvester. (a) The multiplication factor χ defines the amount of power extracted from the available of the system (P_{av}). Although K_{eff} which is proportional to the essential piezoelectric coefficient d is an important parameter, high values of Q_{mec} will always lead to a high χ factor. Examining the product of Q_{mec} and χ the significant importance of Q_{mec} over K_{eff} is highlighted.*

Figure 6.6 should have been plotted against the inverse viscous damping coefficient b instead of Q_{load}. This would most likely decrease the spread observed in the linear tendency.

As stated previously, the exact value and hence variation of the piezoelectric constant and accordingly K_{eff} might be insignificant in comparison with the value and resulting variation of Q_{mec}. This is theoretically illustrated in Figures 6.7a to 6.7b where both the χ factor and $Q_{\text{mec}} \cdot \chi$ is plotted as function of Q_{mec} and K_{eff}. From the thorough analysis it was found that the mechanical quality factor will approach 800. As evident from Figure 6.7a the effect of changes in K_{eff} becomes increasingly insignificant for these high values of Q_{mec}. The major significance of Q_{mec} over K_{eff} and hence d is further highlighted when considering the product of Q_{mec} and χ which determines the harvesting properties in the power expression Equation (6.2a) for a cantilever with a given frequency and input acceleration.

6.2.4 Power Spectrum Bandwidth

The final parameter analysed in the uniformity characterisation is the bandwidth F_{BW} of the power spectrum. Despite the significant influence from the non-linear effects on the bandwidth illustrated in Figure 5.10 on page 89 the bandwidth is an interesting parameter for applications. As mentioned previously, the peak acceleration frequency of a vibration source will in nearly all situations fluctuate slightly, and a harvester with high bandwidth is more likely to cover this shift. The price for a higher bandwidth is naturally a lower peak deflection and hence peak power. The obtained values for bandwidth will additionally be

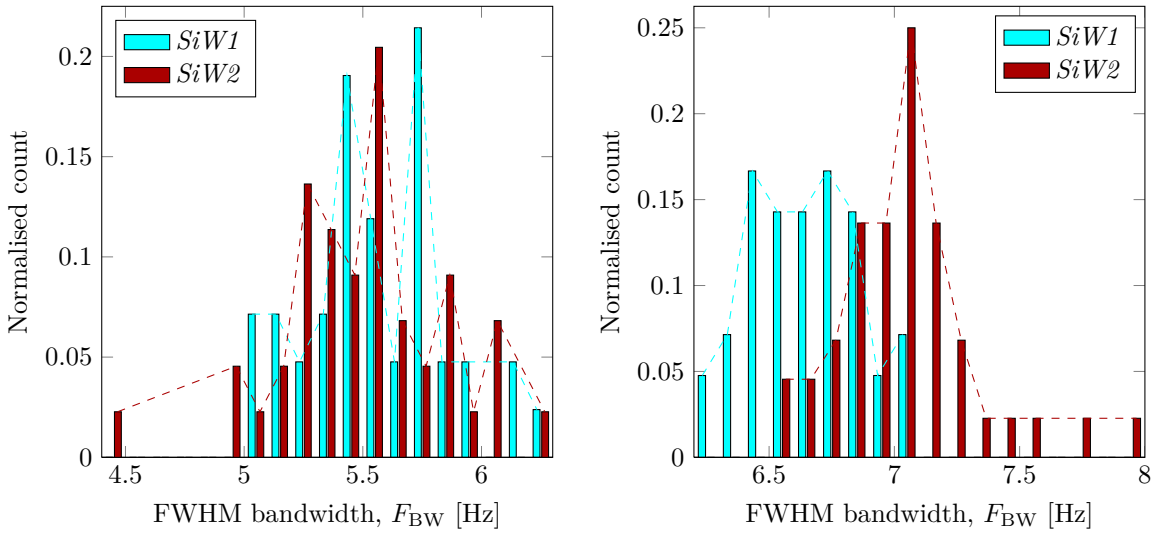

(a) *Bandwidth up sweep.* **(b)** *Bandwidth down sweep.*

Figure 6.8: *Power spectrum bandwidth uniformity analysis. (a) Bandwidth obtained when frequency is swept from low to high. (b) Bandwidth for a sweep from high to low frequency. The non-linearity effect from material softening causes the bandwidth to increased for down sweep.*

used for calculating a figure of merit which can be used to compare the ELBA harvester with other state of the art vibration harvesters.

The bandwidth analysis is shown as histograms in Figure 6.8 for both up and down directions used in the frequency sweeps. For the upwards frequency sweep in Figure 6.8a the bandwidth is almost identical for the two wafers as summarised in Table 6.6. With a normal distribution of the observations, the variations in bandwidth for the two wafers differs only slightly. When evaluating the bandwidth from downwards frequency sweeps which is plotted in Figure 6.8b the bandwidth is increased for both wafers. This is in accordance with the observations in Figure 5.10c. The increase for *SiW1* is 20% while for the *SiW2* wafer the increase in bandwidth is 29% when changing from up to down sweep direction. Since the suggested figure of merit from [12] is proportional to the bandwidth, the evaluation of bandwidth is

Table 6.6: *Results on FWHM bandwidth characterisation of the power spectrum for the two wafers. The bandwidth is higher for the down sweep direction where frequency is changed from high to low. This is an effect of the material softening of PZT. The last section in the table is a count of harvesters with resonant frequency in a range of half the mean bandwidth from the median resonant frequency.*

	F_{BW} up sweep		F_{BW} down sweep		$F_r \lessgtr (\widetilde{F_r} \pm \overline{F_{BW}/2})$	
Wafer ID	$\overline{F_{BW}} \pm \sigma$ Hz	RSD [%]	$\overline{F_{BW}} \pm \sigma$ Hz	RSD [%]	Up [%]	Down [%]
SiW1	5.56 ± 0.29	5.2	6.71 ± 0.45	6.7	35.7	40.5
SiW2	5.50 ± 0.34	6.0	7.07 ± 0.25	3.6	15.9	18.2

Table 6.7: *Development in harvester performance during the ELBA project. The figure of merit (FOM) is defined in order to examine performance across different excitation accelerations, volumes and resonant frequency. Non-linearity is not taken into account, and ideally all evaluations should be performed at an identical low accelerations.* (‡) *Work conducted prior to ELBA.* (*) *PZT thick film is high pressure treated.* (†) *Results are based on average performance for a full wafer.*

Time	Ref.	h_{Si} [µm]	h_{PZT} [µm]	Acc. [g]	Power [µW]	F_{res} [Hz]	F_{BW} [Hz]	Load [kΩ]	FOM [Hz·mW/cm^3/g^2]
June-09‡	[36]	20	30	2.2	2.86	659	13.5	48	0.66
Nov-09‡	[37]	20	30	0.48	2.304	213	4	168	2.24
June-10	[38]	20	12*	1	7.5	185	6	188	2.31
June-10	[40]		2×30	0.09	0.05	337	4	287	1.37
Dec-10	[41]	20	15*	1	13.98	235	8	100	5.74
Feb-11	[58]		2×30	1	7.35	345	7.55	400	2.85
June-11	[43]		$2 \times 20^{*}$	0.5	14	243	7.8	140	22.40
Dec-11	[59]		$2 \times 20^{*}$	1	37.1	248	7	200	13.32
May-12	[60]	20	22*	0.5	7.3	333	9	60	13.48†
Aug-12	*SiW1*	36	25*	0.5	31.0	482.8	6.14	75	39.01†
Aug-12	*SiW2*	36	25*	0.5	34.5	511.6	6.29	50	44.48†
Aug-12	*SiW2-2A*	36	25*	0.5	44.9	543	6.8	50	63.03

vital.

The last section of Table 6.6 contains information of how many fabricated harvesters on each wafer that has a resonant frequency in the range of ± half the mean bandwidth from the median resonant frequency. The analysis is performed for both wafers using bandwidths obtained from both upwards and downwards frequency sweeps. For the *SiW1* wafer 35.7%-40.5% of the fabricated harvesters matches within this range, while only 15.9%-18.2% meets this requirement for *SiW2*. The better matching on wafer *SiW1* is expected since the variation in frequency is slightly lower according to Table 6.3. The number of matching harvesters within this range is important in the process of standardising the fabrication process towards applications.

6.3 Harvester Development and Comparison

The harvester characterisation presented in this chapter until now is primarily based on the latest harvester batch fabricated using conventional silicon wafers. Throughout the project the harvesters from each new progress in the fabrication iteration have been characterised. The results from this development process is listed in Table 6.7. The characterisation is naturally conducted at different stages in the project, hence comparison is complicated slightly. The figure of merit presented in Section 1.4.5 on page 15 of the introduction is therefore used. The normalisation with respect to the acceleration squared is in accordance with the expected proportionality from theory, but as evident in Figure 5.5 on page 80 the power de-

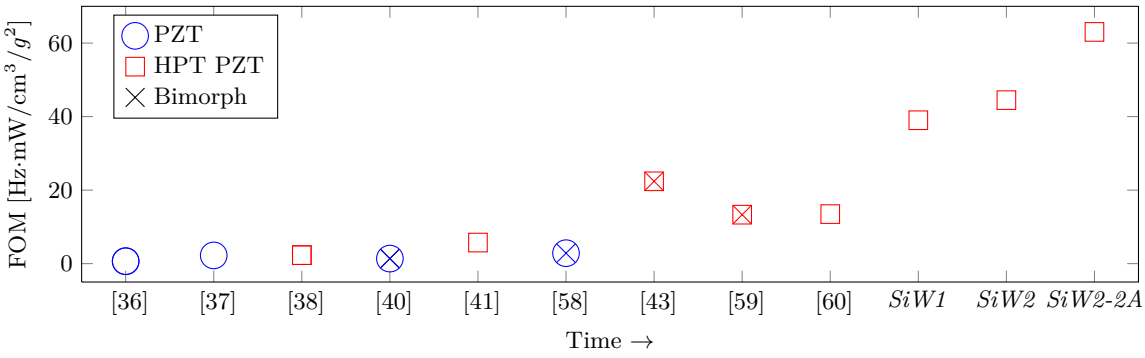

Figure 6.9: *Development in figure of merit prior and during the ELBA project. The achieved FOM continuously increases over time, and especially the introduction of high pressure treatment (HPT) in the screen printing process provided a considerable impact. Meanwhile the fabrication yield has been significantly increased from a single harvester out of a wafer to nearly full yield, accordingly the second to the fourth latest results are based on average values from a full wafer.*

viates from this squared relation at increased acceleration due to the non-linear effects. The degree of discrepancy from the squared tendency depends on the individual harvesters, and consequently the FOM will suffer from this.

The FOM results in Table 6.7 are plotted in Figure 6.9 as a function of time progressing towards right. It should be noted that the first two results are from work conducted prior to the ELBA project. Despite the first attempt which suffered from issues in the fabrication process, the introduction of high pressure treatment (HPT) in the screen printing process increased the performance considerably. Further increase was achieved with the introduction of the bimorph harvester where stress in the full cantilever contributed to the power. This advantage of the bimorph is however succeeded in the latest batch of unimorph harvesters where the thicker silicon support results in a considerable higher quality factor. Parallel with the improvement in FOM the fabrication yield has been significantly increased from a single harvester to a full wafer, with the latest results being based on average values from a full wafer.

From the energy budget in Section 1.2.1 on page 4 of the introduction, it was concluded that a steady DC power supply of 9 µW was required to operate the wireless sensor node with one measurement cycle every minute. With the AC to DC conversion and hence loss in the rectifier combined with loss of charging and storing the power in the sleep intervals, the harvester power of 32 µW at $0.5g$ might be sufficient. Since the purpose of the sensor is to measure long-term characteristics, the measurement cycle rate can be decreased to e.g. once an hour, thereby reducing the required vibration acceleration, or alternatively more harvesters can be combined.

Table 6.8: *Comparison of harvesting performance between the ELBA harvesters and state of the art harvesters with similar resonant frequency and device size. The sol-gel device has the lowest performance due to the limited thickness of the active piezoelectric layer. The AlN harvester is generating reasonable power but the FOM is low due to narrow bandwidth caused by a high quality factor. The highest normalised power density is obtained for the ELBA harvester, by nearly a factor of 3.5 over the bulk PZT harvester. The FOM including bandwidth is highest for the bulk PZT harvester as the bandwidth is 5 times wider than the ELBA harvesters.*

Reference	Type	Acc. [g]	F_{res} [Hz]	P [µW]	F_{BW} [Hz]	P norm. [mW/cm^3/g^2]	FOM [Hz·mW/cm^3/g^2]
Shen [15]	Sol-gel PZT	0.75	183	0.42	0.8	0.31	0.25
Aktakka [12]	Bulk PZT	1.5	415	160.8	33.3	2.65	88.2
Elfink [18]	AlN	2	572	60	2	1.00	2.0
SiW1	Thick film PZT	0.5	482.8	31.0	6.14	6.36	39.0
SiW2	Thick film PZT	0.5	511.6	34.5	6.29	7.08	44.5
SiW2-2A	Thick film PZT	0.5	543.0	44.9	6.8	9.21	63.0

6.3.0.1 Comparison with "State of the Art"

For conclusion, the normalised power density and FOM for the latest batch is compared against other state of the art vibration energy harvesters presented in literature. The devices used in the comparison are all aimed for the low frequencies while keeping the harvester footprint below 10 mm × 10 mm. Secondly they represent each of the four piezoelectric processing techniques sol-gel, sputtering, screen printing and bulk processing which have the potential of being used on a larger scale fabrication. The devices and their fabrication are reviewed in Section 1.4 on page 11. The ELBA harvesters are performing considerable better than the remaining three when considering the normalised power density. The FOM in which the power spectrum bandwidth is included, is highest for the bulk PZT based harvester as the bandwidth is considerable wider than the remaining harvesters. It is clear that the AlN harvester in the FOM comparison suffers from a narrow bandwidth compared the ELBA and bulk PZT harvester. This arises from the high quality for the AlN harvester [61], and consequently the effect in peak power of operating the harvester in vacuum is significantly higher compared to the lower load quality factor for the ELBA harvester [62].

6.4 Summary

This chapter presented the uniformity analysis of four wafers, two SOI wafers and two conventional silicon wafers. From the four wafers a total of 165 harvesters have been characterised. The uniformity analysis showed relative standard deviations in capacitance between 2.4% and 5.3% for all four wafers. With the electrode area determined by lithography the low variation in capacitance indicated a low variation in PZT layer thickness. This is supported by the characterisation of resonant frequency where variations of 1.7% to 4.4% were observed.

The indirect relation between a low capacitance equalling thicker PZT layer and expected higher resonant frequency was illustrated, though with precaution for a significant spread in observations.

The variation in harvester performance was found to be significantly higher for the wafers fabricated on SOI wafers compared to wafers fabricated with conventional silicon wafers. This is believed to originate from a lower quality factor as the silicon part is thinner. Consequently variations in PZT and the multiplication factor χ becomes more dominant. With lower quality factor the general performance was accordingly lower for the SOI wafers compared to the conventional silicon wafers. The average performance of the conventional silicon wafers at $0.5g$ was 31 µW and 34.5 µW respectively. The highest measured power at $0.5g$ was 44.9 µW. By comparing the generated power output with the measured loaded quality factor a linear tendency was observed. This is in accordance with theory since the loaded and mechanical quality factors are linked with a ratio that is difficult to determine due to non-linearities.

Finally the development in harvester performance during the ELBA project was presented, with special notice on the significant impact the high pressure treatment of the PZT film introduced. This improved process was facilitated by the introduction of KOH etching in the fabrication which also increased the yield considerably, culminating with the full wafer analysis presented. Using a normalised power density figure and a commonly used figure of merit that includes the power spectrum bandwidth, the performance of the latest ELBA harvester was compared with state of the art harvesters from literature. The ELBA harvester has the highest normalised power density by a factor of 3.5 compared to the next best. The ELBA harvester is succeeded by a bulk PZT based harvester when comparing the FOM. This is caused by a significant wider bandwidth for the bulk PZT harvester. The importance of a wide bandwidth with regards to applications can be argued, and if a bistable system which is presented in the following chapter is utilised, the bandwidth of the power spectrum peak is of little importance.

Chapter 7

Bistable Energy Harvester

From the characterisations presented in the previous chapters it was found that the ELBA harvester is able to generate an RMS power of approximately 30 µW with an input RMS acceleration of $0.5g$. Compared to the energy budget for the wireless sensor, this power should be adequate since a monitoring cycle with one measurement per hour is sufficient for most applications. This assumption is however only valid if the resonant frequency of the harvester and peak frequency of the source are matched. This crucial matching will needless to say exist at the time of mounting, but over time both the resonant frequency of the harvester and the peak frequency of the source might change. Secondly, pin-pointing one exact resonant frequency in the fabrication process with the numerous parameters involved, not to mention the non-linearity, is a challenge. The suggested solution to both potential critical issues is the implementation of a bistable vibration energy harvester. Preliminary work on such a system will be presented in the following.

7.1 Motivation

The main objective of a bistable energy harvester is to increase the harvesting potential from other frequencies than the harvesters resonant frequency. Since frequency matching is a major challenge in vibration energy harvesting, bistable systems have gained increasing interest in literature with numerous macro-scale proof of concepts presented in [63–68] and a few on micro-scale [69, 70]. The principle behind the bistable system is illustrated in Figure 7.1. For a conventional resonator the force acting on the cantilever is linear with deflection as depicted in Figure 7.1a. Here the non-linearities of the ELBA harvester is ignored. Examining the potential landscape caused by this linear force in Figure 7.1b, the conventional parabola shape emerges with a stable point at zero deflection, hence the system is *monostable*. If an external non-linear force is applied to the cantilever as seen in Figure 7.1a, the acting force will naturally be the sum of the two forces. Accordingly the potential landscape will change from monostable to bistable, since the cantilever is forced into one of two equilibrium positions or *saddle points*. For the cantilever to move between the two saddle points it must

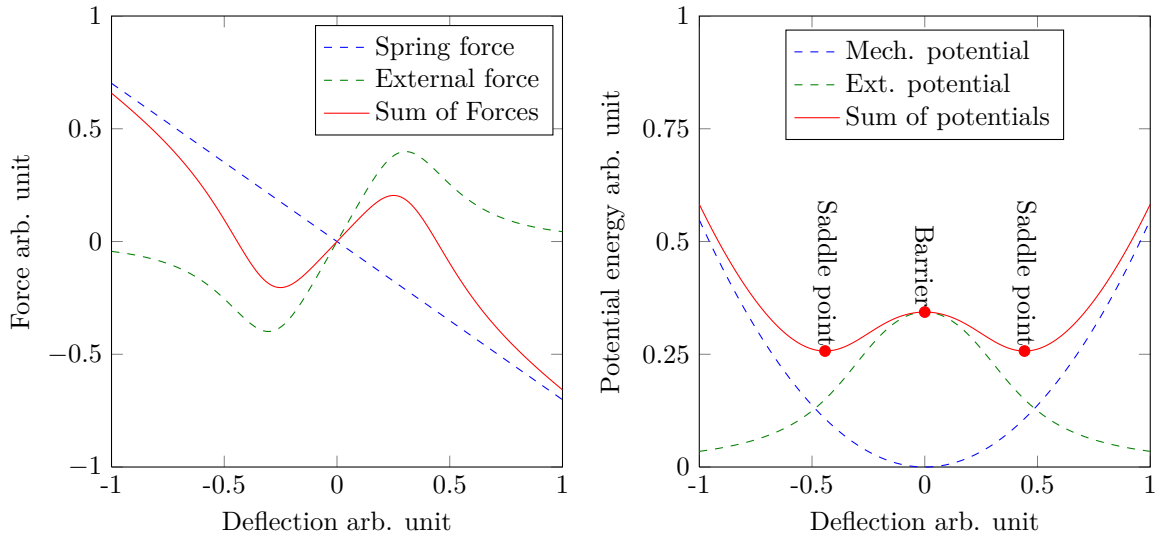

(a) *Force curves.* **(b)** *Potential energy curves.*

Figure 7.1: *(a) Spring force and external induced force acting on the cantilever as function of deflection. The sum of two forces causes the bistable behaviour. (b) Potential energy landscape for the harvester. With only spring force the cantilever is monostable. When external non-linear forces are present the harvester becomes bistable with two separate saddle points with a potential barrier between.*

gain a kinetic energy sufficient to overcome the potential barrier between the saddle points. As a consequence of the bistable characteristics, nearly all parameters in the motion of the harvester becomes non-linear. The spring constant defined by the curvature of the potential energy can be both increased or decreased and similar with the quality factor. For a full analytic description the system must be considered chaotic, and hence only the concepts will be treated here. Thorough reviews can be found in previously referred works.

Although the resonant frequency can be tuned by engineering the external force and consequently the shape of the potential wells, the interesting feature arises when the cantilever shifts from one saddle point to the other. With sufficient kinetic energy the cantilever will cross the potential barrier, and as a result the cantilever will experience an impulse of energy causing a momentarily excitation of the harvester at its resonance frequency [71–73]. Additionally the transition between saddle points will naturally cause a significant change in deflection and hence generated charge which is proportional to the deflection. The amount of power generated is therefore defined by the frequency of the shifts between the saddle points, and not the exact resonant frequency of the harvester.

7.1.1 Magnetic Bistable System

To obtain a bistable energy harvester, an external force is required which acts on the cantilever non-linearly with deflection. The most common method for applying the force is by

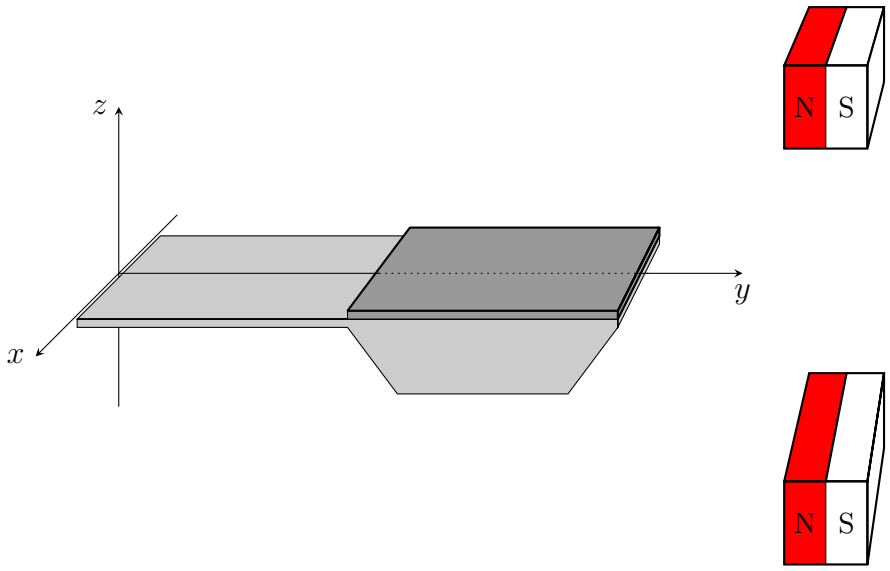

Figure 7.2: *Magnetic setup used with the ELBA harvester to achieve a bistable energy harvester. Instead of the most commonly used approach with a permanent magnet on the cantilever and one located oppositely, a thin iron foil is used for the ELBA harvesters. Two permanent magnets are then located oppositely, and with the attraction between foil and magnets the cantilever is forced into a bistable mode. Image from [75].*

implementing permanent magnets in the setup. The main advantage of permanent magnets compared to capacitive or electromagnetic forces [74] is that no energy is required, hence it is a fully passive system.

The majority of the magnetic bistable harvesters presented in literature uses a setup where a permanent magnet is positioned at the cantilever tip with another permanent magnet located oppositely. The repelling force of the magnets will force the cantilever into the bistable mode depicted Figure 7.1b. The magnetic setup used in the testing for the ELBA harvester is a slight modification sketched in Figure 7.2. Instead of placing a permanent magnet on the cantilever, a thin 50 µm soft magnetic iron foil is positioned on the proof mass of the cantilever and two neodymium magnets are located opposite the cantilever. The setup hence uses the attractive forces between the foil and the magnets, but the resulting potential landscape becomes similar as for the common used approach with repelling forces.

7.1.2 Preliminary Results

The bistable energy harvester has not been thoroughly tested during the ELBA project, hence the following preliminary results mostly serves as illustration of the potential of the bistable system. Figure 7.3 shows the output voltage for an ELBA harvester when it is operated in normal linear mode without magnets and when magnets are used to induce the bistable mode. The input acceleration is in both cases $0.5g$ and the frequency is 50 Hz. The peak voltage of

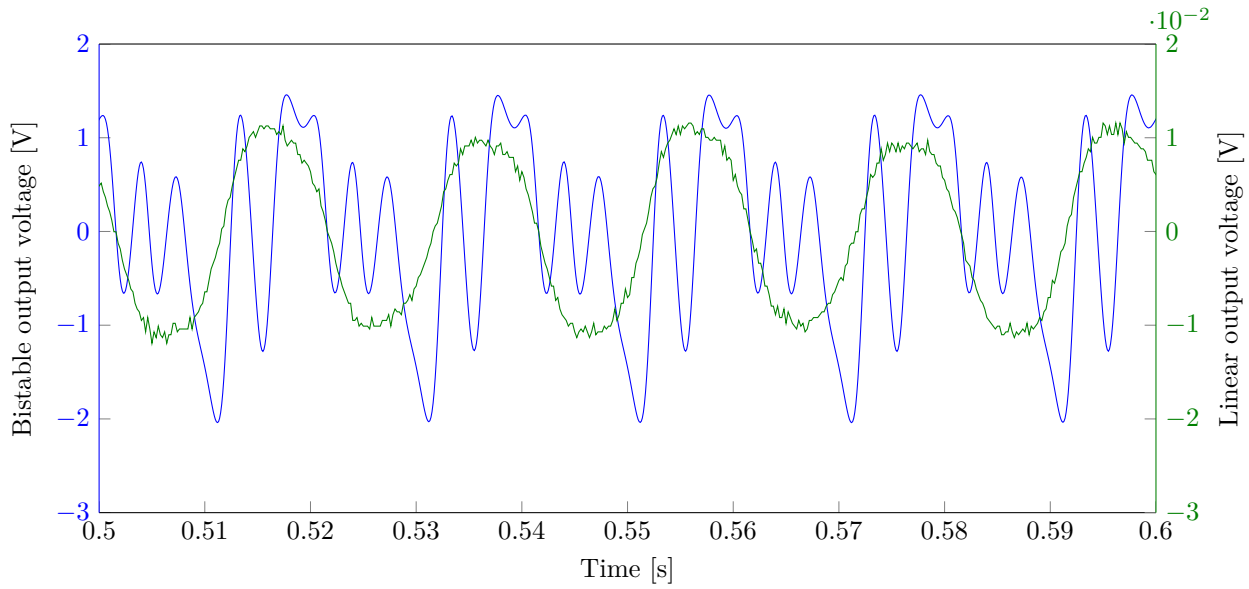

Figure 7.3: *Voltage output for a harvester under normal linear mode and under bistable mode. Both outputs are obtained with a* 50 Hz *input of 0.5g acceleration. The voltage output for the bistable mode is more than a 100 times higher than conventional linear operation.*

the bistable mode is more than a two orders of magnitude higher than for the linear mode. Since voltage is proportional to deflection it gives an indication of the saddle points positions. Besides shifting between saddle points with a frequency corresponding to the input frequency, the harvester also undergo considerable deflections at its resonant frequency. This shows up as an overlying voltage signal with a smaller amplitude but higher frequency.

The resulting frequency response for the generated power is plotted in Figure 7.4 again for the harvester operated in linear compared to bistable mode. In the linear mode without magnets, the harvester is only generating reasonable power around its linear resonant frequency of 340 Hz. When the magnets are forcing the harvester to become bistable, the frequency response changes from power being generated at a single sharp peak around resonance to a broad range of frequencies. Since the input acceleration of $0.5g$ is constant, the kinetic energy of the cantilever will be inversely proportional to the input frequency squared. Accordingly the possibility for the cantilever to cross the potential barrier between the saddle points increases with decreasing input frequency as evident from Figure 7.4. It should be stressed that the results obtained in Figures 7.3 to 7.4 are obtained with a setup where the magnets are decoupled from the shaker. As a consequence the increased displacement of the shaker for lower frequencies contributes to the cantilevers possibilities of crossing the barrier. At 50 Hz and $0.5g$ the shaker displacement is 50 µm giving a equal relative motion in relation to the magnets.

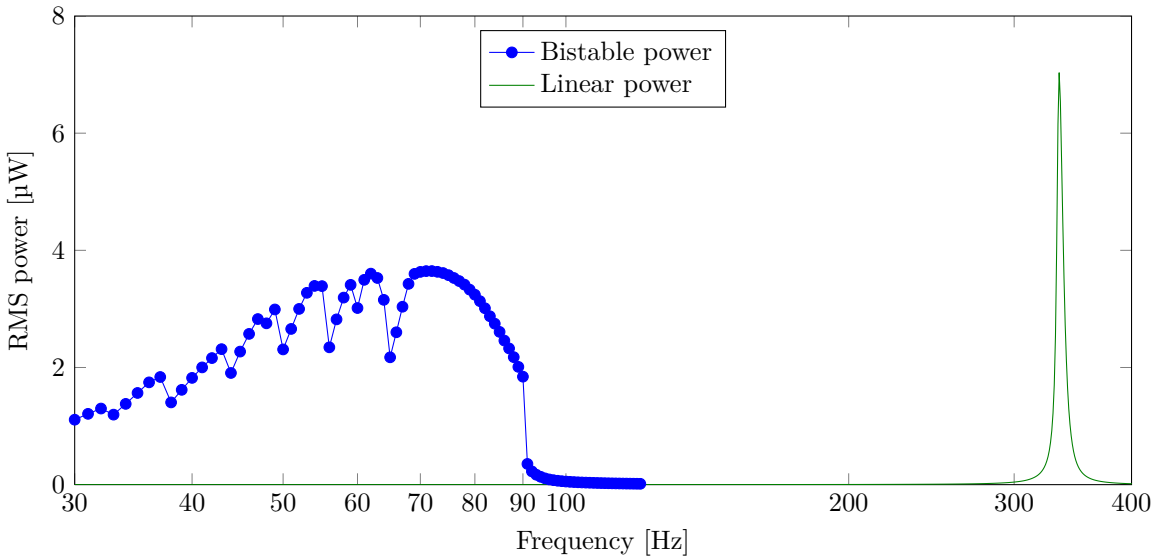

Figure 7.4: *Generated RMS power as function of frequency for both bistable and linear operation. Without magnets the harvesters natural frequency is around* 340 Hz*, and reasonable power is only generated around resonance. For the bistable harvester, power is generated over a frequency range of* 30 Hz *to* 90 Hz*. Excitation acceleration used is 0.5g.*

7.2 Summary

Implementing a bistable energy harvester will enable efficient power generation at low frequency vibration inputs. This will increase the application perspectives of the small-scale energy harvesting unit significantly. Future work will involve the testing with harvester and magnets both positioned on the shaker. As a result it will be more difficult to obtain a bistable system, but the conditions are more realistic from an application point of view. In general, significant development work is required for the bistable system since it is highly sensitive to the magnet positioning, and finally a solution is required for implementing the magnets in a future packaging for the harvester.

Chapter 8

Conclusion and Outlook

The main objective in this work has been to develop and fabricate a small-scale vibration energy harvester aimed towards integration in a wireless sensor system. Ultimately will such a sensor system provide the possibility for long-term autonomous monitoring at inaccessible locations where conventional battery shifts are infeasible.

The vibration harvester which consist of a thin cantilever covered with screen printed PZT and a large proof mass at the tip, was modelled as a single degree of freedom system. The mechanical and electrical domains were connected in a lumped element model with an ideal transformer between the domains. The transformation factor was found using the solutions to the Euler Bernoulli static beam equation. In comparison with numerical simulations from finite element software the derived cantilever characteristics was validated with an error of $<$ 1%. The resonant frequency of the cantilever was estimated using the Rayleigh-Ritz maximum energy method and again validated with an error of $< 1\%$ in a comparison with finite element simulations. The final expression for the generated power by the harvester at the resonant frequency was ultimately expressed as a power available term and a multiplication factor with a maximum value of 1. The power available term is proportional to the input force squared and inversely proportional to the viscous damping coefficient.

For the vibration harvester to generate an adequate amount of power to supply the sensor system, it is essential that the resonant frequency of the harvester matches that of the vibration source. Often do realistic sources of vibration have frequency in the range below 500 Hz which is a challenge since the dimensions of the harvester are restricted. As a consequence the thickness of the cantilever comprising the harvester must be decreased, and the proof mass at the cantilever tip increased. The outcome is a fragile cantilever structure which is challenging to fabricate with a satisfying yield. From extensive process development it has been accomplished to overcome this issue in the fabrication, and harvesters with resonant frequencies ranging from 180 Hz to 530 Hz have been fabricated. By screen printing the PZT thick film at an earlier stage than the cantilever definition, it has been possible to increase both the quality of the PZT thick film with high pressure treatment and the fabrication yield. With the PZT printed, the cantilever definition is performed with KOH etching using a mechanical

front side protection. The final fabrication process routinely achieves yields exceeding 90% and with the majority of the processes being on a batch level, the cost is minimised.

The characterisation of the fabricated harvester was divided into two parts; one with a thorough analysis of a single harvester and one with results from a uniformity analysis of 165 harvesters from four wafers. The thorough analysis of the single harvester representing the average performance of the latest fabrication batch, showed maximum power transfer for a range of connected loads from 20 kΩ to 150 kΩ. A wide range of optimal loads provides a higher degree of freedom and standardisation in the design process of the sensor system electronics. For low accelerations the power output followed the squared relation predicted by theory, but for higher accelerations declining proportionality was observed. Using regression and short-circuit measurements at low accelerations, a mechanical quality factor of 806 was derived for the harvester. From extensive analysis including vacuum characterisation and investigations of a similar silicon cantilever without PZT, it was found that the declining proportionality at increasing accelerations is caused by a significant increase in viscous damping. Furthermore it was unambiguously proven that the decrease in resonant frequency observed for increasing acceleration is caused by a softening effect in the PZT thick film. From vacuum characterisation it was found that the power output increases by 12% at 3 mbar relative to ambient conditions. Considering the increased complexity of achieving vacuum conditions in a future packaging solution, the 12% gain in power from vacuum may not be worthwhile. Using a combination of analysis and regression of different measurements it was possible to validate the theoretic predicted power derived from the theory with an error of $< 10\%$. An error that is considered within the uncertainty of measurements.

The uniformity characterisation of the devices from four wafers, two SOI wafers and two conventional silicon wafers showed a relative standard deviation in measured capacitance between 2.4% and 5.3%. With the electrode area determined by lithography the low variation in capacitance indicated a low variation in PZT layer thickness. This was supported by the characterisation of the resonant frequency where variations of 1.7% to 4.4% were observed. The indirect relation between a low capacitance equalling thicker PZT layer and expected higher resonant frequency was illustrated, though with precaution for a significant spread in observations. The variation in harvester performance was found to be significantly higher for the wafers fabricated on SOI wafers compared to wafers fabricated with conventional silicon wafers. This is believed to originate from a lower quality factor as the silicon part is thinner. Consequently variations in PZT and the multiplication factor χ becomes more dominant. With lower quality factor the general performance was accordingly lower for the SOI wafers compared to the conventional silicon wafers. The average performance of the conventional silicon wafers at $0.5g$ was 31 µW and 34.5 µW respectively. The best performing device generated 44.9 µW at $0.5g$. With a power requirement for the wireless sensor system of 9 µW DC and taking into account the loss in rectifier circuit and storage management, the generated power of the developed ELBA harvester should be adequate as power source.

Using a figure of merit where the generated power is normalised to total vibrating volume and acceleration squared and multiplied by the power spectrum bandwidth [Hz·mW/cm^3/g^2],

the development in harvester performance was examined. Compared to the first batch of harvesters, the figure of merit is for the latest harvester increase by a factor of nearly 30 from 2.31 to 63.03. Comparing the normalised power density [mW/cm^3/g^2] with other state of the art harvesters from literature, the ELBA harvester performs 3.5 times better than the next best which is a bulk PZT based harvester.

Preliminary results on a bistable energy harvester system for low frequency and increased bandwidth harvesting were presented. The attraction between a thin soft magnetic iron foil on the cantilever and two permanent magnets forces the cantilever into a bistable mode with two equilibrium positions in upwards and downwards direction. Measurements showed that the bistable mode increased the voltage output at 50 Hz by more than two orders of magnitude compared to normal linear operation. From a frequency response analysis it was found that the kinetic energy was sufficient between 30 Hz and 90 Hz for the cantilever to shift between the bistable positions. The resulting power in the range was between 25% and 60% of that generated at the linear resonant frequency of the harvester. The bistable system is however complex and future work is part of the outlook.

8.1 Outlook

While the fabrication process of the vibration harvesters routinely achieves a yield exceeding 90%, complications still occasionally arises mainly due to issues with adhesion between bottom electrode and silicon substrate. To prevent this, a new lithography mask with increased margin between trench etch and bottom electrode is implemented, but not yet evaluated. Even so, the use of the 500 nm thick platinum working as both diffusion barrier and bottom electrode is accounting for a substantial share of the fabrication cost. Possibilities of using other diffusion barriers to avoid or at least decrease the thickness of the platinum layers is therefore of great interest. Despite the unsuccessful first attempt of implementing electroplated platinum, this method should be investigated further as the cost is considerable less than e-beam evaporation.

The latest fabricated batch of conventional silicon wafers produced in average slightly over 30 µW at 0.5g RMS acceleration. This was obtained at resonant frequency around 500 Hz which is considered high for vibration harvesting. The high power was achieved due to a low viscous damping and accordingly high mechanical quality factor. Consequently, an attempt to decrease the resonant frequency by decreasing the thickness of the silicon support cantilever is expected to also decrease the mechanical quality factor. This was observed in the comparison between the SOI wafers and the conventional wafers in the uniformity analysis. Investigations should be carried out to see if the resonant frequency can be decreased without a significant decrease in mechanical quality factor. This naturally involves the method of adding a discrete mass in addition to the proof mass.

Overall a couple of challenges concerning frequency matching still exist. Fabricating a wafer aimed towards one single specific resonant frequency has not yet been attempted, and hence further development is required. Secondly the uniformity analysis revealed a high absolute

variation in frequency compared to the bandwidth, accordingly the uniformity across the wafers must be improved if a specific frequency is the objective. Many of the challenges concerning frequency matching can be avoided if a bistable harvester is implemented. Future development for the bistable system requires the base of the harvester and magnets to be coupling and secondly the precision of the magnets positions must be improved. The implementation of magnets with sub-µm alignment in a packaging solutions is expected to be challenging, hence the packaging and bistable solutions must be closely coordinated.

References

[1] David Stevens. Case history no.3 - bearing outer race damage, July 2012.

[2] Yabin Liao and Henry A Sodano. Model of a single mode energy harvester and properties for optimal power generation. *Smart Materials and Structures*, 17(6):065026, December 2008.

[3] Nicholas S Hudak and Glenn G Amatucci. Small-scale energy harvesting through thermoelectric, vibration, and radiofrequency power conversion. *Journal of Applied Physics*, 103(10):101301–101301–24, May 2008.

[4] R.J.M. Vullers, R. van Schaijk, I. Doms, C. Van Hoof, and R. Mertens. Micropower energy harvesting. *Solid-State Electronics*, 53(7):684–693, July 2009.

[5] Adnan Harb. Energy harvesting: State-of-the-art. *Renewable Energy*, 36(10):2641–2654, October 2011.

[6] S P Beeby, R N Torah, M J Tudor, P Glynne-Jones, T O'Donnell, C R Saha, and S Roy. A micro electromagnetic generator for vibration energy harvesting. *Journal of Micromechanics and Microengineering*, 17(7):1257–1265, July 2007.

[7] Daniel Hoffmann, Bernd Folkmer, and Yiannos Manoli. Fabrication, characterization and modelling of electrostatic micro-generators. *Journal of Micromechanics and Microengineering*, 19(9):094001, September 2009.

[8] Cuong Phu Le and Einar Halvorsen. MEMS electrostatic energy harvesters with end-stop effects. *Journal of Micromechanics and Microengineering*, 22(7):074013, July 2012.

[9] Marco Triches, Fei Wang, Andrea Crovetto, Anders Lei, Qiong You, Xiaoqing Zhang, and Ole Hansen. A MEMS energy harvesting device for vibration with low acceleration. *Procedia Engineering*, 47(0):770–773, 2012.

[10] S P Beeby, M J Tudor, and N M White. Energy harvesting vibration sources for microsystems applications. *Measurement Science and Technology*, 17(12):R175–R195, December 2006.

[11] Shad Roundy, Paul K. Wright, and Jan Rabaey. A study of low level vibrations as a power source for wireless sensor nodes. *Computer Communications*, 26(11):1131–1144, July 2003.

[12] E.E. Aktakka, R.L. Peterson, and K. Najafi. Thinned-PZT on SOI process and design optimization for piezoelectric inertial energy harvesting. In *Solid-State Sensors, Actuators and Microsystems Conference (TRANSDUCERS), 2011 16th International*, pages 1649 –1652, June 2011.

[13] Gang Tang, Jing-quan Liu, Bin Yang, Jiang-bo Luo, He-sheng Liu, Yi-gui Li, Chunsheng Yang, Dan-nong He, Viet Dzung Dao, Katsuhiko Tanaka, and Susumu Sugiyama. Fabrication and analysis of high-performance piezoelectric MEMS generators. *Journal of Micromechanics and Microengineering*, 22(6):065017, June 2012.

[14] Hua-Bin Fang, Jing-Quan Liu, Zheng-Yi Xu, Lu Dong, Li Wang, Di Chen, Bing-Chu Cai, and Yue Liu. Fabrication and performance of MEMS-based piezoelectric power generator for vibration energy harvesting. *Microelectronics Journal*, 37(11):1280–1284, November 2006.

[15] Dongna Shen, Jung-Hyun Park, Joo Hyon Noh, Song-Yul Choe, Seung-Hyun Kim, Howard C. Wikle III, and Dong-Joo Kim. Micromachined PZT cantilever based on SOI structure for low frequency vibration energy harvesting. *Sensors and Actuators A: Physical*, 154(1):103–108, August 2009.

[16] H. Jacobsen, H.-J. Quenzer, B. Wagner, K. Ortner, and Th. Jung. Thick PZT layers deposited by gas flow sputtering. *Sensors and Actuators A: Physical*, 135(1):23–27, March 2007.

[17] R. Lou-Moeller, C. C. Hindrichsen, L. H. Thamdrup, T. Bove, E. Ringgaard, A. F. Pedersen, and E. V. Thomsen. Screen-printed piezoceramic thick films for miniaturised devices. *Journal of Electroceramics*, 19(4):333–338, March 2007.

[18] R Elfrink, T M Kamel, M Goedbloed, S Matova, D Hohlfeld, Y van Andel, and R van Schaijk. Vibration energy harvesting with aluminum nitride-based piezoelectric devices. *Journal of Micromechanics and Microengineering*, 19(9):094005, September 2009.

[19] Steven R Anton and Henry A Sodano. A review of power harvesting using piezoelectric materials (2003 to 2006). *Smart Materials and Structures*, 16(3):R1–R21, June 2007.

[20] Heung Kim, Joo-Hyong Kim, and Jaehwan Kim. A review of piezoelectric energy harvesting based on vibration. *International Journal of Precision Engineering and Manufacturing*, 12(6):1129–1141, 2011.

[21] Salem Saadon and Othman Sidek. A review of vibration-based MEMS piezoelectric energy harvesters. *Energy Conversion and Management*, 52(1):500–504, January 2011.

[22] P. Bonello and S. Rafique. Modeling and analysis of piezoelectric energy harvesting beams using the dynamic stiffness and analytical modal analysis methods. *Journal of Vibration and Acoustics*, 133(1):011009–11, February 2011.

[23] A. Erturk and D. J. Inman. A distributed parameter electromechanical model for cantilevered piezoelectric energy harvesters. *Journal of Vibration and Acoustics*, 130(4):041002–15, 2008.

[24] Alper Erturk, Jamil M. Renno, and Daniel J. Inman. Modeling of piezoelectric energy harvesting from an l-shaped beam-mass structure with an application to UAVs. *Journal of Intelligent Material Systems and Structures*, 20(5):529–544, March 2009.

[25] A Erturk and D J Inman. An experimentally validated bimorph cantilever model for piezoelectric energy harvesting from base excitations. *Smart Materials and Structures*, 18(2):025009, February 2009.

[26] S Roundy and P K Wright. A piezoelectric vibration based generator for wireless electronics. *Smart Materials and Structures*, 13(5):1131–1142, October 2004.

[27] NOEL E. DUTOIT, BRIAN L. WARDLE, and SANG-GOOK KIM. DESIGN CONSIDERATIONS FOR MEMS-SCALE PIEZOELECTRIC MECHANICAL VIBRATION ENERGY HARVESTERS. *Integrated Ferroelectrics*, 71(1):121–160, 2005.

[28] Yabin Liao and Henry A. Sodano. Modeling and comparison of bimorph power harvesters with piezoelectric elements connected in parallel and series. *Journal of Intelligent Material Systems and Structures*, 21(2):149–159, January 2010.

[29] Niell G. Elvin and Alex A. Elvin. A general equivalent circuit model for piezoelectric generators. *Journal of Intelligent Material Systems and Structures*, 20(1):3–9, January 2009.

[30] Ruichao Xu. *Energy harvesting for microsystems.* Ph.D. thesis, Technical University of Denmark, Department of Micro- and Nanotechnology, May 2012.

[31] Frank Goldschmidtboeing and Peter Woias. Characterization of different beam shapes for piezoelectric energy harvesting. *Journal of Micromechanics and Microengineering*, 18(10):104013, October 2008.

[32] John M. Dietl and Ephrahim Garcia. Beam shape optimization for power harvesting. *Journal of Intelligent Material Systems and Structures*, 21(6):633–646, April 2010.

[33] Denis Benasciutti, Luciano Moro, Saša Zelenika, and Eugenio Brusa. Vibration energy scavenging via piezoelectric bimorphs of optimized shapes. *Microsystem Technologies*, 16(5):657–668, May 2010.

[34] Thomas Pedersen. *Development of piezoelectric Micromachined Ultrasound Transducers utilizing screen printed PZT thick film.* Ph.D. thesis, Technical University of Denmark, Department of Micro- and Nanotechnology, March 2010.

[35] Christian Gammeltoft Hindrichsen. *Piezoelectric MEMS Accelerometer - PiMEMS.* Ph.D. thesis, Technical University of Denmark, Department of Micro- and Nanotechnology, March 2010.

[36] Louise M. Borregaard and Gustav L. L. Kvaal. *Piezoelectric MEMS energy harvester.* Bachelor thesis, Technical University of Denmark, Department of Micro- and Nanotechnology, June 2009.

[37] Johan Nagstrup. *Piezoelectric MEMS Energy Harvester based on PZT Thick Film.* Master thesis, Technical University of Denmark, Department of Micro- and Nanotechnology, November 2009.

[38] Anders Thyssen and Adam Carsten Stoot. *Design, Fabrication and Characterization of an Optimized PZT/Silicon Cantilever Component for Energy Harvesting.* Bachelor thesis, Technical University of Denmark, Department of Micro- and Nanotechnology, June 2010.

[39] C.G. Hindrichsen, R. Lou-Moeller, K. Hansen, and E.V. Thomsen. Advantages of PZT thick film for MEMS sensors. *Sensors and Actuators A: Physical*, 163(1):9 – 14, 2010.

[40] Thomas Lehrmann Christiansen. *Design, Fabrication and Characterisation of a MEMS PZT/PZT-Cantilever Device for Energy Harvesting.* Bachelor thesis, Technical University of Denmark, Department of Micro- and Nanotechnology, June 2010.

[41] A. Lei, R. Xu, A. Thyssen, A.C. Stoot, T.L. Christiansen, K. Hansen, R. Lou-Moller, E.V. Thomsen, and K. Birkelund. MEMS-based thick film PZT vibrational energy harvester. In *Micro Electro Mechanical Systems (MEMS), 2011 IEEE 24th International Conference on*, pages 125 –128, January 2011.

[42] Michele Guizzetti, Thomaz Zawada, Karsten Hansen, Ruichao Xu, Anders Lei, Adam Carsten Stoot, Anders Thyssen, Ole Hansen, Erik Vilain Thomsen, and Karen Birkelund. Design, fabrication and characterization of piezoelectric power harvesters realized with silicon micromachining and screen-printing technologies, March 2011.

[43] Christian Dahl-Petersen. *Robust Fabrication and Characterization of PZT/PZT Thick Film Bimorph MEMS Energy Harvester.* Bachelor thesis, Technical University of Denmark, Department of Micro- and Nanotechnology, June 2011.

[44] H. Sandmaier, H.L. Offereins, K. Kuhl, and W. Lang. Corner compensation techniques in anisotropic etching of (100)-silicon using aqueous KOH. In *, 1991 International Conference on Solid-State Sensors and Actuators, 1991. Digest of Technical Papers, TRANSDUCERS '91*, pages 456 –459, June 1991.

[45] Wei Fan and Dacheng Zhang. A simple approach to convex corner compensation in anisotropic KOH etching on a (100) silicon wafer. *Journal of Micromechanics and Microengineering*, 16(10):1951–1957, October 2006.

[46] C. C. Hindrichsen, T. Pedersen, E. V. Thomsen, K. Hansen, and R. Lou-Moeller. Investigation of Top/Bottom electrode and diffusion barrier layer for PZT thick film MEMS sensors. *Ferroelectrics*, 367(1):201–213, 2008.

[47] S P Beeby, A Blackburn, and N M White. Processing of PZT piezoelectric thick films on silicon for microelectromechancial systems. *Journal of Micromechanics and Microengineering*, 9(3):218–229, September 1999.

[48] Adnan Silajdzic. *Investigation and Characterisation of Diffusion Barriers for PZT Devices*. Bachelor thesis, Technical University of Denmark, Department of Micro- and Nanotechnology, January 2012.

[49] R.A. Dorey and R.W. Whatmore. Electroceramic thick film fabrication for MEMS. *Journal of Electroceramics*, 12(1):19–32, 2004.

[50] Y.B. Jeon, R. Sood, J.-h. Jeong, and S.-G. Kim. MEMS power generator with transverse mode thin film PZT. *Sensors and Actuators A: Physical*, 122(1):16–22, July 2005.

[51] Qing-Ming Wang, Qiming Zhang, Baomin Xu, Ruibin Liu, and L. Eric Cross. Nonlinear piezoelectric behavior of ceramic bending mode actuators under strong electric fields. *Journal of Applied Physics*, 86(6):3352–3360, September 1999.

[52] L.Q. Yao, J.G. Zhang, L. Lu, and M.O. Lai. Nonlinear dynamic characteristics of piezoelectric bending actuators under strong applied electric field. *Journal of Microelectromechanical Systems*, 13(4):645–652, August 2004.

[53] Dongna Shen, Jung-Hyun Park, Jyoti Ajitsaria, Song-Yul Choe, Howard C Wikle, and Dong-Joo Kim. The design, fabrication and evaluation of a MEMS PZT cantilever with an integrated si proof mass for vibration energy harvesting. *Journal of Micromechanics and Microengineering*, 18(5):055017, May 2008.

[54] IEEE standard on piezoelectricity. *ANSI/IEEE Std 176-1987*, page 0_1, 1988.

[55] S.M. Shahruz. Design of mechanical band-pass filters for energy scavenging. *Journal of Sound and Vibration*, 292(3-5):987–998, May 2006.

[56] Huan Xue, Yuantai Hu, and Qing-ming Wang. Broadband piezoelectric energy harvesting devices using multiple bimorphs with different operating frequencies. *IEEE Transactions on Ultrasonics, Ferroelectrics and Frequency Control*, 55(9):2104 –2108, September 2008.

[57] Marco Ferrari, Vittorio Ferrari, Michele Guizzetti, Daniele Marioli, and Andrea Taroni. Piezoelectric multifrequency energy converter for power harvesting in autonomous microsystems. *Sensors and Actuators A: Physical*, 142(1):329–335, March 2008.

[58] R. Xu, A. Lei, C. Dahl-Petersen, K. Hansen, M. Guizzetti, K. Birkelund, E.V. Thomsen, and O. Hansen. Screen printed PZT/PZT thick film bimorph MEMS cantilever device for vibration energy harvesting. *Sensors and Actuators A: Physical*, 188(0):383–388, December 2012.

[59] R. Xu, L.M. Borregaard, A. Lei, M. Guizzetti, E. Ringgaard, T. Zawada, O. Hansen, and E.V. Thomsen. Preliminary performance evaluation of MEMS-based piezoelectric energy harvesters in extended temperature range. *Procedia Engineering*, 47(0):1434–1437, 2012.

[60] Anders Lei, Ruichao Xu, Louise M. Borregaard, Michele Guizzetti, and Erik V. Thomsen. Homogeneity analysis of a MEMS-based PZT thick film vibration energy harvester manufacturing process. *Procedia Engineering*, 47(0):554–557, 2012.

[61] T M Kamel, R Elfrink, M Renaud, D Hohlfeld, M Goedbloed, C de Nooijer, M Jambunathan, and R van Schaijk. Modeling and characterization of MEMS-based piezoelectric harvesting devices. *Journal of Micromechanics and Microengineering*, 20(10):105023, October 2010.

[62] R Elfrink, M Renaud, T M Kamel, C de Nooijer, M Jambunathan, M Goedbloed, D Hohlfeld, S Matova, V Pop, L Caballero, and R van Schaijk. Vacuum-packaged piezoelectric vibration energy harvesters: damping contributions and autonomy for a wireless sensor system. *Journal of Micromechanics and Microengineering*, 20(10):104001, October 2010.

[63] A. Erturk, J. Hoffmann, and D. J Inman. A piezomagnetoelastic structure for broadband vibration energy harvesting. *Applied Physics Letters*, 94(25):254102–254102–3, June 2009.

[64] Ji-Tzuoh Lin, Barclay Lee, and Bruce Alphenaar. The magnetic coupling of a piezoelectric cantilever for enhanced energy harvesting efficiency. *Smart Materials and Structures*, 19(4):045012, April 2010.

[65] Samuel C. Stanton, Clark C. McGehee, and Brian P. Mann. Nonlinear dynamics for broadband energy harvesting: Investigation of a bistable piezoelectric inertial generator. *Physica D: Nonlinear Phenomena*, 239(10):640–653, May 2010.

[66] David A. W. Barton, Stephen G. Burrow, and Lindsay R. Clare. Energy harvesting from vibrations with a nonlinear oscillator. *Journal of Vibration and Acoustics*, 132(2):021009, 2010.

[67] Helios Vocca, Igor Neri, Flavio Travasso, and Luca Gammaitoni. Kinetic energy harvesting with bistable oscillators. *Applied Energy*, 97(0):771–776, September 2012.

[68] Samuel C. Stanton, Brian P. Mann, and Benjamin A.M. Owens. Melnikov theoretic methods for characterizing the dynamics of the bistable piezoelectric inertial generator in complex spectral environments. *Physica D: Nonlinear Phenomena*, 241(6):711–720, March 2012.

[69] Marco Ferrari, Vittorio Ferrari, Michele Guizzetti, Bruno Ando, Salvatore Baglio, and Carlo Trigona. Improved energy harvesting from wideband vibrations by nonlinear piezoelectric converters. *Procedia Chemistry*, 1(1):1203–1206, September 2009.

[70] B Ando, S Baglio, C Trigona, N Dumas, L Latorre, and P Nouet. Nonlinear mechanism in MEMS devices for energy harvesting applications. *Journal of Micromechanics and Microengineering*, 20(12):125020, December 2010.

[71] Mikio Umeda, Kentaro Nakamura, and Sadayuki Ueha. Analysis of the transformation of mechanical impact energy to electric energy using piezoelectric vibrator. *Japanese Journal of Applied Physics*, 35(Part 1, No. 5B):3267–3273, 1996.

[72] Michael Renaud, Paolo Fiorini, and Chris van Hoof. Optimization of a piezoelectric unimorph for shock and impact energy harvesting. *Smart Materials and Structures*, 16(4):1125–1135, August 2007.

[73] E Jacquelin, S Adhikari, and M I Friswell. A piezoelectric device for impact energy harvesting. *Smart Materials and Structures*, 20(10):105008, October 2011.

[74] Christoffer Moelleskov Pedersen. *Design and Fabrication of a Nonlinear MEMS Based Energy Harvester*. Master thesis, Technical University of Denmark, Department of Micro- and Nanotechnology, August 2011.

[75] Ivan Fugloe and Mikkel Wennemoes Hvitfeld Ley. *Designing a Bistable Energy Harvester*. Bachelor thesis, Technical University of Denmark, Department of Micro- and Nanotechnology, June 2011.

Appendix A

Journal And Conference Publications

A. Lei, R. Xu, A. Thyssen, A.C. Stoot, T. L. Christiansen, K. Hansen, R. Lou-Moeller, E.V. Thomsen and K. Birkelund, "MEMS-Based Thick Film PZT Vibriational Energy Harvester", Proceeding, IEEE micro electro mechanical systems (IEEE MEMS), 2011, pp. 125-128.

R. Xu, A. Lei, T.L. Christiansen, K. Hansen, M. Guizzetti, K. Birkelund, E.V. Thomsen and O. Hansen, "SCREEN PRINTED PZT/PZT THICK FILM BIMORPH MEMS CANTILEVER DEVICE FOR VIBRATION ENERGY HARVESTING", Proceeding, The 16th international conference on solid-state sensors, actuators and microsystems (Transducers'11), 2011, pp. 679-682.

M. Guizzetti, T. Zawada, K. Hansen, R. Xu, A. Lei, A. C. Stoot, A. Thyssen, O. Hansen, E.V. Thomsen and K. Birkelund, "Design, fabrication and characterization of piezoelectric power harvesters realized with silicon micromachining and screen-printing technologies", Proceeding, PIEZO 2011-Electroceramics for End-Users VI, 2011.

A. Lei, R. Xu, C.M. Pedersen, M. Guizzetti, K. Hansen, E.V. Thomsen and K. Birkelund, "HOMOGENEITY ANALYSIS OF HIGH YIELD MANUFACTURING PROCESS OF MEMS-BASED PZT THICK FILM VIBRATIONAL ENERGY HARVESTERS", Proceeding, The 11th international workshop on micro and nanotechnology for power generation and energy conversion applications (PowerMEMS 2011), 2011, pp. 387-390.

R. Xu, A. Lei, C. Dahl-Petersen, K. Hansen, M. Guizzetti, K. Birkelund, E.V. Thomsen and O. Hansen, "MEMS-BASED PZT/PZT BIMORPH THICK FILM VIBRATION ENERGY HARVESTER", Proceeding, The 11th international workshop on micro and nanotechnology for power generation and energy conversion applications (PowerMEMS 2011), 2011, pp. 143-146.

R. Xu, A. Lei, C. Dahl-Petersen, K. Hansen, M. Guizzetti, K. Birkelund, E.V. Thomsen and O. Hansen, "Screen printed PZT/PZT thick film bimorph MEMS cantilever device for

vibration energy harvesting", Sensors and Actuaters A: Physical, vol. 188, no. 0, pp. 383–388, Dec. 2012.

R. Xu, A. Lei, C. Dahl-Petersen, K. Hansen, M. Guizzetti, K. Birkelund, E. V. Thomsen, and O. Hansen, "Fabrication and characterization of MEMS-based PZT/PZT bimorph thick film vibration energy harvesters," Journal of Micromechanics and Microengineering, vol. 22, no. 9, p. 094007, Sep. 2012.

R. Xu, L. M. Borregaard, A. Lei, M. Guizzetti, E. Ringgaard, T. Zawada, O. Hansen, and E. V. Thomsen, "Preliminary Performance Evaluation of MEMS-based Piezoelectric Energy Harvesters in Extended Temperature Range," Procedia Engineering, vol. 47, no. 0, pp. 1434–1437, 2012.

A. Lei, R. Xu, L. M. Borregaard, M. Guizzetti, and E. V. Thomsen, "Homogeneity Analysis of a MEMS-based PZT Thick Film Vibration Energy Harvester Manufacturing Process," Procedia Engineering, vol. 47, no. 0, pp. 554–557, 2012.

A.1 IEEE MEMS 2011

A. Lei, R. Xu, A. Thyssen, A.C. Stoot, T. L. Christiansen, K. Hansen, R. Lou-Moeller, E.V. Thomsen and K. Birkelund, "MEMS-Based Thick Film PZT Vibriational Energy Harvester", Proceeding, IEEE micro electro mechanical systems (IEEE MEMS), 2011, pp. 125-128.

MEMS-BASED THICK FILM PZT VIBRATIONAL ENERGY HARVESTER

A. Lei[1], R. Xu[1], A. Thyssen[1], A.C. Stoot[1], T. L. Christiansen[1], K. Hansen[2], R. Lou-Møller[2], E.V. Thomsen[1] and K. Birkelund[1]

[1]Department of Micro- and Nanotechnology, Technical University of Denmark, DTU Nanotech, Building 345 East, DK-2800 Kongens Lyngby, Denmark

[2]Meggitt A/S, Hejreskovvej 18A, DK-3490 Kvistgaard, Denmark

ABSTRACT

We present a MEMS-based unimorph silicon/PZT thick film vibrational energy harvester with an integrated proof mass. We have developed a process that allows fabrication of high performance silicon based energy harvesters with a yield higher than 90%. The process comprises a KOH etch using a mechanical front side protection of an SOI wafer with screen printed PZT thick film. The fabricated harvester device produces 14.0 μW with an optimal resistive load of 100 kΩ from 1*g* (*g*=9.81 m s^{-2}) input acceleration at its resonant frequency of 235 Hz.

INTRODUCTION

With the development in low power electronics, wireless sensor systems powered by batteries are now applicable in monitoring of e.g. machine and structures. However, the limited lifespan of electrochemical batteries requires periodical replacement for long term operation. For sensors located remotely or inaccessible, this might not be an option, instead larger batteries can be used but this severely compromises the total size of the sensor system. In order to realize long term autonomous wireless sensor systems, much effort has recently been put into the research and development of small scale energy scavenging devices that transforms excess ambient energy into electrical energy. Among the most common ambient sources of energy are thermal, mechanical or unused RF energy [1]. Harvesting of mechanical energy from vibrations usually employs an electrostatic, electromagnetic or piezoelectric transduction mechanism [2]. A piezoelectric transduction device normally consists of an elastic cantilever supporting a piezoelectric layer with metal electrodes on either side. The most common piezoelectric material used is PZT (lead zirconate titanate). PZT can be integrated with an elastic cantilever by either bulk processing or deposition.

Several energy harvesters with bulk PZT have been presented in literature [3], [4]. These harvesters are characterized by having large dimensions, since bulk processing defines some lower limits of feasible processing, hence compromising the incorporation in small sensor systems. Piezoelectric films can also be deposited using sputtering [5], plasma-enhanced chemical vapour deposition (PECVD) [6], sol-gel spin-on [7] or screen printing [8]. Common for the deposition methods are that they can be integrated with MEMS fabrication technologies, enabling small scale devices, well proven fabrication processes, low fabrication costs and high volume production. So far, the majority of MEMS-based vibrational energy harvesters presented [7], [9], have been fabricated using the sol-gel spin-on method, limiting the PZT layer thickness to a few μm. To obtain a sufficiently powerful energy harvester, it is however desirable to use thicker PZT films [10], [11].

In this work we present a unimorph MEMS-based PZT thick film vibrational energy harvester fabricated by combining silicon etching in potassium hydroxide (KOH) using a mechanical front side protection as proposed by [9], a silicon-on-insulator (SOI) wafer to accurately define the thickness of the silicon part of the cantilever also used by [7] and the silicon compatible PZT thick film screen-printing technique presented by [8]. The developed process allows fabrication of high performance silicon based energy harvesters using standard MEMS processes with a yield higher than 90%. The piezoelectric ceramic used is InSensor® TF2100, which has a high coupling coefficient, making it preferable for the MEMS based energy harvesters.

FABRICATION

The unimorph vibrational energy harvester is fabricated using a four mask fabrication process on a 4 inch (100 mm) silicon SOI wafer with a 20 μm device layer, a 1 μm buried oxide layer and a 500 μm thick substrate (Figure 1(a)). A 1 μm silicon oxide layer is thermally grown followed by a deposition of 170 nm stoichiometric LPCVD silicon nitride (Figure 1(b)). Backside openings in the nitride for the KOH etch are defined using UV lithography followed by RIE etching and the front side nitride is removed in a RIE etch (Figure 1(c)). Using UV lithography, e-beam deposition and lift-off, a bottom electrode consisting of a 50 nm titanium adhesion layer and a 500 nm platinum layer, also serving as a diffusion barrier [12], is defined (Figure 1(d)). On top of the bottom electrode a 15 μm PZT thick film is deposited using screen printing (Figure 1(e)). Before the sintering, the PZT thick film is high pressure treated. As top electrode, a 400 nm gold layer is deposited by e-beam evaporation through a shadow mask (Figure 1(f)). The wafer is placed in a mechanical holder that protects the front side of the wafer but exposes the backside. The oxide is removed in a BHF solution, and the cavities are etched in a KOH solution where the buried oxide functions as an etch stop layer (Figure 1(g)). The PZT structures are covered with resist and the cantilevers are released by an oxide etch in BHF followed by a silicon etch using RIE (Figure 1(h)). The PZT thick film is polarized by applying an electric field between the top and bottom electrodes at an elevated temperature. A final energy harvesting device with the dimensions listed in Table 1 is seen in Figure 2.

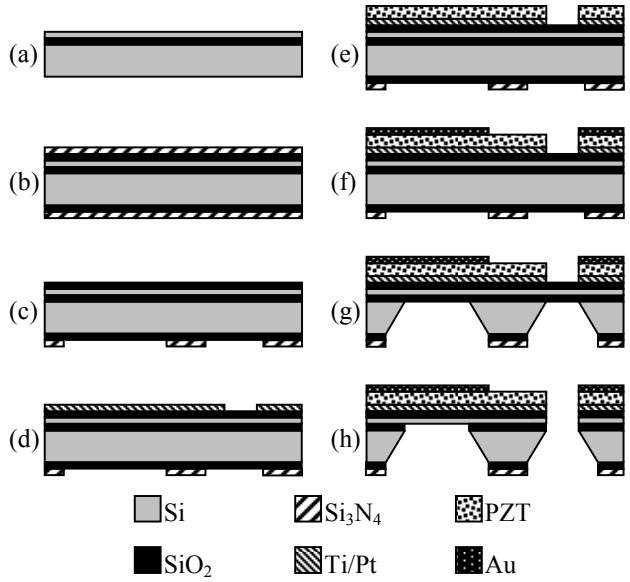

Figure 1: Process flow for the unimorph MEMS-based PZT thick film vibrational energy harvester.

Table 1: Dimensions of the energy harvester

Frame dimensions	10 mm × 10 mm
Medial dimension	< 1 mm
Cantilever width	5.5 mm
Cantilever length	1.95 mm
Mass length	4.55 mm
Mass width	5.5 mm

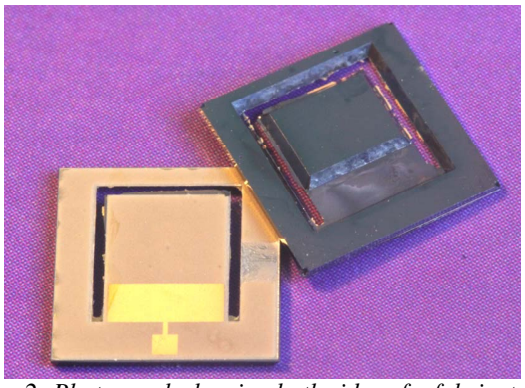

Figure 2: Photograph showing both sides of a fabricated energy harvesting device.

RESULTS

The fabricated energy harvester is characterized by measuring the direct piezoelectric effect using a shaker setup to simulate the excess vibration noise from the surroundings, and the indirect piezoelectric effect using an Agilent 4294A Precision Impedance Analyzer to excite the harvester electrically.

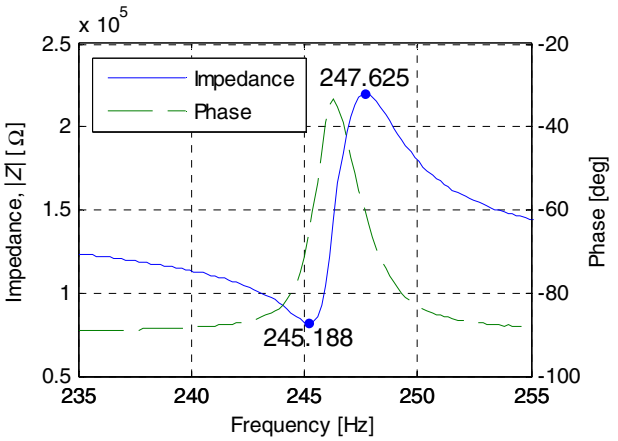

Figure 3: Impedance and phase around resonance. Source voltage set to 500 mV.

From the impedance measurement the resonant frequency, the capacitance, the optimal resistive load and the electromechanical coupling coefficient is determined. The resonance, f_r=245.2 Hz and anti-resonance, f_a=247.6 Hz is shown in Figure 3. The impedance at resonance is the optimal load resistance, R_{opt}=81.8 kΩ. The coupling coefficient is found to be k=0.155 and is calculated using

$$k = \sqrt{\frac{\alpha}{\alpha - \tan\alpha}}, \tag{1}$$

where,

$$\alpha = \frac{\pi}{2}\frac{f_a}{f_r}. \tag{2}$$

For the shaker measurements the harvester is being actuated by a B&K Mini Shaker 4810 driven by an amplified sinusoidal signal from a function generator. The acceleration is measured with a B&K Piezoelectric Accelerometer 8305. The applied input acceleration is stated in fractions of the gravitational acceleration g (9.81 m s^{-2}). From these measurements the resonant frequency and the optimal resistive load is confirmed. Furthermore, the power dissipated in a resistive load for different frequencies and accelerations is found.

The optimal resistive load for the energy harvester is found by extracting the RMS voltage from a resonant peak in a frequency sweep for various resistive loads at an input acceleration of 0.5g. The power dissipated in the load will then be, $P=V_{rms}^2/R_{Load}$. The optimal resistive load, resulting in the highest power at resonance frequency, is found to 100 kΩ, see Figure 4. The increase in the optimal resistive load compared to the impedance measurement in Figure 3 is due to increased mechanical damping associated with the stress in the PZT thick film, caused by the input acceleration [13]. To match the increase in the mechanical damping the electrical damping must be increased accordingly, thus here the optimal resistive load is measured to be higher.

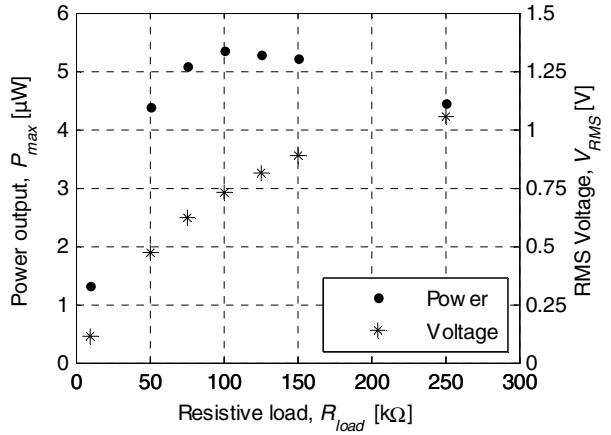

Figure 4: Power output and RMS voltage at resonant frequency as functions of resistive load. Input acceleration is 0.5g.

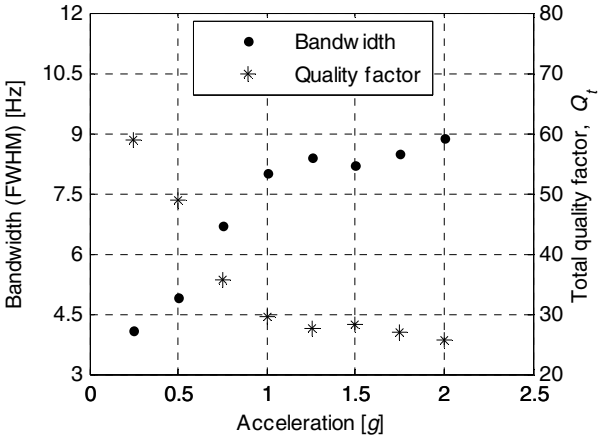

Figure 6: Bandwidth measured as full width at half maximum (FWHM) and total quality factor plotted as functions of input acceleration.

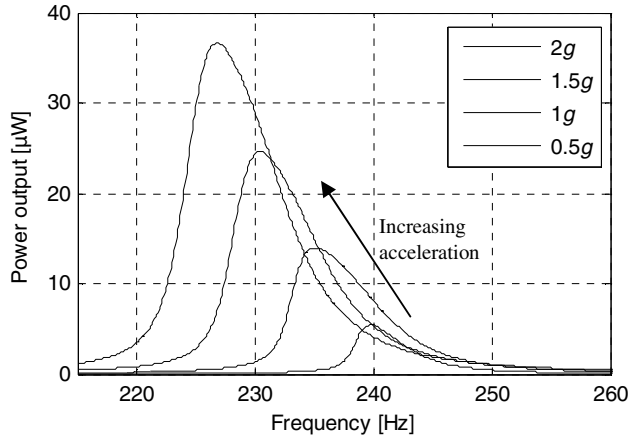

Figure 5: Power output as a function of input frequency for different input accelerations.

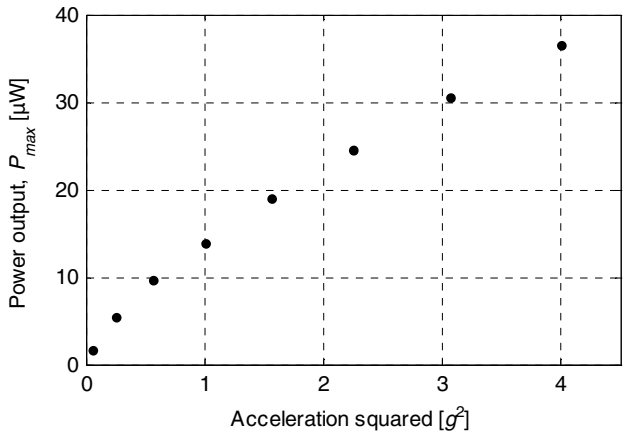

Figure 7: Power output at resonant frequency as a function of input acceleration.

The dissipated power in a resistive load of 100 kΩ as a function of the frequencies near resonance for different accelerations is shown in Figure 5. A maximum power of 36.65 μW is measured at an acceleration of 2*g*. From Figure 5 it is further seen that the resonant frequency decreases with increasing acceleration. This decrease is due to a non-linear response of PZT under stress. With increasing acceleration, thus stress, the Young's modulus and quality factor decreases [13]. The decrease in Young's modulus will directly reduce the spring constant, thus reduces the resonant frequency. The decrease in quality factor will affect the damping of the system and widen the bandwidth of the resonance peaks, as it is confirmed in Figure 6. The bandwidth in Figure 6 is determined directly from the measurements shown in Figure 5, where the full width at half maximum (FWHM) is defined as the bandwidth. The total quality factor is determined by the ratio between resonant frequency and the bandwidth. Figure 6 shows that with increasing accelerations the total quality factor decreases and the bandwidth increases. The widening of the bandwidth will lead to a drop in the potential power gain, thus power will no longer have the theoretical quadratic relation with acceleration as expected. This is confirmed in Figure 7 where the power at resonant frequency is plotted for different input accelerations.

CONCLUSION

A MEMS-based unimorph silicon/PZT thick film vibrational energy harvester with an integrated proof mass has been fabricated and characterized. By defining the 35 μm thick cantilevers as the last processing step by the use of KOH etching with a mechanical front side protection it has been possible to obtain a fabrication yield greater than 90%. The resonant frequency of the harvester is aimed towards the common sources of vibrations measured in [14] with resonant frequencies ranging from 100-200 Hz. The unimorph harvester device produces 13.98 μW with an optimal resistive load of 100 kΩ from 1*g* (g=9.81 m s^{-2}) input acceleration at its resonant frequency of 235 Hz.

REFERENCES

[1] N. S. Hudak and G. G. Amatucci, "Small-scale energy harvesting through thermoelectric, vibration, and radiofrequency power conversion," *Journal of Applied Physics*, vol. 103, no. 10, p. 101301, 2008.

[2] S. P. Beeby, M. J. Tudor, and N. M. White, "Energy harvesting vibration sources for microsystems applications," *Measurement Science and Technology*, vol. 17, no. 12, pp. R175-R195, 2006.

[3] Y. Liao and H. A. Sodano, "Model of a single mode energy harvester and properties for optimal power generation," *Smart Materials and Structures*, vol. 17, no. 6, p. 065026, 2008.

[4] A. Erturk and D. J. Inman, "An experimentally validated bimorph cantilever model for piezoelectric energy harvesting from base excitations," *Smart Materials and Structures*, vol. 18, no. 2, p. 025009, 2009.

[5] H. Jacobsen, H. Quenzer, B. Wagner, K. Ortner, and T. Jung, "Thick PZT layers deposited by gas flow sputtering," *Sensors and Actuators A: Physical*, vol. 135, no. 1, pp. 23-27, Mar. 2007.

[6] Qiang Zou, Wei Tan, Eun Sok Kim, and G. Loeb, "Single- and Triaxis Piezoelectric-Bimorph Accelerometers," *Microelectromechanical Systems, Journal of*, vol. 17, no. 1, pp. 45-57, 2008.

[7] D. Shen et al., "Micromachined PZT cantilever based on SOI structure for low frequency vibration energy harvesting," *Sensors and Actuators A: Physical*, vol. 154, no. 1, pp. 103-108, Aug. 2009.

[8] R. Lou-Moeller et al., "Screen-printed piezoceramic thick films for miniaturised devices," *Journal of Electroceramics*, vol. 19, no. 4, pp. 333-338, 2007.

[9] H. Fang et al., "Fabrication and performance of MEMS-based piezoelectric power generator for vibration energy harvesting," *Microelectronics Journal*, vol. 37, no. 11, pp. 1280-1284, Nov. 2006.

[10] R. Dorey and R. Whatmore, "Electroceramic Thick Film Fabrication for MEMS," *Journal of Electroceramics*, vol. 12, no. 1, pp. 19-32, 2004.

[11] C. Hindrichsen, R. Lou-Møller, K. Hansen, and E. Thomsen, "Advantages of PZT thick film for MEMS sensors," *Sensors and Actuators A: Physical*, vol. 163, no. 1, pp. 9 - 14, 2010.

[12] C. C. Hindrichsen, T. Pedersen, E. V. Thomsen, K. Hansen, and R. Lou-Møller, "Investigation of Top/Bottom Electrode and Diffusion Barrier Layer for PZT Thick Film MEMS Sensors," *Ferroelectrics*, vol. 367, no. 1, pp. 201-213, 2008.

[13] D. Shen, J. Park, J. Ajitsaria, S. Choe, H. C. Wikle, and D. Kim, "The design, fabrication and evaluation of a MEMS PZT cantilever with an integrated Si proof mass for vibration energy harvesting," *Journal of Micromechanics and Microengineering*, vol. 18, no. 5, p. 055017, 2008.

[14] S. Roundy, P. K. Wright, and J. Rabaey, "A study of low level vibrations as a power source for wireless sensor nodes," *Computer Communications*, vol. 26, no. 11, pp. 1131-1144, Jul. 2003.

A.2 Transducers 2011

R. Xu, A. Lei, T.L. Christiansen, K. Hansen, M. Guizzetti, K. Birkelund, E.V. Thomsen and O. Hansen, "SCREEN PRINTED PZT/PZT THICK FILM BIMORPH MEMS CANTILEVER DEVICE FOR VIBRATION ENERGY HARVESTING", Proceeding, The 16th international conference on solid-state sensors, actuators and microsystems (Transducers'11), 2011, pp. 679-682.

SCREEN PRINTED PZT/PZT THICK FILM BIMORPH MEMS CANTILEVER DEVICE FOR VIBRATION ENERGY HARVESTING

R. Xu[1], A. Lei[1], T.L. Christiansen[1], K. Hansen[2], M. Guizzetti[2], K. Birkelund[1], E.V. Thomsen[1] and O. Hansen[1,3]

[1]Department of Micro- and Nanotechnology, Technical University of Denmark, DTU Nanotech, Building 345 East, DK-2800 Kongens Lyngby, Denmark

[2]Meggitt Sensing Systems, DK-3490 Kvistgaard, Denmark

[3]CINF, Center for Individual Nanoparticle Functionality, Technical University of Denmark

ABSTRACT

We present a MEMS-based PZT/PZT thick film bimorph vibration energy harvester with an integrated silicon proof mass. The most common piezoelectric energy harvesting devices utilize a cantilever beam of a non piezoelectric material as support beneath or in-between the piezoelectric material. It provides mechanical support but it also reduces the power output. Our device replaces the support with another layer of the piezoelectric material, and with the absence of an inactive mechanical support all of the stresses induced by the vibrations will be harvested by the active piezoelectric elements.

KEYWORDS

Energy harvester, MEMS, thick film, PZT, bimorph

INTRODUCTION

With the recent development in low power electronics and wireless systems it has become increasingly interesting to use energy harvesters that harness ambient energies to empower electronic sensor systems instead of using electrochemical batteries. The limited lifespan of traditional electrochemical batteries requires periodical replacement and the batteries often take up significant volume in the total sensing system. The MEMS energy harvester addresses these two issues by having large energy to volume ratio [1] and by scavenging energies from external sources, thus the lifetime is only limited by material decay or fatigue. This will reduce the frequency of periodic maintenance from months to years, and maybe even decades.

The most common ambient power sources are solar, thermal, mechanical or unused RF energy. Harvesting vibration energy from a mechanical noise source can either be based on electrostatic, electromagnetic or piezoelectric conversion [2]. The interest in harvesting energy from ambient mechanical vibrations has resulted in a number of review articles in recent years [1-4]. In particular the piezoelectric transduction method has received significant attention. A typical piezoelectric energy harvester is based on a bimorph cantilever beam, which consists of the active piezoelectric ceramic with metal electrodes on both side and a passive mechanical support structure, anchored at one end and with a proof mass at the other [5-8].

There are many different piezoelectric materials available, however the materials of most interest for application in MEMS devices are PZT ($Pb(Zr_xTi_{1-x})O_3$), zinc oxide (ZnO) [9], [10] and aluminium nitride (AlN) [11], [12]. Among these, PZT is the most commonly used in energy harvesters.

Energy harvesters with bulk PZT have been presented in [13] and [14]. These energy harvesters have large dimensions and are thus not compatible with small sensor systems. Energy harvesters made with thin film deposition methods, such as sputtering [15] or sol-gel spin-on [16], [17] are characterized by a very thin layer PZT of just a few micrometers. Fabrication of a pure self supporting PZT beam without any mechanical support structure will be very difficult using these methods. We therefore use thick film screen printing technique, and utilize the advantage of being able to screen print PZT thick film with a thickness of 15 μm to 60 μm to fabricate energy harvesters with a pure PZT beam [18].

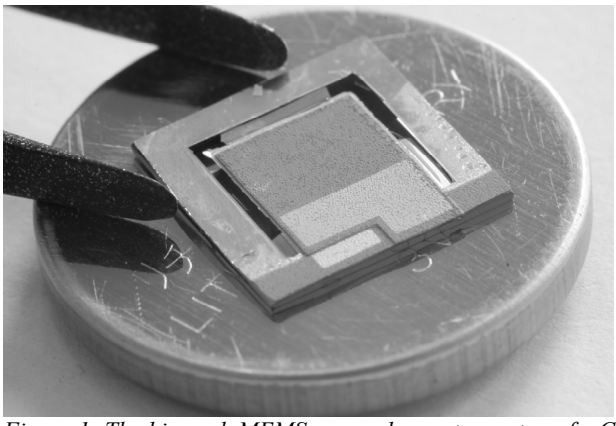

Figure 1: The bimorph MEMS energy harvester on top of a CR 2032 button battery.

In this work the piezoelectric PZT thick film used is InSensor® TF2100; the PZT film was screen printed with a thickness of around 30 μm. This technique has previously been used in fabrication of a piezoelectric accelerometer [19] and energy harvester [20]. With the use of PZT thick film, instead of PZT thin film, a mechanical support material is no longer needed in the final device, since the beam is thick and strong enough to support the proof mass. The fabricated bimorph cantilever energy harvester depicted in Figure 1 consists of two PZT layers separated by a middle electrode. Here both layers are active and thus the strain energy from both layers is

harvested [21]. The advantage of such a structure is that all strain energy is harvested, while in conventional structures with inactive support materials the strain energy in these is not harvested and thus wasted.

FABRICATION

The PZT/PZT thick film energy harvesters are fabricated using a six mask fabrication process on a 4 inch (100 mm) silicon on insulator (SOI) wafer with a 30 µm device layer, a 1 µm buried oxide layer and a 525 µm thick carrier substrate, Figure 2(a). The backside of the SOI wafer is patterned using UV lithography and etched using a DRIE process, Figure 2(b). The buried oxide layer is here used as an etch stop layer. After an RCA clean a 1 µm thick silicon dioxide layer is grown in a furnace by thermal oxidation. This layer will serve as an etch stop for a final RIE etch, releasing the structure, Figure 2(c). The bottom electrode is deposited on the front side of the SOI wafer using e-beam deposition. The bottom electrode layer consists of a 50 nm titanium adhesion layer and 500 nm of platinum which also serves as a diffusion barrier in the PZT sintering process. The bottom electrode layer is patterned using UV lithography and etched in a wet etch solution, H_2O:HCl:HNO_3 (8:7:1) at elevated temperature, Figure 2(d). On top of the patterned bottom electrode a 30 µm PZT thick film is deposited using screen printing and sintered (Figure 2(e)). The middle electrode is then deposited through a prefabricated shadow mask using e-beam deposition, Figure 2(f). The shadow mask was made using a 350 µm silicon wafer, which was patterned using UV lithograph and etched through in a DRIE process. Then the second layer of PZT thick film is screen printed and sintered. The top electrode layer is similarly deposited through a shadow mask using e-beam deposition, Figure 2(g). With the two PZT stacks in place the silicon device layer can now be removed. First, the oxide on the backside is etched in BHF, while the front side of the SOI wafer is protected. The backside of the SOI wafer is then etched in a RIE process until the device layer is removed and the cantilever released, Figure 2(h).

The wafer is diced and the chips polarized individually. The polarization directions of the two layers are aligned opposite to each other, i.e. during polarization the top and bottom electrodes are grounded and a polarization voltage is applied to the middle electrode. The dimensions for the final energy harvester chips are shown in Table 1.

Table 1: Energy harvester dimensions.

Frame dimensions	10 mm × 10 mm
Medial dimensions	< 1 mm
Cantilever width	5.5 mm
Cantilever length	1.95 mm
Total cantilever height	2 × 30 µm
Mass length	4.55 mm

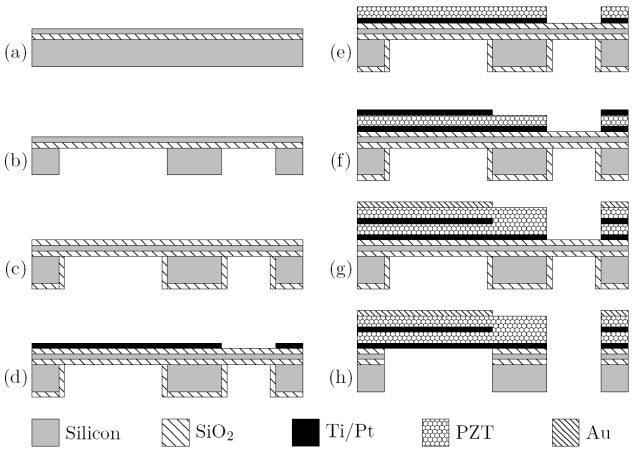

Figure 2: A cross sectional sketch of the process flow for the screen printed PZT/PZT thick film bimorph MEMS energy harvester.

RESULTS

The fabricated energy harvester was characterized both visually and electrically. The electrical characterization is done by measuring the direct and the indirect piezoelectric effect. The indirect piezoelectric effect was measured using an Agilent 4294A Precision Impedance Analyzer to excite the harvester electrically, and then measure the impedance and the phase.

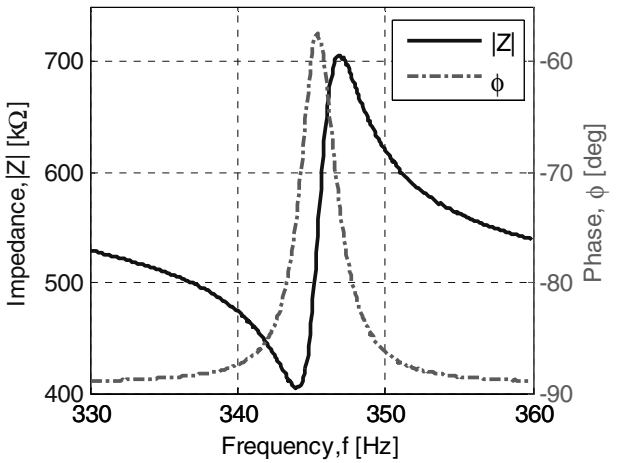

Figure 3: An impedance measurement of the energy harvester probed between the top electrode and the bottom electrode at the resonant frequency.

Figure 3 shows one of such measurements where the bottom electrode and the top electrode are probed. The resonant frequency is $f_r = 344$ Hz and the anti-resonant frequency is $f_a = 347$ Hz. The impedance at resonance is the optimal resistive load $R_{opt} = 405$ kΩ. The same measurements were done between the bottom and middle electrode and between the middle and top electrode. Even though the resonant and anti-resonant frequency stays the same, the optimal resistive load will change mainly due to the change in the layer thickness. The optimal resistive

load between bottom and middle electrode is $R_{opt} = 179$ kΩ. The optimal resistive load between middle and top is $R_{opt} = 345$ kΩ.

The direct piezoelectric effect is measured using the aforementioned resistive loads in a shaker setup. The harvester is actuated by a B&K Mini Shaker 4810 driven by an amplified sinusoidal signal from an Agilent 33220A function generator. A B&K Piezoelectric Accelerometer 8305 is mounted on the shaker along with the harvester. The acceleration from the shaker was measured by the accelerometer and is stated in fractions of the gravitational acceleration *g* (9.81 m s^{-2}). Since the PZT layers are polarized in opposite directions, the power output of both layers was measured with the top electrode and the bottom electrode, connected by the resistive load $R_{opt} = 405$ kΩ. By measuring the RMS voltage drop across the load the dissipated power can be calculated as $P_{rms} = {V_{rms}}^2 / R_{opt}$. Figure 4 shows the power output as a function of the excitation frequency. A maximum power of 7.35 µW was measured at an acceleration of 1 *g*. The asymmetric shape of the power peak and the decrease in resonant frequency with increasing power is probably due to a non-linear response of PZT under stress; with increasing stress in PZT the material's effective Young's modulus and the quality factor decreases [22]. The decrease in Young's modulus decreases the spring constant and thus also the resonant frequency.

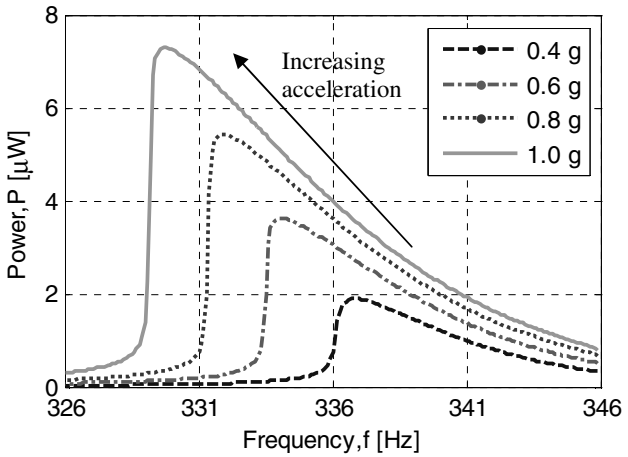

Figure 4: Power output as a function of the excitation frequency for different accelerations. The top electrode was connected to the bottom electrode through a resistive load, R_{opt} = 405 kΩ, optimized for maximum power using the impedance analyzer measurements.

During measurements of the power output of the top PZT layer, the top electrode and the middle electrode was connected through the resistive load of $R_{opt} = 345$ kΩ, while the bottom electrode is kept in open circuit. In a similar to measurement of the power output of the bottom PZT layer the resistive load of $R_{opt} = 179$ kΩ was used, and the top electrode was kept in open circuit. Similar measurements to those shown in Figure 4 are done on the top and bottom PZT layer. The power output from these measurements at resonant frequency are collected and plotted against the input acceleration, as shown in Figure 5. Figure 5 shows that the power output is indeed higher when both layers are measured, but it is not the sum of the power outputs from the other two layers. This is caused by the factor that when more power is extracted from the harvester the more electrically damped the system becomes and thus yields lower power.

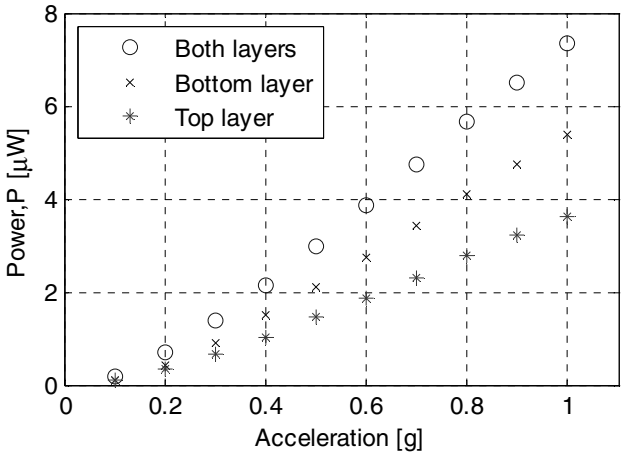

Figure 5: The power output from the top PZT layer, the bottom PZT layer and both layers at resonant frequency as a function of the input acceleration.

The difference in optimal resistive load and power output from the bottom and the top PZT layer is caused by mismatch in PZT film thickness and material properties, which is confirmed by inspection of the cantilever cross section using scanning electron microscopy (SEM). Figure 6 shows the cross section of the PZT/PZT cantilever, and illustrates clearly the undesirable layer mismatch. Besides the bottom PZT layer is thinner than the top layer, the grains of the bottom layer appear to be larger.

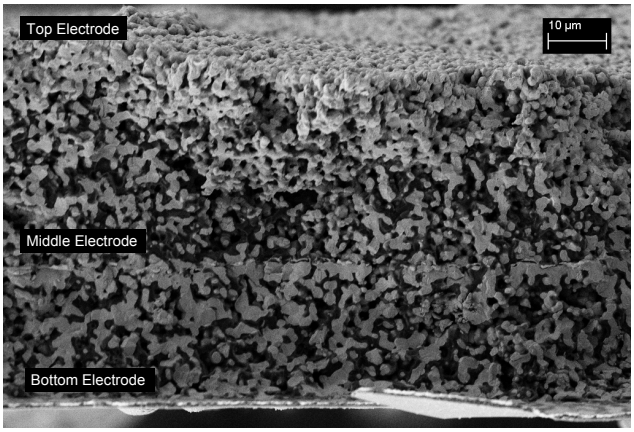

Figure 6: A SEM image showing a cross sectional view of the PZT/PZT bimorph cantilever. The middle electrode separates the two PZT layers.

CONCLUSION

Screen printed PZT/PZT thick film bimorph MEMS cantilever energy harvesters were successfully fabricated and characterized. By replacing the inactive cantilever support with another layer of PZT more power is indeed harvested compared to the power harvested from each individual layer. At 1 *g* the power output from both layers combined is 7.35 μW, while the power output for the individual layers at same input acceleration are 5.39 μW for the bottom layer and 3.62 μW for the top layer.

ACKNOWLEDGEMENTS

This research is part of the ELBA project, which is funded by the Advanced Technology Foundation. Center for Individual Nanoparticle Functionality (CINF) is sponsored by Danish National Research Foundation.

REFERENCES

[1] N. S. Hudak, G. G. Amatucci, "Small-scale energy harvesting through thermoelectric, vibration, and radiofrequency power conversion", Journal of Applied Physics, 103, 2008.

[2] S. P. Beeby, M. J. Tudor, and N. M. White, "Energy harvesting vibration sources for Microsystems applications," Measurement Science and Technology, vol. 17, no. 12, pp. R175-R195, 2006.

[3] K. A. C.-Chennault, N. Thambi, A. M. Sastry, "Powering MEMS portable devices — a review of nonregenerative and regenerative power supply systems with special emphasis on piezoelectric energy harvesting systems", *Smart Materials and Structures*, vol. 17, pp. 1-33, 2008.

[4] E. Lefeuvre, A. Badel, C. Richard, L. Petit, D. Guyomar, "A comparison between several vibration powered piezoelectric generators for standalone systems", Sensors and Actuators A 126, pp. 405-416, 2006.

[5] Hua-Bin Fang et al., "Fabrication and performance of MEMS-based piezoelectric power generator for vibration energy harvesting", Microelectronics Journal, 37:1280-1284, 2006.

[6] W.J. Choi, Y. Jeon, S.G. Kim, "Energy harvesting MEMS device based on thin film piezoelectric cantilevers", Journal of Electroceramics, 17, 2006.

[7] Dongna Shen et al., "The design, fabrication and evaluation of a MEMS PZT cantilever with an integrated Si proof mass for vibration energy harvesting", Journal of Micromechanics and Microengineering, vol. 18, 2008.

[8] Swee-Leong Kok, Neil M. White, Nick R. Harris, "Fabrication and characterization of free-standing thick-film piezoelectric cantilevers for energy harvesting", Measurement Science and Technology, 20, 2009.

[9] John G. Gualtieri, John A. Kosinski, Arthur Ballato, "Piezoelectric Materials for Acoustic Wave Applications", IEEE Transactions on Ultrasonics, Ferroelectrics, and Frequency Control, Vol 41 no. 1, 1994.

[10] G. Carlotti, G. Socino, A. Petri, E. Verona, "Elastic Constancs of Sputtered ZnO Films", *Ultrasonics Symposium*, p. 295-299, 1987.

[11] M. A. Dubois, P. Muralt, "Measurement of the effective transverse piezoelectric coefficient e31 of AlN and $Pb(Zr_x,Ti_{x-1})O3$ thin films", Sensors and Actuators A, Vol.77, p. 106-112, 1999.

[12] R Elfrink, T M Kamel, M Goedbloed,S Matova, D Hohlfeld, Y van Andel, R van Schaijk, "Vibration energy harvesting with aluminum nitride-based piezoelectric devices", Journal of Micromechanics and Microengineering. Vol. 19, 2009.

[13] Y. Liao, H. A. Sodano, "Model of a single mode energy harvester and properties for optimal power generation", *Smart Materials and Structures*, vol. 17, no. 6, p. 065026, 2008.

[14] A. Erturk, D. J. Inman, "An experimentally validated bimorph cantilever model for piezoelectric energy harvesting from base excitations," *Smart Materials and Structures*, vol. 18, no. 2, p. 025009, 2009.

[15] H. Jacobsen, H. Quenzer, B. Wagner, K. Ortner, and T. Jung, "Thick PZT layers deposited by gas flow sputtering," Sensors and Actuators A: Physical, vol. 135, no. 1, pp. 23-27, Mar. 2007.

[16] D. Shen et al., "Micromachined PZT cantilever based on SOI structure for low frequency vibration energy harvesting," Sensors and Actuators A: Physical, vol. 154, no. 1, pp. 103-108, Aug. 2009.

[17] H. Fang et al., "Fabrication and performance of MEMS-based piezoelectric power generator for vibration energy harvesting," Microelectronics Journal, vol. 37, no. 11, pp. 1280-1284, Nov. 2006.

[18] C. Hindrichsen, R. Lou-Møller, K. Hansen, and E.Thomsen, "Advantages of PZT thick film for MEMS sensors," Sensors and Actuators A: Physical, vol. 163, no. 1, pp. 9 - 14, 2010.

[19] R. Lou-Moeller et al., "Screen-printed piezoceramic thick films for miniaturised devices," Journal of Electroceramics, vol. 19, no. 4, pp. 333-338, 2007.

[20] A. Lei, R. Xu, A. Thyssen, A.C. Stoot, T. L. Christiansen, K. Hansen, R. Lou-Moeller, E.V. Thomsen and K. Birkelund, "MEMS-Based Thick Film PZT Vibriational Energy Harvester", *Proceeding, IEEE micro electro mechanical systems*, 2011, pp. 125-128.

[21] R.G. Ballas, "Piezoelectric Multilayer Beam Bending Actuators", Springer, 2007.

[22] D. Shen, J. Park, J. Ajitsaria, S. Choe, H. C. Wikle, and D. Kim, "The design, fabrication and evaluation of a MEMS PZT cantilever with an integrated Si proof mass for vibration energy harvesting", Journal of Micromechanics and Microengineering, vol. 18, no. 5, p. 055017, 2008.

CONTACT

Ruichao Xu, tel: +45-45255692;
RUICHAO.Xu@NANOTECH.DTU.DK

A.3 Piezo 2011

M. Guizzetti, T. Zawada, K. Hansen, R. Xu, A. Lei, A. C. Stoot, A. Thyssen, O. Hansen, E.V. Thomsen and K. Birkelund, "Design, fabrication and characterization of piezoelectric power harvesters realized with silicon micromachining and screen-printing technologies", Proceeding, PIEZO 2011-Electroceramics for End-Users VI, 2011.

Design, fabrication and characterization of piezoelectric power harvesters realized with silicon micromachining and screen-printing technologies

M. Guizzetti[1], T. Zawada[1], K. Hansen[1], R. Xu[2], A. Lei[2], A. C. Stoot[2], A. Thyssen[2], O. Hansen[2], E.V. Thomsen[2], K. Birkelund[2]

[1]Meggitt Sensing Systems, Hejreskovvej 18A, DK-3490 Kvistgård, Denmark.
Email: Michele.Guizzetti@meggitt.com
[2]Department of Micro- and Nanotechnology, Technical University of Denmark, DTU Nanotech, Building 345 East, DK-2800 Kongens Lyngby, Denmark

Abstract
Energy harvesting from the environment is an attractive possibility in order to realize self-powered wireless sensor systems. In this context the presented work focuses on the mechano-electric conversion of environmental vibrations, by means of piezoelectric effect. Piezoelectric MEMS power harvesters have been designed and fabricated with silicon microtechnology processes combined with screen-printing techniques. Different shapes and designs have been considered and fabricated, comparing the performances obtained during the characterization.

Introduction
In the last few years a lot of attention has been focused on the possibility of harvesting free energy from the environment and convert it into electrical energy to power wireless sensors [1-2]. This allows the avoidance of batteries, realizing an autonomous system that can theoretically operate indefinitely without requiring maintenance and costs for batteries replacement. Among the different low grade power sources freely available in the environment, sunlight, mechanical vibrations and thermal gradients are considered the most promising [3]. The presented work focuses on mechanical vibrations due to their widespread distribution (industrial machines, buildings, infrastructures, aircraft, automotive and human movement). Mechano-electric energy conversion can be performed utilizing different principles (electromagnetic, electrostatic and piezoelectric). The piezoelectric effect is the most promising for the high power density, wide availability of fabrication technologies, miniaturization capability and silicon technology compatibility, allowing the realization of small power sources [4].
In this work piezoelectric MEMS (MicroElectroMechanical Systems) devices have been designed, fabricated and characterized, as vibration power harvesters. These devices have been realized using silicon microtechnology processes, in combination with PZT thick films deposited by screen-printing technique.

Power harvesters fabrication
The designed harvesters consist of silicon cantilevers fixed at one end having a silicon proof mass at the opposite end (Fig. 1). The devices have a total planar dimension of 10 mm x10 mm, while the beam-mass together measures 6.5 mm x 5.5 mm with a mass-beam length ratio (MBR) ranging from 30% to 80% (Fig. 2). The bottom electrode, also working as a diffusion barrier, has been sputtered, on top of which a PZT thick film and the top electrode have been screen-printed.

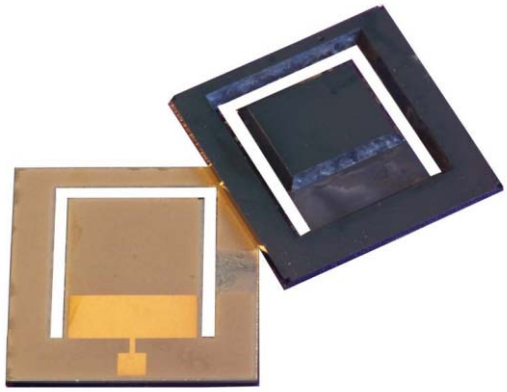

Figure 1: Realized power harvester device seen from two sides. Each device is 1 cm^2.

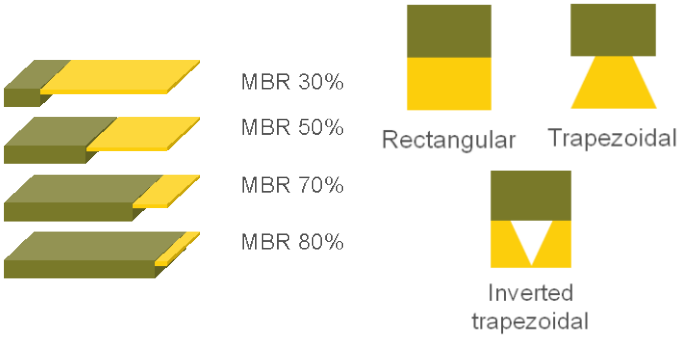

Figure 2: Mass-beam length ratios and shapes used for the harvesters.

Rectangular, trapezoidal and inverted trapezoidal cantilever shapes have been designed and their power conversion performances have been evaluated (Fig. 2).

Experimental results

The devices were glued to PCB fixtures and then mounted on a shaker, imposing a sinusoidal vertical acceleration at the base of the cantilever. A reference accelerometer was fixed to the shaker in order to measure the vertical acceleration. All the measurements were performed with the amplitude of the acceleration set at 0.5 *g* with the device working at the resonance frequency. Typical values for the measured capacitance of the devices vary from 1.0 nF to 5.8 nF, resulting in equivalent internal impedances from 110 kΩ to 2200 kΩ. The generated charge was measured obtaining charge sensitivities up to 37 nC/*g*. The open-circuit output voltage was also measured by means of a high-input buffer obtaining amplitude values up to 3 V. Measured maximum output power is in the range from 12 µW to 16 µW, while resonance frequency varies from 75 Hz to 250 Hz.

The best performances have been obtained from devices with the rectangular cantilever shape having a MBR of 50% and 70%. The devices with MBR of 50% generate a higher output charge (Fig. 3) while those with MBR of 70% have a higher output voltage (Fig. 4). The lowest resonance frequency is given by the trapezoidal and inverse trapezoidal shapes while considering the rectangular devices it is obtained with a mass-beam length ratio of 50%.

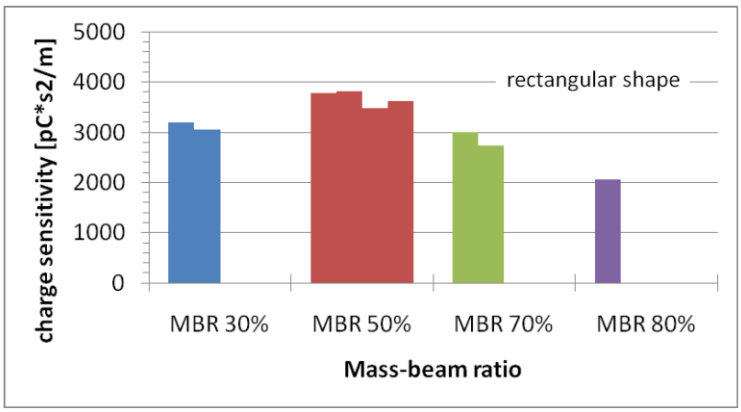

Figure 3: Measured charge sensitivity for rectangular shape harvesters versus mass-beam length ratio, at resonance.

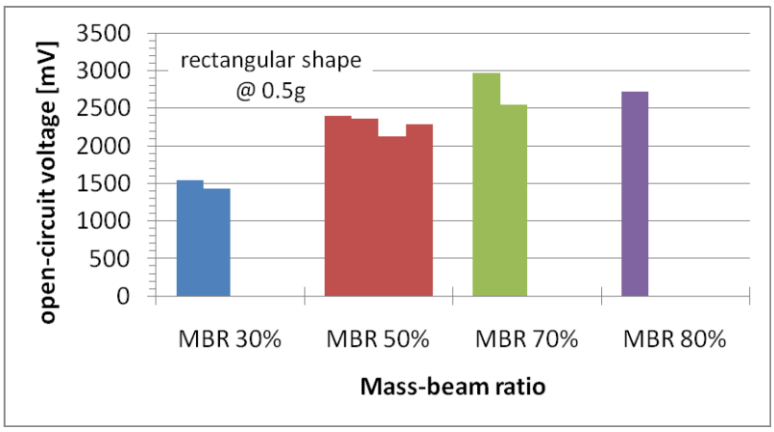

Figure 4: Measured open-circuit output voltage for rectangular shape harvesters versus mass-beam length ratio, at resonance.

Summary and conclusions

PZT thick film based power harvesters were designed, fabricated and tested as vibration power harvesters. Fabrication was done by means of silicon microtechnology processes and screen-printing technique.

Rectangular shaped harvesters with mass-beam length ratio of 50% and 70% gave the best performances in terms of output power.

Open-circuit output voltages and output powers up to 3 V and 16 μW respectively were obtained, exciting the harvesters at resonance with an acceleration amplitude of 0.5 *g*.

References

1. R. J. M. Vullers, R. Van Schaijk, I. doms, C. Van Hoof, R. Mertens, Micropower energy harvesting, Solid-State Electronics, 53, 684-693, 2009.

2. C. O. Matuna, T. O'Donnell, R. V. Martinez-Catala, J. Rohan, B. O'Flynn, Energy scavening for long-term deployable wireless sensor network, Talanta, 75, 613-623, 2008.

3. S. P. Beeby, M. J. Tudor, N. M. White, Energy harvesting vibration sources for microsystems applications, Measurement Science and Technology, 17, R175-R195, 2006.

4. K. A. Cook-Chennault, N. Thambi, A. M. Sastry, Powering MEMS portable devices - a review of non-regenerative and regenerative power supply systems with special emphasis on piezoelectric energy harvesting systems, Smart Materials and Structures, 17, 1-33, 2008.

Acknowledgements

The financial support of the Danish National Advanced Technology Foundation is gratefully acknowledged (project ELBA, contract no. 036-2009-1).

A.4 PowerMEMS-1 2011

A. Lei, R. Xu, C.M. Pedersen, M. Guizzetti, K. Hansen, E.V. Thomsen and K. Birkelund, "HOMOGENEITY ANALYSIS OF HIGH YIELD MANUFACTURING PROCESS OF MEMS-BASED PZT THICK FILM VIBRATIONAL ENERGY HARVESTERS", Proceeding, The 11th international workshop on micro and nanotechnology for power generation and energy conversion applications (PowerMEMS 2011), 2011, pp. 387-390.

HOMOGENEITY ANALYSIS OF HIGH YIELD MANUFACTURING PROCESS OF MEMS-BASED PZT THICK FILM VIBRATIONAL ENERGY HARVESTERS

A. Lei[1*], R. Xu[1], C.M. Pedersen[1], M. Guizzetti[2], K. Hansen[2], E.V. Thomsen[1] and K. Birkelund[1]
[1]Department of Micro- and Nanotechnology, Technical University of Denmark
[2]Meggitt Sensing Systems, Denmark
*Presenting Author: Anders.Lei@nanotech.dtu.dk

Abstract: This work presents a high yield wafer scale fabrication of MEMS-based unimorph silicon/PZT thick film vibrational energy harvesters aimed towards vibration sources with peak frequencies in the range of a few hundred Hz. By combining KOH etching with mechanical front side protection, SOI wafer to accurately define the thickness of the silicon part of the harvester and a silicon compatible PZT thick film screen-printing technique, we are able to fabricate energy harvesters on wafer scale with a yield higher than 90%. The characterization of the fabricated harvesters is focused towards the full wafer/mass-production aspect; hence the analysis of uniformity in harvested power and resonant frequency.

Keywords: MEMS, Energy harvester, High yield, Screen printing, PZT thick film

INTRODUCTION

With the recent development in low power electronics and small-scale energy harvesters, the realization of small long-term autonomous wireless sensors seems to become increasingly realistic. Vibrational harvesting of excess mechanical energy using piezoelectric transducers have gained much attention due to high coupling efficiency and simple design [1], but a major issue is the opposite relationship between size of the energy harvester and the frequency of the vibration source. The criterion for success for energy harvesters is that their size does not exceed the volume batteries would take up to supply the required power in the sensors lifetime. This can be well achieved using MEMS technology, however most applicable vibration sources have peak frequencies in the range of a few hundred Hz [2] which for classical MEMS devices are considered unusually low. Nevertheless, several MEMS technology based vibrational harvesting devices with resonant frequencies aimed for this frequency range have been presented [3], [4]. To achieve these resonant frequencies, designs with high length to thickness ratios and relative large proof masses have been utilized, resulting in devices that are laterally large and fragile during the fabrication processes.

Recently Lei et al. [5] presented a high performance MEMS-based PZT thick film unimorph vibrational energy harvester aimed towards a resonant frequency around 200 Hz. The harvester devices, each consisting of a cantilever design with a 1×1 cm^2 footprint, are fabricated using standard silicon MEMS processes with a yield around or higher than 90 %. The high yield is mainly achieved by the use of KOH etching with a mechanical front side protection for cantilever definition in combination, with a SOI wafer for accurately control of the silicon thickness. The active PZT layer is deposited on the silicon cantilever using a silicon compatible PZT thick film screen-printing technique. In [5], and as for a majority of other MEMS-based vibrational energy harvesters reported, only measurements for a single device is presented. Based on an identical fabrication process as in [5], characterization of each device from a full wafer will be presented in this paper hence, giving a comprehensive assessment of the device uniformity for the high yield wafer fabrication of vibrational PZT thick film energy harvesters.

FABRICATION

The unimorph vibrational energy harvester is fabricated using a five mask fabrication process on a 4 inch SOI wafer with a 20 μm device layer, a 1 μm buried oxide layer and a 500 μm thick substrate (Fig. 1(a)). A 1 μm SiO_2 layer is thermally grown followed by a deposition of 170 nm stoichiometric LPCVD silicon nitride (Fig. 1(b)). Backside openings in the silicon nitride for the KOH etch are defined using UV lithography followed by RIE etching and the front side nitride is removed in a RIE etch (Fig. 1(c)). A bottom electrode consisting of a 50 nm titanium adhesion layer and a 500 nm platinum layer, also serving as a diffusion barrier [6], is deposited using e-beam deposition. The bottom electrode is patterned using UV lithography followed by a wet etch in H_2O:HCl:HNO_3 (8:7:1) at a elevated temperature (Fig. 1(d)). On top of the bottom electrode a 27 μm PZT thick film is deposited using screen printing (Fig. 1(e)). Before the sintering, the PZT thick film is high pressure treated [7]. As top electrode, a 400 nm gold layer is deposited by e-beam evaporation through a shadow mask (Fig. 1(f)). The front side of the wafer is protected using a mechanical holder while the SiO_2 is removed in bHF and the cavities are etched in KOH, with the buried oxide functioning as a etch stop layer (Fig. 1(g)). The PZT structures are covered with resist and the cantilevers are released by a SiO_2 etch in bHF followed by a silicon etch using RIE (Fig. 1(h)). The PZT thick film is polarized by applying an electric field between the top and bottom electrodes.

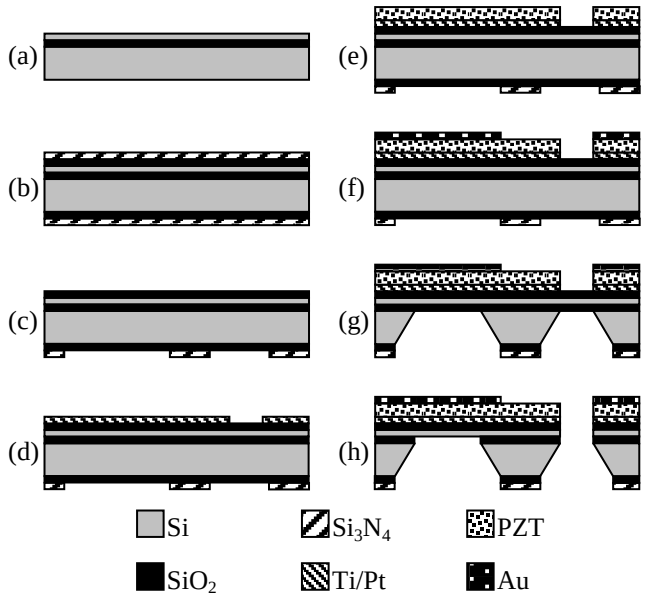

Fig. 1: Process flow for the unimorph MEMS-based PZT thick film vibrational energy harvester.

Fabrication Yield

The fabricated wafer accommodates 45 harvester devices with the dimensions listed in Table 1. The layout consists of 5 rows with 7 harvester devices and 2 rows with 5 harvester devices. A total of four chips were lost resulting in a yield of ~91 %. Fig. 2 shows a photography of the front and backside of two harvester devices.

Table 1: Dimensions of the energy harvesters.

Frame dimensions	10 mm × 10 mm
Medial dimension	< 1 mm
Cantilever width	5.5 mm
Cantilever length	3.25 mm
Mass width	5.5 mm
Mass length	3.25 mm

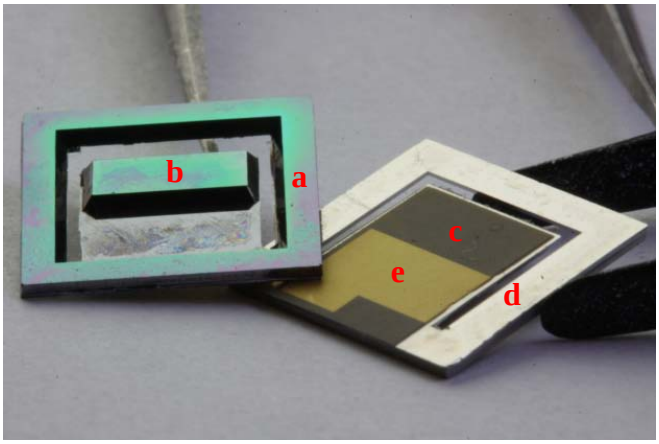

Fig. 2: Photograph showing front and back side of the fabricated energy harvesting devices. (a) frame, (b) proof mass, (c) PZT thick film, (d) bottom electrode and (e) top electrode.

CHARACTERIZATION

The characterization of the harvesters is carried out in the following way: initially, the capacitance together with open circuit voltage (V_{oc}) and resonant frequency (F_{res}) is measured for all harvesters. Secondly, the power output dissipated in a resistive load is measured for a number of representative chips.

For the initial part, the capacitance is measured using a HP 4278A capacitance meter, and the open circuit voltage and resonant frequency are measured by vibrating the harvesters using a TIRA TV51110 shaker driven by a sinusoidal signal from an Agilent 33250A function generator. The excitation acceleration is measured using a PCB Piezotronics 301A11 accelerometer with a PCB Piezotronics 482A23 sensor signal conditioner. The acceleration is measured as RMS values in fractions of the gravitational acceleration g (9.81 m s^{-2}). For the power output analysis, the harvester is connected to a resistive load and the power output, measured as RMS value, is calculated using $P=V_{rms}^2/R_{Load}$. The resistive load providing optimal power output is found by iteratively changing the resistance of the load.

RESULTS

The measured capacitances for the 41 fabricated harvesters listed as the wafer layout with rows and columns is seen Table 2. The average measured capacitance is 5.638 nF with a sample standard variation of 0.246 nF. The average capacitance corresponds to a dielectric constant of 842.

Table 2: Measured capacitance in nF for the 41 fabricated harvesters.

	A	B	C	D	E	F	G	[nF]
1		5.342	5.448	5.495	5.234	5.096		6
2	5.336	5.640	5.693	5.679	5.600	5.506	5.343	
3	5.139		5.799	5.769	5.636	5.564	5.398	
4	5.768	5.766	5.839	5.924		5.724	5.004	5.64
5	5.789	5.868	5.884	5.924	5.934	5.896	5.449	
6	5.765	5.958	5.671		5.779	5.615	5.588	
7			5.812	5.853	5.749	5.869		5

Table 3: Measured RMS open circuit voltage for the 41 harvesters at resonance with an input RMS acceleration of 0.5 g.

	A	B	C	D	E	F	G	[V]
1		0.75	1.06	0.985	1.30	0.507		2.7
2	1.173	0.96	1.21	1.32	1.52	1.07	1.88	
3	2.40		1.08	1.41	1.07	1.27	2.08	
4	2.09	2.15	2.25	1.31		1.72	1.10	1.6
5	2.27	2.20	1.84	1.00	1.28	1.60	2.41	
6	2.70	2.07	2.11		1.55	1.99	1.83	
7			2.10	1.53	1.77	1.79		0.5

The RMS V_{oc} for the fabricated harvesters measured at resonance with an input RMS acceleration of 0.5 *g* is listed in Table 3. The average V_{oc} is 1.6 V with a sample standard variation of 0.52 V. The resonant frequency at which maximum V_{oc} is obtained is listed in Table 4. The average F_{res} is measured to 333.3 Hz with a sample standard deviation of 9.9 Hz.

Table 4: Resonant frequencies determined simultaneously with the maximum open circuit voltage. Measurements performed with an input RMS acceleration of 0.5 g.

	A	B	C	D	E	F	G	[Hz]
1		298.2	331.4	323.9	322.6	341		350.1
2	316	336.8	344.3	331.9	343	330.5	342.8	
3	335.5		323	326.9	335.1	333.2	344.1	
4	332.4	339.5	339.7	326.6		343.8	327	333.3
5	331.8	338.5	334.6	318.3	322.9	330	347.2	
6	328	325.5	340.7		334.9	346.8	350.1	
7			337.2	334.5	341	334.5		298.2

Load Measurements

For the power output measurements a total of 10 representative harvester devices are selected. Three devices are selected from around each of the three quartiles (Q_1=1.17 V, Q_2=1.55 V and Q_3=2.08 V) of the open circuit measurements, the last harvesters selected is the one with highest V_{oc} output. In Table 5 the iteratively found optimal resistive load is listed for each of the selected harvesters together with the measured RMS power output for the three RMS accelerations 0.5 *g*, 0.75 *g* and 1 *g*. The listed bandwidth is measured as full width at half maximum (BW_{FWHM}) at 0.5 *g* acceleration and the total quality factor is calculated as $Q_{total}=F_{res}/BW_{FWHM}$. In Fig. 3 the results are outlined with power output at the three accelerations plotted for each of the 10 harvesters.

Table 5: RMS power output measurements for 10 harvester devices representative for the 41 fabricated devices. Power is measured at three different RMS accelerations with the resistive load listed. Bandwidth (BW_{FWHM}) and total quality factor (Q_{total}) is measured at 0.5 g.

	Chip	Load [kΩ]	BW_{FWHM} [Hz]	Q_{total}	RMS Power [µW]		
					0.5 *g*	0.75 *g*	1 *g*
Peak	A6	150	5.00	65.9	12.5	25.0	39.3
Q3 2.08V	G3	50	6.80	50.7	10.5	22.1	35.0
	B4	50	6.80	49.7	9.6	21.3	35.8
	B6	50	6.60	49.3	9.7	21.4	34.7
Q2 1.55V	F5	50	8.20	40.1	6.7	15.7	25.7
	D7	75	9.00	37.1	6.1	14.8	24.3
	E6	75	8.50	39.2	5.5	13.1	22.5
Q1 1.17V	C2	75	8.75	37.7	4.8	11.1	17.9
	A2	75	8.20	38.4	5.1	10.9	15.3
	C3	75	10.25	31.1	2.9	7.2	13.3

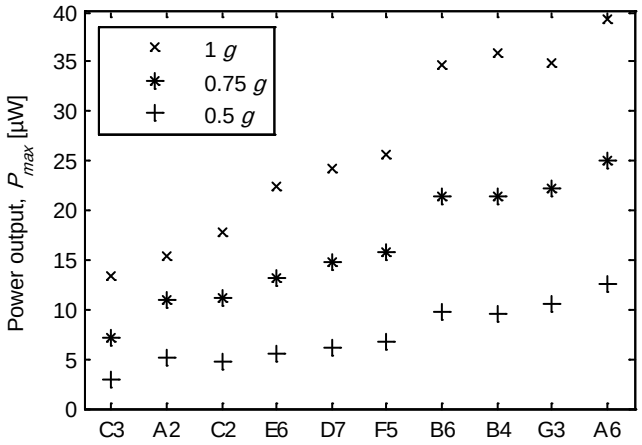

Fig. 3: Measured RMS power output for three different accelerations plotted for the 10 representative harvesters.

DISCUSSION

Assuming that the porosity and thus the dielectric constant of the screen-printed PZT thick film is constant over the wafer, the measured variation in capacitance is an estimate of geometrical variations. The lateral dimensions of the capacitor are defined by the deposited electrodes which are controlled by lithography. It can therefore be assumed that the main contribution to the variation in capacitance is variations in thickness of the PZT thick film. Percentagewise the sample standard deviation is 4.4% relative to the average value. This corresponds to a variation of 1.2 µm out of a PZT film thickness of 27 µm. Ignoring the three lowest measured capacitances, this value decreased to 0.9 µm.

From an application point of view the main success criteria for a linear vibrational energy harvester is the frequency match with the vibration source. The resonant frequency is determined by mechanical properties with the cantilever thickness and distance from cantilever anchoring point to center of mass as the dominating geometrical parameters. The silicon part of the cantilever is determined accurately by the SOI wafer and the capacitance measurements indicated a relatively small thickness variation of the PZT thick film. The distance to the center of mass, width of the cantilever and mass of the proof mass are all determined by lithography. The sample standard deviation relative to the average measured F_{res} is 3.0 %, ignoring the two lowest and highest measurements this value decreases to 2.2 %. Since F_{res} is proportional to the square root of the cantilever thickness cubed, the relative variation is expected to be higher although the silicon part accounts for a high part of the cantilever stiffness. This could indicate that the variation in capacitance across the wafer is caused by both varying dielectric constants and PZT thicknesses.

While the capacitance and F_{res} measurements give estimates of the variation of the mechanical parameters and the dielectric constant, the open circuit voltage measurements will provide information concerning variations in piezoelectric coefficients and quality

factor since $V_{oc}=g_{31}\bar{\sigma}h_{PZT}$, where g_{31} is the piezoelectric voltage coefficient, $\bar{\sigma}$ is the average induced stress in the PZT layer with thickness h_{PZT}. Besides being determined by mechanical properties, which also affects the resonant frequency, the average induced stress is related to the tip displacement at resonance and thus quality factor. The measured sample standard deviation relative to the average V_{oc} is 32.6 %, ignoring the two lowest and highest values gives a percentage of 27.8 % which is still higher than what the variation in PZT thickness can account for. The majority of the variation in V_{oc} is therefore believed to originate from either g_{31} which is determined by how well the PZT thick film is polarized or the quality factor.

Except from the V_{oc} measurements where the harvesters from the lower left corner of the wafer appears to have a general higher output, no significant wafer area tendencies are observed in the capacitance and F_{res} measurements nor in-between all three measurements.

For the output power measurements the best uniformity in performance is observed in-between the three chips from the third quartile. The difference in power output is around or less than 1 µw for the three accelerations. Similar small variations are observed in bandwidth and total quality factor. The resonant frequency varies from 325-344 Hz for the three chips which is considerably more than the measured bandwidth of around 6.8 Hz. The variation in power output of the three chips from the second quartile increases to around 3 µW difference at 1 *g*. For the first quartile chips, the variation is around 4.5 µW at 1 *g*. In average the first quartile devices harvest 30 % and 36 % less power than the second quartile devices at 0.5 *g* and 1 *g*, respectively. Third quartile devices perform 63 % and 45 % better than second quartile devices at 0.5 *g* and 1 *g*, respectively. Compared to the variation of the open circuit measurements this increased variation is expected since the output power is proportional to the voltage squared. The relationship between increasing quality factor and increasing power output indicates that the main cause of variation in performance is variation in quality factor and not piezoelectric coefficients.

CONCLUSION

Using a silicon-based fabrication process involving SOI wafers, KOH etching and screen-printing of PZT thick film, a yield of 41 out of 45 (~91 %) harvester devices for a wafer was achieved. Measurements of the open circuit voltage for the 41 devices showed a relative difference of 32.6 % between the standard deviation and average. Measurements of the capacitance and resonant frequency showed a relative difference between the standard deviation and average value of 4.4 % and 3 % respectively. This indicates that the main variation in open circuit voltage performance is caused by varying quality factor.

Output power measurements using an optimized resistive load, showed good uniformity between chips with similar open circuit voltages from the high performance section. Decreasing uniformity was observed between chips from the less good performing sections of the open circuit voltage measurements. A maximum power output of 39.3 µW was measured at 1 *g* for the best performing harvester. The power harvesting bandwidth was measured to 5-10 Hz, with the best performing harvesters having the lowest bandwidth. The average resonant frequency was measured to 333 Hz with a standard variation of 9.9 Hz. From an application point of view, either the bandwidth should be increased to cover the variation in resonance, or the variation of the resonant frequency must be decreased.

REFERENCES

[1] Beeby S P, Tudor M J, White N M 2006 Energy harvesting vibration sources for microsystems applications *Meas. Sci. Technol.* **17** R175–95

[2] Roundy S, Wright P K, Rabaey J 2003 A study of low level vibrations as a power source for wireless sensor nodes *Computer Communications* **26** 1131–44

[3] Elfrink R, Kamel T M, Goedbloed M, Matova S, Hohlfeld D, van Andel Y, van Schaijk R 2009 Vibration energy harvesting with aluminum nitride-based piezoelectric devices *J. Micromech. Microeng.* **19** 094005

[4] Shen D, Park J-H, Noh J H, Choe S-Y, Kim S-H, Wikle III H C, Kim D-J 2009 Micromachined PZT cantilever based on SOI structure for low frequency vibration energy harvesting *Sensors and Actuators A: Physical* **154** 103–8

[5] Lei A, Xu R, Thyssen A, Stoot A C, Christiansen T L, Hansen K, Lou-Moller R, Thomsen E V, Birkelund K 2011 MEMS-based thick film PZT vibrational energy harvester *Proceedings, IEEE micro electro mechanical systems* 125–8

[6] Hindrichsen C C, Pedersen T, Thomsen E V, Hansen K, Lou-Møller R 2008 Investigation of Top/Bottom Electrode and Diffusion Barrier Layer for PZT Thick Film MEMS Sensors *GFER* **367** 201–13

[7] Hindrichsen C G, Lou-Møller R, Hansen K, Thomsen E V 2010 Advantages of PZT thick film for MEMS sensors *Sensors and Actuators A: Physical* **163** 9–14

A.5 PowerMEMS-2 2011

R. Xu, A. Lei, C. Dahl-Petersen, K. Hansen, M. Guizzetti, K. Birkelund, E.V. Thomsen and O. Hansen, "MEMS-BASED PZT/PZT BIMORPH THICK FILM VIBRATION ENERGY HARVESTER", Proceeding, The 11th international workshop on micro and nanotechnology for power generation and energy conversion applications (PowerMEMS 2011), 2011, pp. 143-146.

MEMS-BASED PZT/PZT BIMORPH THICK FILM VIBRATION ENERGY HARVESTER

R. Xu[1], A. Lei[1], C. Dahl-Petersen[1], K. Hansen[2], M. Guizzetti[2], K. Birkelund[1], E.V. Thomsen[1] and O. Hansen[1,3]

[1]Department of Micro- and Nanotechnology, Technical University of Denmark, DTU Nanotech, Building 345 East, DK-2800 Kongens Lyngby, Denmark

[2]Meggitt Sensing Systems, DK-3490 Kvistgaard, Denmark

[3]CINF, Center for Individual Nanoparticle Functionality, Technical University of Denmark

*Presenting Author: ruichao.xu@nanotech.dtu.dk

Abstract: We describe fabrication and characterization of a significantly improved version of a MEMS-based PZT/PZT thick film bimorph vibration energy harvester with an integrated silicon proof mass. The main advantage of bimorph vibration energy harvesters is that strain energy is not lost in mechanical support materials since only PZT is strained, and thus it has a potential for significantly higher output power. An improved process scheme for the energy harvester resulted in a robust fabrication process with a record high fabrication yield of 98.6%. Moreover, the robust fabrication process allowed a high pressure treatment of the screen printed PZT thick films prior to sintering, improving the PZT thick film performance and harvester power output reaches 37.1 μW at 1 g.

Keywords: Energy harvesting, scavenging, piezoelectric, PZT, bimorph, thick film, MEMS, screen printing.

INTRODUCTION

One of the most severe challenges man is facing today is to fulfil the need for energy without harmful environmental consequences. This complicated, huge challenge must be met by a wide range of solutions; among these are more efficient use of resources and replacement of fossil fuels by renewable energy sources. More efficient use of resources will require more widespread use of sensing micro-systems to control and optimize processes. Some of these systems will be placed in remote areas where it is desirable if the system is self supported with power, a feature that will be equally desirable for the increasing number of portable complex electronic systems in use today.

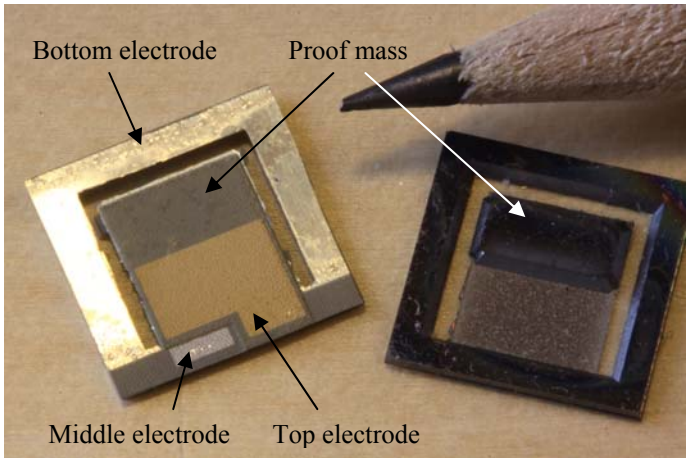

Fig. 1: Photographic image showing the front and back of the 10 mm × 10 mm energy harvesters.

In the external surroundings energy such as ambient light, mechanical vibrations, sound, or thermal gradients is available to be harvested for free. With the advances in micro-technology many useful electronic systems have low enough power requirements to make completely self supported systems realistic. One of the methods to harvest mechanical energy from vibrations is to make use of the piezoelectric transduction mechanism [1]. A typical piezoelectric energy harvester is based on a cantilever beam, which consists of the active piezoelectric ceramic with metal electrodes on both sides and a passive mechanical support structure, anchored at one end and with a proof mass at the other [2, 3, 4, 5]. The main advantage of PZT/PZT thick film bimorph energy harvesters, compared to the aforementioned harvesters, is that strain energy is not lost in mechanical support materials since only PZT is strained, and thus it has a potential for higher power output. The first generation bimorph PZT/PZT thick film harvester was presented in [6], where it was shown that by using PZT thick film, it is possible to realize a self supporting device without the need of a passive mechanical structure. However, the fabrication yield was low due to a process sequence with an early deep reactive ion etch (DRIE) step, which turned most of the structure into a fragile membrane. A revised process plan, using the advantageous process steps introduced in [7], has significantly improved both fabrication yield and performance of the harvesters. The DRIE step was replaced by a KOH wet etch and moved to the last part of the fabrication process; and as a result the fabrication yield was more than tripled to a record high yield of 98.6%. As an added benefit the improved mechanical stability of the structure during PZT thick film, InSensor® TF2100, deposition and processing allowed high pressure treatment of the PZT thick film before sintering, this resulted in more than a fivefold improvement of the harvester power output compared to previous results [6]. Furthermore, the use of KOH etching may facilitate a scalable future mass

production.

FABRCATION

The fabricated energy harvester, shown in Fig. 1, combines PZT thick film screen printing with standard MEMS technology.

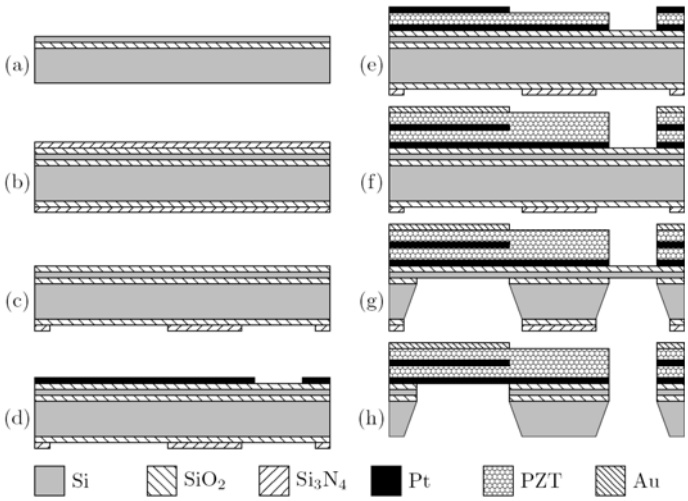

Fig. 2: Cross sectional view of the fabrication scheme.

The fabrication process is illustrated in Fig. 2. The fabrication process starts with a silicon on insulator (SOI) wafer with 20 µm device layer and 1 µm buried oxide on a 525 µm handle substrate, as shown in Fig. 2(a). First, a 1 µm thick silicon dioxide is thermally grown, and then a 170 nm thick silicon nitride is deposited using low pressure chemical vapour deposition (LPCVD), as shown in Fig. 2(b). The nitride is removed on the front side using RIE, and after that the back side of the wafer is patterned using conventional lithography processes and similarly etched in RIE, as shown in Fig. 2(c). A 50 nm Ti adhesion layer and a 500 nm Pt for the bottom electrode are deposited on the front side of the wafer, and subsequently patterned, using AZ4562 resist, followed by an etch in a wet etch solution, H_2O:HCl:HNO_3 (8:7:1) at elevated temperature, as shown in Fig. 2(d). Thereafter the PZT thick film layer is screen printed on the patterned bottom electrode, high pressure treated [8] and sintered, here the bottom electrode serves as a diffusion barrier. Here the advantage in the new fabrication process appears: screen printing and high pressure treatment of the PZT layer on a full wafer; instead of a wafer with thin membranes as it was done in [6], not only prevents any chip loss during this step but also ensures a higher quality thick film that will prevent any cantilever breakage after the final release etch. Next, the 500 nm Pt middle electrode is deposited through a prefabricated silicon shadow mask using e-beam evaporation, as shown in Fig. 2(e). The shadow mask was made using a 350 µm silicon wafer, which was patterned using UV lithography and etched through in a DRIE process. The second PZT thick film layer is then screen printed, high pressure treated and sintered. This is followed by deposition of a 500 nm Au top electrode through another prefabricated shadow mask, fabricated using the aforementioned fabrication steps, see Fig. 2(f). Thereafter the wafer is mounted on a 4" tandem series wafer holder from Advanced Micromachining Tools (AMMT). The oxide on the backside is etched in buffered hydrofluoric acid (bHF), while the front side of the SOI wafer is protected by the holder. Then the silicon is etched in a KOH etch until the buried oxide layer is reached and then the buried oxide layer is removed in bHF, as shown in Fig. 2(g). Finally, the sacrificial device layer is etched in RIE, releasing the cantilevers; see Fig. 2(h).

Figure 3 shows the fabricated harvester wafer before dicing. Notice that all cantilevers are intact, the chip yield on the wafer at this stage is still 100%, while if the fabrication process from [6] was used the chip yield would be much less.

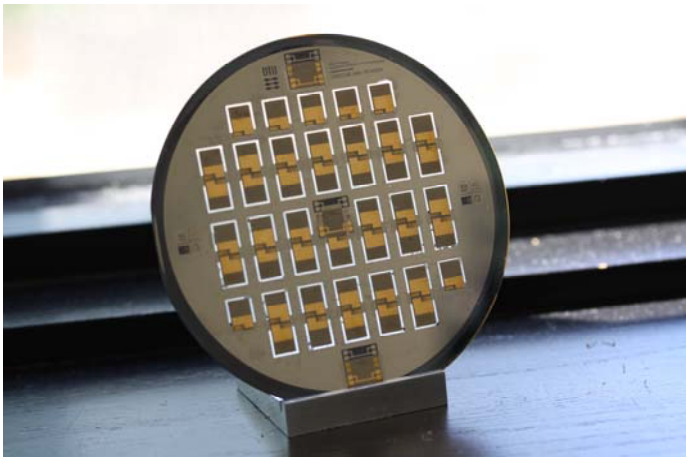

Fig. 3: Image of a fabricated harvester wafer before dicing.

The wafer is diced and the chips polarized individually. The polarization directions of the two layers are aligned opposite to each other, *i.e.* during polarization the top and bottom electrodes are grounded and a polarization voltage is applied to the middle electrode. The dimensions for the final energy harvester chips are shown in Table 1.

Table 1: Energy harvester dimensions.

Frame dimensions	10 mm × 10 mm
Medial dimensions	< 1 mm
Cantilever width	5.5 mm
Cantilever length	3.25 mm
Mass length	3.25 mm
Total cantilever height	2 × 20 µm

RESULTS

The fabricated energy harvesters were characterized in a shaker setup, where a B&K Mini Shaker 4810 driven by an amplified sinusoidal signal from an Agilent 33220A function generator was used to simulate an external vibration from the environment. Both the energy harvester and a B&K Piezoelectric Accelerometer 8305 were mounted on

the Mini Shaker. The accelerometer served as a reference for the input RMS acceleration and measurements are reported in fractions of the gravitational acceleration g (9.81 m s^{-2}). The RMS power output is found by connecting the harvester to a resistive load while the voltage drop across the load was measured. The optimal resistive load, R_{opt}, was found by varying the resistive load in steps of 10 kΩ to achieve maximum dissipated power in the load resistance, *i.e.* $P_{RMS}=V_{RMS}^2/R_{opt}$. Figure 4 shows the power output of the harvester as a function of the frequency for different input accelerations, measured with the PZT layers connected in series, *i.e.* the load is connected between bottom and top electrodes. The optimal resistive load used here was R_{opt}=200 kΩ. At 1 g input acceleration the power output reaches 37.1 μW.

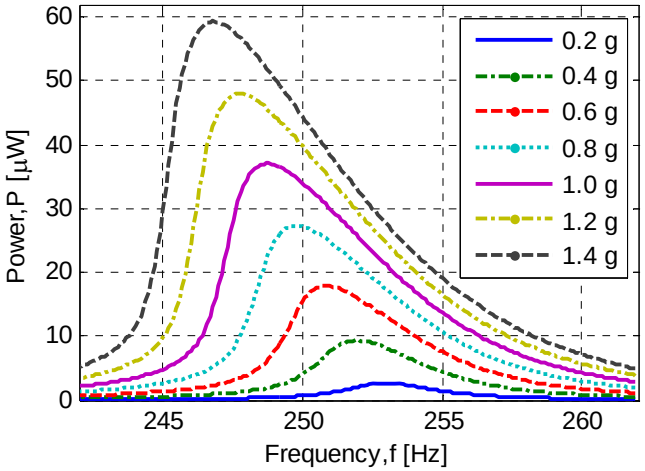

Fig. 4: RMS power output of both PZT layers combined as a function of frequency near the resonant frequency for different input accelerations at an optimal resistive load of 200 kΩ

.

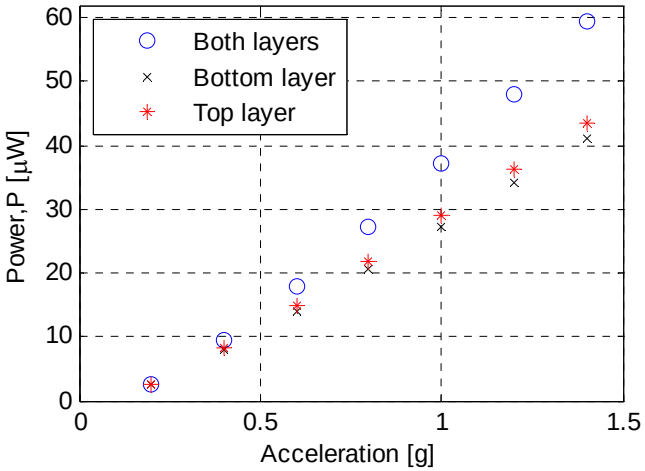

Fig. 5: RMS power output from the top PZT layer, the bottom PZT layer and both layers combined as a function of the input acceleration at their respective optimal resistive loads.

The output power from the bottom PZT layer and the top PZT layer were measured using the same measurement scheme. During measurements on the top PZT layer, the top and middle electrodes were connected while the bottom electrode was left open circuit. The optimal resistive load was found to be 130 kΩ for the top layer. Similarly, during measurements on the bottom PZT layer the bottom and middle electrodes were connected and the top electrode was left open circuit. The optimal resistive load was found to be 90 kΩ for the bottom layer. Collecting the peak output power from the measurements yields the plot reported in Fig. 5, where the output power is shown as a function of the input acceleration. The bandwidth, defined as the full width at half maximum of the data such as those in Fig. 4, was extracted for all measurements and it is reported in Fig. 6.

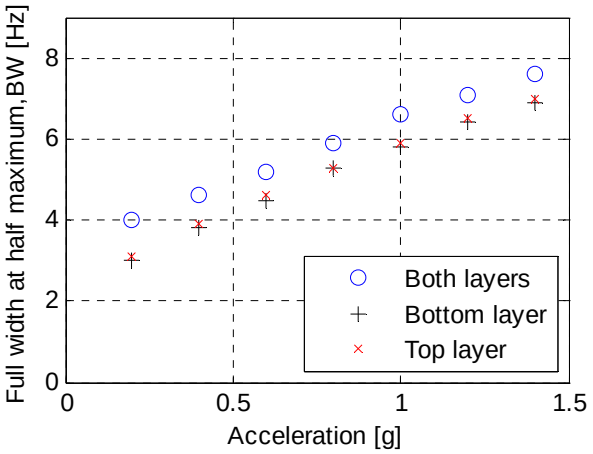

Fig. 6: The full width at half maximum bandwidth for the top PZT layer, the bottom PZT layer and both layers combined as a function of the input acceleration at their respective optimal resistive loads.

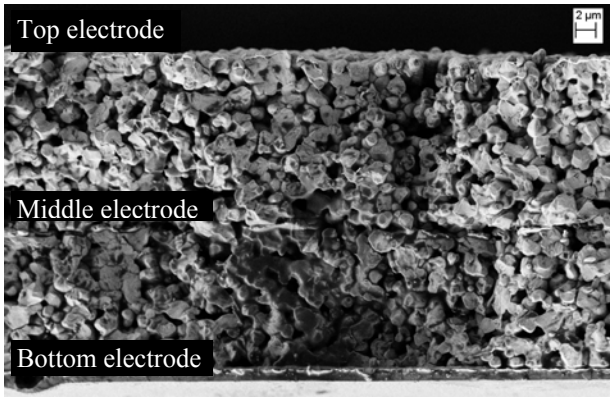

Fig. 7: SEM image showing a cross-sectional view of the PZT/PZT bimorph thick film structure.

DISCUSSION

The resonant frequency shift as a function of the acceleration observed in Fig. 4 was also seen in [6], where it was assumed to be due to a non linear softening effect. Even though such an effect is still present in the pressure treated harvester, the softening effect is much less prominent compared to that in [6].

As a result, the resonant frequency shift with acceleration is smaller, and the frequency responses become more symmetrical around the resonance peaks.

From Fig. 5 it can be noted that the power outputs of the two individual layers are almost identical, this was not the case in [6]. Apparently, the use of high pressure treatments renders the PZT thick film layers quite similar. This is supported by the SEM inspection shown in Fig. 7, where a cross sectional view of the cantilever shows that the two layers are very similar both in thickness and morphology which was not the case in a similar study in [6]. The difference in the optimal resistive loads with such similar films is surprising and thus still needs further investigation. The output power from both layers combined in series is less than the sum of the powers from the two individual layers. This, to some extent, may be explained by Fig. 6, where the bandwidth of both layers combined in series is about 1 Hz larger than that of each layer for all input accelerations. As a result the output power is not doubled by the use of two PZT layers, but it is still increased significantly; moreover, the harvester becomes useful in a wider spectrum of vibrations due to the increase in bandwidth. The measured RMS power output at 1 *g* acceleration is 37.1 μW, which is comparable to the best performing MEMS energy harvesters reported in literature in recent years [5, 9].

CONCLUSION

MEMS-based PZT/PZT bimorph thick film vibration energy harvesters were successfully fabricated and characterized. By implementing an improved fabrication process a fabrication yield of 98.6% was achieved. The revised process plan made high pressure treatment of the PZT thick film layers before sintering feasible. As a result the two PZT layers became denser and more similar in thickness and morphology. The power outputs at 1 *g* for the top and bottom layers were 29.1 μW and 27.2 μW, respectively. The power output with both layers combined was 37.1 μW at 1 *g* with a bandwidth value of 7 Hz.

REFERENCES

[1] Beeby S P, Tudor M J, White N M, 2006 Energy harvesting vibration sources for Microsystems applications *Measurement Science and Technology* **17** no. 12, R175-R195

[2] Fang H, Liu J, Xu Z, Dong L, Wang L, Chen D, Cai B, Liu Y, 2006 Fabrication and performance of MEMS-based piezoelectric power generator for vibration energy harvesting *Microelectronics Journal* **37** 1280-1284.

[3] Choi W J, Jeon Y, Jeong J H, Sood R, Kim S G 2006 Energy harvesting MEMS device based on thin film piezoelectric cantilevers *Journal of Electroceramics* **17** 543-548

[4] Shen D, Park J, Ajitsaria J, Choe S, Wikle H C, Kim D, 2008 The design, fabrication and evaluation of a MEMS PZT cantilever with an integrated Si proof mass for vibration energy harvesting *Journal of Micromechanics and Microengineering* **18** no. 15 055017

[5] Aktakka E E, Peterson R L, Najafi K, 2011 Thinned-PZT on SOI process and design optimization for piezoelectric inertial energy harvesting *Proceeding, Transducers 2011* (Beijing, China Jun 2011) 1649-1652

[6] Xu R, Lei A, Christiansen T L, Hansen K, Guizzetti M, Birkelund K, Thomsen E V, Hansen O, 2011 Screen printed PZT/PZT thick film bimorph MEMS cantilever device for vibration energy harvesting *Proceeding, Transducers 2011* (Beijing, China Jun 2011) 679-682

[7] Lei A, Xu R, Thyssen A, Stoot A C, Christiansen T L, Hansen K, Lou-Moeller R, Thomsen E V, Birkelund K, 2011 MEMS-Based Thick Film PZT Vibriational Energy Harvester *Proceeding, IEEE micro electro mechanical systems 2011* (Cancun, Mexico January 2011) 125-128

[8] Hindrichsen C, Lou-Moeller R, Hansen K, and Thomsen E V, 2010 Advantages of PZT thick film for MEMS sensors *Sensors and Actuators A: Physical* **163** no. 1, 9 - 14

[9] Elfrink R, Kamel T M, Goedbloed M, Matova S, Hohlfeld D, van Andel Y, van Schaijk R, 2009 Vibration energy harvesting with aluminum nitride-based piezoelectric devices *Journal of Micromechanics and Microengineering* **19** 094005

A.6 Sensors and Actuators A 2012

R. Xu, A. Lei, C. Dahl-Petersen, K. Hansen, M. Guizzetti, K. Birkelund, E.V. Thomsen and O. Hansen, "Screen printed PZT/PZT thick film bimorph MEMS cantilever device for vibration energy harvesting", Sensors and Actuaters A: Physical, vol. 188, no. 0, pp. 383–388, Dec. 2012.

Sensors and Actuators A 188 (2012) 383–388

Contents lists available at SciVerse ScienceDirect

Sensors and Actuators A: Physical

journal homepage: www.elsevier.com/locate/sna

Screen printed PZT/PZT thick film bimorph MEMS cantilever device for vibration energy harvesting

R. Xu[a,*], A. Lei[a], C. Dahl-Petersen[a], K. Hansen[b], M. Guizzetti[b], K. Birkelund[a], E.V. Thomsen[a], O. Hansen[a,c]

[a] Technical University of Denmark, Department of Micro and Nanotechnology, Ørsted Plads, Building 345 East, 2800 Kgs. Lyngby, Denmark
[b] Meggitt Sensing Systems, DK-3490 Kvistgaard, Denmark
[c] CINF, Center for Individual Nanoparticle Functionality, Technical University of Denmark, Denmark

ARTICLE INFO

Article history:
Available online 27 December 2011

Keywords:
Energy harvester
MEMS
Thick film
Screen printing
High pressure treatment
PZT
Bimorph

ABSTRACT

We present a microelectromechanical system (MEMS) based PZT/PZT thick film bimorph vibration energy harvester with an integrated silicon proof mass. Most piezoelectric energy harvesting devices use a cantilever beam of a non piezoelectric material as support beneath or in-between the piezoelectric materials; it provides mechanical support but it also reduces the power output. In our device we replace the support material with another layer of the piezoelectric material. With the absence of an inactive mechanical support all stresses induced by vibrations will be harvested by the active piezoelectric elements. We show experimental results from two types PZT/PZT harvesting devices, one where the $Pb(Zr_xTi_{1-x})O_3$ (PZT) thick films are high pressure treated during the fabrication and the other where the treatment is omitted. We find that with the high pressure treatment prior to PZT sintering, the films become denser and the harvester efficiency increases significantly.

1. Introduction

With the recent development in low power electronics and wireless systems it has become increasingly interesting to use energy harvesters that harness ambient energy to supply electronic sensor systems with power, and thereby replace electrochemical batteries. The limited energy capacity of traditional electrochemical batteries makes periodical battery replacement necessary; moreover, the batteries often take up a significant volume in the total sensing system. The microelectromechanical system (MEMS) energy harvester addresses both issues with its large energy to volume ratio [1] and by scavenging energy from external sources. As a result, the service lifetime is only limited by material decay or fatigue. Thus the frequency of periodic maintenance may be reduced from months to years, and maybe even decades.

The most common ambient power sources are solar, thermal, mechanical or unused RF energy. Harvesting of vibration energy from a mechanical noise source can be based either on electrostatic, electromagnetic or piezoelectric conversion [2]. The interest in harvesting energy from ambient mechanical vibrations has resulted in a number of review articles in recent years [1–4]. In particular the piezoelectric transduction method has received significant attention. A typical piezoelectric energy harvester is based on a bimorph cantilever beam, which consists of the active piezoelectric ceramic with metal electrodes on both sides on top of a passive mechanical support structure, which is anchored at one end and attached to a proof mass at the other [5–8].

Several different piezoelectric materials are available, the materials of prime interest for application in MEMS devices, however, are $Pb(Zr_xTi_{1-x})O_3$ (PZT), zinc oxide (ZnO) [9,10] and aluminum nitride (AlN) [11,12]. Among these, PZT is the material most commonly used in energy harvesters, due to its large piezoelectric coefficients [1,13].

Energy harvesters using bulk PZT have been presented in [14] and [15]. These energy harvesters have large dimensions and are thus not compatible with small sensor systems. Energy harvesters made using thin film deposition methods, such as sputtering [16] or sol–gel spin-on [17,18] are characterized by very thin PZT layers with a thickness of just a few micrometers. We wish to fabricate a PZT/PZT bimorph cantilever energy harvester, where two PZT layers are separated by a middle electrode. Here both layers are active and thus the strain energy from both layers is harvested [19]. The advantage of such a structure is that all strain energy is harvested, while in conventional structures with inactive support materials the strain energy in these is not harvested and thus wasted. Fabrication of a pure self supporting PZT beam without any mechanical support structure will be very difficult using those aforementioned thin film methods. Therefore we use thick film screen printing

* Corresponding author. Tel.: +45 45255692.
E-mail address: Ruichao.Xu@nanotech.dtu.dk (R. Xu).

0924-4247/$ – see front matter © 2011 Elsevier B.V. All rights reserved.
doi:10.1016/j.sna.2011.12.035

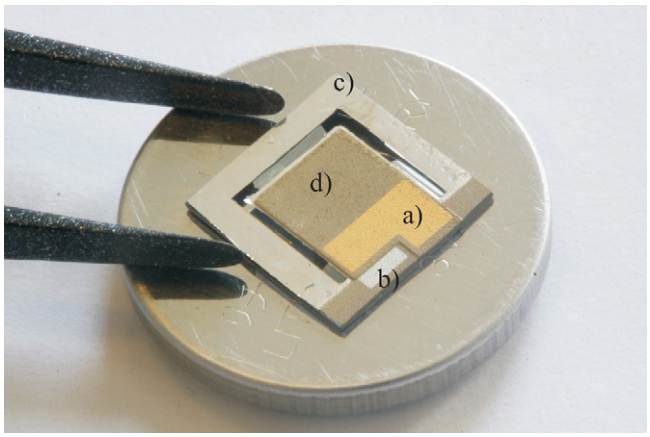

Fig. 1. The bimorph MEMS energy harvester on top of a CR2032 button battery. (a) The area of the Au top electrode. (b) The middle electrode contact pad. (c) The bottom electrode contact pad on top of the chip frame. (d) The area of the proof mass.

technique, and take advantage of the ability to screen print PZT thick films with a thicknesses of 15–60 μm to fabricate energy harvesters with a pure PZT beam [22]. With the use of PZT thick film, instead of PZT thin film, it was confirmed that a mechanical support material is indeed no longer needed in the final device, since the beam is thick and strong enough to support the proof mass.

In this work the piezoelectric PZT thick film used is InSensor® TF2100; the PZT thick films were screen printed onto the wafers then sintered. This technique has previously been used in fabrication of a piezoelectric accelerometer [23] and an energy harvester [24]. The fabricated PZT/PZT bimorph cantilever energy harvester is shown in Fig. 1.

2. Fabrication

The PZT/PZT thick film energy harvesters are fabricated using a six mask fabrication process on double sided polished 4 in. (100 mm) silicon on insulator (SOI) wafers with a 30 μm device layer, a 1 μm buried oxide layer and a 525 μm thick carrier substrate, see Fig. 2(a). The backside of the SOI wafers are patterned using UV lithography and etched using a deep reactive ion etching (DRIE) process (STS Pegasus, running a Bosch process), see Fig. 2(b). A 10 μm AZ4562 photoresist is sufficient to mask the etch process, which lasts for about 40 min. Here, the buried oxide layer is used as an etch stop layer. After an RCA clean [25], a 1 μm thick silicon dioxide layer is grown by a wet thermal oxidation at 1100 °C for 160 min. This layer will serve as an etch stop for a final reactive ion etch (RIE), releasing the structure, see Fig. 2(c). The bottom electrode is deposited on the front side of the SOI wafers using e-beam deposition. The bottom electrode layer consists of a 50 nm titanium adhesion layer and 500 nm of platinum which also serves as a diffusion barrier in the PZT sintering process. The bottom electrode layer is patterned using UV lithography and etched in a wet etch solution, H_2O:HCl:HNO_3 (8:7:1) at 85 °C, see Fig. 2(d). On top of the patterned bottom electrode a PZT thick film is deposited using screen printing. Some of the wafers were subsequently high pressure treated in a process where a fluid mixture is used to apply high pressure to the wafers [22]. All wafers were then sintered [23], see Fig. 2(e). Next, a middle electrode (50 nm titanium and 500 nm platinum) was deposited through a prefabricated shadow mask using e-beam deposition, see Fig. 2(f). The shadow mask was fabricated using a 350 μm thick silicon wafer, which was patterned using UV lithography and etched through in a DRIE process (STS Pegasus). Next the second layer of PZT thick film was screen printed. The pressure treated wafers were pressure treated again, and then all wafers were sintered [23]. The 500 nm Au top electrode layer was also deposited through a shadow mask using e-beam deposition, see Fig. 2(g). With the two PZT stacks in place the silicon device layer was removed. First, the oxide on the backside was etched in buffered hydrofluoric acid (bHF), while the front side of the SOI wafer was protected with photoresist. The backside of the SOI wafer was finally etched in a RIE process (STS Multiplex system, running an SF_6/O_2 plasma at 80 mTorr and 30 W) until the device layer was completely removed and the cantilever released, see Fig. 2(h). The wafers were diced and the

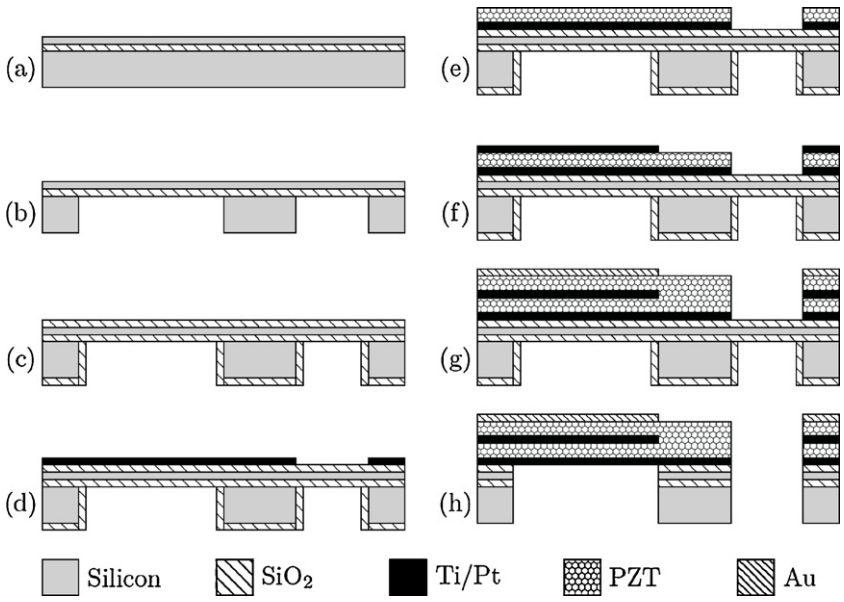

Fig. 2. A cross sectional sketch of the process flow for the screen printed PZT/PZT thick film bimorph MEMS energy harvester. The backside of a SOI wafer (a) is patterned and etched using a DRIE process (b). Then a 1 μm thick silicon dioxide is grown as an etch stop for a final RIE etch (c). The front side of the SOI wafer is then patterned and a Pt bottom electrode deposited (d), followed by deposition of PZT thick film (e), Pt middle electrode (f), another layer of PZT thick film and Au top electrode (g). The oxide on the backside is etched in bHF, while the front side of the SOI wafer is protected. The backside of the SOI wafer is then etched in RIE until the device layer is removed and the cantilever released (h).

Table 1
Energy harvester dimensions.

Frame dimensions	10 mm × 10 mm
Medial dimensions	<1 mm
Cantilever width	5.5 mm
Cantilever length	1.95 mm
Mass length	4.55 mm
Total cantilever height (standard)	2 × 30 μm
Total cantilever height (high pressure treated)	2 × 20 μm

chips polarized individually. The polarization directions of the two layers are aligned opposite to each other, *i.e.* during polarization the top and bottom electrodes were grounded and a polarization voltage applied to the middle electrode. The dimensions of the final energy harvester chips are shown in Table 1.

3. Results

Results from two energy harvesters will be shown and discussed, harvester A is a standard harvester, while the PZT thick films on harvester B were high pressure treated before sintering. During electrical characterizations the direct and the indirect piezoelectric effects are measured. The indirect piezoelectric effect was measured using an Agilent 4294A Precision Impedance Analyzer to excite the harvester electrically, and then measure the harvester impedance magnitude and phase.

Fig. 3 shows impedance measurements on harvester A, the impedance was measured between the top and bottom electrodes. The resonant frequency is f_r = 344 Hz while the anti-resonant frequency is f_a = 347 Hz. The impedance at resonance is the optimal resistive load, R_{opt} = 400 kΩ. Similar measurements were done between the bottom and middle electrodes and between the middle and top electrodes. Even though the resonant and anti-resonant frequency remains the same, the optimal resistive load differ mainly due to differences in the layer thickness. The optimal resistive load between bottom and middle electrodes is R_{opt} = 180 kΩ, while the optimal resistive load between middle and top electrodes is R_{opt} = 350 kΩ.

The direct piezoelectric effect was measured using the aforementioned optimal resistive loads on the harvester mounted in a shaker setup. Harvester A was actuated by a B&K Mini Shaker 4810 driven by an amplified sinusoidal signal from an Agilent 33220A function generator. A B&K Piezoelectric Accelerometer 8305 was mounted on the shaker along with the harvester for reference measurements. The root mean square (RMS) acceleration from the shaker was measured using the accelerometer and is stated in

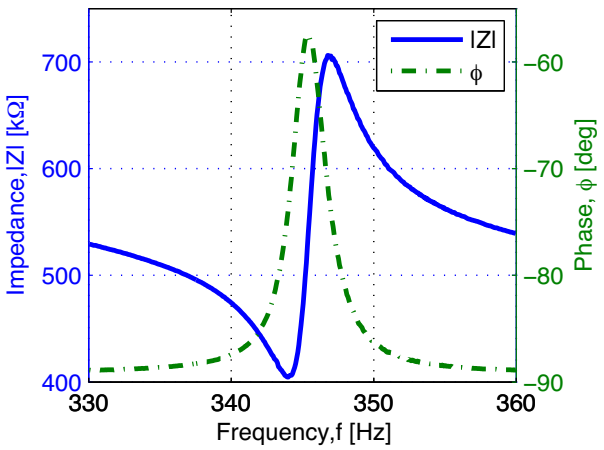

Fig. 3. Impedance magnitude and phase of energy harvester A probed between the top and bottom electrodes measured at frequencies near the resonant frequency.

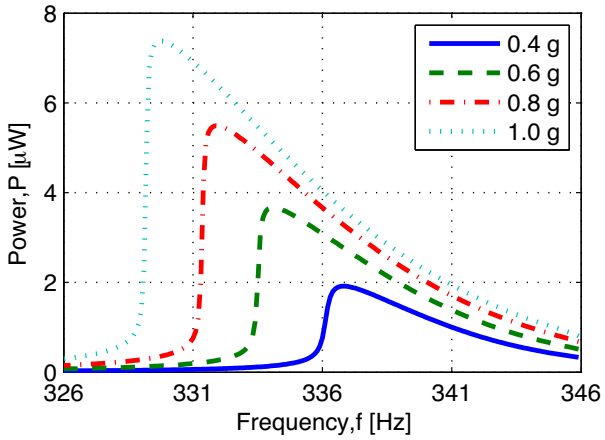

Fig. 4. Power output of the energy harvester A as a function of the excitation frequency at different accelerations. The top electrode was connected to the bottom electrode through a resistive load, R_{opt} = 400 kΩ, optimized for maximum power using the impedance analyzer measurements.

fractions of the gravitational acceleration g (9.81 m s^{-2}). Since the PZT layers are polarized in opposite directions, the power output of both layers may be measured with the top and the bottom electrodes connected by the resistive load R_{opt} = 400 kΩ. With the RMS voltage drop measured across the load the dissipated power can be calculated as $P_{RMS} = V_{RMS}^2/R_{opt}$. Fig. 4 shows the power output as a function of the excitation frequency with acceleration as a parameter. A maximum power of 7.35 μW was measured at an acceleration of 1 g. The asymmetric shape of the power peak and the decrease in resonant frequency with increasing acceleration is probably due to a non-linear response of PZT under stress; with increasing stress in PZT the material's effective Young's modulus and the quality factor decreases [26]. The decrease in Young's modulus reduces the spring constant and thus also the resonant frequency, this is also known as a softening effect.

During measurements of the power output from the top PZT layer, the top and middle electrodes were connected by a resistive load of R_{opt} = 350 kΩ, while the bottom electrode was kept open circuit. In the similar measurement of the power output of the bottom PZT layer a resistive load of R_{opt} = 180 kΩ was used, while the top electrode was kept open circuit and results similar to those shown in Fig. 4 were obtained. The output power extracted from these measurements at resonant frequency are plotted as a function of the input acceleration in Fig. 5. Fig. 5 shows that the power

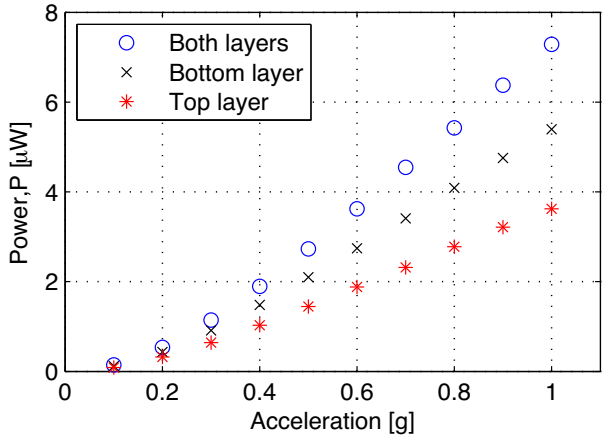

Fig. 5. Power output of energy harvester A from the top PZT layer, the bottom PZT layer and both layers combined at resonant frequency as a function of the input acceleration.

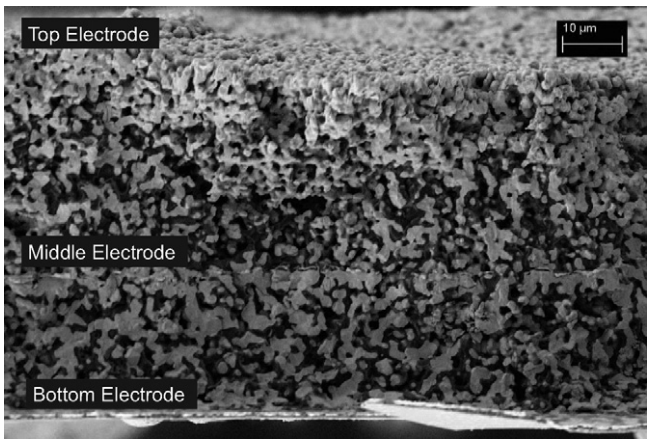

Fig. 6. A SEM image showing a cross sectional view of the PZT/PZT bimorph cantilever of harvester A with PZT thick films that were not high pressure treated. The middle electrode separates the two PZT layers.

output is indeed higher when both layers are used, but it differs from the sum of the power outputs from the two individual layers. This is probably due to mismatch between the two layers as manifested *e.g.* through the different optimal load resistances for the two layers.

The difference in optimal resistive load and power output from the bottom and the top PZT layer is caused by mismatch in PZT film thickness and material properties, which is confirmed by inspection of the cantilever cross section using scanning electron microscopy (SEM). Fig. 6 shows the cross section of the PZT/PZT cantilever, and illustrates clearly the undesirable layer mismatch. Where the bottom PZT layer is thinner than the top layer, while the grains of the bottom layer appear to be larger.

The same series of measurements were also performed on the energy harvester B, *i.e.* the harvester with high pressure treated PZT thick films. The optimal resistive load for both layers combined was found to be $R_{opt} = 250\,k\Omega$. The output power at optimal load as a function of frequency with acceleration as a parameter is shown in Fig. 7. Table 2 shows some of the important measured results. Compared to the same measurements on harvester A, shown in Fig. 4, the power output of harvester B is significantly larger, and the softening effect is less prominent. This is evident since the resonance peaks are more symmetric and the frequency shift as a function of input acceleration is smaller.

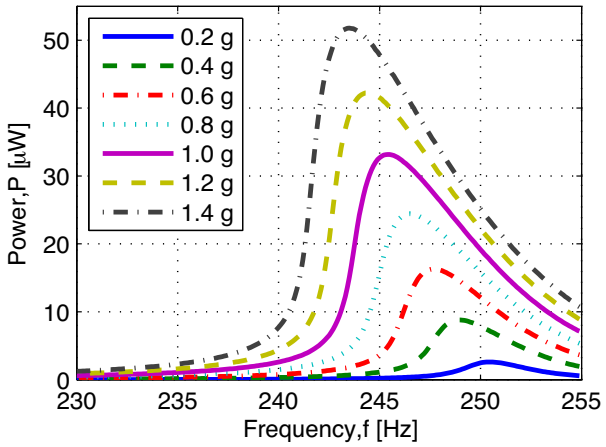

Fig. 7. Power output of the energy harvester B as a function of the excitation frequency for different accelerations. The top electrode was connected to the bottom electrode through a resistive load, $R_{opt} = 250\,k\Omega$.

Table 2
Summary of measured output power P_{out} at 1 *g* and optimal resistive load resistance R_{opt}.

	P_{out} [μW] at 1 *g*/R_{opt} [kΩ]		
	Both layers	Bottom layer	Top layer
Harvester A	7.35/400	5.39/180	3.62/350
Harvester B	33.2/250	18.9/150	23.6/180

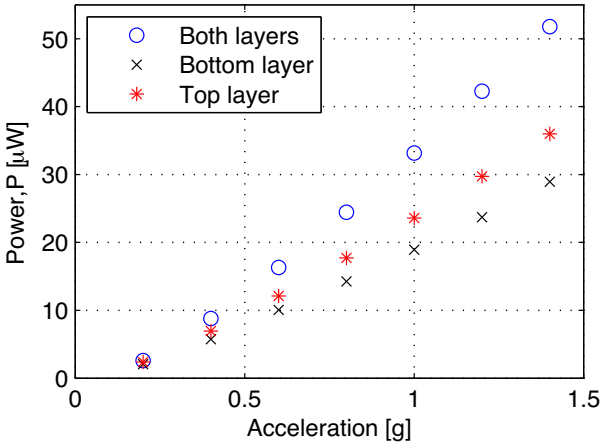

Fig. 8. The power output of the energy harvester B from the top PZT layer, the bottom PZT layer and both layers at resonant frequency as a function of the input acceleration.

The optimal resistive load for the top PZT and the bottom PZT layers was found to be 180 kΩ and 150 kΩ, respectively. Fig. 8 shows the RMS power output of harvester B across both layers, the top layer and the bottom layer as a function of the RMS acceleration. Again the power output of the two layers are not identical and the power output of both layers combined is not the sum of the powers for the two individual layers. Notice that both the difference in the optimal resistive load and in output power between the two layers is now smaller compared to harvester A. The relative power output difference for harvester B at 1 *g* is about 20% whereas it is almost 50% for the harvester A. The difference between the two harvesters is also evident during the SEM inspection of harvester B shown in Fig. 9, where it is noted that the thickness and the grain size of the layers are now more similar than for harvester A. A series of SEM images of focused ion beam (FIB) cross-sections (see Fig. 10) of high pressure treated as well as untreated PZT thick films were used to quantify the difference in morphology

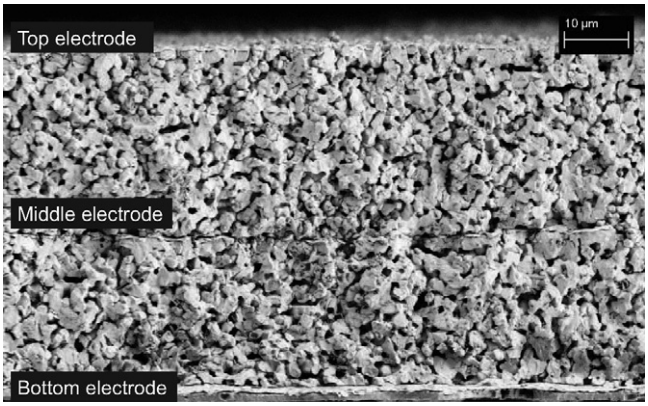

Fig. 9. A SEM image showing a cross sectional view of the PZT/PZT bimorph cantilever of harvester B with PZT thick films that were high pressure treated. The middle electrode separates the two PZT layers.

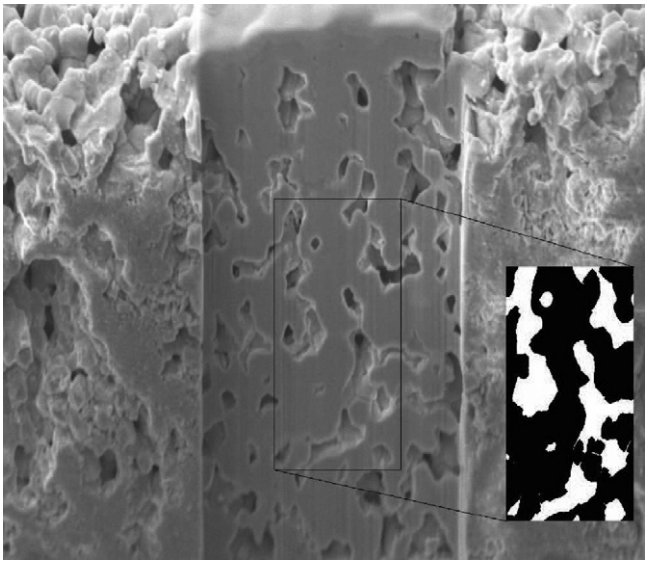

Fig. 10. An example of the FIB-SEM image analyzed in Matlab.

between the films. The images were analyzed using Matlab to extract an apparent porosity defined as the fractional pore area on the cross-sections. For untreated PZT the average apparent porosity is 35%, while the high pressure treatment reduces the average apparent porosity to 20%. The relative change in apparent porosity is expected to represent well the relative change in real porosity, whereas the absolute real porosity values depend on the three dimensional pore structure of the films and may differ from the apparent porosity values. The decreased porosity due to pressure treatment also results in changes of the effective material parameters as shown in Table 3. Since the decreased porosity also leads to an increase in the inter-grain contact area the reduced spring softening effect for the pressure treated energy harvesters may be explained. We speculate that the softening effect is due to sliding at grain boundaries at large stress, and with an increased inter-grain contact the grain boundary sliding will be reduced. This may also be part of the explanation for the rather dramatic increase in output power from harvester B compared to harvester A, since a reduced grain boundary sliding also results in reduced mechanical losses. The increased magnitude of the piezoelectric coefficient d_{31} (see Table 3) is of course the main reason for the increased output power of harvester B. The effect of decreased porosity on the piezoelectric coefficient is discussed in [20,21]. Furthermore, the decrease in porosity will also increase the permittivity, as it is seen in Table 3, and thus the capacitance of the layers. This seems to be confirmed by the decrease in optimal resistive load for harvester B.

In Fig. 11 the the full width at half maximum bandwidth is shown as a function of acceleration, the data were extracted from the measurements shown in Fig. 7. The increase in full width half maximum bandwidth with acceleration is a clear indication of an increased damping with increasing acceleration. The increased damping is not necessarily a drawback since the harvester becomes useful in a wider spectrum of vibrations.

Table 3
Piezoelectric and dielectric coefficients of untreated as well as high pressure treated TF2100 [22], for comparison values for Pz26 [27], which is the bulk counterpart of TF2100, are also shown.

Parameter	TF2100	TF2100 pressure treated	Pz26 bulk
$-d_{31}$ [pC/N]	50–60	89	130
ϵ_{33}/ϵ_0	500–640	825	1300

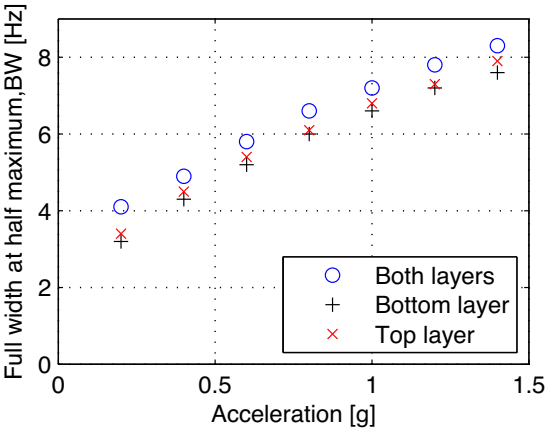

Fig. 11. The full width at half maximum bandwidth for the resonance peaks of harvester B as a function of the excitation acceleration.

4. Conclusion

Screen printed PZT/PZT thick film bimorph MEMS cantilever energy harvesters were successfully fabricated and characterized. By replacing the inactive cantilever support with another layer of PZT more power is indeed harvested than the power harvested from each individual layer in this case, however, the same amount of PZT sandwiched around an inactive support beam may yield even larger output power. For the standard harvester at 1 *g*, the power output from both layers combined is 7.35 μW, while the power output for the individual layers with the same input acceleration is 5.39 μW for the bottom layer and 3.62 μW for the top layer. The harvester with high pressure treated PZT thick film performed significantly better, with 33.2 μW power output from both layers combined at 1 *g*. The top and bottom layers have a power output at 1 *g* of 23.6 μW and 18.9 μW, respectively. Further improvements in the fabrication process are still needed since the fabrication yield is unacceptable. Moreover, methods to increase the proof mass without a significant increase in harvester volume is desirable.

Acknowledgments

This research is part of the ELBA project, which is funded by the Advanced Technology Foundation. Center for Individual Nanoparticle Functionality (CINF) is sponsored by Danish National Research Foundation.

References

[1] N.S. Hudak, G.G. Amatucci, Small-scale energy harvesting through thermoelectric, vibration, and radiofrequency power conversion, Journal of Applied Physics 103 (2008).
[2] S.P. Beeby, M.J. Tudor, N.M. White, Energy harvesting vibration sources for microsystems applications, Measurement Science and Technology 17 (12) (2006) R175–R195.
[3] K.A. C.-Chennault, N. Thambi, A.M. Sastry, Powering MEMS portable devices—a review of nonregenerative and regenerative power supply systems with special emphasis on piezoelectric energy harvesting systems, Smart Materials and Structures 17 (2008) 1–33.
[4] E. Lefeuvre, A. Badel, C. Richard, L. Petit, D. Guyomar, A comparison between several vibration powered piezoelectric generators for standalone systems, Sensors and Actuators A 126 (2006) 405–416.
[5] H.-B. Fang, et al., Fabrication and performance of MEMS-based piezoelectric power generator for vibration energy harvesting, Microelectronics Journal 37 (2006) 1280–1284.
[6] W.J. Choi, Y. Jeon, S.G. Kim, Energy harvesting MEMS device based on thin film piezoelectric cantilevers, Journal of Electroceramics 17 (2006).
[7] D. Shen, et al., The design, fabrication and evaluation of a MEMS PZT cantilever with an integrated Si proof mass for vibration energy harvesting, Journal of Micromechanics and Microengineering 18 (2008).

[8] S.-L. Kok, N.M. White, N.R. Harris, Fabrication and characterization of free-standing thick-film piezoelectric cantilevers for energy harvesting, Measurement Science and Technology 20 (2009).
[9] J.G. Gualtieri, J.A. Kosinski, A. Ballato, Piezoelectric materials for acoustic wave applications, IEEE Transactions on Ultrasonics, Ferroelectrics, and Frequency Control 41 (1) (1994).
[10] G. Carlotti, G. Socino, A. Petri, E. Verona, Elastic constants of sputtered ZnO films, Ultrasonics Symposium (1987) 295–299.
[11] M.A. Dubois, P. Muralt, Measurement of the effective transverse piezoelectric coefficient e_31 of AlN and $Pb(Zr_x,Ti_{x-1})O_3$ thin films, Sensors and Actuators A 77 (1999) 106–112.
[12] R. Elfrink, T.M. Kamel, M. Goedbloed, S. Matova, D. Hohlfeld, Y. van Andel, R. van Schaijk, Vibration energy harvesting with aluminum nitride-based piezoelectric devices, Journal of Micromechanics and Microengineering 19 (2009).
[13] S.T. Anton, H.A. Sodano, A review of Power harvesting using piezoelectric materials, Smart Materials and Structures 16 (2007) R1–R21.
[14] Y. Liao, H.A. Sodano, Model of a single mode energy harvester and properties for optimal power generation, Smart Materials and Structures 17 (6) (2008) 065026.
[15] A. Erturk, D.J. Inman, An experimentally validated bimorph cantilever model for piezoelectric energy harvesting from base excitations, Smart Materials and Structures 18 (2) (2009) 025009.
[16] H. Jacobsen, H. Quenzer, B. Wagner, K. Ortner, T. Jung, Thick PZT layers deposited by gas flow sputtering, Sensors and Actuators A: Physical 135 (March (1)) (2007) 23–27.
[17] D. Shen, et al., Micromachined PZT cantilever based on SOI structure for low frequency vibration energy harvesting, Sensors and Actuators A: Physical 154 (August (1)) (2009) 103–108.
[18] H. Fang, et al., Fabrication and performance of MEMS-based piezoelectric power generator for vibration energy harvesting, Microelectronics Journal 37 (November (11)) (2006) 1280–1284.
[19] R.G. Ballas, Piezoelectric Multilayer Beam Bending Actuators, Springer, 2007.
[20] H. Banno, Theoretical equations for dielectric and piezoelectric properties of ferroelectric composites based on modified cubes model, Japanese Journal of Applied Physics 24 (Suppl. 24-2) (1985) 445–447.
[21] T. Zeng, X. Dong, C. Mao, Z. Zhou, H. Yang, Effects of pore shape and porosity on the properties of porous PZT 95/5 ceramics, Journal of the European Ceramic Society 27 (2007) 2025–2029.
[22] C. Hindrichsen, R. Lou-Moeller, K. Hansen, E. Thomsen, Advantages of PZT thick film for MEMS sensors, Sensors and Actuators A: Physical 163 (1) (2010) 9–14.
[23] R. Lou-Moeller, et al., Screen-printed piezoceramic thick films for miniaturised devices, Journal of Electroceramics 19 (4) (2007) 333–338.
[24] A. Lei, R. Xu, A. Thyssen, A.C. Stoot, T.L. Christiansen, K. Hansen, R. Lou-Moeller, E.V. Thomsen, K. Birkelund, MEMS-based thick film PZT vibrational energy harvester, in: Proceeding, IEEE Micro Electro Mechanical Systems, 2011, pp. 125–128.
[25] W. Kern, D. Puotinen, Cleaning solutions based on hydrogen peroxide for use in silicon semiconductor technology, RCA Review 13 (issue 2) (1970) 187.
[26] D. Shen, J. Park, J. Ajitsaria, S. Choe, H.C. Wikle, D. Kim, The design, fabrication and evaluation of a MEMS PZT cantilever with an integrated Si proof mass for vibration energy harvesting, Journal of Micromechanics and Microengineering 18 (5) (2008) 055017.
[27] http://www.ferroperm-piezo.com/.

Biographies

Ruichao Xu received the B.Sc. degree and the M.Sc. degree in applied physics from the Technical University of Denmark (DTU), Lyngby, Denmark, in 2007 and 2009, respectively. He has been working with the development and fabrication of microreactors for catalysis. He is currently working towards the Ph.D. degree in the field of PZT-based MEMS devices with special focus on energy harvesting for microsystems under the supervision of Ole Hansen at the Department of Micro- and Nanotechnology (DTU Nanotech). He is a board member of the Electrical Engineering Society of Denmark.

Anders Lei received the M.Sc. degree in physics and nanotechnology in 2009 from the Department of Micro and Nanotechnology at the Technical University of Denmark. During his master he worked with prototyping of NEMS and MEMS devices using focused ion beam milling in the Nanointegration group at DTU Nanotech. He is currently Ph.D. student in the MEMS-Applied Sensors group at DTU Nanotech working with MEMS-based PZT vibration energy harvesters for autonomous wireless sensor systems.

Christian Dahl-Petersen received his B.Sc. in physics and nanotechnology in 2011 from the Technical University of Denmark (DTU), Lyngby, Denmark. He is currently studying on the Master program in Physics and Nanotechnology at DTU with specialization in nanosystems engineering.

Karsten Hansen graduated in 2006 from the Technical University of Denmark (DTU) with a M.Sc. in chemical engineering and have since the beginning of 2007 been working at MEGGITT A/S on the optimization of piezoelectric properties in PZT thick film ceramics. He is currently employed at Topsoe Fuel Cell A/S. His research interests are ceramics, thick films, new technologies and high tech devices.

Michele Guizzetti was born in Brescia, Italy, in 1981. In February 2006, he obtained the electronics engineering degree at the University of Brescia while in March 2010 he received the research doctorate degree in electronic instrumentation at the same university. Until August 2010 he collaborated with the Department of Information Engineering of the University of Brescia on research activities dealing with power harvesting and autonomous systems. In particular he was involved with piezoelectric and thermoelectric energy conversion. Now he is employed as senior research engineer in Meggitt Sensing System R&D Group in Kvistgaard, Denmark, working on projects regarding power harvesting.

Karen Birkelund received her Ph.D. degree in electrical engineering in 1997 from the Technical University of Denmark (DTU). From 1998 to 2002 she was at Danfoss A/S as research engineer within MEMS pressure sensors. From 2002 to 2004 she was at Cantion A/S as research engineer within cantilever based sensor systems. From 2004 to 2006 she was with TopSpin A/S also as research engineer within silicon based dispensing systems for biotechnology research. In 2006 she joined the Department of Micro and Nanotechnolgy, Technical University of Denmark as assistant professor working mainly on MEMS devices and encapsulation for harsh environments. In September 2011 she got employed as a process generalist at the National Centre for Micro- and Nanofabrication, DTU-Danchip.

Erik V. Thomsen is a group leader for the MEMS Applied Sensors activities at the MEMS section at the Department of Micro and Nanotechnology, Technical University of Denmark, DTU, where he is affiliated as professor. He holds a M.Sc. in physics from Odense University and a Ph.D. in electrical engineering from DTU. He has been affiliated with MIC, now DTU Nanotech, since 1992 and has been working with fabrication of semiconductor devices. His current interests include research and teaching within micromechanical multi-sensors, piezoresistivity of strained layers, piezoelectric MEMS devices, and micro-system packaging. He teaches classes in solid-state electronics, microtechnology and nano- and microfabrication.

Ole Hansen received the M.Sc. degree from the Semiconductor Laboratory, DTU, in 1977. Since then he has done research in silicon-based micro and nanotechnology and its applications, first at the Semiconductor Laboratory, and later at the Department of Micro and Nanotechnology, DTU Nanotech. Current research interests include deep reactive ion etching of silicon, $Si_{1-x}Ge_x$/Si heterostructures, microreactors for catalysis, and cantilever-based microprobes for nano-science. He is presently teaching three lecture courses: semiconductor technology, semiconductor devices and micro-electromechanical systems. Since 1990, he has been an associate professor at MIC, now DTU Nanotech. Since 2005 he has been part of the Danish National Research Foundation Center CINF, Center for Individual Nanoparticle Functionality.

A.7 Journal of Micromechanics and Microengineering 2012

R. Xu, A. Lei, C. Dahl-Petersen, K. Hansen, M. Guizzetti, K. Birkelund, E. V. Thomsen, and O. Hansen, "Fabrication and characterization of MEMS-based PZT/PZT bimorph thick film vibration energy harvesters," Journal of Micromechanics and Microengineering, vol. 22, no. 9, p. 094007, Sep. 2012.

J. Micromech. Microeng. **22** (2012) 094007 (9pp) doi:10.1088/0960-1317/22/9/094007

Fabrication and characterization of MEMS-based PZT/PZT bimorph thick film vibration energy harvesters

R Xu[1], A Lei[1], C Dahl-Petersen[1], K Hansen[2], M Guizzetti[2], K Birkelund[1], E V Thomsen[1] and O Hansen[1,3]

[1] Department of Micro- and Nanotechnology, Technical University of Denmark (DTU Nanotech), Building 345 East, DK-2800 Kongens Lyngby, Denmark
[2] Meggitt Sensing Systems, DK-3490 Kvistgaard, Denmark
[3] Center for Individual Nanoparticle Functionality (CINF), Technical University of Denmark, DK-2800 Kongens Lyngby, Denmark

E-mail: ruichao.xu@nanotech.dtu.dk

Received 25 January 2012, in final form 16 June 2012
Published 24 August 2012
Online at stacks.iop.org/JMM/22/094007

Abstract
We describe the fabrication and characterization of a significantly improved version of a microelectromechanical system-based PZT/PZT thick film bimorph vibration energy harvester with an integrated silicon proof mass; the harvester is fabricated in a fully monolithic process. The main advantage of bimorph vibration energy harvesters is that strain energy is not lost in mechanical support materials since only $Pb(Zr_xTi_{1-x})O_3$ (PZT) is strained; as a result, the effective system coupling coefficient is increased, and thus a potential for significantly higher output power is released. In addition, when the two layers are connected in series, the output voltage is increased, and as a result the relative power loss in the necessary rectifying circuit is reduced. We describe an improved process scheme for the energy harvester, which resulted in a robust fabrication process with a record high fabrication yield of 98%. The robust fabrication process allowed a high pressure treatment of the screen printed PZT thick films prior to sintering. The high pressure treatment improved the PZT thick film performance and increased the harvester power output to 37.1 μW at 1 g root mean square acceleration. We also characterize the harvester performance when only one of the PZT layers is used while the other is left open or short circuit.

(Some figures may appear in colour only in the online journal)

1. Introduction

Wireless monitoring and sensing systems have received significant attention in recent years, since they offer several advantages compared to their wired counterparts. In health care, for instance, a patient with a wireless monitoring system may still be mobile, while a wired monitoring system leaves the patient rather immobile. Some monitoring systems will be placed in remote areas where it is desirable that the system is wireless, a feature that will be equally desirable for the increasing number of portable complex electronic systems in use today. Conventionally, these systems are powered by batteries; however, the maintenance costs related to battery replacement can be quite significant. As a result, energy harvester solutions offering maintenance-free power supply of sensing or monitoring systems have attracted significant attention recently.

In the external surroundings, energy such as ambient light, mechanical vibrations, sound, or thermal gradients is available to be harvested for free. With the advances in micro-technology, many useful electronic systems have low enough power requirements to make completely self-supported systems realistic [1]. One of the methods to harvest mechanical energy from vibrations is to make use of the piezoelectric transduction mechanism [2]. A typical piezoelectric energy harvester is based on a cantilever beam,

which consists of the active piezoelectric ceramic with metal electrodes on both sides and a passive mechanical support structure, anchored at one end and with a proof mass at the other [3–6]. The main advantage of PZT/PZT thick film bimorph energy harvesters, compared to the aforementioned harvesters, is that strain energy is not lost in mechanical support materials since only PZT is strained, and thus it has a potential for higher power output. An additional advantage arises from a significantly increased output voltage of a series-connected bimorph harvester, which reduces the relative magnitude of the inevitable losses in rectifying support circuitry. Bulk PZT bimorph energy harvesters and models of these were presented in [7, 8], while a microelectromechanical system (MEMS)-sized bimorph energy harvester was recently introduced in [9]. Screen printed PZT thick film was used in [10], where multimorph energy harvesters were fabricated and characterized. We presented a first generation MEMS bimorph PZT/PZT thick film harvester in [11, 12], where it was shown that by using PZT thick film, it is possible to realize a self-supporting device without the need for a passive mechanical structure. However, the fabrication yield was low due to a process sequence with an early deep reactive ion etch (DRIE) step, which turned most of the structure into a fragile membrane. A revised process plan, using the advantageous process steps introduced in [13], has significantly improved both fabrication yield and performance of the harvesters. The DRIE step was replaced by a potassium hydroxide (KOH) wet etch and moved to the last part of the fabrication process; as a result, the fabrication yield was more than triple to a record high yield of 98.6%. As an added benefit, the improved mechanical stability of the structure during PZT thick film (InSensor® TF2100) deposition and processing allowed high pressure treatment of the PZT thick film before sintering; this resulted in more than a fivefold improvement of the harvester power output compared to previous results [11]. Furthermore, the use of KOH etching may facilitate a scalable future mass production.

2. Fabrication

The fabricated energy harvester, shown in figure 1, combines PZT thick film screen printing with standard MEMS technology into a monolithic fabrication process. The harvester comprises a 10 mm × 10 mm silicon frame fitted with a wide PZT/PZT bimorph cantilever beam with bottom, top and middle electrodes. At the free end of the cantilever beam, a silicon proof mass is fixed. Contacts to the three electrodes are placed on the silicon frame.

In the design of the fabrication process, the main emphasis was on ensuring high mechanical stability of the wafers until completion the PZT/PZT stack by postponing bulk silicon structuring; this was accomplished by the use of KOH etching of silicon just prior to the release of the cantilever beams. As a result, high pressure treatment of the thick film PZT layers prior to sintering became feasible. This significantly improved the quality of the PZT material and the fabrication yield. The electrode materials for the PZT/PZT stack were chosen for compatibility with the PZT sintering process (∼850 °C); in this process, the bottom metal layer has to serve also as a diffusion barrier to prevent diffusion of silicon into the PZT layers, since silicon contamination ruins the piezoelectric material. For this reason, Pt was chosen for both the bottom electrode and the middle electrode, while for the top electrode, which is not sintered, Au was the material of choice since it does not oxidize readily.

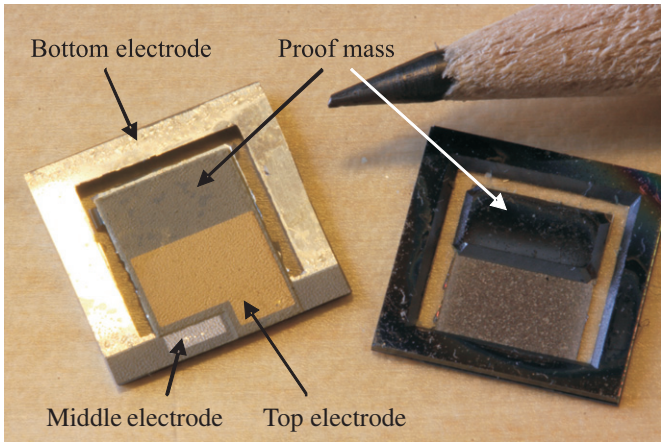

Figure 1. Photographic image showing the front and back of the 10 mm × 10 mm energy harvesters.

The fabrication process is illustrated in figure 2. The fabrication process starts with a double-sided polished 4 inch (100 mm) silicon on insulator (SOI) wafer with a 20 μm device layer and 1 μm buried oxide on a 525 μm handle substrate, as shown in figure 2(*a*). First, a 1 μm thick silicon dioxide is thermally grown at 1150 °C, and then a 170 nm thick silicon nitride is deposited using low pressure chemical vapor deposition (LPCVD), as shown in figure 2(*b*). The nitride is removed on the front side using reactive ion etch (RIE), and after that the back side of the wafer is patterned using conventional lithography processes and similarly etched in RIE, as shown in figure 2(*c*). Next, a 50 nm titanium (Ti) adhesion layer and a 500 nm platinum (Pt) bottom electrode are deposited using e-beam evaporation on the front side of the wafer, which is subsequently patterned using AZ4562 resist, followed by an etch in a wet etch solution, H_2O:HCl:HNO_3 (8:7:1) at 85 °C for 8 min, as shown in figure 2(*d*). Thereafter, the PZT thick film layer is screen printed on the patterned bottom electrode, high pressure treated [14] and sintered; here the bottom electrode also serves as a diffusion barrier. The advantage of using the new fabrication scheme appears here: screen printing and high pressure treatment of the PZT layer is done on a full wafer, instead of a wafer with thin membranes as it was done in [11, 12]; this not only prevents any chip loss during PZT processing but also ensures a higher quality and more uniform thick film that will prevent any cantilever breakage after the final release etch. Next, the 500 nm Pt middle electrode is deposited through a prefabricated silicon shadow mask using e-beam evaporation, as shown in figure 2(*e*). The shadow mask was made using a 350 μm thick silicon wafer, which was patterned using UV lithography and etched through in a DRIE process. The second PZT thick film layer is then screen printed, high pressure treated and sintered. This is followed by the deposition of a 500 nm gold (Au)

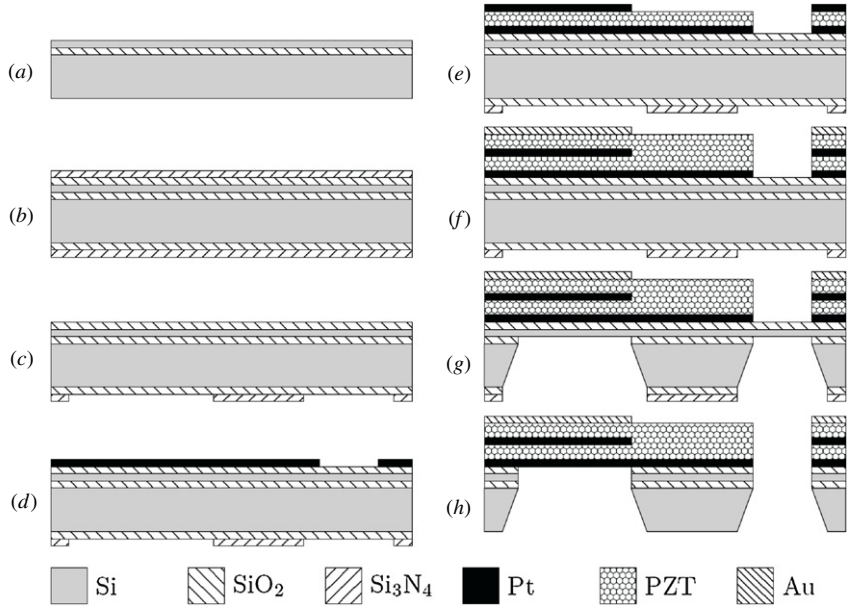

Figure 2. Cross-sectional view of the fabrication scheme. First, a 1 μm thick silicon dioxide is thermally grown on a SOI wafer (*a*), and then a 170 nm thick silicon nitride is deposited using LPCVD (*b*). The nitride is removed on the front side and patterned on the back side using conventional lithography processes (*c*). A Pt bottom electrode is deposited on the front side of the wafer and patterned (*d*), followed by deposition of the first PZT thick film layer, the Pt middle electrode (*e*), the second PZT thick film layer and the Au top electrode (*f*). The oxide on the back side is etched in bHF, while the front side of the SOI wafer is protected. The back side of the SOI wafer is then etched in KOH until the buried oxide layer is reached and then the buried oxide layer is removed in bHF (*g*). Finally, the sacrificial device layer is etched in RIE, releasing the cantilevers (*h*).

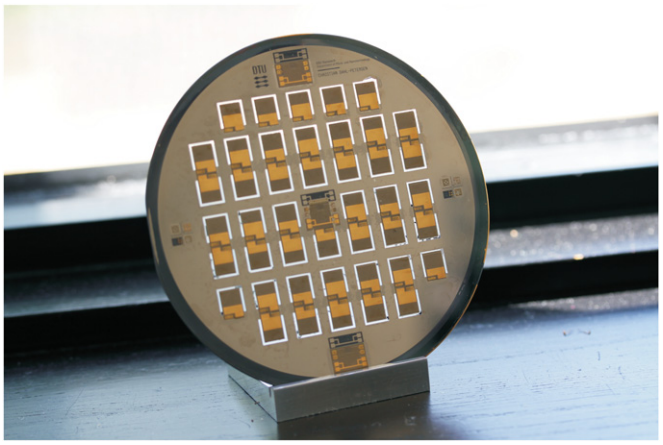

Figure 3. Image of a fabricated harvester wafer before dicing.

top electrode through another prefabricated shadow mask, fabricated using the aforementioned fabrication steps; see figure 2(*f*). Thereafter, the wafer is mounted on a 4 inch tandem series wafer holder from advanced micromachining tools. The oxide on the back side is etched in buffered hydrofluoric acid (bHF), while the front side of the SOI wafer is protected by the holder. Then, the silicon is etched in a KOH etch until the buried oxide layer is reached and then the buried oxide layer is removed in bHF, as shown in figure 2(*g*). Finally, the sacrificial device layer is etched in RIE, releasing the cantilevers; see figure 2(*h*).

Figure 3 shows the fabricated harvester wafer before dicing. Note that all cantilevers are intact; the chip yield on the wafer at this stage is still 100%, while if the fabrication process from [11, 12] was used, the chip yield would be much less.

Table 1. Energy harvester dimensions.

Frame dimensions	10 mm × 10 mm
Medial dimensions	< 1 mm
Cantilever width	5.5 mm
Cantilever length	3.25 mm
Total cantilever height	2 × 20 μm
Proof mass length	3.25 mm
Mass of the proof mass	25 mg

The wafer is diced and the chips are polarized individually. The polarization directions of the two layers are aligned opposite to each other, i.e. during polarization the top and bottom electrodes are grounded and a polarization voltage is applied to the middle electrode. The dimensions for the final energy harvester chips are shown in table 1.

In figure 4 a scanning electron microscope (SEM) image of a cross-section of the PZT/PZT bimorph cantilever beam resulting from this fabrication process is shown. The two PZT layers are seen to be similar both with respect to thickness and morphology, and they have a rather low porosity as a result of the high pressure treatment prior to sintering.

3. Theory

The PZT/PZT bimorph beam energy harvester is really a distributed system and full distributed models have been derived [8], but since the harvester is operated near the first resonant frequency, a lumped model of the system is sufficiently accurate [7]. Here we will develop such a

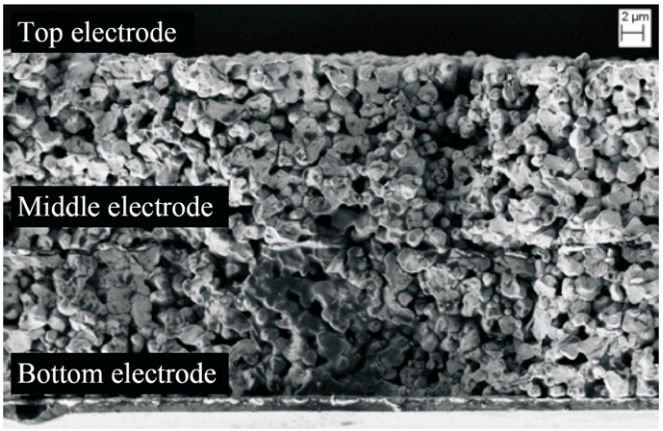

Figure 4. SEM image showing a cross-sectional view of the PZT/PZT bimorph thick film structure. The thin top, middle and bottom electrodes are barely visible in this magnification.

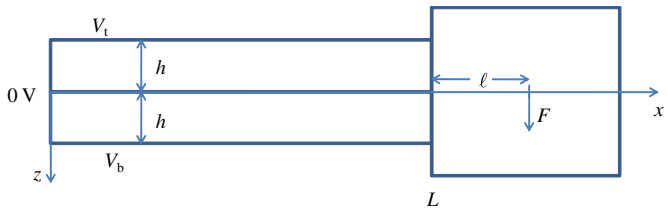

Figure 5. Schematic cross-section of the bimorph energy harvester. The bimorph PZT beam consists of two PZT layers, which are assumed to have the thickness h. At $x = 0$ the beam is rigidly clamped to a frame, and at $x = L$ a proof mass (of mass m) is fixed to the beam. The center of gravity for the proof mass is at $x = L + \ell$, where $\ell = L_m/2$ is half of the length of the proof mass.

lumped model based on a bimorph piezoelectric beam model, derived from the constitutive piezoelectric materials equations [15, 16], and a solution to Euler's beam equation. We shall consider a symmetric piezoelectric bimorph beam where each layer has the thickness h, length L and width W. On the beam, top and bottom electrodes covering the full top and bottom surfaces are assumed to be thin enough that their contribution to the beam stiffness may be ignored; likewise, the middle electrode that separates the two PZT layers is assumed infinitely thin. The potentials on the top, bottom and middle electrodes are V_t, V_b, and 0 V, respectively. The beam is clamped to a rigid frame in one end and has an attached proof mass of mass m on the other end; the center of gravity for the proof mass is positioned at the distance ℓ from the end of the beam, as illustrated in figure 5.

In the appendix, we show the that the harvester may be reasonably well described by a lumped element model comprising a force balance equation evaluated at the center of mass for the proof mass including forces from the voltages on the top and bottom electrodes

$$Z_m v_c = F + \frac{\Gamma_b}{\Lambda} V_b + \frac{\Gamma_t}{\Lambda} V_t, \tag{1}$$

combined with two equations for the currents I_t and I_b flowing into the top and bottom electrodes, respectively,

$$I_t = \frac{\Gamma_t}{\Lambda} v_c + sC_t V_t, \tag{2}$$

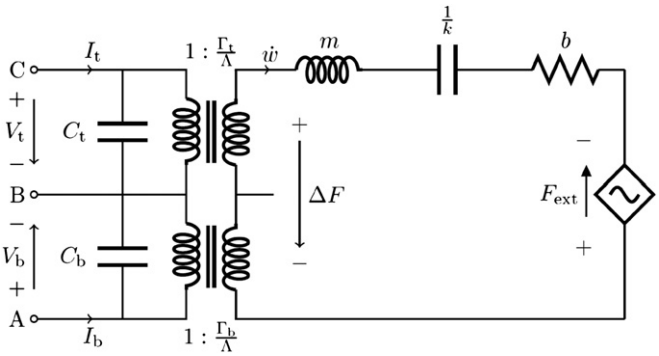

Figure 6. Equivalent circuit diagram for the bimorph PZT/PZT energy harvester.

$$I_b = \frac{\Gamma_b}{\Lambda} v_c + sC_b V_b, \tag{3}$$

where F is the external force acting on the proof mass, v_c is the velocity of the proof mass, $Z_m = sm + b + k/s$ is the mechanical impedance of the proof mass–spring system and $s = j\omega$ is the complex frequency. The proof mass has the mass m, k is the effective spring constant of the cantilever beam as seen from the proof mass, b is the loss coefficient for the mass–spring system and C_t and C_b are the total capacitances including parasitics of the top and bottom layers, respectively. Γ_t/Λ and Γ_b/Λ are transduction coefficients from velocity to current and from voltage to force for the top and bottom layers, respectively.

Equations (1)–(3) may be used to predict the behavior of the energy harvester when connected to external loads or under open circuit conditions, and the equations may be represented by the equivalent circuit diagram (figure 6).

The PZT/PZT bimorph energy harvester may be connected to external loads in several ways; one active layer may be used while the other is left open (1o) or short circuit (1s) or both layers may be used in parallel (2P) or in series (2S).

3.1. Single layer connected (1s)

The 1s situation essentially corresponds to a simple single PZT layer harvester, and may thus serve as a performance reference. This situation is easily analyzed, since e.g. $V_b = 0$, and $I_t = -G_L V_t$, where G_L is the load conductance, if the top layer is taken as the active layer. The output voltage V_t is then easily calculated

$$V_t = -F \frac{(\Gamma_t/\Lambda)}{(\Gamma_t/\Lambda)^2 + (sC_t + G_L)Z_m}, \tag{4}$$

while the input admittance of the harvester is

$$Y_{in_t} = \left(\frac{\Gamma_t}{\Lambda}\right)^2 \frac{1}{Z_m} + sC_t. \tag{5}$$

The resonant frequency becomes the native mechanical resonant frequency $\omega_r = \omega_0 = \sqrt{k/m}$, while the anti-resonant frequency is $\omega_a = \omega_0\sqrt{1 + K_t^2}$, where $K_t^2 = (\Gamma_t/\Lambda)^2/(kC_t)$ is the square of the system coupling coefficient for the top layer.

The output power is maximized at frequencies close to the anti-resonant frequency ω_a, and is approximately

$$P_{\max_t} = \frac{|F|^2_{\mathrm{RMS}}}{4b}\frac{2}{1+\sqrt{1+\frac{1+K_t^2}{Q^2K_t^4}}} = \frac{ma^2Q}{4\omega_0}\frac{2}{1+\sqrt{1+\frac{1+K_t^2}{Q^2K_t^4}}}, \tag{6}$$

where the first term is the available power. Here we have used that $|F|_{\mathrm{RMS}} = ma$ where a is the root mean square (RMS) acceleration amplitude of the external vibration, and that $b = m\omega_0/Q$ where Q is the mechanical quality factor. This power is obtained at an optimal load conductance of

$$G_{L\mathrm{opt}_t} = \frac{\omega_0 C_t\left(1+K_t^2\right)}{\sqrt{\left(1+K_t^2+Q^2K_t^4\right)}} = \frac{\omega_a C_t\sqrt{1+K_t^2}}{\sqrt{\left(1+K_t^2+Q^2K_t^4\right)}}. \tag{7}$$

3.2. Single connected layer (1o)

In the situation with one connected layer while the other is left open (1o), $I_b = 0$ and $I_t = -G_L V_t$ if the top layer is loaded. Solving equations (1)–(3) for the output voltage V_t yields

$$V_t = -F_{\mathrm{ext}}\frac{(\Gamma_t/\Lambda)}{(\Gamma_t/\Lambda)^2+\left(Z_m+(\Gamma_b/\Lambda)^2\frac{1}{sC_b}\right)\left(sC_t+G_L\right)}, \tag{8}$$

where it may be recognized that the open bottom layer causes an increase in the apparent spring constant such that the effective spring constant becomes $k + (\Gamma_b/\Lambda)^2/C_b$. This is also apparent in the input admittance

$$Y_{\mathrm{in}_t} = \frac{(\Gamma_t/\Lambda)^2}{\left(Z_m+(\Gamma_b/\Lambda)^2\frac{1}{sC_b}\right)} + sC_t. \tag{9}$$

As a result of the increased effective spring constant, the resonant frequency is larger than the native mechanical resonant frequency $\omega_r = \omega_0\sqrt{1+K_b^2}$ where $K_b^2 = (\Gamma_b/\Lambda)^2/(kC_b)$ is the coupling coefficient of the bottom layer. The anti-resonant frequency becomes $\omega_a = \omega_0\sqrt{1+K_b^2+K_t^2}$ as may easily be verified by inspection of the admittance.

The output power is maximized at frequencies near the anti-resonant frequency ω_a

$$P_{\max}(\omega_r) = \frac{|F|^2_{\mathrm{RMS}}}{4b}\frac{2}{1+\sqrt{1+\left(1+K_b^2+K_t^2\right)/\left(K_t^4Q^2\right)}}; \tag{10}$$

the output power is slightly smaller than the output power with the bottom layer short circuited due to the additional term K_b^2 and possibly due to a frequency-dependent quality factore.g. for thermo-mechanical losses, $Q\omega$ is approximately constant at low frequencies [17]). The power is maximized at the load conductance

$$G_{L\mathrm{opt}_t} = \frac{\omega_0 C_t\left(1+K_b^2+K_t^2\right)}{\sqrt{1+K_b^2+K_t^2+K_t^4Q^2}} = \frac{\omega_a C_t\sqrt{\left(1+K_b^2+K_t^2\right)}}{\sqrt{1+K_b^2+K_t^2+K_t^4Q^2}}. \tag{11}$$

3.3. Two loaded layers in parallel (2P)

When the two PZT layers are operated in parallel, the output voltage $V_{\mathrm{out}} = V_t = V_b$ and $I = I_t + I_b = -G_L V_{\mathrm{out}}$ and as a result equations (1)–(3) simplify to

$$Z_m v_c = F + (\Gamma_b/\Lambda + \Gamma_t/\Lambda)V_{\mathrm{out}}, \tag{12}$$

$$-G_L V_{\mathrm{out}} = (\Gamma_b/\Lambda + \Gamma_t/\Lambda)v_c + s(C_t+C_b)V_{\mathrm{out}}. \tag{13}$$

It follows that mathematically, the situation is exactly the same as in 1s, except for the increased capacitance and increased transduction coefficient. Note, in this configuration the two layers should be poled in the same direction to ensure that Γ_b and Γ_t have the same sign. The system coupling coefficient is in this case obtained from $K_p^2 = (\Gamma_b/\Lambda + \Gamma_t/\Lambda)^2/[k\,(C_t+C_b)]$. If the two layers are assumed identical $\Gamma_b = \Gamma_t = \Gamma_0$ and $C_t = C_b = C_0$, we see that as a result of the parallel layers the system coupling coefficient is increased to $K_p^2 = 2(\Gamma_0/\Lambda)^2/(kC_0)$, and as a result more power is harvested.

3.4. Two layers loaded in series

When the two PZT layers are loaded in series with a single load conductance $I_t = -I_b = -G_L V_{\mathrm{out}} = -G_L\,(V_t - V_b)$, and with these conditions equations (1)–(3) may be solved for V_{out} after tedious, but simple calculations, we shall not reproduce the result here, but rather consider only the much simpler situation where the two layers are identical but poled in opposite directions, and thus $V_t = -V_b = V_{\mathrm{out}}/2$. Then we may simplify equations (1)–(3) to

$$Z_m v_c = F + \frac{1}{2}\left(\frac{\Gamma_t}{\Lambda} - \frac{\Gamma_b}{\Lambda}\right)V_{\mathrm{out}}, \tag{14}$$

$$I_t = \frac{1}{2}\left(\frac{\Gamma_t}{\Lambda} - \frac{\Gamma_b}{\Lambda}\right)v_c + s\frac{C_t+C_b}{4}V_{\mathrm{out}}. \tag{15}$$

Mathematically, the situation is again identical to the 1s case, but the system coupling coefficient K_s is increased such that $K_s^2 = (\Gamma_t/\Lambda - \Gamma_b/\Lambda)^2/[k\,(C_t+C_b)] = 2\,(\Gamma_0/\Lambda)^2/(kC_0) = 2K_0^2$. With the perfect symmetry, the resonant frequency equals the native mechanical resonant frequency and the anti-resonant frequency becomes $\omega_a = \omega_0\sqrt{1+K_s^2}$. The output power is maximized near the anti-resonant frequency, and may be obtained by substitution into the equation for the 1s case, but we shall write it in full

$$P_{\max_s} = \frac{|F|^2_{\mathrm{RMS}}}{4b}\frac{2}{1+\sqrt{1+\frac{1+K_s^2}{Q^2K_s^4}}} = \frac{|F|^2_{\mathrm{RMS}}}{4b}\frac{2}{1+\sqrt{1+\frac{1+2K_0^2}{Q^24K_0^4}}}. \tag{16}$$

In devices where the product $K_0^{-4}Q^{-2}$ is relatively large (low coupling coefficient and moderate Q) the improvement in output power is significant. The optimal load conductance becomes

$$G_{L\mathrm{opt}_s} = \frac{\frac{1}{2}\omega_0 C_0\left(1+K_s^2\right)}{\sqrt{\left(1+K_s^2+Q^2K_s^4\right)}} = \frac{\frac{1}{2}\omega_0 C_0\left(1+2K_0^2\right)}{\sqrt{\left(1+2K_0^2+Q^24K_0^4\right)}}, \tag{17}$$

which is different from half of the optimal load conductance ($\omega_0 C_0 \frac{1+2K_0^2}{\sqrt{(1+2K_0^2+Q^2K_0^4)}}$) of the individual layers in an open circuit, or in other words, the optimal load resistance differs from the sum of optimal load resistances for the individual layers.

The output voltage becomes

$$V_{\text{out}} = -F \frac{(\Gamma_0/\Lambda)}{(\Gamma_0/\Lambda)^2 + \left(s\frac{C_0}{2} + G_L\right)Z_m}, \tag{18}$$

and especially at low coupling coefficients K_0 for the individual layers, the output voltage is significantly increased by series connection of the two layers. This is significant since the relative magnitude of rectifier losses is then reduced.

In addition, a detailed study of the power as a function of frequency shows that the bandwidth of the output power peak is increased when the system coupling coefficient is increased at fixed mechanical Q; this effect is most significant at rather low coupling coefficients for the individual layers. This is also true for the parallel-connected layers, which with respect to output power and bandwidth improvements performs equal to the series-connected layers. The two double-layer structures only differ (for symmetrical layers) with respect to the output voltage level and optimal load conductance, where the series-connected structure outperforms the parallel-connected structure due to the higher output voltage.

4. Results

The fabricated energy harvesters were characterized in a shaker setup, where a B&K Mini Shaker 4810 driven by an amplified sinusoidal signal from an Agilent 33220A function generator was used to simulate an external vibration from the environment. Both the energy harvester and a B&K Piezoelectric Accelerometer 8305 were mounted on the Mini Shaker. The accelerometer served as a reference for the input RMS acceleration a, and measurements are reported in fractions of the gravitational acceleration g (9.81 m s^{-2}). The RMS power output is found by connecting the harvester to a resistive load while the voltage drop across the load was measured. The optimal resistive load, R_{opt}, was found by varying the resistive load in steps of 10 kΩ to achieve maximum dissipated power in the load resistance, i.e. $P_{\text{RMS}} = V_{\text{RMS}}^2/R_{\text{opt}}$. Figure 7 shows the power output of the harvester as a function of the frequency for different input accelerations, measured with the PZT layers connected in series, i.e. the load is connected between bottom and top electrodes. The optimal resistive load used here was R_{opt}=200 kΩ. At 1 g input acceleration, the power output reaches 37.1 μW.

The output power from the bottom PZT layer and the top PZT layer was measured using the same measurement scheme. During measurements on the top PZT layer, the top and middle electrodes were connected to the load, while the bottom electrode was left open circuit. The optimal resistive load was found to be 130 kΩ for the top layer. Similarly, during measurements on the bottom PZT layer, the bottom and middle electrodes were connected to the load and the top electrode was left open circuit. The optimal resistive load was found to be 90 kΩ for the bottom layer. The peak output power from the

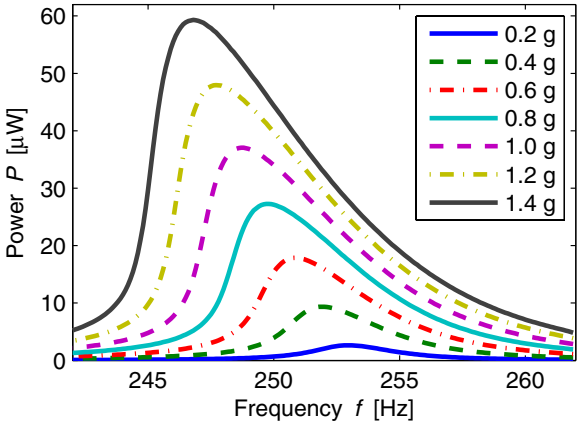

Figure 7. RMS power output of both PZT layers combined as a function of frequency near the resonant frequency for different RMS input accelerations at an optimal resistive load of 200 kΩ.

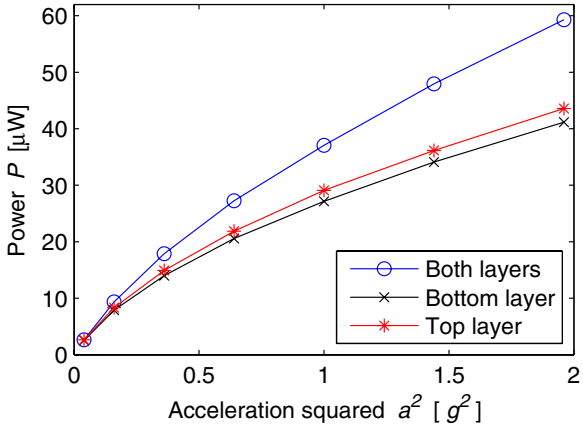

Figure 8. RMS power output from the top PZT layer, the bottom PZT layer and both layers combined as a function of the RMS input acceleration squared a^2 at their respective optimal resistive loads.

measurements yields the plot reported in figure 8, where the output power in the three cases (top layer, bottom layer and both layers connected to the load) is shown as a function of the input acceleration squared. The bandwidth, defined as the full-width at half-maximum of the data such as those in figure 7, was extracted for all measurements and is reported in figure 9.

4.1. Short versus open circuit

In measurements of the output power from the individual PZT layers, e.g. the bottom PZT layer, the top electrode may either be left open circuit as was done above or short circuited to the middle electrode. In figures 10 and 11, we compare the RMS output power from the top and bottom layers, respectively, when the third electrode is left open or short circuit.

Figures 10 and 11 both show an increase in the peak power frequency in the case of the open circuit configuration compared to that of the short circuit configuration. This is expected as shown in section 3. The shift is slightly larger for the bottom PZT layer than for the top PZT layer; the reason is that the top layer has a slightly larger system coupling coefficient than the bottom layer (partly due to a larger parasitic

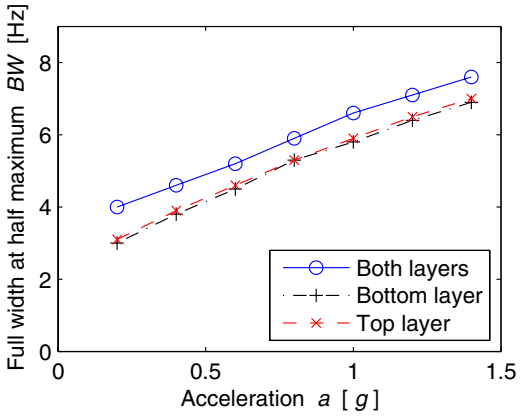

Figure 9. The full-width at half-maximum bandwidth for the top PZT layer, the bottom PZT layer and both layers combined as a function of the RMS input acceleration at their respective optimal resistive loads.

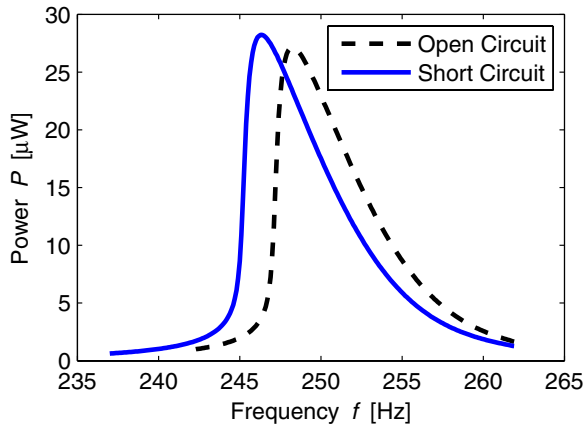

Figure 10. RMS power output of the bottom PZT layer as a function of frequency near the resonant frequency at 1 *g* RMS input acceleration where the top electrode is open or short circuit with respect to the middle electrode.

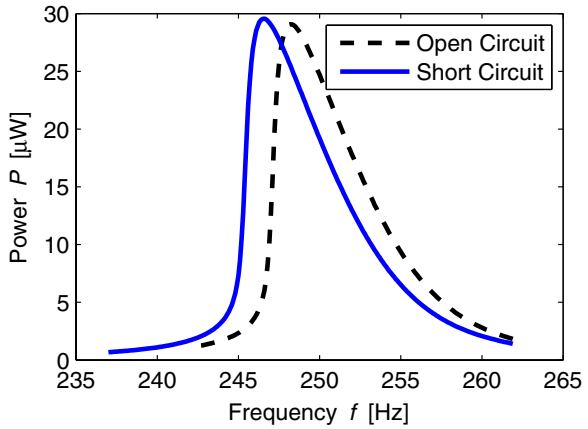

Figure 11. RMS power output of the top PZT layer as a function of frequency near the resonant frequency at 1 *g* RMS input acceleration where the bottom electrode is open or short circuit with respect to the middle electrode.

capacitance of the bottom PZT layer), and the shift in peak power frequency for the bottom layer is due to added effective spring constant from the top layer as shown in section 3.

Table 2. The relative change in the output power $(P_{sc} - P_{oc})/P_{oc}$ and peak power frequency shift $\Delta f_0 = f_{0oc} - f_{0sc}$ when short circuit configuration measurements are compared to open circuit configuration measurements during characterization of the individual layers.

RMS acceleration a (g)	0.6	0.8	1.0	1.2	1.4
$(P_{sc} - P_{oc})/P_{oc}$ (%)					
Bottom layer	3.06	2.92	3.94	4.40	4.98
Top layer	0.51	1.83	1.67	3.11	4.03
$f_{0oc} - f_{0sc}$ (Hz)					
Bottom layer	1.9	1.9	2.0	2.0	1.9
Top layer	1.7	1.7	1.6	1.7	1.7

Explicitly, we expect that $f_{0oc_b}^2 - f_{0sc_b}^2 = f_0^2 K_t^2$, where f_{0oc_b} and f_{0sc_b} are the peak frequencies in open and short circuit conditions, respectively, and f_0 is the mechanical resonance frequency. The slightly lower output power from the bottom layer compared to the top layer is caused by the slightly lower coupling coefficient for the bottom layer compared to that of the top layer.

Another trend is that the short circuit configuration generates slightly higher output power than that of the open circuit configuration. This is also expected as shown in section 3. Table 2 shows the relative change in output power $(P_{sc} - P_{oc})/P_{oc}$ and the shift in peak power frequency $\Delta f_0 = f_{0oc} - f_{0sc}$ when the short circuit (subscript sc) configuration measurements are compared to the open circuit (subscript oc) configuration measurements of the individual layers.

5. Discussion

The resonant frequency shift as a function of the acceleration observed in figure 7 was also seen in [11, 12], where it was explained to be caused by a nonlinear softening effect. Even though such an effect is still present in the pressure treated harvester, the softening effect is much less prominent compared to that in [11]. As a result, the resonant frequency shift with acceleration is smaller, and the frequency responses become more symmetrical around the resonance peaks. From figure 8 it can be noted that the power outputs of the two individual layers are almost identical; this was not the case in [11, 12]. Apparently, the use of high pressure treatments renders the two PZT thick film layers quite similar. This is supported by the SEM inspection shown in figure 4, where a cross-sectional view of the cantilever shows that the two layers are very similar both in thickness and morphology which was not the case in a similar study in [11]. The difference in the optimal resistive loads with such similar films is partly due to a larger parasitic capacitance and thus a larger total capacitance of the bottom layer compared to the top layer caused by layout differences. The output power from both layers combined in series is as expected higher than the output power from the individual layers due to the increased system coupling coefficient, but significantly less than the sum of the powers from the two individual layers. The increased system coupling coefficient also improves the useful bandwidth as shown in figure 9 where the bandwidth of both layers combined in series is about 1 Hz larger than that of each layer for all input

accelerations. As a result, the output power and the useful bandwidth are both increased by the use of two PZT layers, and the harvester becomes useful in a wider spectrum of vibrations. The measured RMS power output at 1 g acceleration is 37.1 μW, which is comparable to the best performing MEMS energy harvesters reported in the literature in recent years [6, 18].

6. Conclusion

MEMS-based PZT/PZT bimorph thick film vibration energy harvesters were successfully fabricated and characterized. By implementing an improved fabrication process, a fabrication yield of 98.6% was achieved. The revised process plan made high pressure treatment of the PZT thick film layers before sintering feasible. As a result, the two PZT layers became denser and more similar in thickness and morphology. The power outputs at 1 g for the top and bottom layers were 29.1 and 27.2 μW, respectively. The power output with both layers combined was 37.1 μW at 1 g with a bandwidth value of 7 Hz.

Acknowledgments

This research is part of the ELBA project, which is funded by the Advanced Technology Foundation. Center for Individual Nanoparticle Functionality (CINF) is sponsored by the Danish National Research Foundation.

Appendix

The starting point for the piezoelectric beam model is the constitutive piezoelectric material equations [16]. Since both the electric field **E** (due to the electrodes) and the stress **T** (due to pure bending) are unidirectional, the simplest material relations are obtained if electric displacement **D** and strain **S** are expressed as functions of the non-zero electric field E_3 and the stress T_1, and then the simplified material relations [16]

$$S_1 = s_{11}T_1 + \mathrm{d}_{31}E_3, \tag{A.1}$$

$$D_3 = d_{31}T_1 + \varepsilon_{33}E_3, \tag{A.2}$$

result, where only three material parameters, the compliance s_{11}, the piezoelectric coefficient d_{31} and the permittivity ε_{33}, are needed. Ideally, these parameters should have superscripts T or E to indicate that they are material parameters at constant stress or electric field, but in the interest of a simple notation the superscripts are omitted. The beam is subject to pure bending and thus the geometrical strain $S_1 = -zw''_{xx}$ results, where w is the beam deflection, while z is the position relative to the neutral axis of the beam. We shall ignore longitudinal beam displacement u.

Since the strain is known, it is useful to rearrange equations (A.1) and (A.2) to yield

$$T_1 = \frac{1}{s_{11}}S_1 - \frac{\mathrm{d}_{31}}{s_{11}}E_3, \tag{A.3}$$

$$D_3 = \frac{\mathrm{d}_{31}}{s_{11}}S_1 + \varepsilon_{33}\left(1 - \frac{\mathrm{d}_{31}^2}{s_{11}\varepsilon_{33}}\right)E_3 = \frac{\mathrm{d}_{31}}{s_{11}}S_1 + \varepsilon_{33}\left(1 - k_{31}^2\right)E_3, \tag{A.4}$$

where $k_{31} = \sqrt{d_{31}^2/(s_{11}\varepsilon_{33})}$ is the piezoelectric coupling coefficient. The currents flowing into the top ($I_{\mathrm{t}0}$) and bottom electrodes ($I_{\mathrm{b}0}$) may be calculated from integrals of equation (A.4) over the volumes of the individual layers using the space charge free condition ($\nabla \cdot \mathbf{D} = 0$) and the beam boundary conditions ($w(0) = 0$, and $w'_x(0) = 0$)

$$I_{\mathrm{t}0} = \dot{Q}_{\mathrm{t}0} = \frac{\mathrm{d}_{31\mathrm{t}}}{s_{11}}\frac{Wh_{\mathrm{t}}}{2}\dot{w}'_x(L) + \frac{\varepsilon_{33}\left(1 - k_{31\mathrm{t}}^2\right)WL}{h_{\mathrm{t}}}\dot{V}_{\mathrm{t}}, \tag{A.5}$$

$$I_{\mathrm{b}0} = \dot{Q}_{\mathrm{b}0} = \frac{\mathrm{d}_{31\mathrm{b}}}{s_{11}}\frac{Wh_{\mathrm{b}}}{2}\dot{w}'_x(L) + \frac{\varepsilon_{33}\left(1 - k_{31\mathrm{b}}^2\right)WL}{h_{\mathrm{b}}}\dot{V}_{\mathrm{b}}, \tag{A.6}$$

where $\dot{X}$ is a shorthand for $\partial X/\partial t$. Here subscripts t and b are used on material parameters to allow for e.g. different poling directions of the layers; in addition, subscript is also added to the layer thicknesses even though they are assumed identical. The currents are seen to depend on the slope rate $\dot{w}'_x(L)$ at the end of the beam, but that is identical to the slope rate of the proof mass and from the solution to Euler's beam equation, the slope and center of gravity deflection of the proof mass w_c are related by $w_c = \Lambda w'_x(L)$, with $\Lambda = 2\left(L^2 + 3L\ell + 3\ell^2\right)/\left[3\left(L + 2\ell\right)\right]$.

In addition to the capacitances $C_{\mathrm{t}0} = \varepsilon_{33}\left(1 - k_{31\mathrm{t}}^2\right)WL/h_{\mathrm{t}}$ and $C_{\mathrm{b}0} = \varepsilon_{33}\left(1 - k_{31\mathrm{b}}^2\right)WL/h_{\mathrm{b}}$ of the active piezoelectric layers additional parasitic capacitances, $C_{\mathrm{t}p}$ and $C_{\mathrm{b}p}$ may be present on the electrodes due to e.g. contact pads. As a result, the total currents I_{t} and I_{b} to the electrodes may be expressed as follows:

$$I_{\mathrm{t}} = \frac{\Gamma_{\mathrm{t}}}{\Lambda}\dot{w}_c + C_{\mathrm{t}}\dot{V}_{\mathrm{t}}, \tag{A.7}$$

$$I_{\mathrm{b}} = \frac{\Gamma_{\mathrm{b}}}{\Lambda}\dot{w}_c + C_{\mathrm{b}}\dot{V}_{\mathrm{b}}, \tag{A.8}$$

with the coupling coefficients $\Gamma_{\mathrm{t}} = (d_{31\mathrm{t}}Wh_{\mathrm{t}})/(2s_{11})$ and $\Gamma_{\mathrm{b}} = (d_{31\mathrm{b}}Wh_{\mathrm{b}})/(2s_{11})$, and total capacitances $C_{\mathrm{t}} = C_{\mathrm{t}0} + C_{\mathrm{t}p}$ and $C_{\mathrm{b}} = C_{\mathrm{b}0} + C_{\mathrm{b}p}$.

The bending moment is the moment of stress T_1 around the y-axis, and is thus obtained from an integral of equation (A.3)

$$M = -w''_{xx}\int \frac{W}{s_{11}}z^2\,\mathrm{d}z + \frac{d_{31\mathrm{b}}}{s_{11}}\frac{Wh_{\mathrm{b}}}{2}V_{\mathrm{b}} + \frac{\mathrm{d}_{31\mathrm{t}}}{s_{11}}\frac{Wh_{\mathrm{t}}}{2}V_{\mathrm{t}}, \tag{A.9}$$

and thus we may write the total bending moment

$$M = -YIw''_{xx} + \Gamma_{\mathrm{b}}V_{\mathrm{b}} + \Gamma_{\mathrm{t}}V_{\mathrm{t}}, \tag{A.10}$$

where $YI = \int (W/s_{11})\,z^2\,\mathrm{d}z$ is the effective product of Young's modulus and area moment of inertia for the beam. It follows that the static beam deflection is governed by the usual Euler beam equation $\left(YIw''_{xx}\right)''_{xx} = q$ where q is the load force per unit length, and thus the piezoelectric effects only affect the boundary conditions of the beam.

An approximate vertical force balance at the center of mass for the proof mass affected by the external force F yields

$$m\ddot{w}_c + b\dot{w}_c + kw_c = F + \frac{\Gamma_{\mathrm{b}}}{\Lambda}V_{\mathrm{b}} + \frac{\Gamma_{\mathrm{t}}}{\Lambda}V_{\mathrm{t}}, \tag{A.11}$$

where $k = 3YI/\left[L\left(L^2 + 3L\ell + 3\ell^2\right)\right]$ is the spring constant as seen from the center of mass, which results from a steady state solution of Euler's beam equation, and b represents viscous losses in the beam–mass system. Here we have ignored the effects of a finite moment of inertia for the proof mass and the mass of the cantilever beam. The bending moments due to piezoelectric effects have been recast into effective forces acting on the center of mass by use of the length parameter Λ.

We may, with Laplace transformed quantities, write the final lumped model equations as

$$Z_m v_c = F + \frac{\Gamma_\mathrm{b}}{\Lambda} V_\mathrm{b} + \frac{\Gamma_\mathrm{t}}{\Lambda} V_\mathrm{t}, \tag{A.12}$$

$$I_\mathrm{t} = \frac{\Gamma_\mathrm{t}}{\Lambda} v_c + sC_\mathrm{t} V_\mathrm{t} \tag{A.13}$$

$$I_\mathrm{b} = \frac{\Gamma_\mathrm{b}}{\Lambda} v_c + sC_\mathrm{b} V_\mathrm{b}, \tag{A.14}$$

where v_c is the velocity of the proof mass, $Z_m = sm + b + k/s$ is the mechanical impedance of the proof mass–spring system and $s = j\omega$ is the complex frequency.

References

[1] Hudak N S and Amatucci G G 2008 Small-scale energy harvesting through thermoelectric, vibration, and radiofrequency power conversion *J. Appl. Phys.* **103** 101301

[2] Beeby S P, Tudor M J and White N M 2006 Energy harvesting vibration sources for microsystems applications *Meas. Sci. Technol.* **17** R175–95

[3] Fang H, Liu J, Xu Z, Dong L, Wang L, Chen D, Cai B and Liu Y 2006 Fabrication and performance of MEMS-based piezoelectric power generator for vibration energy harvesting *Microelectron. J.* **37** 1280–4

[4] Choi W J, Jeon Y, Jeong J H, Sood R and Kim S G 2006 Energy harvesting MEMS device based on thin film piezoelectric cantilevers *J. Electroceram.* **17** 543–8

[5] Shen D, Park J, Ajitsaria J, Choe S, Wikle H C and Kim D 2008 The design, fabrication and evaluation of a MEMS PZT cantilever with an integrated Si proof mass for vibration energy harvesting *J. Micromech. Microeng.* **18** 055017

[6] Aktakka E E, Peterson R L and Najafi K 2011 Thinned-PZT on SOI process and design optimization for piezoelectric inertial energy harvesting *Proc. Transducers (Beijing, China, June)* pp 1649–52

[7] Roundy S and Wright P K 2004 A piezoelectric vibration based generator for wireless electronics *Smart Mater. Struct.* **13** 1131–42

[8] Erturk A and Inman D J 2009 An experimentally validated bimorph cantilever model for piezoelectric energy harvesting from base excitations *Smart Mater. Struct.* **19** 025009

[9] Aktakka E E, Peterson R L and Najafi K 2011 Multi-layer PZT stacking process for piezoelectric bimorph energy harvesters *11th Int. Conf. on Micro and Nanotechnology for Power Generation and Energy Conversion Applications (Seoul, Republic of Korea, Nov.)* pp 139–42

[10] Kok S, White N M and Harris N R 2009 Fabrication and characterization of free-standing thick-film piezoelectric cantilevers for energy harvesting *Meas. Sci. Technol.* **20** 124010

[11] Xu R, Lei A, Christiansen T L, Hansen K, Guizzetti M, Birkelund K, Thomsen E V and Hansen O 2011 Screen printed PZT/PZT thick film bimorph MEMS cantilever device for vibration energy harvesting *Proc. Transducers (Beijing, China, June)* pp 679–82

[12] Xu R, Lei A, Dahl-Petersen C, Hansen K, Guizze M, Birkelund K, Thomsen E V and Hansen O 2012 Screen printed PZT/PZT thick film bimorph MEMS cantilever device for vibration energy harvesting *Sensors Actuators* A at press doi:10.1016/j.sna.2011.12.035

[13] Lei A, Xu R, Thyssen A, Stoot A C, Christiansen T L, Hansen K, Lou-Moeller R, Thomsen E V and Birkelund K 2011 MEMS-based thick film PZT vibriational energy harvester *Proc. IEEE Micro Electro Mechanical Systems (Cancun, Mexico, Jan.)* pp 125–8

[14] Hindrichsen C, Lou-Moeller R, Hansen K and Thomsen E V 2010 Advantages of PZT thick film for MEMS sensors *Sensors Actuators* A **163** 9–14

[15] Hagood N W and von Flotow A 1991 Damping of structural vibrations with piezoelectric materials and passive electrical networks *J. Sound Vib.* **146** 243–68

[16] The Institute of Electrical and Electronics Engineers 1978 *IEEE Std 1976-1978 IEEE Standard on Piezoelectricity* pp 9–14

[17] Lifshitz R and Roukes M L 2000 Thermoelastic damping in micro- and nanomechanical systems *Phys. Rev.* B **61** 5600–9

[18] Elfrink R, Kamel T M, Goedbloed M, Matova S, Hohlfeld D, van Andel Y and van Schaijk R 2009 Vibration energy harvesting with aluminum nitride-based piezoelectric devices *J. Micromech. Microeng.* **19** 094005

A.8 Eurosensors-1 2012

R. Xu, L. M. Borregaard, A. Lei, M. Guizzetti, E. Ringgaard, T. Zawada, O. Hansen, and E. V. Thomsen, "Preliminary Performance Evaluation of MEMS-based Piezoelectric Energy Harvesters in Extended Temperature Range," Procedia Engineering, vol. 47, no. 0, pp. 1434–1437, 2012.

Available online at www.sciencedirect.com

SciVerse ScienceDirect

Procedia Engineering 47 (2012) 1434 – 1437

Procedia Engineering

www.elsevier.com/locate/procedia

Proc. Eurosensors XXVI, September 9-12, 2012, Kraków, Poland

Preliminary performance evaluation of MEMS-based piezoelectric energy harvesters in extended temperature range

R. Xu[a]*, L. M. Borregaard[a], A. Lei[b], M. Guizzetti[a], E. Ringgaard[a], T. Zawada[a], O. Hansen[b], E. V. Thomsen[b]

[a]*Meggitt A/S,* Hejreskovvej 20*, Kvistgaard 3490, Denmark*
[b] *Department of Micro- and Nanotechnology, Technical University of Denmark, Kongens Lyngby 2800, Denmark*

Abstract

In this work a batch of MEMS-based vibration energy harvesters consisting of a silicon/PZT thick film cantilever with integrated proof mass is characterized. The purpose of a vibration energy harvester is to convert low grade vibrations to useful electrical power. Optimally, the natural frequency of the harvester should match the frequency of the ambient vibration. The first step to achieve this is to evaluate the uniformity of the fabricated harvesters and understand the effects of temperature on the harvesters during operation. Therefore, the uniformity of 40 energy harvesters from one wafer has been evaluated. Thereafter the performance of the energy harvesters operating at temperatures between -30ºC to 100ºC was measured.

Keywords: Energy harvester; MEMS; piezoelectric; temperature range; performance

Introduction

The MEMS vibration energy harvesters have received significant attention in recent years. However, the effects of non-uniformity from the fabrication process and the influence of the operation temperature have not been the focus. For an optimal implementation of an energy harvester in any real vibrating environments, both the resonant frequency and the voltage output are vital parameters that should be understood. The resonant frequency of the energy harvester must match the available vibrating frequency from the environment to maximize the voltage output. The voltage output must then be sufficiently high for optimal operation of the power management circuitry. This paper evaluates the challenges related to frequency matching and variations in voltage output with respect to temperature for the presented MEMS-based piezoelectric energy harvesters [1].

1877-7058
doi:10.1016/j.proeng.2012.09.427

Fabrication

The piezoelectric energy harvesters were fabricated on 525 µm thick 4 inch silicon on insulator (SOI) wafers with a 20 µm device layer (Fig. 1(I, a)). A silicon oxide layer was thermally grown, followed by a deposition of stoichiometric low pressure chemical vapor deposition (LPCVD) silicon nitride (Fig. 1(I, b)). Backside windows in the nitride for a later KOH etch were defined using UV lithography followed by reactive ion etch (RIE) and then the front side nitride was removed in a RIE etch (Fig. 1(I, c)). A Pt bottom electrode, also serving as a diffusion barrier, was deposited using e-beam evaporation and patterned (Fig. 1(I, d)). On top of the bottom electrode a PZT thick film (InSensor® TF2100) was deposited using screen printing (Fig. 1(I, e)). An Au top electrode layer was deposited by e-beam evaporation (Fig. 1(I, f)). The silicon dioxide in the backside windows was removed in a buffered hydrofluoric acid (bHF) solution, and cavities were etched in a KOH solution (Fig. 1(I, g)). The PZT structures were covered with photoresist and the cantilevers released by an oxide etch in bHF followed by a RIE silicon etch (Fig. 1(I, h)). Finally, the wafers were diced (Fig. 1(II)) and the PZT film poled by applying an electric field between the top and bottom electrodes at elevated temperature.

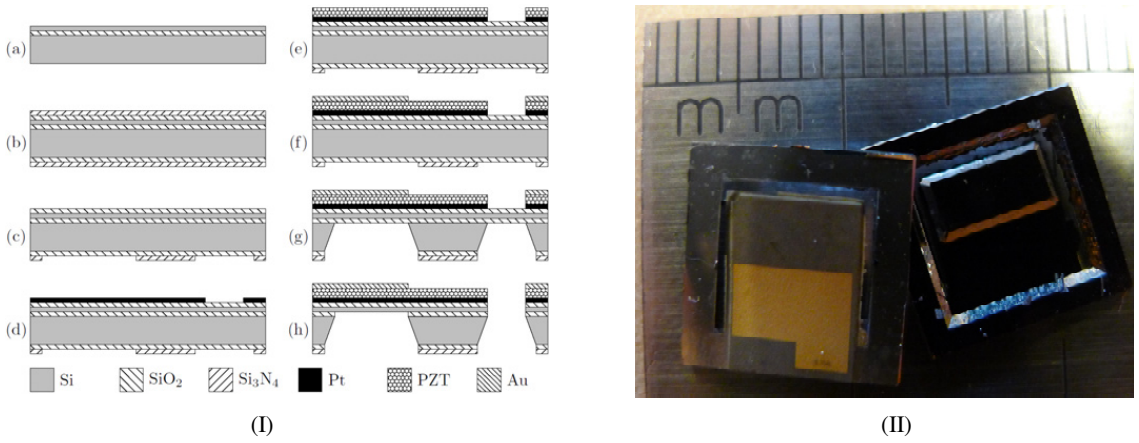

Fig. 1. (I) Cross sectional view of the fabrication process; (II) Photograph of the fabricated energy harvesters, one is viewed from the front and another is viewed from the back.

Results and discussion

From one of the fabricated wafers 40 energy harvesters were characterized using a shaker setup to evaluate the fabrication uniformity. The open circuit voltage was measured as a function of the input frequency at 0.5 *g* RMS acceleration. The peak voltage frequency and the peak voltage for the 40 energy harvesters are shown in Fig. 2(a). The relative standard deviation of peak voltage frequency in the sample population was found to be 2.4% and relative standard deviation of peak voltage was around 30%. The frequency variation could be explained by variations in proof mass or cantilever spring constant due to variations in cantilever thickness; the fabrication process of the mass however is quite well controlled and thus the variation is presumably due to variations in cantilever spring constant.

From another wafer, 6 energy harvesters were characterized at 0.1 *g* RMS acceleration between temperatures from -30ºC to 100ºC in 10ºC increments using a climatic chamber integrated with the shaker setup. The measurements of one selected harvester are shown in Fig. 2(b) as a contour plot of the open circuit voltage V_{oc} as a function of frequency f and temperature T. Note, there is at clear break line at T=0ºC. This is believed to be caused by the condensation of water vapor and ice formation on the

cantilever, which increases the effective thickness of the cantilever and hence the spring constant. In Fig. 3(a) the peak voltage frequencies of all 6 harvesters are plotted as a function of the temperature. Since the frequency variation between the harvesters is comparable to the effect of the temperature, the frequencies are normalized with respect to the room temperature (20ºC) value for better comparison as shown in Fig. 3(b). One can observed from Fig. 3 that the peak voltage frequencies decrease as the temperature increases, which has been also reported in [2]. This is caused by the decrease in Young's modulus of the cantilever materials, *i.e.* silicon and PZT, with temperature. The change in the peak frequency in the temperature range is around 2% as it is seen in Fig. 3(b). Even though the change is smaller than the frequency variation between the different harvesters, it is still a significant change compared to the harvester bandwidth (~2 Hz) and the often narrow frequency bandwidth of the vibrating source. Similarly, the peak output voltage is shown as a function of the temperature in Fig. 4(a) and the voltage normalized with respect to that at 20ºC is shown in Fig. 4(b). These measured results show that compared the peak voltage frequency the peak output voltage is highly dependent on the temperature, where the output voltage can drop below 60% of its original value at 20ºC. The variation with temperature seems to cluster in two classes, four devices with high output voltage show almost identical behavior at temperatures above 0ºC (the differences below 0ºC could be caused by differences in ice formation), while two devices (7E and 6F) have a significantly lower output voltage and a smaller variation with temperature.

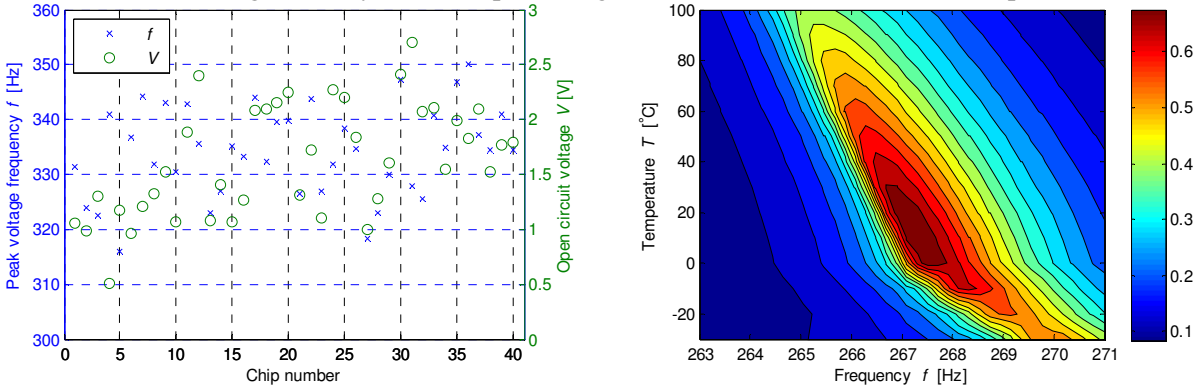

(a) (b)

Fig. 2. (a) The performance of 40 chips from one wafer in terms of peak output voltage frequency and peak open circuit output voltage. (b) A contour plot of the open circuit voltage V_{oc} [V] as a function of the input frequency and temperature.

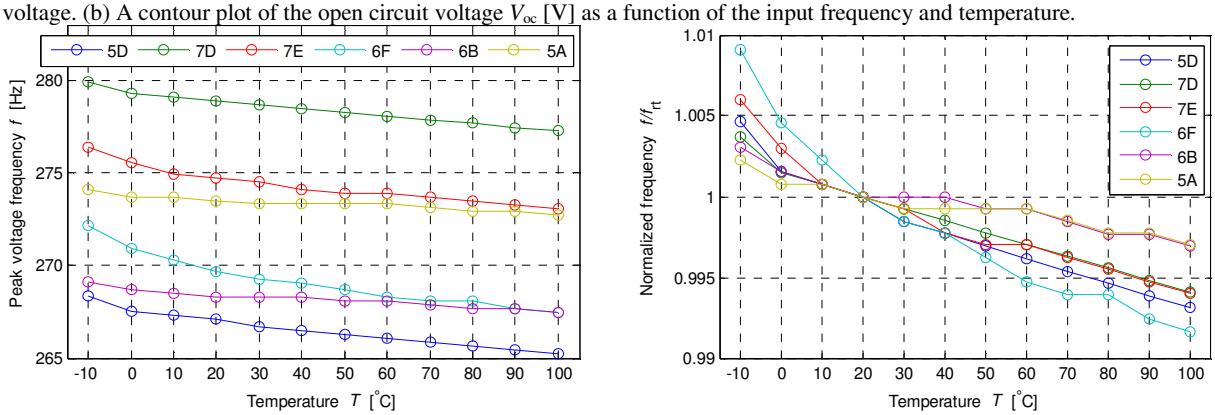

(a) (b)

Fig. 3. (a) The peak output voltage frequency as a function of the temperature at 0.1 *g* RMS acceleration; (b) The peak output voltage frequency normalized to that at room temperature shown as a function of the temperature.

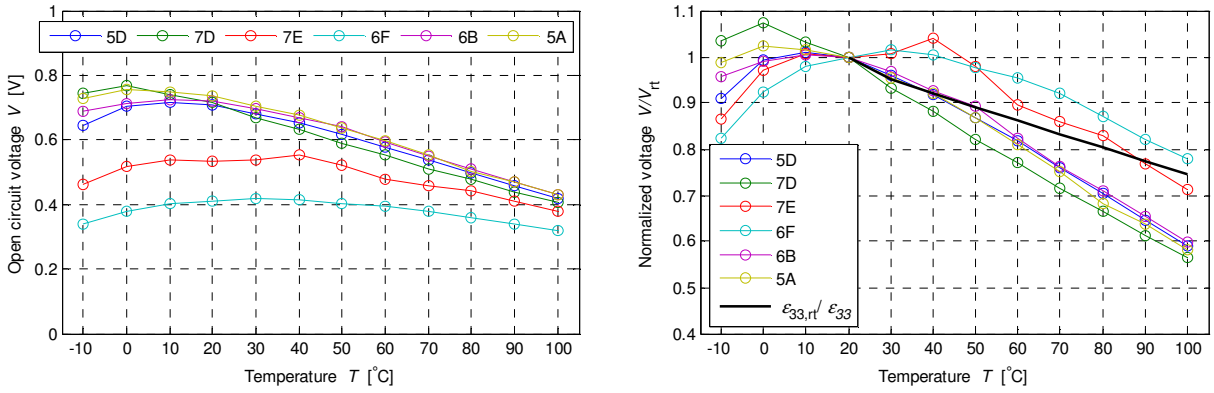

(a) (b)

Fig. 4. (a) The peak open circuit output voltage as a function of the temperature at 0.1 *g* RMS acceleration; (b) The peak open circuit output voltage normalized to that at room temperature shown as a function of the temperature. The normalized reciprocal dielectric constant in the temperature range 20ºC to100ºC is also shown for comparison.

Since the piezoelectric coupling coefficient is relatively low for the fabricated energy harvesters (~0.2), the output voltage will be roughly proportional to d_{31}/ε_{33}, where d_{31} is the piezoelectric coefficient and ε_{33} is the dielectric constant of the PZT thick film. The dielectric constant was measured at temperatures in the range 20-100ºC, and the reciprocal value normalized with respect to its value at 20ºC is shown in Fig. 4(b) along with the normalized voltages. Fig. 4(b) shows that the reciprocal dielectric constant decreases at a lower rate than the voltage, which indicates that the change in the dielectric constant is not the only contributing factor to the decrease in voltage. However, the voltage decrease is not believed to be caused by d_{31}, since d_{31} is expected to increase with increasing temperature [3]. The aforementioned decrease in Young's modulus of the PZT material and the increased mechanical damping at higher temperature observed in [2] are two other contributing factors to a decreasing voltage output.

Conclusion

The presented results indicate that temperature has a significant effect on the resonant frequency as well as the output voltage of the energy harvesters, which is of high practical importance.

Acknowledgements

This research is part of the ELBA project, which is funded by the Danish National Advanced Technology Foundation.

References

[1] Lei A, Xu R, Thyssen A, Stoot A C, Christiansen T L, Hansen K, Lou-Moller R, Thomsen E V, Birkelund K. MEMS-based thick film PZT vibrational energy harvester. *IEEE MEMS 2011*. 2011, p. 125-128

[2] Barker S, Vassilevski K V, Wright N G, Horsfall A B. High Temperature Vibration Energy harvester System. *IEEE Sensors 2010*. 2010, p. 300-303

[3] Wolf R A, Trolier-McKinstry S. Temperature dependence of the Piezoelectric response in lead zirconate titanate films *Journal of applied physics*. 2004, **95**, nr. 3, p.1397-1406

A.9 Eurosensors-2 2012

A. Lei, R. Xu, L. M. Borregaard, M. Guizzetti, and E. V. Thomsen, "Homogeneity Analysis of a MEMS-based PZT Thick Film Vibration Energy Harvester Manufacturing Process," Procedia Engineering, vol. 47, no. 0, pp. 554–557, 2012.

Available online at www.sciencedirect.com

SciVerse ScienceDirect

Procedia Engineering 47 (2012) 554 – 557

Procedia Engineering

www.elsevier.com/locate/procedia

Proc. Eurosensors XXVI, September 9-12, 2012, Kraków, Poland

Homogeneity Analysis of a MEMS-based PZT Thick Film Vibration Energy Harvester Manufacturing Process

Anders Lei[a]*, Ruichao Xu[b], Louise M. Borregaard[b], Michele Guizzetti[b], Erik V. Thomsen[a]

[a]*Department of Micro- and Nanotechnology, Technical University of Denmark, DTU Nanotech, Building 345B, DK-2800 Kongens Lyngby, Denmark*

[b]*Meggitt A/S, Hejreskovvej 20, Kvistgaard 3490, Denmark*

Abstract

This paper presents a homogeneity analysis of a high yield wafer scale fabrication of MEMS-based unimorph silicon/PZT thick film vibration energy harvesters aimed towards vibration sources with peak vibrations in the range of around 300 Hz. A wafer with a yield of 91% (41/45 devices) has been characterized. Measurements of the open circuit voltage showed a relative difference of 32.6% between the standard deviation and average. Measurements of the capacitance and resonant frequency showed a relative difference between the standard deviation and average value of 4.3% and 2.9% respectively, thus indicating that the main variation in open circuit voltage performance is caused by varying quality factor. The average resonant frequency was measured to 333 Hz with a standard variation of 9.8 Hz and a harvesting bandwidth of 5-10 Hz. A maximum power output of 39.3 μW was achieved at 1 *g* for the best performing harvester.

Keywords: Energy harvesting; Vibration harvesting; MEMS; PZT; Thick film

1. Introduction

With the recent development in low power electronics and small-scale energy harvesters, the realization of small long-term autonomous wireless sensors seems to become increasingly realistic. The criterion for success for energy harvesters is that their size does not exceed the volume batteries would

* Corresponding author. Tel.: +45 4525 5700; fax: +45 4588 7762.
E-mail address: anders.lei@nanotech.dtu.dk.

1877-7058 © 2012 Elsevier Ltd....Selection and/or peer-review under responsibility of the Symposium Cracoviense Sp. z.o.o.
doi:10.1016/j.proeng.2012.09.207

take up to supply the required power in the sensors lifetime. This can be well achieved using MEMS technology, however most applicable vibration sources have peak frequencies in the range of a few hundred Hz [1], which for classical MEMS devices are considered unusually low. To achieve these resonant frequencies, designs with high length to thickness ratios and relative large proof masses have been utilized, resulting in devices that are laterally large and fragile during the fabrication processes. Recently Lei *et al.* [2] presented a high performance MEMS-based PZT thick film vibration energy harvester Fig. 1(a). In [2], and as for a majority of other MEMS-based vibration energy harvesters reported [3], [4] only measurements for a single device is presented. Based on an identical fabrication process as in [2], resulting in a yield of ~91% (41/45), characterization of each device from a full wafer will be presented in this paper, hence giving a comprehensive assessment of the device uniformity.

2. Results

The characterization is carried out in the following way: initially, the capacitance together with RMS open circuit voltage (V_{oc}) and resonant frequency (F_{res}) is measured for all harvesters. Secondly, the RMS power output dissipated in a resistive load is measured for a number of representative chips.

Fig. 1(b) shows a map of the measured capacitance for the 41 fabricated harvesters listed as the wafer layout with rows and columns. The average measured capacitance is 5.638 nF with a standard deviation of 0.243 nF. The average capacitance corresponds to a dielectric constant of 842. The peak RMS V_{oc} measured with an input RMS acceleration of 0.5 *g* is seen in Fig. 2(a). The average V_{oc} is 1.6 V with a standard deviation of 0.52 V. The resonant frequency at which peak V_{oc} is obtained is mapped in Fig. 2(b). The average F_{res} is measured to 333.3 Hz with a standard deviation of 9.8 Hz.

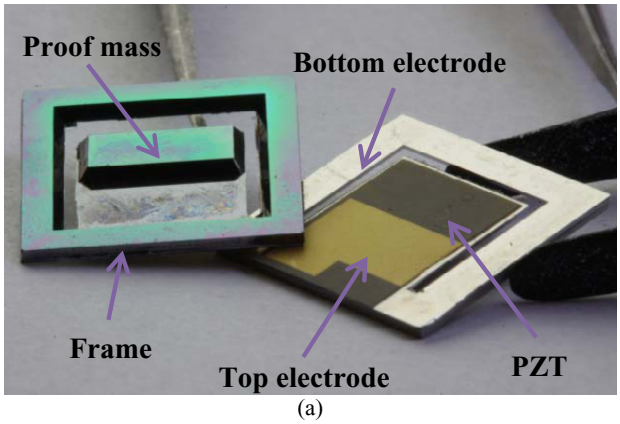

(a)

	A	B	C	D	E	F	G
1		5.342	5.448	5.495	5.234	5.096	
2	5.336	5.640	5.693	5.679	5.600	5.506	5.343
3	5.139		5.799	5.769	5.636	5.564	5.398
4	5.768	5.766	5.839	5.924		5.724	5.004
5	5.789	5.868	5.884	5.924	5.934	5.896	5.449
6	5.765	5.958	5.671		5.779	5.615	5.588
7			5.812	5.853	5.749	5.869	

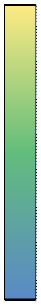

(b)

Fig. 1. (a) Photograph of the front and backside of the fabricated vibration energy harvester. (b) Characterization map of the measured PZT layer capacitance.

2.1. Load measurements

For the power output measurements a total of 10 representative harvester devices are selected. Three devices are selected from around each of the three quartiles (Q_1=1.17 V, Q_2=1.55 V and Q_3=2.08 V) of the V_{oc} measurements, the last harvester selected is the one with highest V_{oc} output. In Fig. 3(a) the iteratively found optimal resistive load (R_{load}) is listed for each of the selected harvesters together with the measured RMS power output ($P=V_{rms}^2/R_{load}$) for the three RMS accelerations 0.5 *g*, 0.75 *g* and 1 *g*. The bandwidth is measured as full width at half maximum (BW_{FWHM}) at 0.5 *g* acceleration and the total quality factor is calculated as $Q_{total}=F_{res}/BW_{FWHM}$. In Fig. 3(b) the results are outlined with power output at the three accelerations plotted for each of the 10 harvesters.

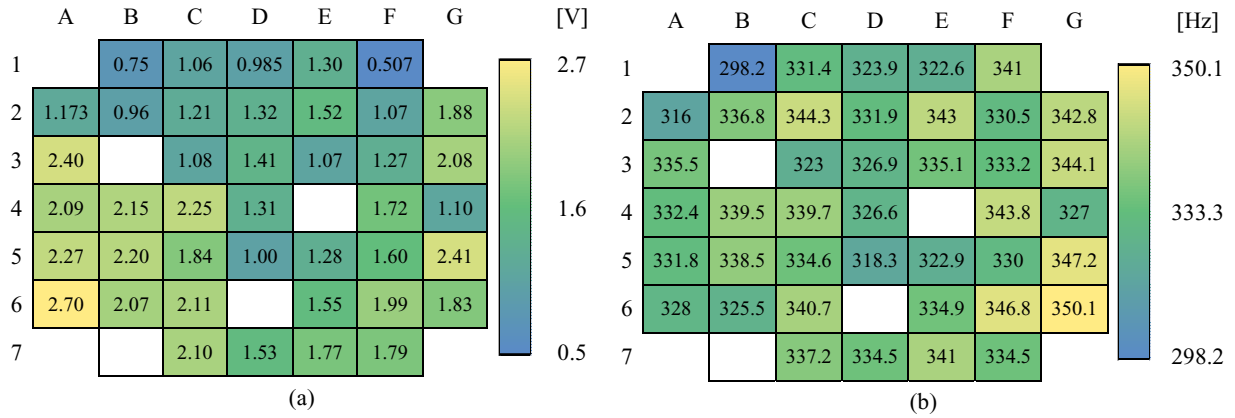

Fig. 2. (a) Map of the maximum measured RMS open circuit voltage during frequency sweeps with an input RMS acceleration of 0.5 *g*. (b) Map of the corresponding measured resonant frequency.

3. Discussion

Assuming that the porosity and thus the dielectric constant of the screen-printed PZT thick film is constant over the wafer, the variation in capacitance is an estimate of geometrical variations. The lateral dimensions of the capacitor are defined by the deposited electrodes which are controlled by lithography. It can therefore be assumed that the main contribution to the variation in capacitance is variations in thickness of the PZT thick film. Percentagewise, the standard deviation is 4.3% relative to the average value. This corresponds to a variation of 1.2 µm out of a PZT film thickness of 27 µm.

From an application point of view the main success criteria for a linear vibration energy harvester is the frequency match with the vibration source. F_{res} is determined by mechanical properties with the cantilever thickness and distance from cantilever anchoring point to center of mass as the dominating geometrical parameters. The silicon part of the cantilever is determined accurately by the device layer thickness of the silicon-on-insulator wafer, and the capacitance characterization indicated a relatively small thickness variation of the PZT. The distance to the center of mass, width of the cantilever and mass of the proof mass are all determined by lithography. The standard deviation relative to the average measured F_{res} is 2.9%. Ignoring the two lowest and highest measurements this value decreases to 2.2%. Since F_{res} is proportional to the square root of the cantilever thickness cubed, the relative variation is expected to be higher, although the silicon part accounts for a significant part of the cantilever stiffness.

	Chip	Load [kΩ]	BW_{FWHM} [Hz]	Q_{total}	RMS Power [µW]		
					0.5*g*	0.75*g*	1*g*
Peak	A6	150	5.00	65.9	12.5	25.0	39.3
Q3 2.08V	G3	50	6.80	50.7	10.5	22.1	35.0
	B4	50	6.80	49.7	9.6	21.3	35.8
	B6	50	6.60	49.3	9.7	21.4	34.7
Q2 1.55V	F5	50	8.20	40.1	6.7	15.7	25.7
	D7	75	9.00	37.1	6.1	14.8	24.3
	E6	75	8.50	39.2	5.5	13.1	22.5
Q1 1.17V	C2	75	8.75	37.7	4.8	11.1	17.9
	A2	75	8.20	38.4	5.1	10.9	15.3
	C3	75	10.25	31.1	2.9	7.2	13.3

(a)

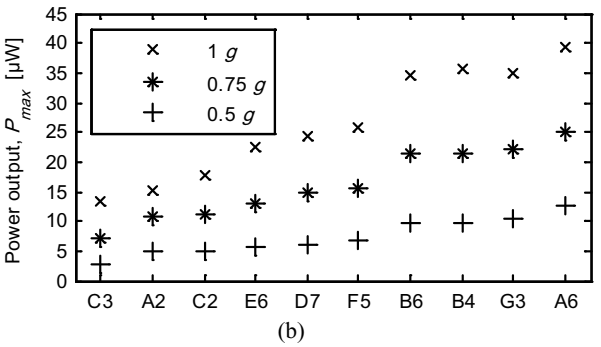

(b)

Fig. 3. (a) RMS power output measurements for 10 harvester devices representative for the 41 fabricated devices. Power is measured at three different RMS accelerations with the resistive load listed. Bandwidth (BW_{FWHM}) and total quality factor (Q_{total}) is measured at 0.5 *g*. (b) Measured RMS power output for three different accelerations for the 10 representative harvesters.

This could indicate that the variation in capacitance across the wafer is caused by both varying dielectric constants and PZT thicknesses.

While the capacitance and F_{res} measurements give estimates of the variation of the mechanical parameters and the dielectric constant, the open circuit voltage measurements will provide information concerning variations in piezoelectric coefficients and quality factor since $V_{oc}=g_{31}\ \bar{\sigma}\ h_{PZT}$, where g_{31} is the piezoelectric voltage coefficient, $\bar{\sigma}$ is the average induced stress in the PZT layer with thickness h_{PZT}. Besides being determined by mechanical properties, which also affects the resonant frequency, the average induced stress is related to the tip displacement at resonance and thus quality factor. The measured standard deviation relative to the average V_{oc} is 32.2%, ignoring the two lowest and highest values gives a percentage of 27.4% which is still higher than what the variation in PZT thickness can account for. The majority of the variation in V_{oc} is therefore believed to originate from either g_{31} which is determined by how well the PZT thick film is polarized or the quality factor.

Except from the V_{oc} measurements where the harvesters from the lower left corner of the wafer appears to have a general higher output, no significant wafer area tendencies are observed in the capacitance and F_{res} measurements nor in-between all three measurements.

For the power output measurements the best uniformity in performance is observed in-between the three chips from the third quartile where the difference in power output is around or less than 1 μw for the three accelerations. Similar small variations are observed in bandwidth and quality factor. The resonant frequency varies from 325-344 Hz for the three chips which are considerably more than the measured bandwidth of around 6.8 Hz. The variation in power output of the three chips from the second quartile increases to around 3 μW difference at 1 *g*. For the first quartile chips, the variation is around 4.5 μW at 1 *g*. In average the first quartile devices harvest 30% and 36% less power than the second quartile devices at 0.5 *g* and 1 *g*, respectively. Third quartile devices perform 63% and 45% better than second quartile devices at 0.5 *g* and 1 *g*, respectively. Compared to the variation of the open circuit measurements this increased variation is expected since the output power is proportional to the voltage squared.

4. Conclusion

Measurements of the open circuit voltage for the 41 devices showed a relative difference of 32.6% between the standard deviation and average. Measurements of the capacitance and resonant frequency showed a relative difference between the standard deviation and average value of 4.3% and 2.9% respectively. This indicates that the main variation in open circuit voltage performance is caused by varying quality factor. Power output measurements showed good uniformity between chips with similar open circuit voltages from the high performance section. Decreasing uniformity was observed between chips from the section with lower open circuit voltage. A maximum power output of 39.3 μW was measured at 1 *g* for the best performing harvester. The power harvesting bandwidth was measured to 5-10 Hz, with the best performing harvesters having the lowest bandwidth. The average resonant frequency was measured to 333 Hz with a standard variation of 9.8 Hz.

References

[1] S. Roundy, P. K. Wright, and J. Rabaey, *Computer Communications*, vol. 26, no. 11, pp. 1131–1144, Jul. 2003.

[2] A. Lei *et al.*, *Micro Electro Mechanical Systems (MEMS), 2011 IEEE 24th International Conference*, 2011, pp. 125 –128.

[3] R. Elfrink *et al.*, *J. Micromech. Microeng.*, vol. 19, no. 9, p. 094005, Sep. 2009.

[4] D. Shen *et al.*, *Sensors and Actuators A: Physical*, vol. 154, no. 1, pp. 103–108, Aug. 2009.

Appendix B

Schematic Processflows Used Prior and During ELBA

B.1 Borregaard and Kvaal 2009

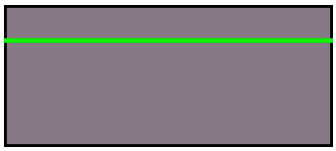

(a) The wafer with a 1 µm buried SiO_2 layer, the device layer is 20 µm and the handle layer 500 µm.

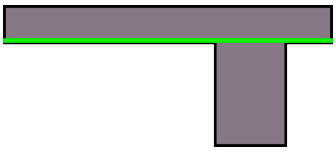

(b) In this step the proof mass is etched out from the backside using a highly anisotropic silicon etcher (ASE).

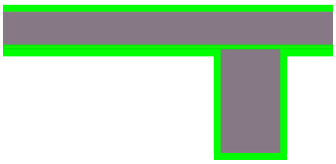

(c) To create an electrically insulating layer, diffusion barrier and a mask for the KOH etch, the wafers are oxidized.

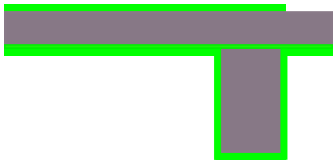

(d) The silicon oxide mask is etched out using buffered HF acid, outlining the cantilevers.

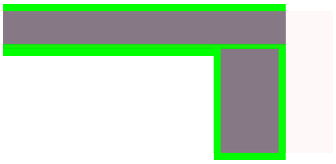

(e) To release the cantilevers, the device layer and remaining buried oxide is etched using a KOH base etch. The buried SiO_2 layer is expected to break when the device layer is etched through.

(f) The bottom electrode is made of a 500 nm thick platinum film, patterned using a metal etch to get the desired structures.

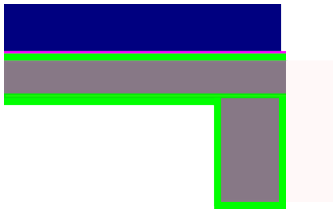

(g) The PZT is screen printed on the wafer at Ferroperm Piezoceramics A/S, creating a layer of about 30 µm.

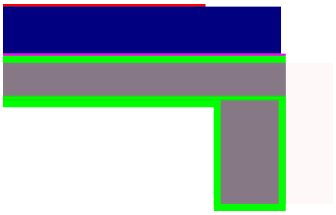

(h) The top electrode consist of a 400 nm thick gold film which is patterned using a liftoff process.

(i) Legend for figures 14a to 14h.

B.2 Nagstrup 2009

(a) SOI wafer

(b) Resist mask and ASE etch

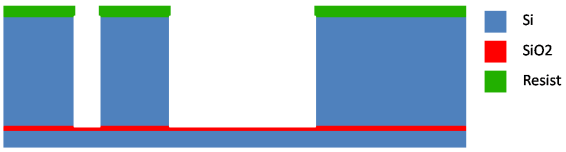

(c) ASE etch

(d) Oxide removal

(e) Oxidation

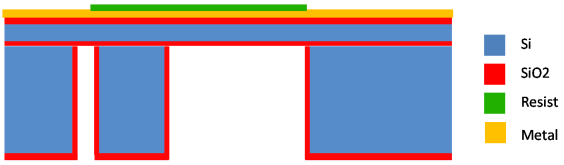

(f) Bottom electrode titanium/platinum and photoresist etch mask

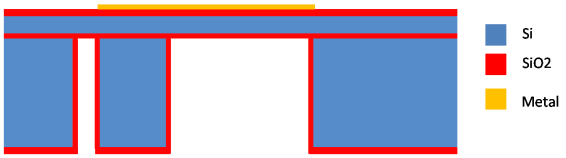

(g) Metal etch

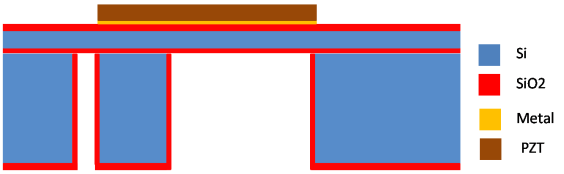

(h) PZT silk screen printing

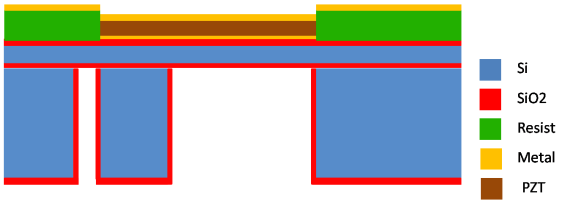

(i) Top electrode deposition chromium/gold

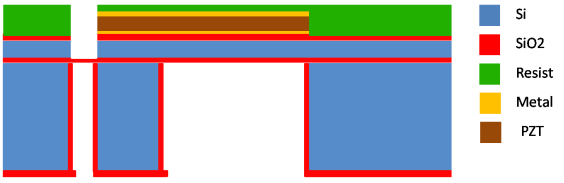

(j) Release etch by RIE

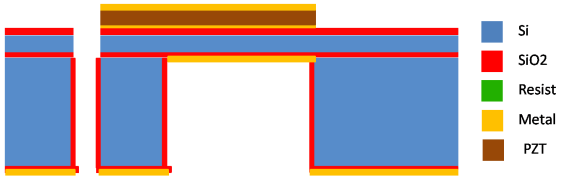

(k) Photoresist removal

B.3 Thyssen and Stoot 2010

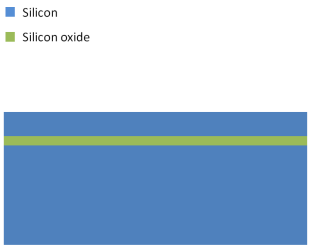

(a) *The SOI-wafer which will become the energy harvester.*

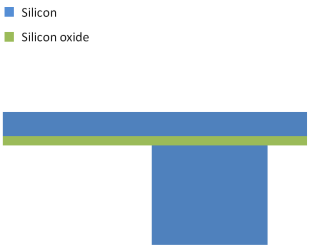

(b) *The proof mass is etched out from the backside. The energy harvester is seen from the side.*

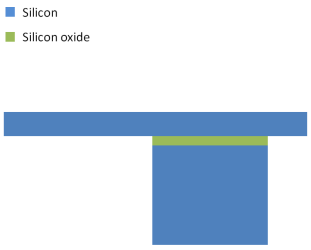

(c) *The silicon oxide is removed.*

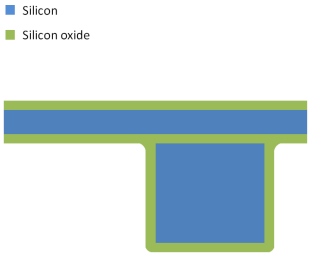

(d) *A new silicon oxide is grown, which is of higher quality and more homogeneous than the previous one.*

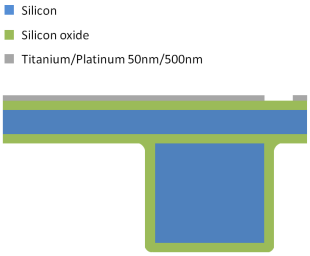

(e) *The bottom electrode is evaporated, it consist of 50 nm Ti and 500 nm Pt.*

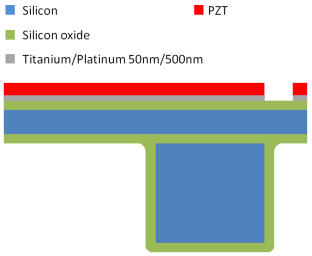

(f) *The PZT is screen printed by Ferroperm.*

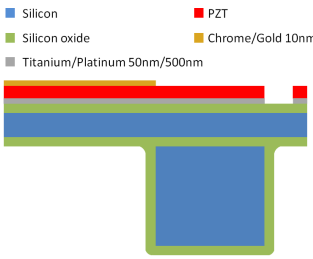

(g) *The top electrode is evaporated, it consist of 10 nm Cr and 400 nm Au.*

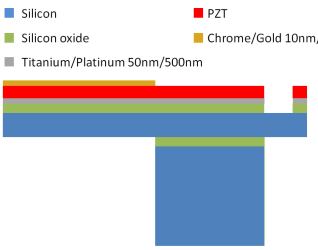

(h) *The silicon oxide which served as a sacrificial layer is removed.*

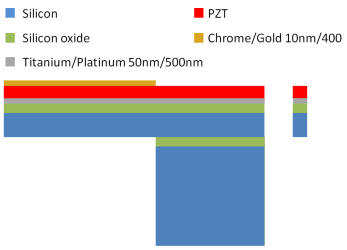

(i) *The cantilever is etched free, and the unit is ready for dicing.*

B.4 Christiansen 2010

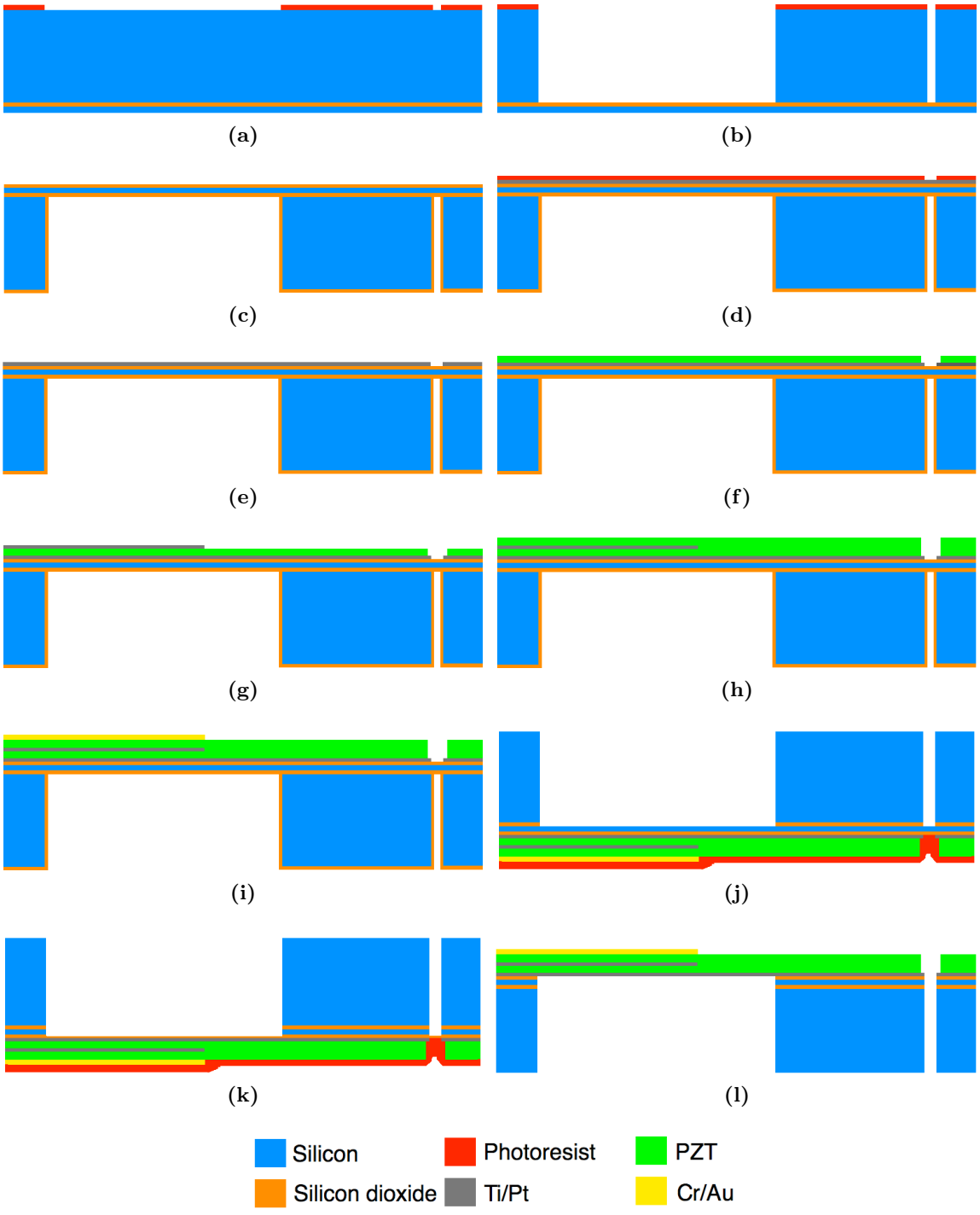

B.5 Pedersen 2011

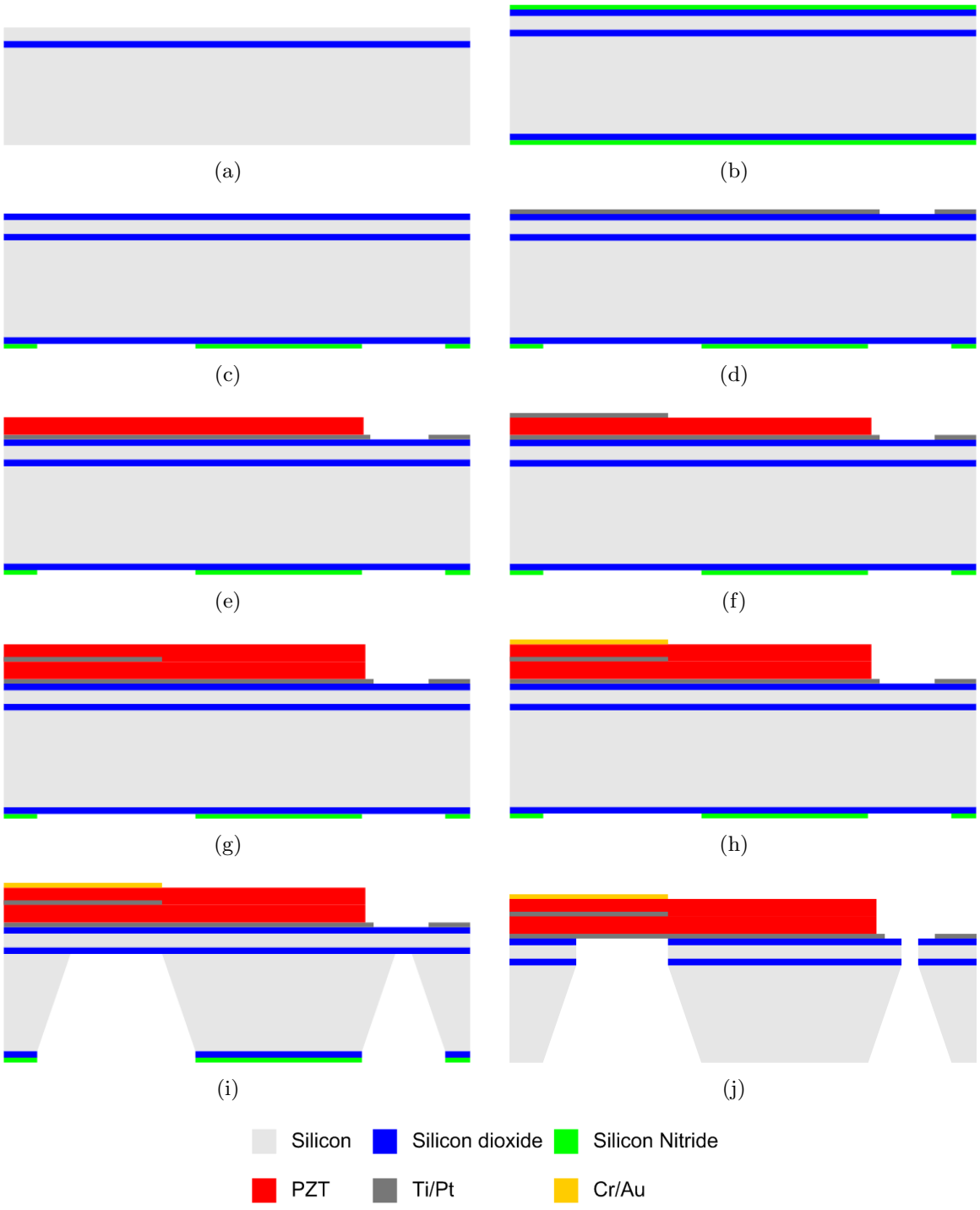

Appendix C

L-Edit T-Cell Code for Harvester Design

```
/*****************************************************************************
 * Cell Name: EH T-Cell
 * Creator  :
 *
 * Revision History:
 * 8 Aug 2012  Generated by L-Edit
 *****************************************************************************/
#include <cstdlib>
#include <cmath>
#include <cstring>
#include <cstdio>
#include <string>

#define EXCLUDE LEDIT_LEGACY_UPI
#include <ldata.h>


/* Begin -- Uncomment this block if you are using L-Comp. */
//#include <lcomp.h>
/* End */

/* TODO: Put local functions here. */
void EH_T_Cell_main(void)
{
   int iTmpUpiReturnCode = LUpi_GetReturnCode();
   /* Begin DO NOT EDIT SECTION generated by L-Edit */
   LCell          cellCurrent    = (LCell)LMacro GetNewTCell();
   double       L Beam       = LCell GetParameterAsDouble(cellCurrent, "L Beam");
   double       W Beam       = LCell GetParameterAsDouble(cellCurrent, "W Beam");
   double       Mass Ratio   = LCell GetParameterAsDouble(cellCurrent, "Mass Ratio");
   double       Width Ratio  = LCell GetParameterAsDouble(cellCurrent, "Width_Ratio");
   /* End DO NOT EDIT SECTION generated by L-Edit */

   if(LUpi_GetReturnCode())
   {
      LDialog_MsgBox("Error: Tcell failed to read parameters.");
      return;
   }
   LUpi_SetReturnCode(iTmpUpiReturnCode);


   /* Begin -- Uncomment this block if you are using L-Comp. */
   /*LC InitializeState();
   /*LC CurrentCell = cellCurrent;
   /* End */


   /* TODO: Put local variables here. */

   double         ChipSize=10*1e6;           // Overall size of the chip

   double         DiceM Width=10*1e3;        // Dimensions of dicemarks
   double         DiceM Length=70*1e3;       // Dimensions of dicemarks
   double         DiceM_Dist=20*1e3;         // Position of dicemarks

   double         W_Trench=500*1e3;          // Width of the trench

   double         T KOH EH=500*1e3;          // KOH etch depth of the cavity etch
   double         W_KOH_EH=T_KOH_EH/sqrt(2); // KOH width of cavity etch

   double         T KOH_SM=350*1e3;          // KOH etch depth of the shadow mask etch
(set=0 for DRIE etch)
   double         W_KOH_SM=T_KOH_SM/sqrt(2); // KOH width of shadow mask etch

   double         KOH Width_Ratio=2;         // Width of KOH compensation structure
relative to etch depth
   double         KOH Length_Ratio=1.6;      // Length of KOH compensation structure
relative to KOH_Width_Ratio

   double         PZT1Margin=150*1e3;        // Margin from bottom electrode to PZT1
   double         MEMargin=150*1e3;          // Margin from PZT1 to middle electrode
   double         PZT2Margin=150*1e3;        // Margin from bottom electrode to PZT2
   double         TEMargin=150*1e3;          // Margin from PZT2 to top electrode

   double         FrameElecMargin=100*1e3;   // Margin from frame/anchoring to electrode

   double         PadPadMargin=600*1e3;      // Margin between middel and top electrode
pads
```

```
   double         PZT2PadMargin=300*1e3;     // PZT margin from cantilever start to
electrode pads
   double         PadFrameMargin=400*1e3;    // Margin between frame and electrode pads

   double         PZTMassLTRMargin=350*1e3;  // Left, top, right margin from cantilever
edge to PZT mass
   double         PZTMassBMargin=350*1e3;    // Bottom margin from electrode to PZT mass


   // Helping coordinates
   double         TB_Frame=(ChipSize-L_Beam-W_Trench)/2;

   double         Cant L=ChipSize/2-W Beam/2;
   double         Cant R=ChipSize/2+W Beam/2;
   double         Cant B=(ChipSize-L Beam-W_Trench)/2;
   double         Cant T=Cant B+L Beam;
   double         Cant_M=Cant_B+L_Beam*(1-Mass_Ratio);

   double         Trench L=Cant L-W Trench;
   double         Trench T=Cant T+W Trench;
   double         Trench_R=Cant_R+W_Trench;



   LTransform_Ex99   TransRotE;
   LTransform Ex99   TransE;
   LPoint            DeltaE, ArrayE, OffsetE;
   LMagnification    MagE;

   MagE.num   = 1;
   MagE.denom = 1;

   DeltaE.x = ChipSize;
   DeltaE.y = 0;
   TransRotE.translation   = DeltaE;
   TransRotE.orientation   = LRotate0MirrorX;
   TransRotE.magnification = MagE;

   LFile pFile = LFile GetVisible();
   LLayer Layer_Outline = LLayer_Find ( pFile , "Cell Outline Layer" ) ;
   LLayer Layer Temp = LLayer Find ( pFile , "Origin Layer" ) ;
   LLayer Layer KOH = LLayer Find ( pFile , "Mass" ) ;
   LLayer Layer BE = LLayer Find ( pFile , "Bottom electrode" ) ;
   LLayer Layer PZT1 = LLayer Find ( pFile , "PZT layer1" ) ;
   LLayer Layer SPME = LLayer Find ( pFile , "SP Middle electrode" ) ;
   LLayer Layer EBME = LLayer Find ( pFile , "EB Middle electrode" ) ;
   LLayer Layer PZT2 = LLayer Find ( pFile , "PZT layer2" ) ;
   LLayer Layer PZTM = LLayer Find ( pFile , "PZT Mass" ) ;
   LLayer Layer TE = LLayer Find ( pFile , "Top electrode" ) ;
   LLayer Layer_Trench = LLayer_Find ( pFile , "Trench" ) ;

   /* TODO: Begin custom generator code.*/

   /* Chip Outline*/
   LObject Chip_Outline=LBox_New(cellCurrent , Layer_Outline, 0, 0, ChipSize, ChipSize);

   /* Dice marks */

   LBox New(cellCurrent , Layer_KOH, 0, DiceM_Dist, DiceM_Width,
DiceM Dist+DiceM Length);
   LBox New(cellCurrent , Layer KOH, 0, ChipSize-DiceM_Dist, DiceM_Width,
ChipSize-DiceM_Dist-DiceM_Length);
   LBox New(cellCurrent , Layer_KOH, ChipSize, DiceM_Dist, ChipSize-DiceM_Width,
DiceM Dist+DiceM Length);
   LBox New(cellCurrent , Layer KOH, ChipSize, ChipSize-DiceM_Dist, ChipSize-DiceM_Width,
ChipSize-DiceM_Dist-DiceM_Length);

   LBox New(cellCurrent , Layer_KOH, DiceM_Dist, 0, DiceM_Dist+DiceM_Length,
DiceM Width);
   LBox_New(cellCurrent , Layer_KOH, DiceM_Dist, ChipSize, DiceM_Dist+DiceM_Length,
ChipSize-DiceM Width);
   LBox New(cellCurrent , Layer KOH, ChipSize-DiceM Dist, ChipSize,
ChipSize-DiceM Dist-DiceM Length, ChipSize-DiceM Width);
   LBox New(cellCurrent , Layer KOH, ChipSize-DiceM_Dist, 0,
ChipSize-DiceM_Dist-DiceM_Length, DiceM_Width);

   /* Trench Outline*/
   LObject Trench[5];
   // Trench Rectangles
```

```
   Trench[0]=LBox New(cellCurrent , Layer Temp, Trench L, Cant B, Cant L, Trench T);
   Trench[1]=LBox New(cellCurrent , Layer Temp, Cant L, Cant T, Cant R, Trench T);
   Trench[2]=LBox_New(cellCurrent , Layer_Temp, Cant_R, Trench_T, Trench_R, Cant_B);

   // Trench for triangle harvesters
   LPoint TrenchArray1[] ={
   Cant B         ,Cant L,
   Cant M         ,Cant L,
   Cant M         ,ChipSize/2-W Beam*Width Ratio/2};
   Trench[3]=LPolygon_New(cellCurrent, Layer_Temp, TrenchArray1, 3);

   LPoint TrenchArray2[] ={
   Cant B         ,Cant R,
   Cant M         ,Cant R,
   Cant M         ,ChipSize/2+W Beam*Width Ratio/2};
   Trench[4]=LPolygon_New(cellCurrent, Layer_Temp, TrenchArray2, 3);

   // Merging trench object
   LCell_BooleanOperation(cellCurrent, LBoolOp_OR, 0, Trench, 5, NULL, 0, Layer_Temp,
LFALSE);
   LObject TrenchMerge = LObject_GetList(cellCurrent, Layer_Temp);

   /* Bottom Electrode */
   LObject BT_Electrode1=LBox_New(cellCurrent , Layer_BE, 0, 0, ChipSize, ChipSize);

   LCell BooleanOperation(cellCurrent, LBoolOp_SUBTRACT, 0, &BT_Electrode1, 1,
&TrenchMerge, 1, Layer_BE, LTRUE);

   /* KOH*/
   LObject KOH = LBox New(cellCurrent, Layer_KOH, Trench_L-W_KOH_EH , Cant_B-W_KOH_EH,
Trench_R+W_KOH_EH, Trench_T+W_KOH_EH);

   LObject KOHSub[5];
   KOHSub[0]=LBox New(cellCurrent, Layer_Temp , Cant_L+W_KOH_EH, Cant_M+W_KOH_EH,
Cant R-W KOH_EH, Cant_T-W_KOH_EH);

   /* Drawing KOH corner compensation structures */
   double         cornerxS=Cant L+W KOH EH;
   double         corneryS=Cant_T-W_KOH_EH;

   double         KOH EH Comp Width=T KOH EH*KOH Width Ratio;
   double         KOH EH Comp Length=KOH EH Comp Width*KOH Length_Ratio;
   double         KOH_EH_Comp_Temp=(KOH_EH_Comp_Width/2)*sqrt(2);

   double         cornerxE=cornerxS-KOH EH Comp Length*sqrt(2)/2;
   double         corneryE=corneryS+KOH_EH_Comp_Length*sqrt(2)/2;

   LPoint PointArray1[] ={
   corneryS-KOH EH Comp Temp     ,cornerxS,
   corneryE-KOH EH Comp Temp     ,cornerxE,
   corneryE                      ,cornerxE,
   corneryE                      ,cornerxE+KOH EH Comp Temp,
   corneryS                      ,cornerxS+KOH EH Comp Temp};
   KOHSub[1]=LPolygon_New(cellCurrent, Layer_Temp, PointArray1, 5);

   KOHSub[2] = LObject Copy(cellCurrent, Layer Temp, KOHSub[1]);
   KOHSub[3] = LObject Copy(cellCurrent, Layer Temp, KOHSub[1]);
   KOHSub[4] = LObject_Copy(cellCurrent, Layer_Temp, KOHSub[1]);

   LObject Transform Ex99(KOHSub[2], TransRotE );
   LObject_Transform_Ex99(KOHSub[4], TransRotE );

   DeltaE.x = 0;
   DeltaE.y = corneryS+Cant M+W KOH EH;
   TransRotE.translation   = DeltaE;
   TransRotE.orientation   = LRotate180MirrorX;
   TransRotE.magnification = MagE;

   LObject Transform Ex99(KOHSub[3], TransRotE );
   LObject_Transform_Ex99(KOHSub[4], TransRotE );

   LCell_BooleanOperation(cellCurrent, LBoolOp_OR, 0, KOHSub, 5, NULL, 0, Layer_Temp,
LTRUE);
   LObject KOHSubMerge = LObject_GetList(cellCurrent, Layer_Temp);

   LCell BooleanOperation(cellCurrent, LBoolOp_SUBTRACT, 0, &KOH, 1, &KOHSubMerge, 1,
Layer_KOH, LTRUE);

   /* PZT 1 */
```

```
   double      Mar1=PZT1Margin;
   LObject     PZT1[4];
   PZT1[0]=LBox_New(cellCurrent , Layer_PZT1, Cant_L+Mar1, 0, Cant_R-Mar1, Cant_B);

   LPoint PZT1Array[] ={
   Cant_B         ,Cant_L + Mar1,
   Cant M         ,ChipSize/2-W Beam*Width Ratio/2 + Mar1,
   Cant M         ,ChipSize/2+W Beam*Width_Ratio/2 - Mar1,
   Cant B         ,Cant R - Mar1};
   PZT1[1]=LPolygon_New(cellCurrent, Layer_PZT1, PZT1Array, 4);

   PZT1[2]=LBox New(cellCurrent , Layer PZT1, ChipSize/2-W Beam*Width_Ratio/2 + Mar1,
Cant M, ChipSize/2+W Beam*Width Ratio/2 - Mar1, Cant M+Mar1);
   PZT1[3]=LBox_New(cellCurrent , Layer_PZT1, Cant_L + Mar1, Cant_M+Mar1, Cant_R - Mar1,
Cant T-Mar1);
   LCell_BooleanOperation(cellCurrent, LBoolOp_OR, 0, PZT1, 4, NULL, 0, Layer_PZT1,
LTRUE);


   /* Middle Electrode */
   // Screen printed
   double      Mar2=PZT1Margin+MEMargin;
   LObject     SPME[2];
   SPME[0]=LBox New(cellCurrent , Layer SPME, Cant L+Mar2, PadFrameMargin,
ChipSize/2-PadPadMargin/2, Cant_B-FrameElecMargin);

   LPoint MEArray[] ={
   Cant B-FrameElecMargin        ,Cant L + Mar2,
   Cant M                        ,ChipSize/2-W Beam*Width Ratio/2 + Mar2,
   Cant M                        ,ChipSize/2+W Beam*Width_Ratio/2 - Mar2,
   Cant B-FrameElecMargin        ,Cant R - Mar2};
   SPME[1]=LPolygon_New(cellCurrent, Layer_SPME, MEArray, 4);

   LCell_BooleanOperation(cellCurrent, LBoolOp_OR, 0, SPME, 2, NULL, 0, Layer_SPME,
LFALSE);

   // E-beam deposited
   LCell_BooleanOperation(cellCurrent, LBoolOp_OR, 0, SPME, 2, NULL, 0, Layer_EBME,
LTRUE);
   LObject EBME = LObject_GetList(cellCurrent, Layer_EBME);
   LCell BooleanOperation(cellCurrent, LBoolOp_GROW, W_KOH_SM, &EBME, 1, NULL, 0,
Layer EBME, LTRUE);
   LObject EBMEGrow = LObject_GetList(cellCurrent, Layer_EBME);

   double         cornerxS2=ChipSize/2-PadPadMargin/2+W KOH SM;
   double         corneryS2=Cant_B-FrameElecMargin-W_KOH_SM;

   double         KOH SM Comp Width=T KOH SM*KOH Width Ratio;
   double         KOH SM Comp Length=KOH SM Comp Width*KOH Length_Ratio;
   double         KOH_SM_Comp_Temp=(KOH_SM_Comp_Width/2)*sqrt(2);

   double         cornerxE2=cornerxS2-KOH SM Comp Length*sqrt(2)/2;
   double         corneryE2=corneryS2+KOH_SM_Comp_Length*sqrt(2)/2;

   LPoint PointArray2[] ={
   corneryS2-KOH SM Comp Temp       ,cornerxS2,
   cornerxE2-KOH SM Comp Temp       ,cornerxE2,
   cornerxE2                        ,cornerxE2,
   cornerxE2                        ,cornerxE2+KOH SM Comp Temp,
   cornerxS2                        ,cornerxS2+KOH SM Comp Temp};
   LObject EBMESub=LPolygon_New(cellCurrent, Layer_EBME, PointArray2, 5);

   LCell BooleanOperation(cellCurrent, LBoolOp_SUBTRACT, 0, &EBMEGrow, 1, &EBMESub, 1,
Layer_EBME, LTRUE);

   /* PZT2 */
   double      Mar3=PZT2Margin;
   LObject     PZT2[5];
   PZT2[0]=LBox New(cellCurrent , Layer PZT1, ChipSize/2, 0, Cant R-Mar3, Cant B);
   PZT2[1]=LBox_New(cellCurrent , Layer_PZT1, Cant_L+Mar3, Cant_B-PZT2PadMargin,
Cant_R-Mar3, Cant_B);

   LPoint PZT2Array[] ={
   Cant B         ,Cant L + Mar3,
   Cant M         ,ChipSize/2-W Beam*Width Ratio/2 + Mar3,
   Cant M         ,ChipSize/2+W Beam*Width_Ratio/2 - Mar3,
   Cant_B         ,Cant_R - Mar3};
   PZT2[2]=LPolygon_New(cellCurrent, Layer_PZT2, PZT2Array, 4);
```

```
   PZT2[3]=LBox New(cellCurrent , Layer PZT1, ChipSize/2-W Beam*Width_Ratio/2 + Mar3,
Cant M, ChipSize/2+W Beam*Width Ratio/2 - Mar3, Cant M+Mar3);
   PZT2[4]=LBox_New(cellCurrent , Layer_PZT1, Cant_L + Mar3, Cant_M+Mar3, Cant_R - Mar3,
Cant T-Mar3);
   LCell BooleanOperation(cellCurrent, LBoolOp_OR, 0, PZT2, 5, NULL, 0, Layer_PZT2,
LTRUE);

   /* Top Electrode */
   // E Beam deposited
   double      Mar4=PZT2Margin+TEMargin;
   LObject     TE[2];
   TE[0]=LBox New(cellCurrent , Layer_TE, ChipSize/2+PadPadMargin/2, PadFrameMargin,
Cant_R-Mar4, Cant_B-FrameElecMargin);

   LPoint TEArray[] ={
   Cant B-FrameElecMargin        ,Cant L + Mar4,
   Cant M                        ,ChipSize/2-W Beam*Width Ratio/2 + Mar4,
   Cant M                        ,ChipSize/2+W Beam*Width_Ratio/2 - Mar4,
   Cant B-FrameElecMargin        ,Cant R - Mar4};
   TE[1]=LPolygon New(cellCurrent, Layer TE, TEArray, 4);
   LCell_BooleanOperation(cellCurrent, LBoolOp_OR, 0, TE, 2, NULL, 0, Layer_TE, LTRUE);
   LObject TETemp = LObject GetList(cellCurrent, Layer TE);
   LCell BooleanOperation(cellCurrent, LBoolOp_GROW, W_KOH_SM, &TETemp, 1, NULL, 0,
Layer TE, LTRUE);
   LObject TEGrow = LObject_GetList(cellCurrent, Layer_TE);

   double         cornerxS3=ChipSize/2+PadPadMargin/2-W KOH SM;
   double         corneryS3=Cant_B-FrameElecMargin-W_KOH_SM;

   double         cornerxE3=cornerxS3+KOH SM Comp Length*sqrt(2)/2;
   double         cornerYE3=cornerYS3+KOH_SM_Comp_Length*sqrt(2)/2;

   LPoint PointArray3[] ={
   cornerYS3-KOH SM Comp Temp       ,cornerxS3,
   cornerYE3-KOH SM Comp Temp       ,cornerxE3,
   cornerYE3                        ,cornerxE3,
   cornerYE3                        ,cornerxE3-KOH SM Comp Temp,
   cornerYS3                        ,cornerxS3-KOH SM Comp Temp};
   LObject TESub=LPolygon_New(cellCurrent, Layer_TE, PointArray3, 5);

   LCell BooleanOperation(cellCurrent, LBoolOp_SUBTRACT, 0, &TEGrow, 1, &TESub, 1,
Layer TE, LTRUE);

   /* Trench */
   LCell_BooleanOperation(cellCurrent, LBoolOp_OR, 0, Trench, 5, NULL, 0, Layer_Temp,
LTRUE);
   LObject TrenchMerge2 = LObject GetList(cellCurrent, Layer Temp);
   LCell BooleanOperation(cellCurrent, LBoolOp_SHRINK, 100e3, &TrenchMerge2, 5, NULL, 0,
Layer_Trench, LTRUE);

   /* Extra PZT mass */
   LBox New(cellCurrent , Layer PZTM, Cant L + PZTMassLTRMargin, Cant_M+PZTMassBMargin,
Cant_R - PZTMassLTRMargin, Cant_T-PZTMassLTRMargin);

   /* End custom generator code.*/
}
extern "C" int UPI_Entry_Point(void)
{
   EH T Cell_main();
   return 1;
}
```

Appendix D

Relevant Documents

D.1 TF2100 Datasheet

InSensor A/S

TF2100

PZT thick film based on Ferroperm Pz26

Pz26 is an all-round hard PZT material with good coupling factors, high Curie temperature, high mechanical quality factor, low dielectric loss and very good stability over time. Pz26 can be used as a direct replacement for all other Navy I materials. Benefits include strongly improved ageing rates, and extremely stable performance from orders ranging over several years.

The material is compatible with thick film technology and the properties are almost fully conserved in the change from bulk to thick film. The change in properties is mainly attributed to increased porosity in the thick film compared to the bulk material.

Typical applications are:

- High frequency medical imaging
- Miniaturised accelerometers
- Integrated miniaturised phased array ultrasound scanners

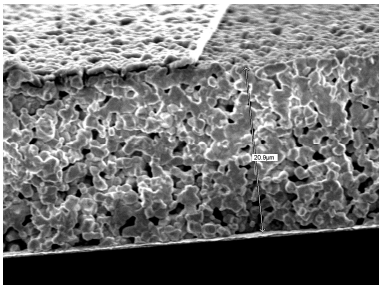

FIG. 1 SEM picture of TF2100

Main characteristics of TF2100

	Symbol	Unit	TF2100
Electrical properties			
Relative dielectric constant at 1 kHz	K_{33}^T		520
Dielectric dissipation factor at 1 kHz	$\tan\delta$	10^{-3}	8
Electromechanical properties			
Coupling coefficients	k_p		29
	k_t		49
Piezoelectric charge coefficients	d_{33}	pC/N	200
	d_{31}	pC/N	-50
Piezoelectric voltage coefficients	g_{33}	10^{-3} Vm/N	50
	g_{31}		-10
Mechanical properties			
Acoustic impedance	Z_a	MRayl	~15
Mechanical Quality Factor	$Q_{m,t}$		100

D.2 KOH Wafer Holder

WAFER HOLDER — TANDEM
WITH BACKSIDE PROTECTION

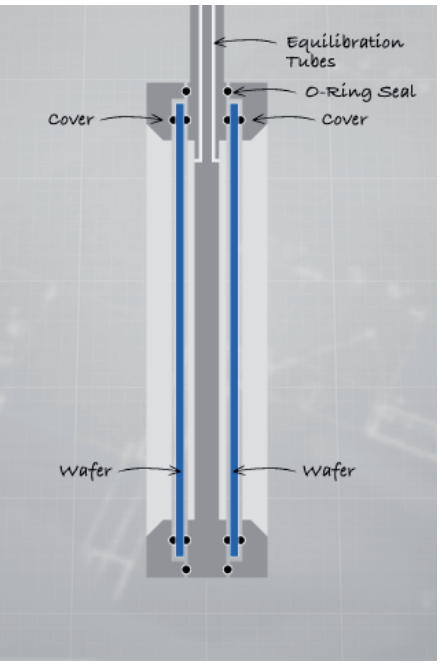

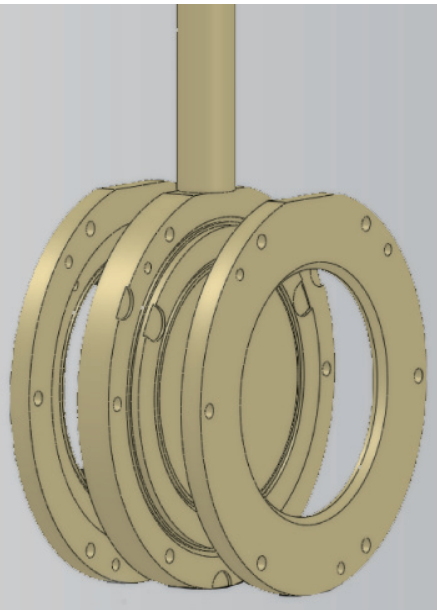

Working principle of the Tandem wafer holder

The Tandem wafer holders have been used for more than 15 years in MEMS industry and research. Tandem wafer holders are available for wafers with 3", 4", 5", 6", and 8" diameters. The Tandem series wafer holder protects the wafer's back side and the edge from the etchant solution. A unique feature of AMMT's Tandem holders is their symmetrical, small-footprint construction that allows one to mount two wafers with the etchant protected sides facing each other. However, it is important to note that both sides are fully independent from each other. Consequently, even a small etchant bath can be used to etch a number of wafers simultaneously. If only one wafer needs to be processed, blind covers are available for purchase.

All holders are made entirely from PEEK, in order to avoid any risk of etchant contamination by metal parts. They are suitable for nearly all etchants (KOH, TMAH, HF, H3PO4, etc.) over an extended temperature range.

The wafer is sealed by a double precision O-ring system that reduces mechanical stress on the wafer to a minimum. Two covers on the front and back side hold the wafers in place, fixed by six screws. As the customer-specific wafer thickness is machined as a recess into the cover, all screws can be tightened using a regular wrench without sensitivity to the applied torque. This ensures a minimum mechanical stress on the fragile wafer.

Upon ordering the holder, the wafer thickness machined as a recess into the cover-ring needs to be specified. The holder tolerates wafers with a thickness of +/- 80 um around the specified target thickness. If more flexibility is required, additionally cover-rings with different recesses can always be ordered.

Furthermore, the volume between the wafer and holder's body is connected by a venting tube (one separate for each side) to the ambient atmosphere in order to avoid pressure caused by temperature changes.

The standard Tandem series is designed for single side etching processes that do not require electrical contact, e. g. time based etching, etch-stop on oxide or nitride layers, SOI wafers, glass/quartz etching in HF, etc.

In order to keep maintenance costs low, all O-rings have dimensions in accordance with the American AS-568 standards.

TECHNICAL SPECIFICATIONS

Product code	Tandem 3	Tandem 4	Tandem 5
Wafer size	3" or 75 mm	4" or 100 mm	5" or 125 mm
Internal dimensions			
Width of the O-ring seal	1.78 mm	1.78 mm	1.78 mm
Recommended edge exclusion width	7 mm	7 mm	10 mm
Diameter of usable area	61 mm	86 mm	105 mm
External dimensions			
Diameter	114 mm	140 mm	158 mm
Thickness	34 mm	38 mm	38 mm

AMMT

AMMT GmbH – Advanced Micromachining Tools
Anselm-Feuerbach-Strasse 6, 67227 Frankenthal, Germany
Tel.: +49-6233-4960014, Fax:+49-6233-436214
E-Mail: info@ammt.com, http://www.ammt.com

Product code	Tandem 3	Tandem 4	Tandem 5
Materials			
Main Body and corver-ring material	PEEK		
O-ring material	EPDM 70		
Etchant compatibility	KOH, TMAH, HF and various acids		
Temperature range	5 °C – 150 °C		

Product code	Tandem 6	Tandem 6 LAA*	Tandem 8
Wafer size	6" or 150 mm	6" or 150 mm	8" or 200 mm
Internal dimensions			
Width of the O-ring seal	1.78 mm	2.62 mm	2.62 mm
Recommended edge exclusion width	10 mm	5.5 mm	5.5 mm
Diameter of usable area	130 mm	140.5 mm	189 mm
External dimensions			
Diameter	186 mm	186 mm	240 mm
Thickness	38 mm	38 mm	41 mm
Materials			
Main Body and corver-ring material	PEEK		
O-ring material	EPDM 70		
Etchant compatibility	KOH, TMAH, HF and various acids		
Temperature range	5 °C – 150 °C		

** Wafer holder with enlarge active area option (LAA), the o-ring shape is adapted to wafers flat.*

Standard configuration the o-ring shape is fully around.

OPTIONS

The handle length is customer specific. Please inquire for customer specific mounting options.

NOTE

AMMT manufactures wafer holders for all sizes of wafers. Holders for single chips and rectangular substrates are available as well. Please inquire for specifications and prices.

D.3 B&K Mini-Shaker Type 4810

PRODUCT DATA

Mini-shaker — Type 4810

USES

- Calibration of accelerometers
- Vibration testing of small objects
- Educational demonstrations
- Mechanical impedance measurements

FEATURES

- Force rating 10 newton (2.25 lbf) sine peak
- Frequency range DC to 18 kHz
- First axial resonance above 18 kHz
- Max. bare table acceleration 550 m/s^2
- Rugged construction
- Optimised to obtain full output force when used with Power Amplifier Type 2718

951138e

Description

Mini-shaker Type 4810 is of the electrodynamic type with a permanent field magnet. It is well-suited as the motive force generator in mechanical impedance measurements where only smaller forces are required. It can also be used in the calibration of vibration transducers, both to determine their sensitivity, by comparison with a standard accelerometer, as well as their frequency response, up to 18 kHz.

The suspension system consists of radial flexure springs that restrict the moving element to almost perfectly rectilinear motion. Laminated flexure springs provide a high degree of damping to minimise distortion due to flexure resonances.

The object to be vibrated is attached to the table by means of a 10–32 UNF screw, the thread size commonly used for mounting accelerometers. Performance limits defined by the maximum displacement (6 mm), maximum force (10 N or 7 N depending on frequency), and the first axial resonance of the moving element (above 18 kHz), are shown in Fig. 1.

Fig. 1
Sine performance curves for Type 4810

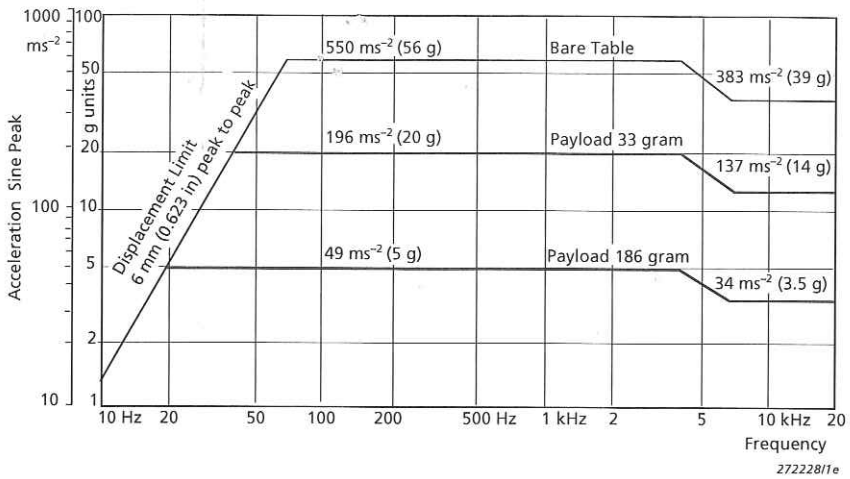

Specifications – Mini-shaker Type 4810

COMPLIANCE WITH STANDARDS
CE compliance with EMC Directive

compliance with EMC Requirements of Australia and New Zealand

Safety, EMC Emission and Immunity: According to relevant standards: EN 61010–1, IEC 61010–1, UL 3111–1, EN 50081–1/2, IEC 61000–6–1/2/3/4, EN 61326–1, CISPR22 Class B limits, FCC Rules Part 15, EN 50082–1/2, EN 61326–1
Temperature: According to IEC 60068–2–1 & IEC 60068–2–2
Operating temperature: +5 to +40°C (41 to 104°F)
Storage temperature: –25 to +70°C (–13 to 158°F)
Humidity: According to IEC 60068–2–3, Damp Heat: 90% RH (non-condensing at 40°C (104°F))
Mechanical: Non-operating according to IEC 60068–2–6, IEC 60068–2–27, IEC 60068–2–29

SPECIFICATIONS
FREQUENCY RANGE: DC to 18 kHz

FIRST MAJOR ARMATURE RESONANCE: Above 18 kHz

FORCE RATING (PEAK):
10 N (2.25 lbf). 65 Hz to 4 kHz
7 N (1.5 lbf). 65 Hz to 18 kHz

MAX. BARE TABLE ACCELERATION (PEAK):
550 m/s^2 (65 Hz to 4 kHz)
383 m/s^2 (6.5 kHz to 18 kHz)
(1 m/s^2 = 0.102 g)

MAX. DISPLACEMENT (PEAK-TO-PEAK): 6 mm (0.236 in)

DYNAMIC FLEXURE STIFFNESS: 2 N/mm (11.5 lb./in)

DYNAMIC WEIGHT OF THE MOVING SYSTEM: 18 grams

MAGNETIC FIELD: Permanent magnet

MAX. INPUT CURRENT: 1.8 A RMS

COIL IMPEDANCE: 3.5 Ω at 500 Hz

CONNECTION: Microsocket 10–32 UNF

TABLE SIZE: 14 mm (0.55 in) diameter

FASTENING THREAD: 10–32 UNF

WEIGHT: 1.1 kg (2.4 lb)

DIMENSIONS
Diameter: 76 mm (3 in)
Height: 75 mm (2.9 in)

Ordering Information

Type 4810	Mini-shaker
Includes the following accessories:	
AO 0069	Cable for connection of Type 4810 to Power Amplifier Type 2718
YQ 2962	Threaded Steel Stud, 0.3 in 10–32 UNF

Optional Accessories

EE 0112	ENDEVCO 2311-1 ISOTRON® Force Transducer
EE 0113	ENDEVCO 2311-10 ISOTRON Force Transducer
EE 0114	ENDEVCO 2311-100 ISOTRON Force Transducer
EE 0115	ENDEVCO 2311-500 ISOTRON Force Transducer
EE 0357	ENDEVCO Model 2312 Force Transducer
Type 8203	Force Transducer/Impact Hammer
UA 0125	Mounting Equipment (includes isolated studs YP 0150 and non-isolated studs YQ 2960)
WA 0429	Trunnion
WZ 0066	Nylon Stinger Kit
EE 5227-002	Bushing Adaptor, ¼–28 UNF to 10–32 UNF
EE 5004	Adaptor, Male 10–32 UNF to Male ¼–28 UNF
JP 0150	Adaptor, 4 mm Socket Pair to BNC Plug for use with old Type 2706

Brüel & Kjær reserves the right to change specifications and accessories without notice.

BP 0232–14 01/08

HEADQUARTERS: DK-2850 Nærum · Denmark · Telephone: +4545800500 · Fax: +4545801405 · http://www.bksv.com · e-mail: info@bksv.com
Australia (02)9450-2066 · Austria 0043-1-8657400 · Brazil (011)5182-8166 · Canada (514)695-8225 · China (86) 1068029906
Czech Republic 02-67021100 · Finland (0)9-755 950 · France (01)69907100 · Germany 06103/733 5-0 · Hong Kong 25487486 · Hungary (1)2158305
Ireland (01)803 7600 · Italy 02 57 68061 · Japan 03-3779-8671 · Republic of Korea (02)3473-0605 · Netherlands (31)318 559290 · Norway 66771155
Poland (22)858 9392 · Portugal (1)4711453 · Singapore (65) 377-4512 · Slovak Republic 421 2 5443 0701 · Spain (91)6590820 · Sweden (08)4498600
Switzerland (0)1 880 70 35 · Taiwan (02)7139303 · United Kingdom (0) 1438 739 000 · USA 800 332 2040
Local representatives and service organisations worldwide

D.4 ILD2300-10 Laser Triangulation Sensors

Extreme dynamic laser sensor with integrated controller

- **Six models with measuring ranges from 2 to 200mm**
- **Compact design with integrated controller**
- **Adjustable measuring rate up to 49.02kHz**
- **Ethernet / Ethercat / RS422**
- **Advanced Real Time Surface Compensation**
- **Calibration certificate included**
- **Measurement of diffuse and specular surfaces**
- **Thickness measurement of transparent materials**
- **Configuration via Web-Interface**

The optoNCDT 2300 is the latest high-end model of laser triangulation sensors from Micro-Epsilon. The new series offers an adjustable measuring rate up to 49.02 kHz. An impressive and worldwide unique fact regarding this sensor class is that the complete electronics has already been integrated in the compact sensor..

The new A-RTSC (Advanced Real-Time-Surface-Compensation) is a further development of the proven RTSC. Therefore, a more precise real-time surface compensation during the measuring process is ensured due to an increased dynamic range.
By means of the software, the threshold of the areas for compensation can be set easily.

The data are output via Ethernet, Ethercat or RS422. The complete sensor configuration is effected via a comfortably designed web interface.
The optoNCDT 2300 is especially used in the case of fast measurements such as vibration monitoring or measurements against challenging surfaces.

optoNCDT 2300-2 ... 2300-100
Diffuse reflection

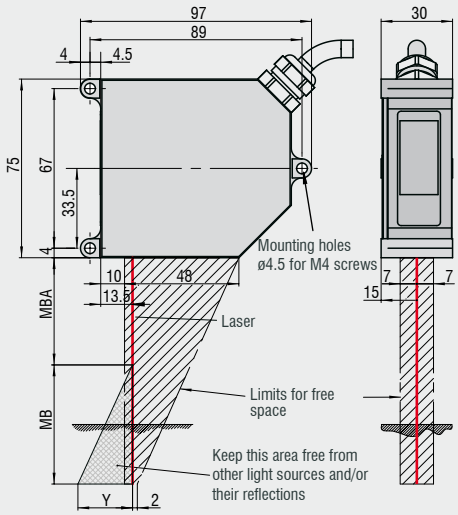

MR	SMR	Y
2	24	1.5
10	30	6.5
20	40	10.0
50	45	23.0
100	70	33.5

optoNCDT 2300-2 ... 2300-20
Direct reflection

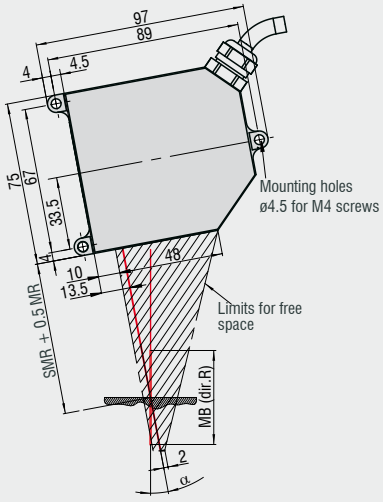

MR	SMR + 0.5 MR	α
2	25	20.5°
10	35	17.5°
20	50	13.8°

optoNCDT 2300-200

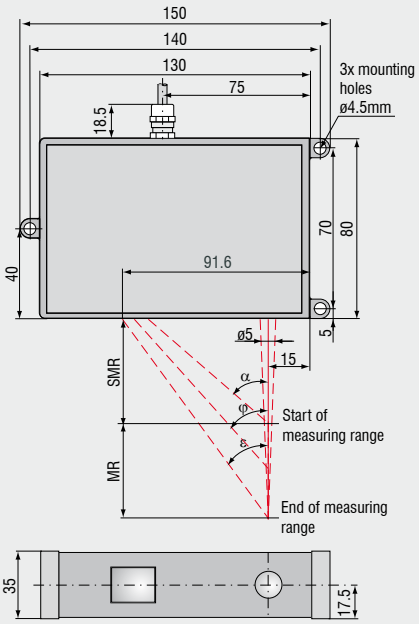

α	φ	ε
25.1°	16.7°	13.1°

Model		ILD 2300-2	ILD 2300-10	ILD 2300-20	ILD 2300-50	ILD 2300-100	ILD 2300-200
Measuring range [1]		2 (2) mm	10 (5 mm	20 (10) mm	50 (25) mm	100 (50) mm	200 (100) mm
Start of measuring range	SMR	24 (24) mm	30 (35) mm	40 (50) mm	45 (70) mm	70 (120) mm	130 (230) mm
Midrange	MMR	25 (25) mm	35 (37.5) mm	50 (55) mm	70 (82.5) mm	120 (145) mm	230 (280) mm
End of measuring range	EMR	26 (26) mm	40 (40) mm	60 (60) mm	95 (95) mm	170 (170) mm	330 (330) mm
Linearity		0.6µm	2µm	4µm	10µm	20µm	60µm
		≤ ±0.03% FSO	≤ ±0.02% FSO				≤ ±0.03% FSO
Resolution (20kHz)		0.03 µm	0.15µm	0.3µm	0.8µm	1.5µm	3µm
		0.0015% FSO					
Measuring rate		adjustable via software 49.02 / 30 / 20 / 10 / 5 / 2.5 / 1.5kHz (49.02kHz with reduced measuring range)					
Permissable ambient light		10,000…40,000lx					
Spot diameter	SMR	80µm	110µm	160µm	215µm	350µm	1300µm
	MMR	23 x 23µm	32 x 45µm	46 x 45µm	70 x 70µm	130µm	1300µm
	EMR	35 x 85µm	110 x 160µm	140 x 200µm	255 x 350µm	350µm	1300µm
Light source		semiconductor laser <1mW / 670nm (red)					
Protection class		IP 65					
Operation temperature		0 ... +50°C					
Storage temperature		-20 ... +70°C					
Inputs / Outputs		Ethernet / Ethercat RS422 analogue ouput via CSP2008					
Inputs		Laser on/off; synchronization/trigger input					
Power supply		24 Vdc (11…30V); PV < 3W					
LED		Status / Power / Ethernet / Ethercat					
Sensor cable	Standard	0.25m (with cable connector)					
	Option	3 / 6 / 9m with Sub D 15 pin connector					
Electromagnetic compatibility (EMC)		EN 61326-1: 2006-10 DIN EN 55011: 2007-11 (group 1. class B) EN 61 000-6-2: 2006-03					
Vibration		2g / 20 ... 500Hz					
Shock		15g / 6ms / 3 axes					

FSO = Full Scale Output All specifications apply for a diffusely reflecting matt white ceramic target
SMR = Start of measuring range MMR = Midrange EMR = End of measuring range
[1] Numbers in brackets refer to full measurement rate 49.02 kHz

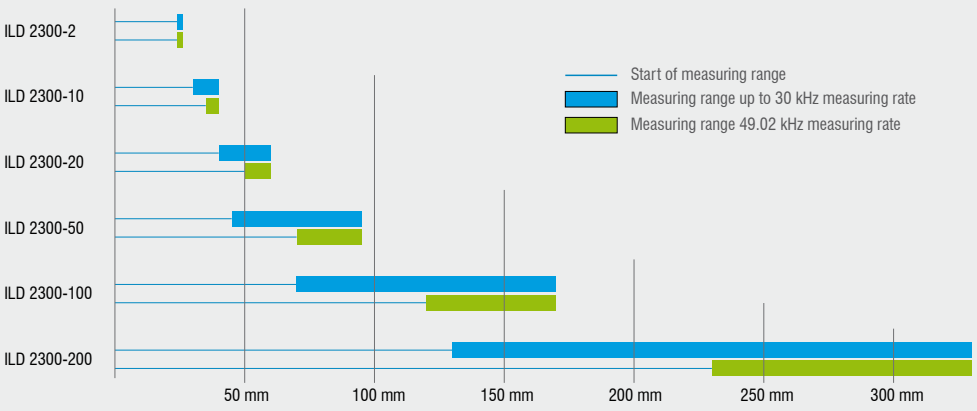

D.5 B&K Piezoelectric Accelerometer Type 8305

PRODUCT DATA

Piezoelectric Accelerometer
Standard Reference Accelerometer — Type 8305

FEATURES

- Calibration traceable to the National Institute of Standards and Technology
- Laser interferometry calibration of reference sensitivity in accordance with ISO 5347
- Excellent isolation from base strains and low sensitivity to loading

Description

Type 8305 is a piezoelectric accelerometer with side connector. The transducer features two 10–32 UNF receptacles for input/output connection. It can be mounted on the object by means of a 10–32 UNF threaded steel stud. The accelerometer subject to calibration, is mounted on top of Type 8305, also by means of a 10–32 UNF threaded steel stud.

Characteristics

This piezoelectric accelerometer may be treated as a charge source. Its sensitivity is expressed in terms of charge per unit acceleration (pC/g).

In order to ensure a high degree of accuracy for calibration, Type 8305 is based on an inverted, centre-mounted compression design. This construction isolates the active element of the accelerometer from base strains and gives a low transverse sensitivity.

The piezoelectric element used in Type 8305 is the PZ 100 quartz crystal. The housing material is stainless steel.

Calibration

The sensitivity given in the calibration chart has been measured at 160 Hz with an acceleration of 100 ms^{-2}.

For a 99.9% confidence level, the accuracy of the factory calibration is ±2%.

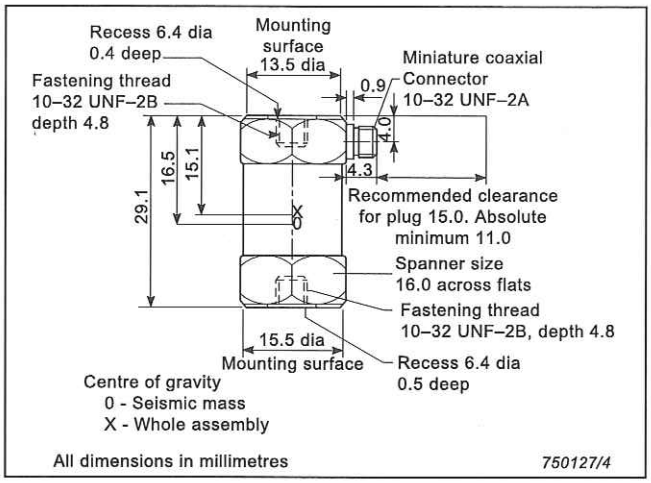

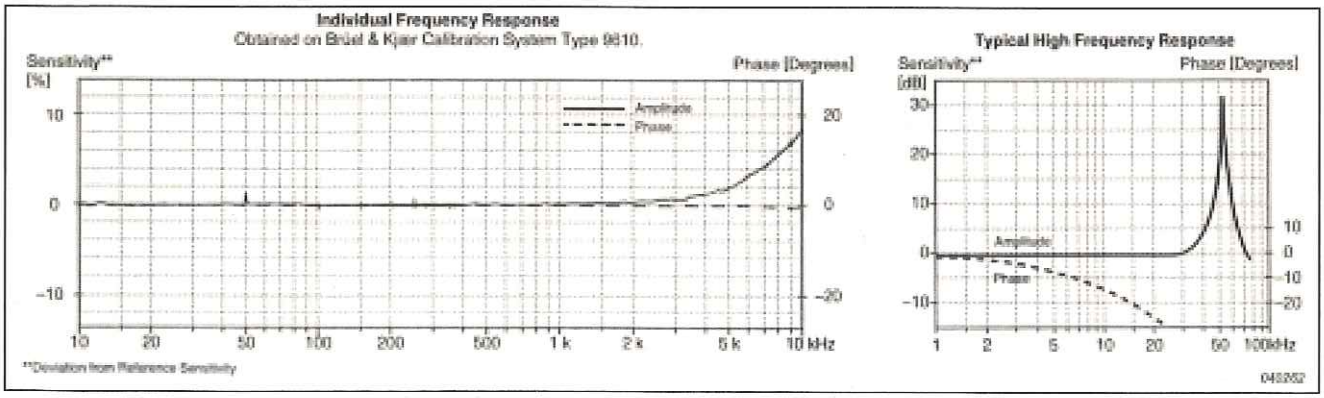

Brüel & Kjær

0,048

Specifications – Standard Reference Accelerometer Type 8305

	Units	8305
Dynamic Characteristics		
Charge Sensitivity (@ 160 Hz)	pC/g	1.25
Frequency Response		See typical amplitude curve
Mounted Resonance Frequency	kHz	38
Amplitude Response [1]: ±2% ±1%	Hz	0.2 to 4400 0.2 to 3100
Transverse Sensitivity	%	<2
Electrical Characteristics		
Min. Leakage Resistance @ 20°C	GΩ	1000
Capacitance	pF	180
Grounding		Signal ground
Environmental Characteristics		
Temperature Range	°C (°F)	–74 to 200 (–101 to 392)
Humidity		Welded, sealed
Max. Operational Sinusoidal Vibration (peak)	g pk	1000
Max. Operational Shock (± peak)	g pk	1000
Base Strain Sensitivity	Equiv. g/μ strain	Top: 0.001 Base: 0.0003
Thermal Transient Sensitivity	Equiv. g/°C (g/°F)	0.05 (0.028)
Magnetic Sensitivity (50 Hz–0.03 Tesla)	g/T	0.1
Physical Characteristics		
Dimensions		See outline drawing
Weight	gram (oz.)	40 (0.58)
Case Material		Stainless steel
Connector		10–32 UNF
Mounting		10–32 UNF threaded hole

[1] Low-end response of the transducer is a function of its associated electronics

Ordering Information

Type 8305 Includes the following accessories:

- AO 0038: 260°C Teflon® low-noise cable, 10–32 UNF, length 1.2 m (4 ft.)
- YQ 2962: 10–32 UNF threaded steel stud. Length 7.62 mm
- YQ 2960: 10–32 UNF threaded steel stud. Length 12.7 mm
- UA 0329 Accessory Box

HEADQUARTERS: DK-2850 Nærum · Denmark · Telephone: +45 4580 0500 · Fax: +45 4580 1405
www.bksv.com · info@bksv.com

Australia (+61) 2 9889-8888 · Austria (+43) 1 865 74 00 · Brazil (+55) 11 5188-8166 · Canada (+1) 514 695-8225
China (+86) 10 680 29906 · Czech Republic (+420) 2 6702 1100 · Finland (+358) 9-521 300 · France (+33) 1 69 90 71 00
Germany (+49) 421 17 87 0 · Hong Kong (+852) 2548 7486 · Hungary (+36) 1 215 83 05 · Ireland (+353) 1 807 4083
Italy (+39) 0257 68061 · Japan (+81) 3 5715 1612 · Korea (+82) 2 3473 0605 · Netherlands (+31) 318 55 9290
Norway (+47) 66 77 11 55 · Poland (+48) 22 816 75 56 · Portugal (+351) 21 47 11 4 53 · Singapore (+65) 6377 4512
Slovak Republic (+421) 25 443 0701 · Spain (+34) 91 659 0820 · Sweden (+46) 8 449 8600
Switzerland (+41) 44 880 7035 · Taiwan (+886) 2 2502 7255 · United Kingdom (+44) 14 38 739 000
USA (+1) 800 332 2040

Local representatives and service organisations worldwid

Brüel & Kjær

BP 2052 – 11 05/06 Rosendahls Bogtrykkeri

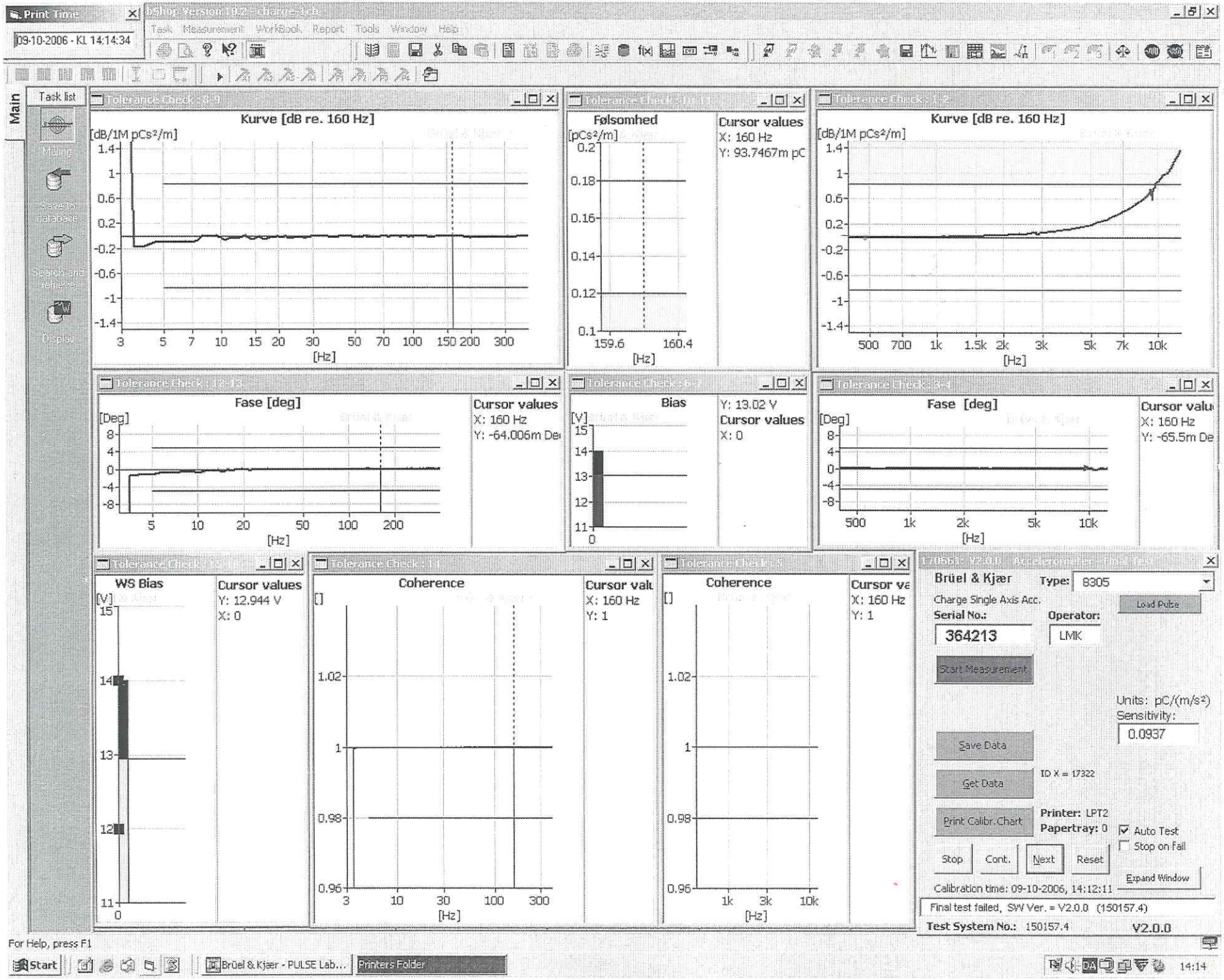
Print Time
09-10-2006 - KL 14:14:34
Task Measurement WorkBook Report Tools Window Help
Main
Task list
Tolerance Check - 8-0
Kurve [dB re. 160 Hz]
[dB/1M pCs²/m]
[Hz]
Følsomhed
[pCs²/m]
Cursor values
X: 160 Hz
Y: 93.7467m pC
Tolerance Check - 8-2
Kurve [dB re. 160 Hz]
[dB/1M pCs²/m]
[Hz]
Tolerance Check - 8-3
Fase [deg]
[Deg]
Cursor values
X: 160 Hz
Y: -64.006m De
[Hz]
Tolerance Check - 8-1
Bias
[V]
Y: 13.02 V
Cursor values
X: 0
Tolerance Check - 8-4
Fase [deg]
[Deg]
Cursor valu
X: 160 Hz
Y: -65.5m De
[Hz]
Tolerance Check - 10-0
WS Bias
[V]
Cursor values
Y: 12.944 V
X: 0
Tolerance Check - 10-1
Coherence
[]
Cursor valu
X: 160 Hz
Y: 1
[Hz]
Tolerance Check - 10-2
Coherence
[]
Cursor va
X: 160 Hz
Y: 1
[Hz]
Brüel & Kjær
Type: 8305
Charge Single Axis Acc.
Load Pulse
Serial No.:
364213
Operator:
LMK
Start Measurement
Units: pC/(m/s²)
Sensitivity:
0.0937
Save Data
Get Data
ID X = 17322
Print Calibr. Chart
Printer: LPT2
Papertray: 0
Auto Test
Stop on Fail
Stop
Cont.
Next
Reset
Expand Window
Calibration time: 09-10-2006, 14:12:11
Final test failed, SW Ver. = V2.0.0 (150157.4)
Test System No.: 150157.4
V2.0.0
For Help, press F1
Start
Brüel & Kjær - PULSE Lab...
Printers Folder
14:14

D.6 Charge Amplifier

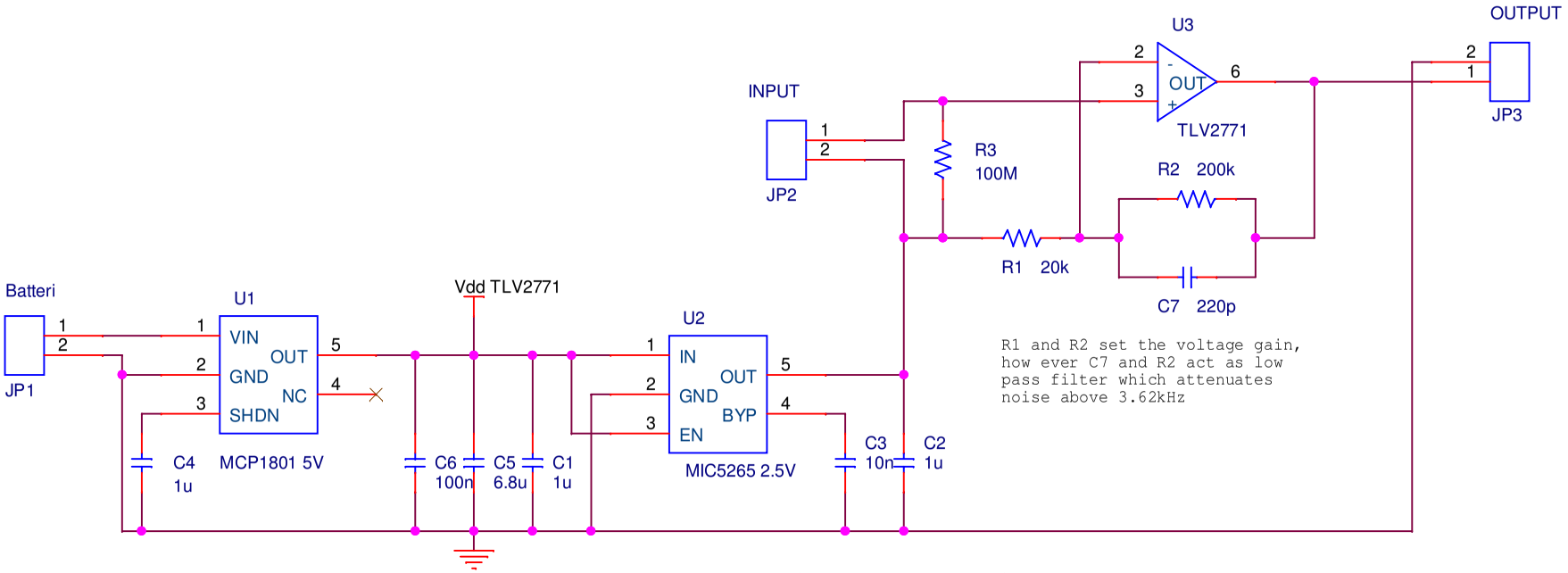

-Vdd of TLV2771 are tired to GND and Vdd til 5V
Then Input signal is rised to 2.5V so that
signal from the acc operates symetricly around
2.5V istead of 0V this allow a single supply
aka Vdd and GND.

Title <Title>		
Size A	Document Number <Doc>	Rev <RevCode>
Date: Thursday, November 08, 2012	Sheet 1 of 1	

Appendix E

Uniformity Characterisation Mappings

E.1 SOI Wafers: C, $F_{\mathbf{res}}$ and V_{oc}

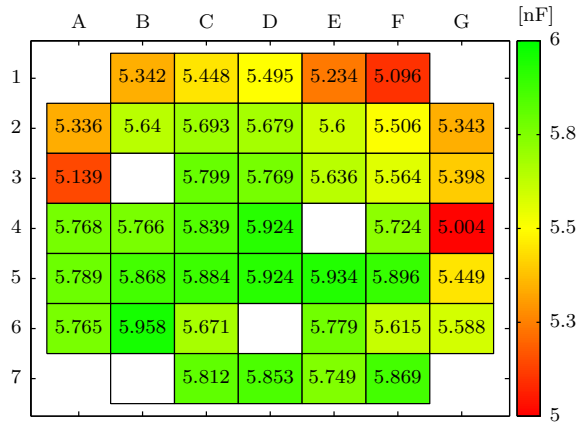

(a) *SOIW1: Capacitance mapping.*

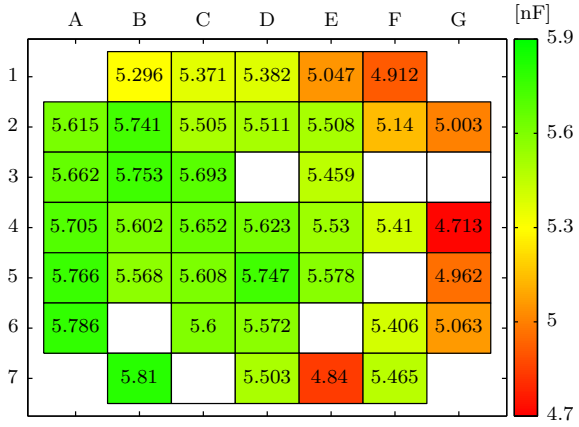

(b) *SOIW2: Capacitance mapping.*

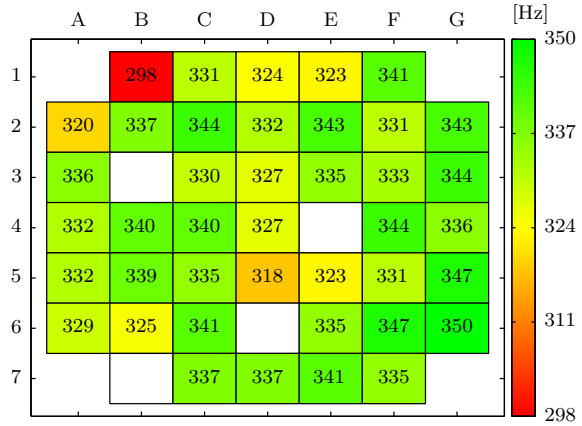

(c) *SOIW1: Resonant frequency.*

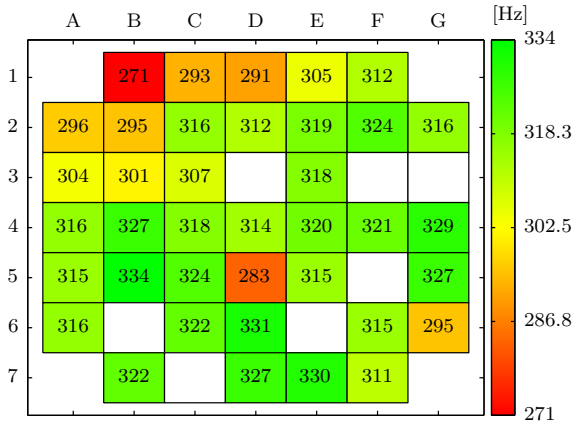

(d) *SOIW2: Resonant frequency.*

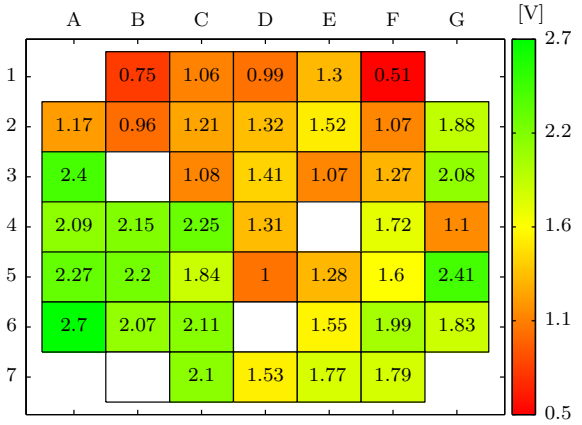

(e) *SOIW1: Voltage mapping.*

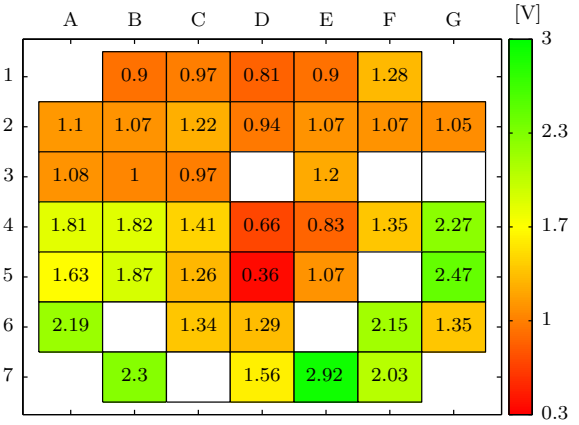

(f) *SOIW2: Voltage mapping.*

Figure E.1: *Measured quantities listed as wafer layout with major flat towards south.*

E.2 Si Wafers: C, $F_{\mathbf{res}}$ and $F_{\mathbf{BW}}$

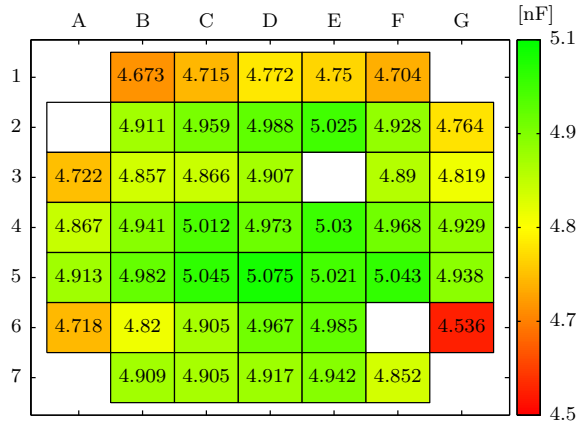

(a) *SiW1: Capacitance mapping.*

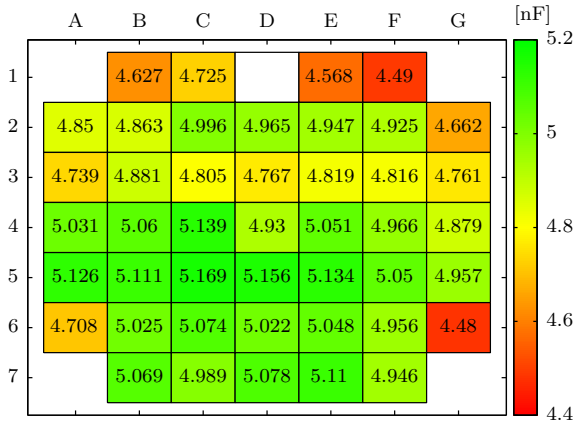

(b) *SiW2: Capacitance mapping.*

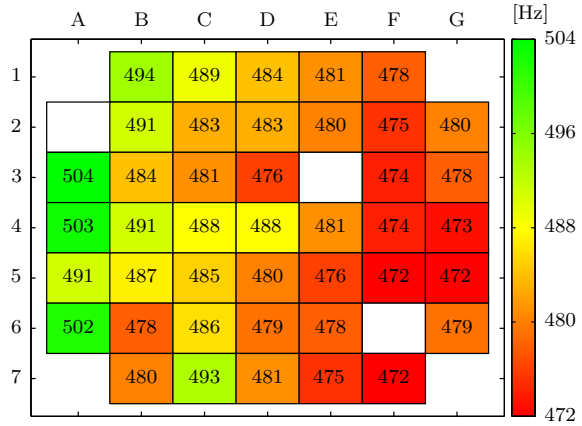

(c) *SiW1: Frequency mapping.*

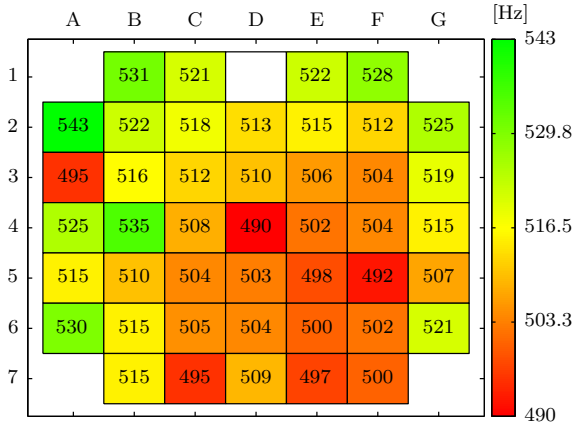

(d) *SiW2: Frequency mapping.*

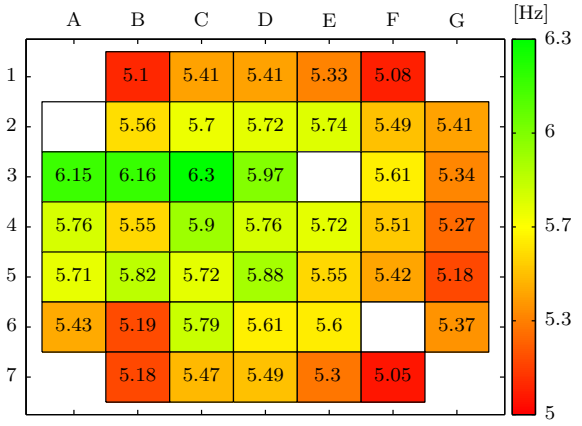

(e) *SiW1: Power spectrum bandwidth.*

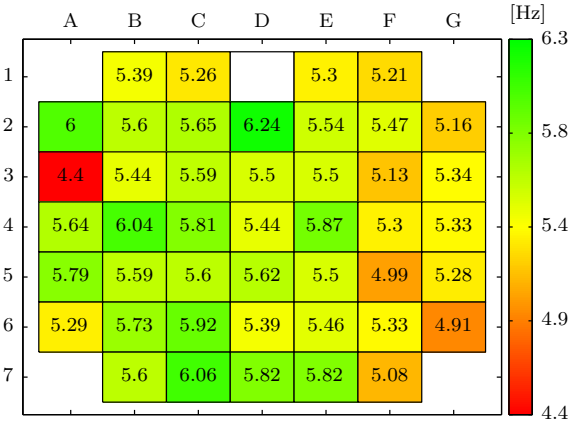

(f) *SiW2: Power spectrum bandwidth.*

Figure E.2: *Measured quantities listed as wafer layout with major flat towards south.*

E.3 Si Wafers: P, $K_{\mathbf{eff}}$ and $Q_{\mathbf{load}}$

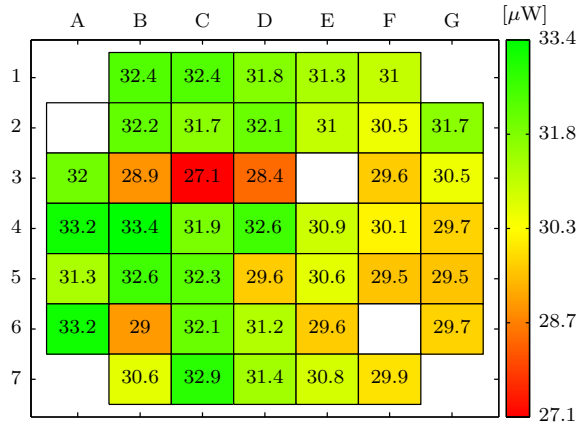

(a) *SiW1: Power mapping.*

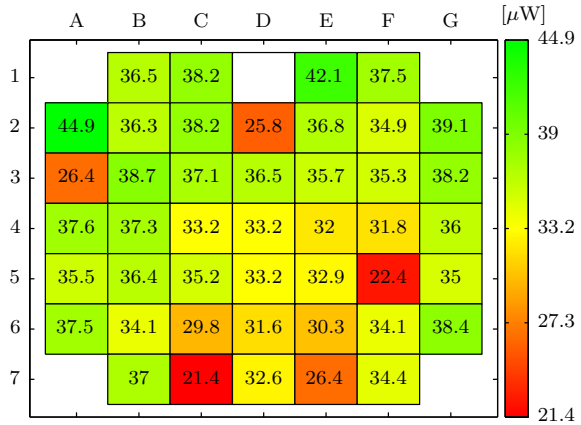

(b) *SiW2: Power mapping.*

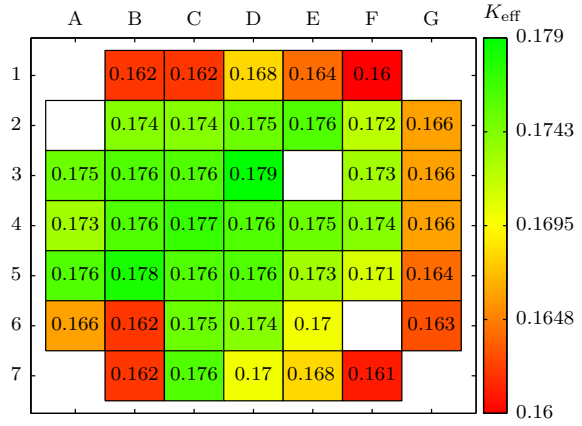

(c) *SiW1: Effective system coupling.*

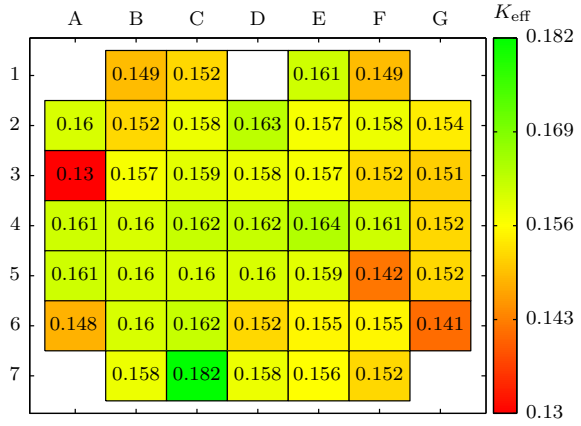

(d) *SiW2: Effective system coupling.*

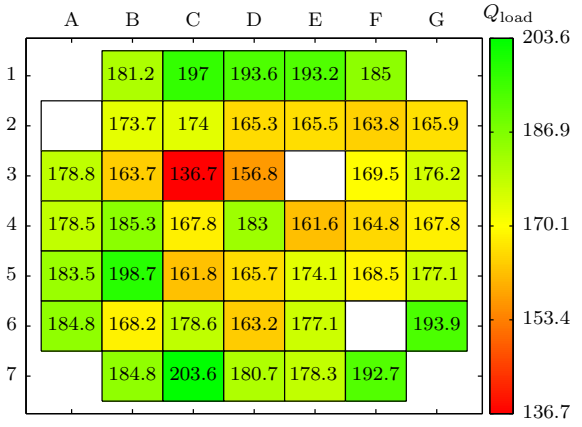

(e) *SiW1: Loaded quality factor.*

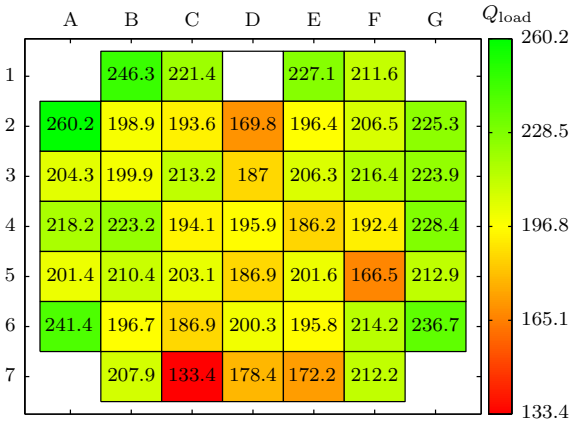

(f) *SiW2: Loaded quality factor.*

Figure E.3: *Measured quantities listed as wafer layout with major flat towards south.*